Conference Proceedings of the Society for Experimental Mechanics Series

Leslie E. Lamberson *Editor*

Dynamic Behavior of Materials, Volume 1

Proceedings of the 2019 Annual Conference on Experimental and Applied Mechanics

SEM

Springer

Conference Proceedings of the Society for Experimental Mechanics Series

Series Editor

Kristin B. Zimmerman, Ph.D.
Society for Experimental Mechanics, Inc.,
Bethel, CT, USA

The Conference Proceedings of the Society for Experimental Mechanics Series presents early findings and case studies from a wide range of fundamental and applied work across the broad range of fields that comprise Experimental Mechanics. Series volumes follow the principle tracks or focus topics featured in each of the Society's two annual conferences: IMAC, A Conference and Exposition on Structural Dynamics, and the Society's Annual Conference & Exposition and will address critical areas of interest to researchers and design engineers working in all areas of Structural Dynamics, Solid Mechanics and Materials Research.

More information about this series at http://www.springer.com/series/8922

Leslie E. Lamberson
Editor

Dynamic Behavior of Materials, Volume 1

Proceedings of the 2019 Annual Conference on Experimental and Applied Mechanics

Springer

Editor
Leslie E. Lamberson
Mechanical Engineering
Drexel University
Philadelphia, PA, USA

ISSN 2191-5644 ISSN 2191-5652 (electronic)
Conference Proceedings of the Society for Experimental Mechanics Series
ISBN 978-3-030-30020-3 ISBN 978-3-030-30021-0 (eBook)
https://doi.org/10.1007/978-3-030-30021-0

This Springer imprint is published by the registered company Springer Nature Switzerland AG.
The registered company address is: Gewerbestrasse 11, 6330 Cham, Switzerland

Preface

Dynamic Behavior of Materials represents one of six volumes of technical papers presented at the 2019 SEM Annual Conference and Exposition on Experimental and Applied Mechanics organized by the Society for Experimental Mechanics and held in Reno, NV, June 3–6, 2019. The complete proceedings also include volumes on *Challenges in Mechanics of Time-Dependent Materials; Fracture, Fatigue, Failure and Damage Evolution; Advancement of Optical Methods & Digital Image Correlation in Experimental Mechanics; Mechanics of Biological Systems and Materials & Micro- and Nanomechanics; Mechanics of Composite, Hybrid and Multifunctional Materials; and Residual Stress, Thermomechanics & Infrared Imaging and Inverse Problems.*

Each collection presents early findings from experimental and computational investigations on an important area within Experimental Mechanics. Dynamic Behavior of Materials is one of these areas.

The Dynamic Behavior of Materials track was initiated in 2005 and reflects our efforts to bring together researchers interested in the dynamic behavior of materials and structures and to provide a forum to facilitate technical interaction and exchange. Over the years, this track has been representing the ever-growing interests in dynamic behavior to the SEM community, working toward expanding synergy with other tracks and topics, and improving diversity and inclusivity, as evidenced by the increasing number and diversity of papers and attendance.

The contributed papers span numerous technical divisions within SEM, demonstrating its relevance not only in the dynamic behavior of materials community but also in the mechanics of materials community as a whole. The track organizers thank the authors, presenters, organizers, and session chairs for their participation, support, and contribution to this track. The SEM support staff is also acknowledged for their devoted efforts in accommodating the large number of paper submissions this year, making the 2019 Dynamic Behavior of Materials track a success.

Philadelphia, PA, USA — Leslie E. Lamberson
Gaithersburg, MD, USA — Steven Mates
San Diego, CA, USA — Veronica Eliasson

Contents

Chapter 1
Dynamic Tensile Behavior of Soft Ferromagnetic Alloy Fe-Co-2V

Brett Sanborn, Bo Song, Don Susan, Kyle Johnson, Jeff Dabling, Jay Carroll, Adam Brink, Scott Grutzik, and Andrew Kustas

Abstract Fe-Co-2V is a soft ferromagnetic alloy used in electromagnetic applications due to excellent magnetic properties. However, the discontinuous yielding (Luders bands), grain-size-dependent properties (Hall-Petch behavior), and the degree of order/disorder in the Fe-Co-2V alloy makes it difficult to predict the mechanical performance, particularly in abnormal environments such as elevated strain rates and high/low temperatures. Thus, experimental characterization of the high strain rate properties of the Fe-Co-2V alloy is desired, which are used for material model development in numerical simulations. In this study, the high rate tensile response of Fe-Co-2V is investigated with a pulse-shaped Kolsky tension bar over a wide range of strain rates and temperatures. Effects of temperature and strain rate on yield stress, ultimate stress, and ductility are discussed.

Keywords Kolsky tension bar · Fe-Co-2V alloy · Temperature effects · Magnetic · Material properties

Introduction

Soft ferromagnetic alloys are used in electromagnetic applications where good magnetic properties are needed. Fe-Co-2V is an example of a soft ferromagnetic alloy used in magnetic bearings and electrical generators. While Fe-Co-2V was chosen for these applications due to its desirable magnetic properties, the material may undergo mechanical loading at different rates and temperatures. Quasi-static tension experiments have been conducted on Fe-Co-2V up to 800 °C [1]. The behavior was elastic, followed by a plastic plateau (Lüders banding) before significantly hardening. In general, the yield strength increased with increasing strain rate. When the temperature was below 300 °C, the yield strength decreased with increasing temperature. The yield strength of the material as highly dependent on grain size, which followed a Hall-Petch relationship. Despite being well-characterized quasi-statically at elevated temperatures, Fe-Co-2V used in applications may be subjected to impact loading at elevated or even low temperatures. Hence, the high rate tensile response over a range of temperatures is needed to improve material models used in numerical simulations for improved design. In this study, the dynamic properties of Fe-Co-2V were investigated over a wide range of strain rates and temperatures.

Materials and Experiments

In this study, Fe-Co-2V alloy was characterized over strain rates from 40 to 230 s^{-1} using two different experimental setups. Intermediate rate experiments (40–110 s^{-1}) were conducted on a drop-Hopkinson bar setup wherein a drop table is used to provide a long loading pulse at a speed lower than what is usually conducted with a Kolsky/split Hopkinson bar. Experiments at 230 s^{-1} were conducted with a Kolsky tension bar. The Kolsky tension bar had a thermal chamber installed at the testing section which subjected the material to a temperature range of −100 to 100 °C. A recently developed specimen-strain correction method [2] was applied to the dynamic tensile tests of the Fe-Co-2V alloy such that the specimen stress-strain response over the gage section was obtained.

B. Sanborn (✉) · B. Song · D. Susan · K. Johnson · J. Dabling · J. Carroll · A. Brink · S. Grutzik · A. Kustas
Sandia National Laboratories, Albuquerque, NM, USA
e-mail: bsanbor@sandia.gov

L. E. Lamberson (ed.), *Dynamic Behavior of Materials, Volume 1*, Conference Proceedings of the Society for Experimental Mechanics Series, https://doi.org/10.1007/978-3-030-30021-0_1

Strain Rate and Temperature Effects

Stress-strain curves for the Fe-Co-2V alloy at 40, 110, and 230 s^{-1} at ambient temperature are shown in Fig. 1.1. A quasi-static stress-strain curve is also shown for comparison. As shown in Fig. 1.1, the upper yield strength increased with increasing strain rate. At low strain rates, the stress-strain curves showed a typical Lüders banding response prior to hardening. However, at high strain rates, i.e., 230 s^{-1}, the material exhibited a significant upper and lower yield response.

The effect of temperature on material response at a strain rate of 230 s^{-1} is shown in Fig. 1.2. While the overall shape of the stress-strain curve is similar at different temperatures, the yield and flow stresses increased with decreasing temperature.

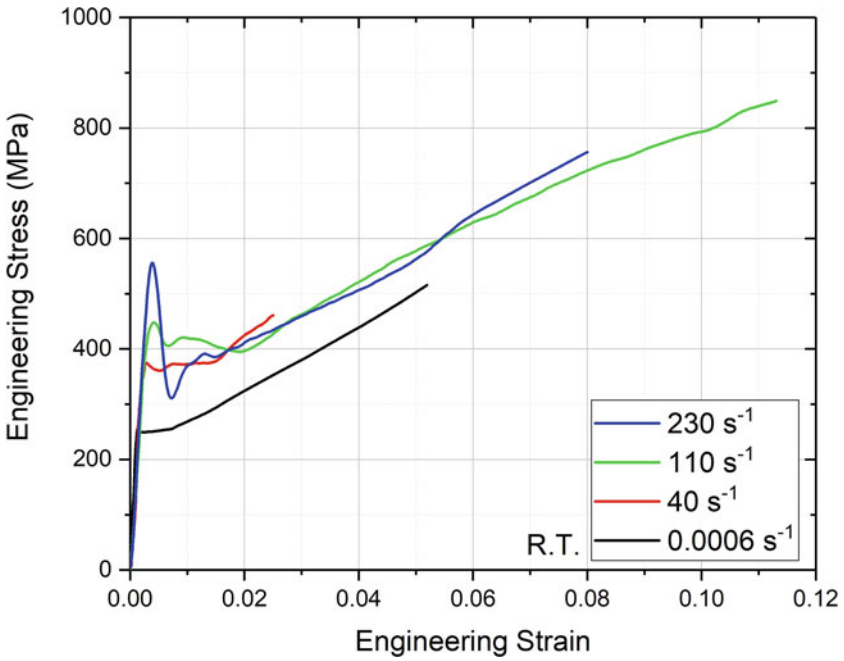

Fig. 1.1 Stress-strain behavior of Fe-Co-2V at various strain rates at 20 °C

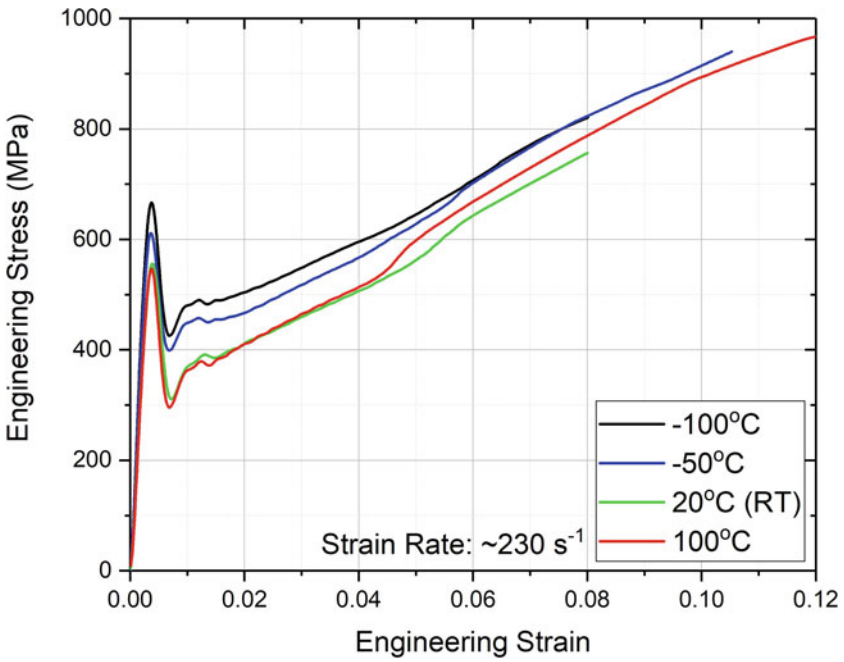

Fig. 1.2 Tensile stress-strain curves at various temperatures at a strain rate of 230 s^{-1}

The upper yield stress increased about 18% at −100 °C compared to ambient temperature. No necking was observed for any of the failed specimens at any of the temperatures.

Conclusion

The strain rate- and temperature-dependent tensile properties of Fe-Co-2V alloy were measured using a Kolsky bar and drop-Hopkinson bar. The material displayed an elastic, followed by either upper/lower yield behavior at high strain rates or a Lüders banding behavior at lower rates, prior to linearly hardening until failure. The specimens failed in a brittle manner. The yield stress increased with increasing strain rate, while the hardening rate was constant. The yield strength of the material increased with decreasing temperature. The hardening rate was independent of temperature. The material behavior measured in this study can be used for material model development.

Acknowledgements Sandia National Laboratories is a multimission laboratory managed and operated by National Technology and Engineering Solutions of Sandia, LLC, a wholly owned subsidiary of Honeywell International, Inc., for the U.S. Department of Energy's National Nuclear Security Administration under contract DE-NA0003525. The views expressed in the article do not necessarily represent the views of the U.S. Department of Energy or the United States Government.

References

1. Ren, L., Basu, S., Yu, R.-H., Xiao, J.Q., Parvizi-Majidi, A.: Mechanical properties of Fe-Co soft magnets. J. Mater. Sci. **36**, 1451–1457 (2001)
2. Song, B., Sanborn, B., Susan, D., Johnson, K., Dabling, J., Carroll, J., Brink, A., Grutzik, S., Kustas, A.: Correction of specimen strain measurement in Kolsky tension bar experiments on linear work-hardening materials, 2019 SEM Annual Conference on Experimental and Applied Mechanics, June 3–6, 2019, Reno, NV (2019)

Chapter 2
Toward Paradoxical Inconsistency in Electrostatics of Metallic Conductors

Michael Grinfeld, Pavel Grinfeld, and Steven B. Segletes

Abstract In a recent report, we drew attention to the paradoxical inconsistency of classical electrostatics with the model of a crystalline conductor. There are different ways to avoid this inconsistency. Mostly, they rely on physical *ad hoc* assumptions associated with the introduction of additional constants and models of charged liquids. In this report, we suggest another approach, which does not require the introduction of any additional physical constants. The proposed theory includes classical electrostatics as a special case.

Keywords Electrostatics · Laplace and Poisson equations · Simple layers · Thermodynamics

Introduction

Electromagnetism is in the background of various military applications, including the problem of protection against shaped charges, which Russian adversaries call "cumulative" jets [1].

One of the many problems faced in the computer implementation of physical models is associated with the fact that certain physical fields experience discontinuities across boundaries and interfaces. Some fields (the models thereof) even become infinitely large when approaching such interfaces. Theorists have accumulated various sophisticated mathematical tools for handling these problems when treating the problems analytically. The problem of infinite charge density in the vicinity of boundaries in metals is further aggravated when using numerical modeling, since the singularities in the underlining physical theories are in violent discord with the inability of finite discretizations to handle sharp gradients. One of the methods for handling this violent discord is based on the replacement of the classical physical theories with modified ones that allow for the avoidance of infinite charge density at the boundaries. We suggested one approach of this sort in a prior report [2] and continue developing the approach in this one.

Let us recall the paradoxical inconsistency of classical electrostatics first noted in our prior report [2]. According to classical electrostatics, all excess electric charges, positive or negative, concentrate on the conductor's boundary with a finite 2-D density. In mathematical physics, these sort of boundaries are known as "simple layers" of charges [3, 4]. This surface density can be either positive or negative, depending on the total excess charge of the conductor. What is the physical meaning of this finite 2-D density of electric charge? Actually, this concept implies that the associated 3-D density of the electric charge is infinite. Of course, this infinity, on its own, is an essential inconsistency of classical electrostatics. However, in many cases, this particular limitation is not very important and classical electrostatics provides researchers with reasonable results [3, 4]. It is not, however, this inconsistency that we discussed in our prior work [2].

The paradoxical inconsistency that we introduced [2] is different. In fact, the density of the easily movable negative charges can grow and reach quite large values (for example, on the surface of a body), in accordance with classical electrostatics. If the positive charges are easily movable and compressible also, like in the case of ionized gas, the same can be said about the gas of positive ions. In this sense, classical electrostatics can be applied to a gaseous plasma. The situation, however, changes dramatically when the positive charges belong to a (near rigid) lattice. In this case, the maximum positive charge density is basically fixed, and we cannot expect that it might assume infinite values, even in an idealized sense. In other words, there cannot be *surfaces* (or *interfaces*) with finite positive charges—excess positive charge can only

M. Grinfeld (✉) · S. B. Segletes
Weapons and Materials Research Directorate, Army Research Laboratory, Aberdeen Proving Ground, MD, USA

P. Grinfeld
Drexel University, Philadelphia, PA, USA

L. E. Lamberson (ed.), *Dynamic Behavior of Materials, Volume 1*, Conference Proceedings of the Society for Experimental Mechanics Series, https://doi.org/10.1007/978-3-030-30021-0_2

manifest in *regions* (*i.e.*, *domains*). Thus, we deal in this case with the asymmetry of how to treat the situations of negative *versus* positive excess charge. This very asymmetry dictates the necessity to revise classical electrostatics.

To address this inconsistency, we have to reformulate classical electrostatics in such a way that nowhere does the positive 3-D charge density exceeding the value q_+ appear.

A Simple Consistent Model of Electrostatics to Avoid the Paradoxical Inconsistency

We propose the following model of a crystalline rigid conductor. The model is shown schematically in Fig. 2.1.[1]

The key suggestion is the following: the total domain Ω of the conductor is split into two subdomains, Ω_n and Ω_a. Generally speaking, both subdomains may comprise several separate regions. In Fig. 2.1, the subdomains of Ω_n are shown in gray, whereas the subdomains of Ω_a are shown in red. We assume that, in Ω_n, the macroscopic density of both positive and negative charges (q_+ and q_-, respectively) are equal to each other. Thus, the net macroscopic charge density q vanishes in Ω_n:

$$q = q_+ + q_- = 0 \qquad \text{within } \Omega_n. \tag{2.1}$$

Within the subdomain Ω_a, our assumption is different. We just assume that the density of negative charges q_- vanishes; in other words, we arrive at the following relationships:

$$q_- = 0, \quad q = q_+ \qquad \text{within } \Omega_a. \tag{2.2}$$

Thus, by the construction, the positive charge density exceeds the value q_+ nowhere.

Also, from Fig. 2.1, we point out that, between the two Ω domains and between each domain and the vacuum surround, we postulate zero-thickness interface layers. These interfaces are denoted Σ, S_a, and S_n and are further described and analyzed later in this report.

Let us formulate the system of equations in the mathematical form of a boundary value problem. In view of Eqs. 2.1 and 2.2, the electrostatics bulk equations inside the domains Ω_n and Ω_a read

$$\nabla^i \nabla_i \varphi = 0 \tag{2.3}$$

and

$$\nabla^i \nabla_i \varphi = -4\pi q_+ \quad , \tag{2.4}$$

respectively.

Outside the external boundary S (the union of S_n and S_a), we also have to use the Poisson equation

$$\nabla^i \nabla_i \varphi = -4\pi q_{\text{ext}} \quad , \tag{2.5}$$

where q_{ext} is a given distribution of the external sources of the electrostatic field.

Within the domain Ω_n (with the mobile negative charges potentially on the adjoining interface), the electrostatic potential is assumed constant everywhere:

$$\varphi = \varphi_0 = \text{const.} \qquad \text{inside } \Omega_n \quad , \tag{2.6}$$

as always in classical electrostatics. Equation 2.6 automatically satisfies the electrostatics Eq. 2.3; thus, there is no need to deal with the Laplace equation (Eq. 2.3) inside the domain Ω_n.

[1] In this and the figures to follow (though its justification remains to be assumed or derived later in this report), one may follow the heuristic rule-of-thumb that dark- and light-gray denote electrically neutral domains and interfaces, respectively, red denotes a domain void of negative charges, while blue denotes an interface comprised solely of mobile negative charges and characterized by a surface charge density.

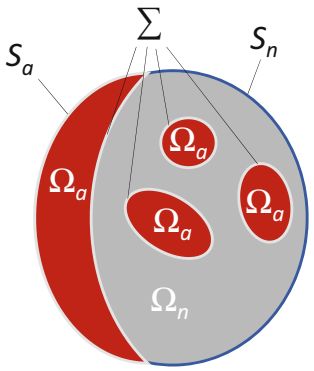

Fig. 2.1 The cross-sectional (cutaway) geometry of a conductor

Let us now discuss the boundary conditions for our bulk equations of electrostatics. Per Fig. 2.1, a priori, there are three sorts of zero-thickness interfaces. First, there are interfaces S_n between the domain Ω_n and vacuum. Secondly, there are interfaces S_a between the domain Ω_a and vacuum. Lastly, there are interfaces Σ between the domains Ω_n and Ω_a. For all three types of interfaces, the boundary conditions are different:

1. We begin with the S_n interfaces. Those are the traditional interfaces of classical electrostatics, possessing the boundary conditions

$$\begin{aligned} \left[\varphi\right]_{-}^{+} &= 0 \\ N^i \nabla_i \varphi\big|_{S_n} &= -4\pi\sigma_{S_n} \end{aligned} \tag{2.7}$$

   where N^i is the interface's outward normal and σ_{S_n} is the 2-D density of the surface charges. The former of the boundary conditions given as Eq. 2.7 reflects the continuity of the electrostatic potential; the latter is the consequence of the Gauss law applied to the interface with the finite 2-D density of electric charges (the so-called "simple layer of charges"). It is essential that this density is negative since only negative charges are mobile and are able to generate the unlimited 3-D density of the electric charge (as the boundary layer near S_n approaches zero thickness).
2. We proceed with the S_a interfaces. Since, by the postulated models, there are no surface charges at these interfaces, we suggest using the standard boundary conditions of continuity of electrostatic potential and its first derivatives:

$$\begin{aligned} \left[\varphi\right]_{-}^{+} &= 0 \\ \left[\nabla_i \varphi\right]_{-}^{+} N^i &= 0 \end{aligned} \quad . \tag{2.8}$$

3. Finally, we consider the Σ-interfaces, separating the Ω_n and Ω_a domains. Across those interfaces, we are still using the electrostatics boundary conditions

$$\begin{aligned} \left[\varphi\right]_{-}^{+} &= 0 \\ \left[\nabla_i \varphi\right]_{-}^{+} N^i &= -4\pi\sigma_{an} \end{aligned} \tag{2.9}$$

Thus, a priori, we assume that there can be 2-D accumulations of the negative charges. This is a quite plausible assumption for the Σ-interfaces since there is a source of negative mobile charges from the domain Ω_n.

There is, however, a significant difference between the S_n and S_a interfaces, on the one hand, and the Σ interfaces, on the other hand. The difference is the following: the location of S_n and S_a are known up-front, from the conductor geometry, whereas the location of the Σ interfaces are not. In order to determine the location of the Σ interfaces, we need one more equation. This additional equation can be chosen based on various principles. We postulate this additional condition in the simplest form, rejecting the possibility of charge accumulation on Σ interfaces:

$$\sigma_{an} = 0 \quad . \tag{2.10}$$

Finally, we need a charge balance equation for the mobile negative charges. Let their total charge be equal to Q_-. These charges are located within the domain Ω_n with the volumetric density $q_- = q_+$ and at the interface S_n with the surface

density σ_{S_n}. Thus, we arrive at the charge balance relationship:

$$\int_{\Omega_n} d\Omega\, q_- + \int_{S_n} dS\, \sigma_{S_n} = Q_- \quad . \tag{2.11}$$

As a side note, the assumption given by Eq. 2.10 can be substantiated on the basis of a rigorous mathematical analysis if we accept the principle of minimum electrostatic energy [5, 6].

1-D Solutions for a Flat Layer

Consider a flat 1-D system, which carries the total number of Q mobile charges per unit cross section. We explore the distributions of charges that are symmetric with respect to the plane $z = 0$. Since both S_a and Σ interfaces accumulate zero charge and possess zero thickness, their visible presence is omitted in the figures that follow.

Configuration 1

If the net bounded charge Q_+, which includes the positive charges of the lattice ions and negative charge of the bounded negative charges, is less than $|Q_-|$, we get the standard configuration of classical electrostatics, shown in Fig. 2.2.

According to our terminology, there is no Ω_a domain, which is free of the mobile negative charges. The whole domain between the boundaries appears to be the neutral domain Ω_n, having the S_n-type interfaces with the negative surface charge density equal to

$$\sigma_{S_n} = \frac{Q_+ - |Q_-|}{2} \quad . \tag{2.12}$$

Configuration 2

Consider a flat 1-D system presented in Fig. 2.3.

Within the gray Ω_n domain, the 1-D Laplace equation reads

$$\frac{d^2\varphi}{dz^2} = 0 \qquad \text{for } |z| \le H_\Sigma \quad . \tag{2.13}$$

Within the red Ω_a domain, the 1-D Laplace equation reads

$$\frac{d^2\varphi}{dz^2} = -4\pi q_+ \qquad \text{for } H_\Sigma < |z| \le H_a \quad . \tag{2.14}$$

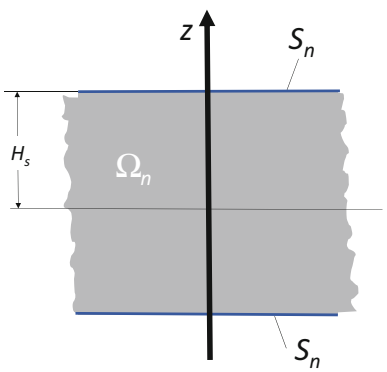

Fig. 2.2 The "standard" configuration of classical electrostatics

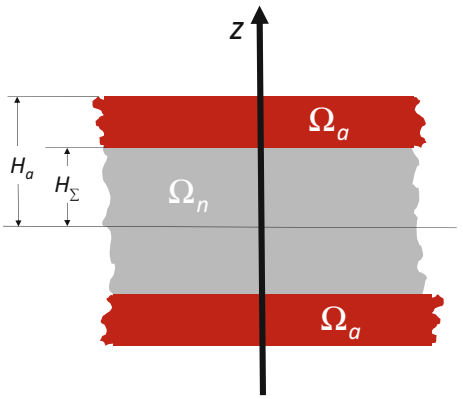

Fig. 2.3 A configuration with finite Ω_a domains (red) at the external boundaries

Outside the plate, in the absence of the outside charges, we arrive at the Laplace equation again:

$$\frac{d^2\varphi}{dz^2} = 0 \qquad \text{for } |z| > H_a \quad . \tag{2.15}$$

Boundary conditions at both interfaces H_Σ and H_a are the same; namely,

$$\begin{aligned} \left[\varphi\right]_-^+ &= 0 \\ \left[\frac{d\varphi}{dz}\right]_-^+ &= 0 \end{aligned} \quad . \tag{2.16}$$

At $z = 0$, we choose the following boundary conditions:

$$\begin{aligned} \varphi(0) &= 0 \\ \left.\frac{d\varphi}{dz}\right|_0 &= 0 \end{aligned} \quad . \tag{2.17}$$

The charge balance equation (Eq. 2.11) is

$$2H_\Sigma\, q_- = Q_- \quad . \tag{2.18}$$

In view of the bulk Laplace equation (Eq. 2.13) and the boundary conditions (Eq. 2.17), the electrostatic potential φ vanishes everywhere inside the gray Ω_n domain:

$$\varphi(z) = 0 \qquad \text{for } |z| \le H_\Sigma \quad . \tag{2.19}$$

Now, combining Eqs. 2.1 and 2.18, we arrive at the following relationship for the thickness of the neutral domain:

$$H_\Sigma = \frac{1}{2q_+}\,|Q_-| \quad . \tag{2.20}$$

The general solution of the Poisson equation (Eq. 2.14) inside the red Ω_a domain reads

$$\varphi(z) = -2\pi q_+ z^2 + C_1 z + C_2 \qquad \text{for } H_\Sigma < |z| \le H_a \quad , \tag{2.21}$$

where C_1 and C_2 are the constants that should be determined from the boundary conditions (Eq. 2.16) and solution (Eq. 2.19) within the gray Ω_n domain, which gives us two linear equations

$$\begin{aligned} -2\pi q_+ H_\Sigma^2 + C_1 H_\Sigma + C_2 &= 0 \\ -4\pi q_+ H_\Sigma + C_1 &= 0 \end{aligned} \tag{2.22}$$

with the solution

$$\begin{aligned} C_1 &= 4\pi q_+ H_\Sigma \\ C_2 &= -2\pi q_+ H_\Sigma^2 \end{aligned} \quad . \tag{2.23}$$

Using Eq. 2.23, we can rewrite the general solution Eq. 2.21 as follows

$$\varphi(z) = -2\pi q_+ \big(z - H_\Sigma\big)^2 \qquad \text{for } H_\Sigma < |z| \le H_a \quad . \tag{2.24}$$

The solution given by Eq. 2.24 implies

$$\begin{aligned} \varphi(H_a) &= -2\pi q_+ \big(H_a - H_\Sigma\big)^2 \\ \left.\frac{d\varphi}{dz}\right|_{H_a} &= -4\pi q_+ \big(H_a - H_\Sigma\big) \end{aligned} \quad . \tag{2.25}$$

The general solution of the Laplace equation (Eq. 2.15) within the vacuum domain has the following general solution

$$\varphi(z) = \varphi\big|_{z=H_a} + \big(z - H_a\big) \left.\frac{d\varphi}{dz}\right|_{z=H_a} \qquad \text{for } |z| \ge H_a \quad . \tag{2.26}$$

Using Eq. 2.25, we can rewrite the general solution (Eq. 2.26) as follows:

$$\varphi(z) = -2\pi q_+ \big(H_a - H_\Sigma\big)^2 - 4\pi q_+ \big(z - H_a\big)\big(H_a - H_\Sigma\big) \qquad \text{for } |z| \ge H_a \quad . \tag{2.27}$$

Configuration 3

Consider now the same flat 1-D system but with a different arrangement of the domains, presented in Fig. 2.4. For this configuration, we arrive at the system

$$\frac{d^2\varphi}{dz^2} = -4\pi q_+ \qquad \text{for } |z| \le H_\Sigma \quad , \tag{2.28}$$

$$\varphi = \text{const} \qquad \text{for } H_\Sigma < |z| \le H_S \quad , \tag{2.29}$$

$$\frac{d^2\varphi}{dz^2} = 0 \qquad \text{for } |z| > H_S \quad . \tag{2.30}$$

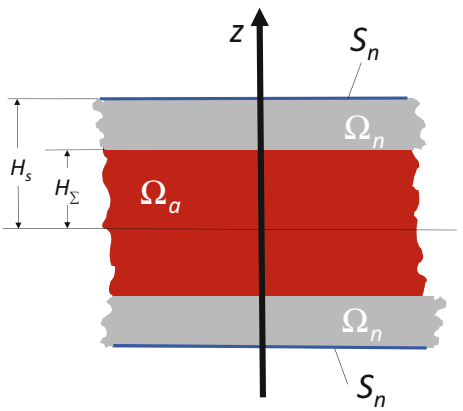

Fig. 2.4 A configuration with a finite Ω_a domain (red) in the middle of the body

The system of bulk equations, Eqs. 2.28–2.30, should be considered with the following boundary conditions:

1. at $z = 0$, we choose the following boundary conditions:

$$\begin{aligned} \varphi(0) &= 0 \\ \left.\frac{d\varphi}{dz}\right|_0 &= 0 \end{aligned} \tag{2.31}$$

2. at $z = H_\Sigma$, we use the following boundary conditions; namely, continuity of φ and its derivative across the Σ interface:

$$\begin{aligned} \left[\varphi\right]_-^+ &= 0 \\ \left[\frac{d\varphi}{dz}\right]_-^+ &= 0 \end{aligned} \tag{2.32}$$

3. at $z = H_S$, the surface charges can accumulate and we choose the boundary conditions

$$\begin{aligned} \left[\varphi\right]_-^+ &= 0 \\ N^i \nabla_i \phi\big|_{S_n} &= -4\pi\sigma_{S_n} \end{aligned} \tag{2.33}$$

The charge balance equation (Eq. 2.11) reads

$$(H_S - H_\Sigma) q_- + \sigma_{S_n} = \frac{Q_-}{2} \quad . \tag{2.34}$$

We then obtain

$$\varphi = -2\pi q_+ z^2 \qquad \text{for } |z| \leq H_\Sigma \quad , \tag{2.35}$$

$$\varphi = -2\pi q_+ H_\Sigma^2 \qquad \text{for } H_\Sigma < |z| \leq H_S \quad . \tag{2.36}$$

According to the solutions given by Eq. 2.36, φ is constant in the domain Ω_n, and so $d\varphi/dz = 0$ when approaching the interface at $z = H_\Sigma$ from above. In contrast, the parabolic form of Eq. 2.35 for the central Ω_a domain would lead us to the conclusion that $d\varphi/dz = -4\pi q_+ H_\Sigma$ when approaching the interface at $z = H_\Sigma$ from below. These two violate the interface boundary condition for $d\varphi/dz$ at $z = H_\Sigma$, given by Eq. 2.32, which calls for continuity of the derivative of φ across the Σ interface.

Therefore, one must conclude that the hypothetical configuration 3 represents a nonphysical configuration of the electric charge distribution.

Conclusion

In an earlier report [2], we demonstrated the paradoxical inconsistency of classical electrostatics for the models permitting only finite density of positive charges. To handle this paradox, classical electrostatics should be significantly modified. There are several possibilities of reasonable modifications. Basically, they lead to the introduction of additional physical mechanisms and additional material constants.

Introduction of additional material constants and effects is the precursor of significant changes in the technical complexity of the associated boundary value problems. The growth of the complexity can entail the disappearance of the keynote feature of classical electrostatics: this feature is the possibility of analytical exploration of the interesting physical problems.

To minimize the complexification of classical electrostatics, we suggested another approach, which is *not* associated with the introduction of any additional material constants. After formulation of the novel boundary value problem, we demonstrated how it can be solved analytically in the simplest instructive 1-D cases of the flat plate.

References

1. Fedorov, S.V.: Electrodynamic protection against shaped charge weapons: physics aspects of functioning. Vestnik of the Baumann's Technical University: Mashinostroenie (3) (2014)
2. Grinfeld, M., Segletes, S.B.: Toward paradoxical inconsistency in electrostatics of metallic conductors. Technical Report ARL-TR-8365, Army Research Laboratory (US), Aberdeen Proving Ground (2018)
3. Stratton, J.A.: Electromagnetic Theory. McGraw Hill, New York (2008). Originally published 1941
4. Landau, L.D., Lifshitz, E.M.: Electrodynamics of Continuous Media. Pergamon, Oxford (1960)
5. Grinfeld, P.A., Grinfeld, M.A.: Towards thermodynamics of elastic electric conductors. Phil Mag. A **81**(6), 1341–1354 (2001)
6. Grinfeld, P.: Introduction to Tensor Analysis and the Calculus of Moving Surfaces. Springer, New York (2013)

Chapter 3
Ballistic Response of Woven Kevlar Fabric as a Function of Projectile Sharpness

Julia Cline, Paul Moy, Doug Harris, Jian Yu, and Eric Wetzel

Abstract Right circular cylinders (RCC) are a common fragment-simulating projectile used to simulate debris resulting from an improvised explosive device (IED) blast. The specifications for ballistic performance of soft body armor specify the geometry and mass of RCC projectiles used for testing. The edges on the impacting side of an RCC projectile have a fillet radius, and recent investigations indicate that the fillet radius (or "sharpness") of the projectile may affect the ballistic limit velocity, V_{50}. It is hypothesized that this happens because the sharpness of the projectile changes the fiber failure mechanism, so to test this, 4 gr RCC projectiles with varying fillet radii (0.64 mm, 1.27 mm and 1.70 mm) are precisely manufactured. Previously collected, unpublished data for 4 gr RCC projectiles with fillet radii of 0.10 mm, 0.18 mm and 0.25 mm are also included to assess a range of projectile sharpness values. Ballistic impact tests on single layer woven Kevlar K706 fabric are conducted using a laboratory gas gun to measure the limit velocity, and it is found that the limit velocity decreases with increasing fillet radii. Back surface images and impacted targets are examined post-mortem to identify failure mechanisms.

Keywords Limit velocity · Kevlar · RCC · Ballistic response

Introduction

RCCs are non-deformable projectiles commonly used to simulate airborne fragments accelerated by an IED blast that pose a risk to soft body armor. Requirements for fragmentation protection against several masses of RCC projectiles are outlined in the Enhanced Combat Helmet (ECH) purchase description [1]. For 4 gr (259 mg) RCCs, the mass is specified within a tolerance of 0.15 gr (10 mg), an outer diameter of 3.40 ± 0.03 mm and a length of 3.73 mm. The corners of each RCC are fillet machined with a radius of 0.18 ± 0.08 mm.

The limit velocity (V_{50}) is defined as the velocity at which 50% of impacting projectiles will penetrate a given target. A previous, unpublished study of the limit velocity for RCC projectiles with precisely machined fillet radii of 0.10 mm, 0.18 mm and 0.25 mm indicates that the fillet radii may have an effect on the limit velocity. The cause of this has not been studied extensively and merits further investigation. It is hypothesized that the "sharpness" of the projectile will govern the mechanism needed to penetrate the fabric, which will affect the limit velocity. For computational models aimed at predicting V_0–V_{100} probability curves, realistic failure mode information is critical to obtaining accurate predictions. This work investigates sensitivity to the fillet radii within the current specified tolerance and characterizes the trends related to limit velocity and fillet radii in order to better inform fiber/yarn-level computational models of ballistic impact.

Background

For woven fabrics, there are several mechanisms by which a projectile can penetrate [2, 3]. If the yarns are stretched beyond the maximum fiber failure strain, they will fail in tension. Transverse shear failure of the yarns can occur when a blunt nose projectile (RCC) cuts or shears through the fabric yarns. For loosely woven fabrics or projectiles with smooth curvature (ex. hemisphere or spherical shape), it is possible for the projectile to push the yarns aside and "window" through the fabric without cutting or failing the yarns.

J. Cline (✉) · P. Moy · D. Harris · J. Yu · E. Wetzel
CCDC Army Research Laboratory, Aberdeen Proving Ground, Aberdeen, MD, USA
e-mail: julia.e.cline@nasa.gov

L. E. Lamberson (ed.), *Dynamic Behavior of Materials, Volume 1*, Conference Proceedings of the Society for Experimental Mechanics Series, https://doi.org/10.1007/978-3-030-30021-0_3

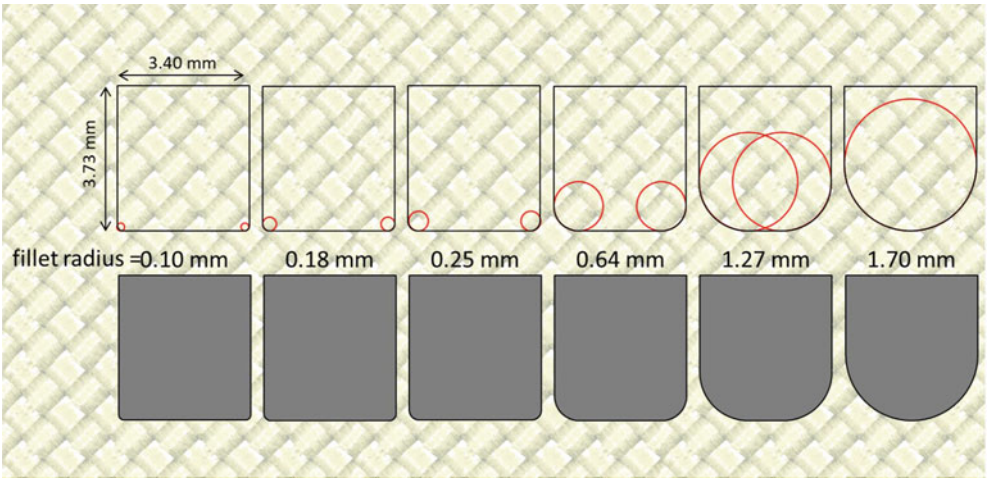

Fig. 3.1 The dimensions and fillet radius of the 4 gr RCC projectiles tested in this study. Projectile length is adjusted for the rounder nosed projectiles to maintain projectile mass

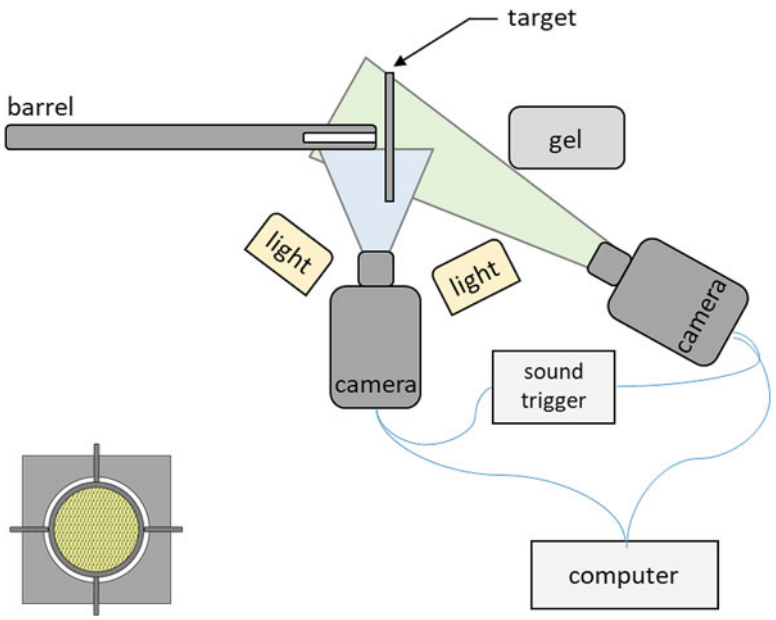

Fig. 3.2 Experimental setup for ballistic impact testing. Two cameras are set-up to record velocity and yaw data as well as images of the back surface of the target during impact. Cameras are triggered using a sound trigger. Ballistic gel is placed behind the target to catch penetrating projectiles. Inset is a schematic of the circular mount for Kevlar targets

To evaluate the effect of projectile sharpness (fillet radii) on the limit velocity, we choose a single layer, scoured state Kevlar K706 fabric consisting of 60 denier KM2 Kevlar yarns woven at 13 × 13 yarns per centimeter. Targets are cut from fabric into 10 cm squares and mounted on a circular frame that is secured using a hose clamp and torqued to 14 N · m. To observe any pull-in from the frame edge, a thin, black sharpie line is drawn around the outer edge of the frame on the target to denote the original location.

4 gr RCC projectiles are precisely machined with fillet radii of progressively decreasing sharpness as shown in Fig. 3.1. Mass and fillet radius of a sample set of projectiles are verified prior to testing.

A laboratory gas gun is used to accelerate projectiles toward the targets. A 3.40 mm diameter barrel is installed on the laboratory gas gun with the end of the barrel set at 7.11 mm from the target. A 10 cm slot at the end of the barrel allows for high speed imaging of the projectile before it leaves the barrel and impacts the target, enabling both projectile velocity and yaw angle measurements. Figure 3.2 shows a full schematic of the experimental setup. A second high speed camera is placed behind the target to capture images of the impact and penetration.

SenTest [4] software is used to guide target velocity choices. SenTest is based on the Neyer D-Optimal test method and is a generic software designed for conducting and analyzing sensitivity tests. For our use, we specify the upper and lower bounds of the velocity measurements and SenTest selects target velocity values to test based on whether the previous velocity test was a success (complete penetration) or a failure (partial penetration). The limit velocity bound we use is 50m/s to 200 m/s with a standard deviation of 10 m/s.

Analysis

Approximately 40 shots are taken per projectile geometry and any shots with significant yaw prior to impact are disregarded in the limit velocity calculation. SenTest software is used to calculate the limit velocity and standard deviations for each projectile type. Figure 3.3 is a plot of the limit velocity for each RCC fillet radius tested in this study. It shows a clear linear, decreasing relationship indicating that penetration is more likely for the rounder nose projectiles at lower velocities.

Further analysis of the back surface images of the impacts and examination of the impacted targets allows for understanding of the failure mechanisms occurring during penetration. For the hemispherical nosed projectiles, penetration is commonly achieved by windowing or sliding through gaps in the weave (Fig. 3.4a) or by a yarn spreading around the projectile nose (Fig. 3.4b). As the fillet radius is decreased, the edges of the projectile become sharper and more broken and cut fibers/yarns are observed which indicates that the failure mechanism is transverse shearing (Fig. 3.4c).

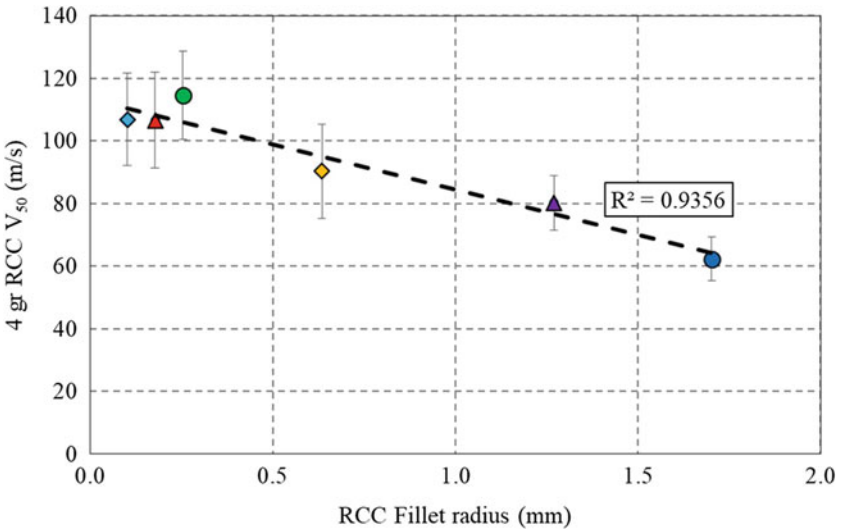

Fig. 3.3 Limit Velocity (V_{50}) decreases as the RCC projectile fillet radius increases

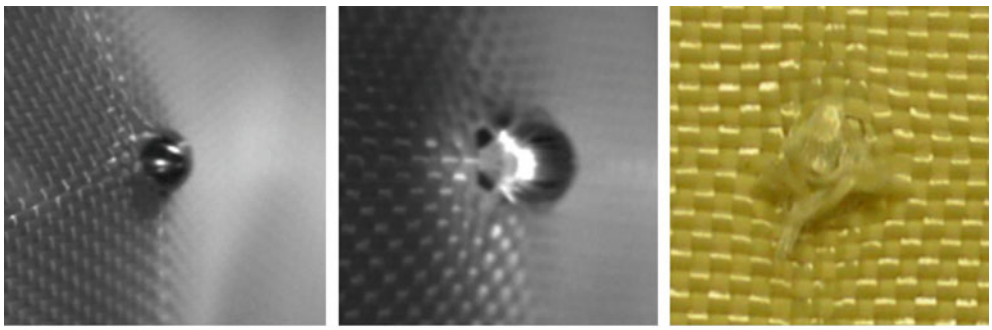

Fig. 3.4 Penetration occurs by (**a**) a hemispherical projectile windowing through the Kevlar weave, (**b**) a yarn spreading and sliding out of the way of a hemispherical projectile, and (**c**) the cutting of some fibers/yarns around the nose of a sharp projectile

Conclusion

A study of the effect of varying fillet radius of RCC projectiles on limit velocity of Kevlar K706 woven fabric shows that protective capabilities reduce as projectiles become more rounded and smooth. Round-nosed (hemispherical) projectiles can easily find gaps in the weave and slide through to defeat the armor material whereas sharper filleted projectiles are forced to expend more energy to cut through yarns/fibers to achieve penetration. To extend this study, newer materials such as ultra-high molecular weight polyethylene (UHMWPE) fiber cross-ply composite could be evaluated in the same manner. The matrix should prevent the projectile from sliding through the fibers and could allow study of other relevant failure mechanisms.

Acknowledgements This research was supported in part by an appointment to the Postgraduate Research Participation Program at the U.S. Army Research Laboratory administered by the Oak Ridge Institute for Science and Education through an interagency agreement between the U.S. Department of Energy and USARL.

References

1. Department of the Army: "Purchase Description Enhanced Combat Helmet (ECH)," PD-ECH-ICE-PG16-0001. Project Manager – Infantry Combat Equipment, Quantico, VA (2009)
2. Nilakantan, G., Merrill, R., Keefe, M., Gillespie, J., Wetzel, E.: Experimental investigation of the role of frictional yarn pull-out and windowing on the probabilistic impact response of Kevlar fabrics. Compos. Part B. **68**, 215–229 (2015)
3. Nilakantan, G., Wetzel, E., Bogetti, T., Gillespie, J.: A deterministic finite element analysis of the effects of projectile characteristics on the impact response of fully clamped flexible woven fabrics. Compos. Struct. **95**, 191–201 (2013)
4. SenTest. Neyer Software LLC. http://neyersoftware.com/SensitivityTest/SensitivityTestFlyer.htm. Accessed Feb 2019

Chapter 4
Effect of Thermomechanical Couplings on Viscoelastic Behaviour of Polystyrene

Pankaj Yadav, André Chrysochoos, Olivier Arnould, and Sandrine Bardet

Abstract Analysis of the thermo-mechanical behaviour of the polymers has been and still is the subject of many rheological studies both experimentally and theoretically. For small deformations, the modelling framework retained by rheologists is often of linear viscoelasticity which led us to the definition of complex moduli and to the rules of the renowned time-temperature superposition principle (TTSP). In this context, the effect of time (i.e., rate dependence) is almost unanimously associated with viscous effects. It has however been observed that the dissipative effects associated with viscous effects may be superimposed with thermo-elastic coupling effects, indicating a high sensitivity of polymeric materials to temperature variations (thermodilatability). Indeed, because of heat diffusion, it was also noticed that these strong thermo-mechanical couplings may induce a time dependence of the material behaviour. Using traditional experimental methods of visco-analysis i.e., dynamic mechanical thermal analysis (DMTA) and via an experimental energy analysis of the behaviour using quantitative infrared techniques, the relative importance of thermoelastic heat sources compared to viscous dissipation was analysed with the increasing frequency of monochromatic cyclic tensile tests made at different ambient temperatures.

Keywords Time-temperature superposition (TTSP) · Viscoelasticity · Dissipation · Thermo-mechanical coupling · DMTA

Introduction

Polymeric materials are widely known for their high viscoelasticity, which signifies wide dependence of their mechanical responses on the applied strain rate which is very important in duration for numerous engineering applications. This is one of the reasons why a protocol capable of predicting the viscoelastic behaviour of polymeric materials over time scales and temperatures of use has been developed. This protocol gave rise to DMTA techniques which allow to gather viscoelastic behaviour characteristics at easily adaptable frequencies and temperature of use in laboratories and extrapolate them to very large ranges of strain rate and temperatures. During the DMTA tests, a monochromatic sinusoidal signal is applied on the specimen to observe the stress-strain response and derive the so called dynamic moduli i.e., E' and E'' respectively named as storage and loss moduli. In general, the storage modulus is associated with the stored elastic energy which is recoverable during unloading while the loss modulus is supposed to be associated with the viscous dissipated energy. The viscous part of the behaviour is equivalently characterised by the loss tangent defined by $\tan\delta = E''/E'$ [1]. The DMTA constitutive equations can then be summarized as follows:

$$\begin{cases} \varepsilon = \varepsilon_0 \sin \omega t \\ \sigma = \sigma_0 \sin(\omega t + \delta) = E' \sin \omega t + E'' \cos \omega t \\ E' = \sigma_0/\varepsilon_0 \cos\delta \\ E'' = \sigma_0/\varepsilon_0 \sin\delta \end{cases} \tag{4.1}$$

where ε_0 is the loading amplitude, σ_0 the stress amplitude and $\omega = 2\pi f$, the pulsation and f being the loading frequency.

Mechanical tests, performed at constant temperature and carried at several frequencies (also known as frequency sweep), permit the investigation of viscoelastic characteristics on a small time scale equivalent to few decades. According to the literature, the obtained data, extracted from tests carried out at different frequencies and constant temperature, show the

P. Yadav · A. Chrysochoos (✉) · O. Arnould · S. Bardet
Laboratory of Mechanics and Civil Engineering (LMGC), University of Montpellier, CNRS, Montpellier, France
e-mail: andre.chrysochoos@umontpellier.fr

L. E. Lamberson (ed.), *Dynamic Behavior of Materials, Volume 1*, Conference Proceedings of the Society for Experimental Mechanics Series, https://doi.org/10.1007/978-3-030-30021-0_4

same evolutions of E' and E'' as those obtained from isochronal tests conducted at different temperatures [2]. This implies that the variation of temperature corresponds to a shift in time scale and this relation between time (or loading frequency) and temperature is termed as time-temperature superposition principle [3] and is known to be valid only for "thermorheologically simple" materials. These are the materials which show that the variation of temperature corresponds to a shift in time scale [4]. For example, considering a given relaxation time τ, its changes with the temperature then introduce a shift factor a_T such that:

$$\tau(T) = \frac{\tau\,(T_0)}{a_T(T)} \tag{4.2}$$

According to Eq. 4.1, the linear viscoelastic behaviour of materials leads to stabilized hysteretic responses (stress-strain loops) whose area corresponds to the mechanical energy lost in form of the dissipated mechanical energy over a cycle, often leading to a self-heating of the specimen. The intensity of the self-heating naturally depends on the material characteristics, on the loading frequency and on the thermal boundary conditions. However, Zener [5] observed that the stress-strain loop may not only be induced by the dissipation mechanisms but also by thermoelastic effects. For all purposes, a theoretical thermodynamic description of these "thermoelastic damping" can be found in [6].

This present work analysed the experimental results obtained from DMTA device equipped with an Infrared camera. The Infrared data were used to estimate the temperature variations of the specimen during the cyclic loading in order to detect the possible thermo-mechanical coupling and/or dissipative effects. The outputs of the different tests are discussed in terms of energy balance. This paper also presents an analytical way to derive the concept of thermorheologically simple materials used in the DMTA protocol within a thermomechanical viscoelastic framework where the status of the temperature is the one of a controlled parameter but not (yet) those of a thermodynamic variable.

Experimental Methods

Firstly, the standard DMTA setup used for polystyrene samples was shown followed by the experimental home-made arrangement developed to allow us to perform a thermographic analysis during the DMTA tests.

Standard DMTA

Polystyrene (PS) sample with a weight averaged molecular weight (M_w) of 111,500 and a polydispersity of 3, was used to carry out the DMTA tests. The samples of dimension 85 × 13 × 4 mm were made from the sheets (300 × 300 mm) of PS from Goodfellow. The tests were made on a classical DMTA (BOSE ELF 3230) equipped with strain control module (Fig. 4.1). The samples were tested in the temperature range from 40 °C to 90 °C and for 3 decades of frequency from 0.01 Hz to 10 Hz i.e., frequency sweep was made with 5 points per decade in the tension mode with a strain ratio of $R = -1$. A virgin sample was utilized for each new loading parameter to avoid possible damage or ageing [7].

The glass transition temperature of PS samples, measured using the Dynamic Scanning Calorimetry (DSC) was 108 °C. This glass transition temperature value was not the exact value of glass transition but was an adequate value for us to stay below the glass transition region.

Thermographic Approach

The thermography techniques were used during the DMTA measurements to observe the temperature variations of the sample during the cyclic loading. The pixel-to-pixel calibration [9] was performed for each temperature for the Infrared (IR) camera (CEDIP SC7000 series) before using it on the DMTA tests as the temperature variations induced by material deformation

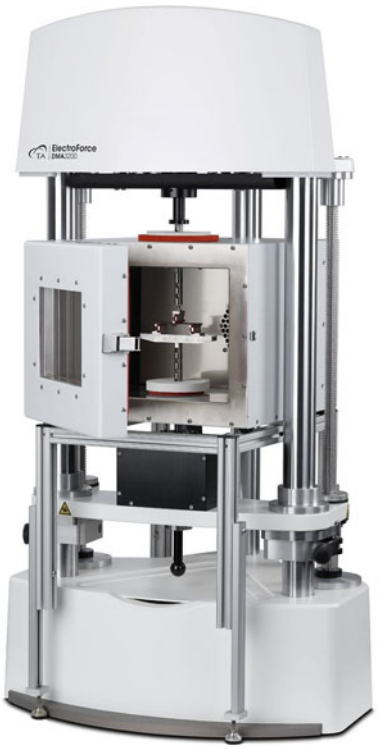

Fig. 4.1 BOSE Electroforce 3230 DMTA equipped with a standard furnace [8]

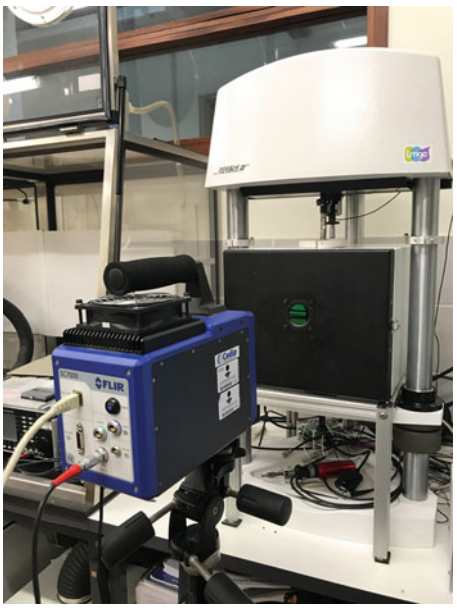

Fig. 4.2 Extended DMTA measurements where the furnace door was equipped with a special infrared transparent window

might be very small. The IR camera was used during DMTA tests for few frequencies like 0.1 and 1 Hz at each temperature of 25°, 50° and 75 °C. The experimental setup is shown in Fig. 4.2. A special infrared lens was placed in the home-made door of the furnace to allow weakly attenuated infrared assessments. Moreover, two samples were placed, inside the furnace, in the vision field of the camera, one under loading and the other free (reference sample) to observe the small thermal fluctuations induced by the furnace regulation system.

Results and Discussion

Standard DMTA Results

The DMTA results on PS are shown in Fig. 4.3a, b for several temperatures in the range mentioned previously, where the storage modulus (E') and loss tangent (tan δ) were plotted against loading frequency. The plots of E' and tan δ do not include the rubbery state regions since the chosen temperature remained below the glass transition temperature and chosen frequency was not enough to show the relaxation near the glass transition of PS.

The results obtained from the frequency sweep measurements were in accordance with the results of the literature as the storage moduli was increasing with the frequency but contrarily decreasing with the increasing temperature. Whereas, in case of loss tangent, it was observed to be inverse of the evolution of storage modulus i.e., decreasing with the increasing frequency but increasing with the temperature.

As it is traditionally done, the frequency sweep results plotted in Fig. 4.3a, b obtained at several temperatures were shifted manually by a shift factor (a_T) along the frequency scale to get the master curves i.e., the horizontal shift factor was applied to get the master curve at reference temperature 90 °C. The master curves obtained after horizontal shift are shown in Fig. 4.4a, b.

The application of horizontal shift to build the master curve leads us to the observation that the superposition by displacement along the frequency scale alone cannot yield a master curve in case of loss tangent. A small vertical shift (b_T) has also be applied to improve the quality of the tan δ master curve as shown in Fig. 4.5.

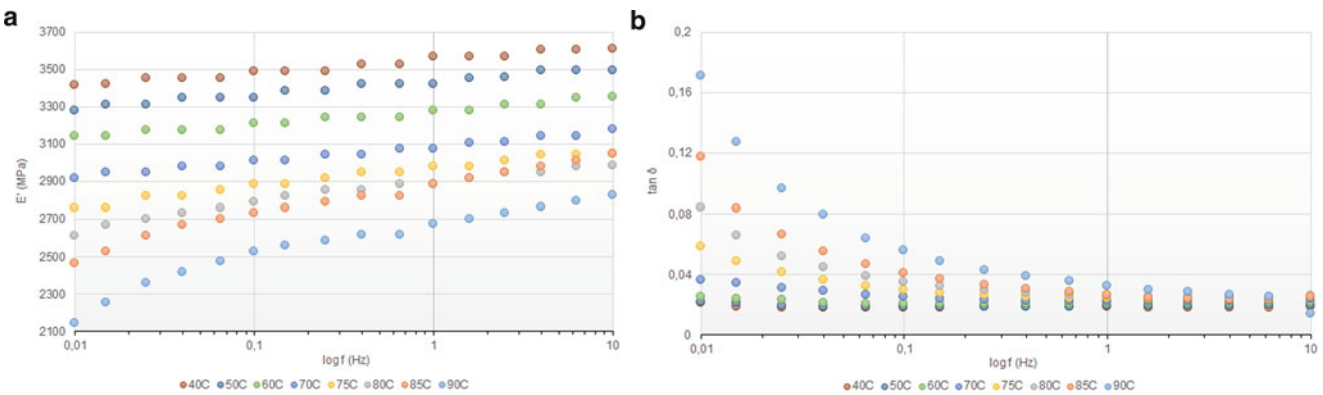

Fig. 4.3 (**a**) Storage modulus vs. frequency. (**b**) Loss tangent vs. frequency

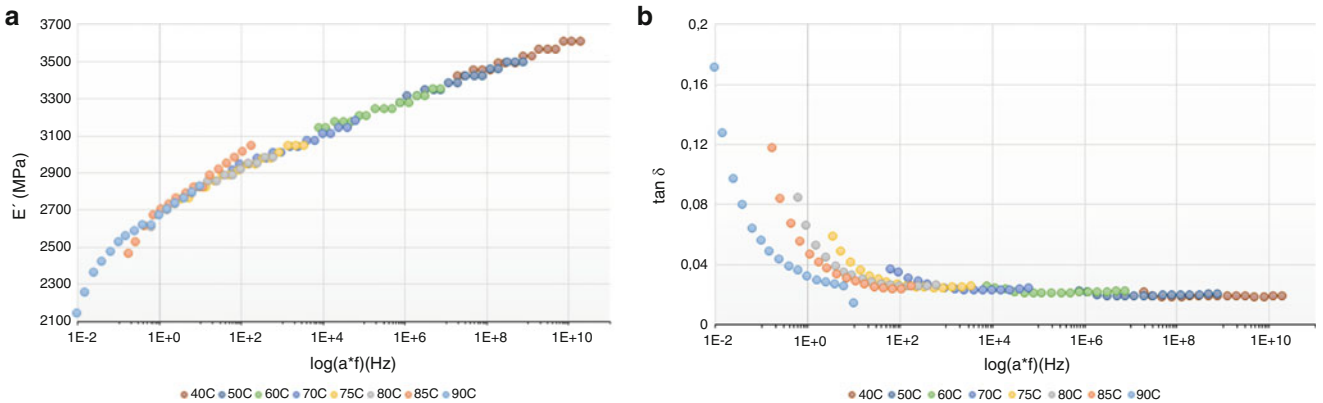

Fig. 4.4 (**a**) Master curve for E'. (**b**) Master curve for tan δ (reference temperature 90 °C)

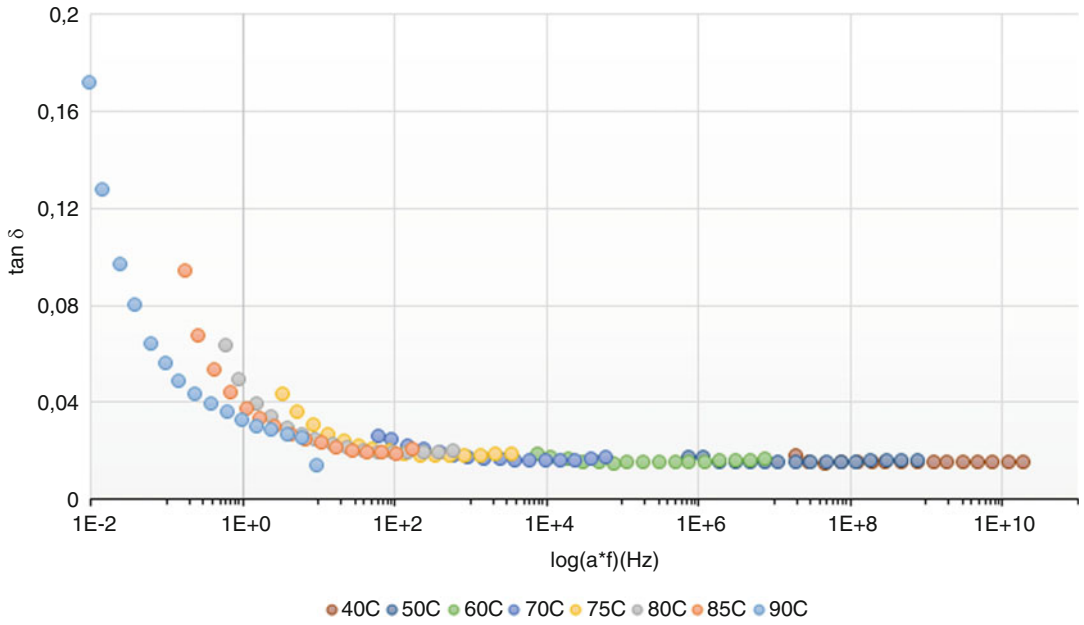

Fig. 4.5 Master curve for tan δ with both shift factors

Discussion About the Time-Temperature Superposition Principle

The previous construction of the master curve leads us to the concept of TTSP that could be expressed by the following assertion: for a given viscoelastic behaviour at given temperature and loading frequency, there exists an equivalent behaviour at "higher/lower" temperature and "lower/higher" frequency. In other words, this behavioural equivalence can be mathematically defined by:

$$\begin{cases} E'(T_0, \omega_0) = E'(T, \omega) \\ E''(T_0, \omega_0) = E''(T, \omega) \end{cases} \tag{4.3}$$

where (T_0, ω_0) represents the reference couple and (T, ω) the equivalent couple.

Now, let us consider a generalized form of linear viscoelastic model (generalized Maxwell model [4]) made of $n + 1$ branches, the mathematical expressions of the dynamic moduli E' and E'' can be written as:

$$E' = E_0 + \sum_{i=1}^{n} \frac{E_i \tau_i^2 \omega^2}{1 + \tau_i^2 \omega^2} \tag{4.4}$$

$$E'' = \sum_{i=1}^{n} \frac{E_i \tau_i \omega}{1 + \tau_i^2 \omega^2} \tag{4.5}$$

where, index "i" refers to each branch, E_i being the elastic modulus of the ith branch, E_0 is the elastic modulus of a pure elastic branch and τ_i its temperature dependent relaxation time. For such moduli expressions, if we now apply the TTSP consequences (Eq. 4.3), we must have:

$$E' = E_0 + \sum_{i=1}^{n} E_i(T, \omega) \frac{\tau_i^2(T)\omega^2}{1 + \tau_i^2(T)\omega^2} = E_0 + \sum_{i=1}^{n} E_i(T_0, \omega_0) \frac{\tau_i^{0^2} \omega_0^2}{1 + \tau_i^{0^2} \omega_0^2} \tag{4.6}$$

$$E'' = \sum_{i=1}^{n} E_i(T, \omega) \frac{\tau_i(T)\omega}{1 + \tau_i^2(T)\omega^2} = \sum_{i=1}^{n} E_i(T_0, \omega_0) \frac{\tau_i^0 \omega_0}{1 + \tau_i^{0^2} \omega_0^2} \tag{4.7}$$

where $\tau_i{}^0 = \tau_i\,(T_0)$. As it is known that elasticity is rate independent, if we admit that E_0 is also temperature independent, or if we do not consider any pure elastic branch in the generalized Maxwell model, the Eqs. (4.6 and 4.7) will be verified if, for each branch "*i*" (sufficient condition), we impose:

$$\begin{cases} E_i\,(T,\omega)\,\frac{\tau_i^2(T)\omega^2}{1+\tau_i^2(T)\omega^2} = E_i\,(T_0,\omega_0)\,\frac{\tau_i^{0^2}\omega_0^2}{1+\tau_i^{0^2}\omega_0^2} & (a) \\ E_i\,(T,\omega)\,\frac{\tau_i(T)\omega}{1+\tau_i^2(T)\omega^2} = E_i\,(T_0,\omega_0)\,\frac{\tau_i^0\omega_0}{1+\tau_i^{0^2}\omega_0^2} & (b) \end{cases} \tag{4.8}$$

Multiplying now Eq. 4.8b by $\tau_i^0\omega_0$, we obtain:

$$E_i\,(T,\omega)\,\frac{\tau_i(T)\omega}{1+\tau_i^2(T)\omega^2} \times \tau_i^0\omega_0 = E_i\,(T,\omega)\,\frac{\tau_i^2(T)\omega^2}{1+\tau_i^2(T)\omega^2} \tag{4.9}$$

Finally, if $E_i(T,\omega) > 0$, Eq. (4.9) leads to $\tau_i(T)\omega = \tau_i(T_0)\omega_0$, whatever the relaxation time spectrum and its temperature evolution.

In order to get the correspondence between (T, ω) and (T_0, ω_0) satisfying Eqs. (4.6 and 4.7), it is sufficient to introduce a unique function a_T, so that:

$$\tau_i(T) = \frac{\tau_i\,(T_0)}{a_T(T)} \text{ and then } \omega = a_T(T)\omega_0 \tag{4.10}$$

In Eq. 4.10, we recognize the characteristics of so called Thermo-rheologically simple material.

Thermographic Results

Thermographic recordings were performed during the DMTA tests at certain temperatures and frequencies to observe the thermo-mechanical couplings and dissipative effects. As mentioned previously, two different samples were used during thermography where one sample (load free) was used to observe the regulation of the furnace temperature (dummy specimen). Henceforth, the mean temperature over the central surface of the load free sample was considered and was subtracted to the mean temperature over a central surface of a loaded sample, in order to minimize the disturbing effects of temperature fluctuations of the furnace. In such conditions, we considered that the observed temperature variation was the one of the specimen under loading at an arbitrarily constant temperature. The monotonous increase of these temperature variations can then be associated with the existence of dissipation, while, periodic oscillation corresponds to thermoelastic effects. Using this thermal data, it was also possible to compute the hysteresis area associated with thermo-elastic couplings and estimate the mean dissipation per cycle during the test.

Some thermographic results are shown in Fig. 4.6, where the cyclic variation of the temperature of the sample due to thermoelastic coupling is clearly highlighted together with the slight drift of the mean temperature (due to self heating). Despite the narrowness of the temperature variation, Fig. 4.6 clearly shows the presence of the temperature oscillation while any self-heating of the specimen was difficult to observe. These results are in accordance with what was found in [11], for PMMA and PC specimens. This observation of thermoelastic coupling, during the DMTA tests at low frequencies also made a question mark on the viscous origin of loss modulus, which is assumed to be the result of energy dissipation. That's the reason why we computed the different hysteresis areas in Table 4.1 for the different loading frequencies and furnace temperature used during the tests.

The hysteresis area was first calculated using the stress-strain data given by the DMTA device:

$$A_h = \oint_{\text{cycle}} \sigma \cdot \dot{\varepsilon}\, dt \tag{4.11}$$

The hysteresis area was then computed for pure linear viscoelastic material:

$$A_{HL} = \pi\, E'' \varepsilon_0^2 \tag{4.12}$$

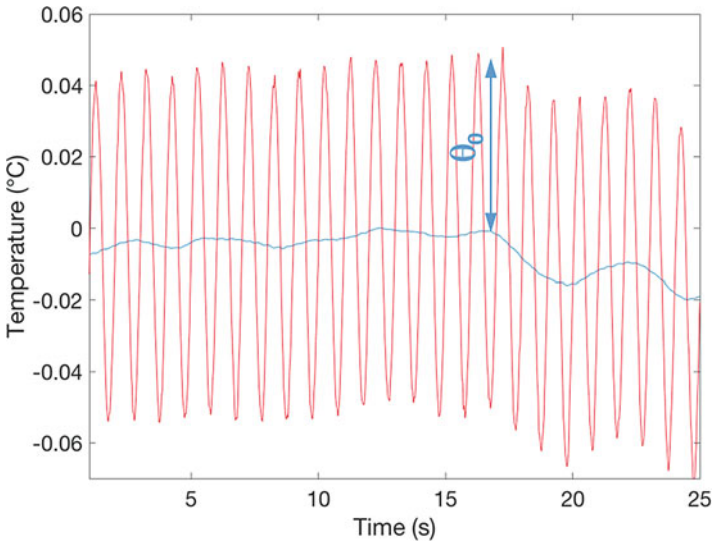

Fig. 4.6 Variation of the temperature of the sample, compared to the reference sample, due to the thermo-elastic coupling and drift (blue line) at 40 °C and 1 Hz

Table 4.1 Derived hysteresis area

Loading frequency f (Hz)	Furnace temperature T (°C)	A_h (J/m^3)	A_{HL} (J/m^3)	A_{the} (J/m^3)
0.1	40	137	138	~0
	75	296	297	~0
1	40	132	133	~0
	75	230	232	~0
10	40	131	129	~0
	75	220	219	~0

We finally estimated the hysteresis area induced by the thermoelastic effects following the equation:

$$A_{the} = -E'\alpha\theta_0\varepsilon_0\pi \sin\delta_{th} \tag{4.13}$$

where, α represents the coefficient of thermal expansion, θ_0 is the amplitude of the thermoelastic coupling and δ_{th} is the phase lag between temperature and strain variations due to heat losses of the sample with the environment.

Fortunately, the results of column 3 and 4 (Table 4.1) are consistent. This consistency shows that the numerical scheme integration of the hysteresis area was correctly performed as the identification of the loss modulus using the least square fitting method. The results of column 5 show that the hysteresis area induced by thermoelastic effects remains negligible compared to the mechanical hysteresis area. The origin of this hysteresis area may be attributed to either dissipation or stored energy variations induced by microstructural transformation during the loading cycles. In this last case, the mechanical cycle cannot be longer a thermodynamic cycle.

If we finally associate the hysteresis area with only dissipative mechanisms, a temperature drift can be computed using the following simplified heat diffusion equation (Eq. 4.14), [12].

$$\dot{\theta} + \frac{\theta}{\tau_{\text{th}}} = A_h f/\rho C_p \tag{4.14}$$

where $A_h f$ represents the mean dissipation per cycle, τ_{th} a time constant related to the heat losses, ρ and C_p the mass density and specific heat capacity of the material. In each case, the temperature drift remained less than 1/100 °C which is currently experimentally unreachable via IR techniques.

Concluding Comments

1. The narrowness of the temperature variation of the specimen during the DMTA tests legitimates the assumption that the temperature imposed by the furnace can be considered as the temperature of the sample (very small self-heating) which is in agreement with the DMTA protocol. In such conditions, the sample temperature is then a controlled parameter
2. Nevertheless, small temperature oscillations were observed, which lead us to wonder about the pure viscous origin of the loss modulus. The computation of the thermoelastic hysteresis area showed that latter remains small compared to the mechanical one.
3. Conversely, we computed the asymptotic self-heating temperature induced by the entire hysteresis area assuming its dissipated origin. In all observed cases, the temperature variations remained under the thermal resolution of the camera.
4. At this level, it is then impossible to confirm the dissipative origin of the hysteresis area that could also be generated by the stored energy variations.

Perspectives

The further study about this discussion has to be done by strengthen our experimental database. In particular, polyamide samples are to be tested in a near future. We already know [13] that this material is strongly dissipative even if its cyclic deformation is accompanied by non negligible coupling effects.

Besides, the identification of thermo-visco-elastic Maxwell model is underway. This model will be constructed within the framework of "generalized standard material" framework [6] considering the temperature of the specimen as a state variable and not a controlled parameter. The first step is to construct the relaxation time spectra at different temperatures using the E' and E'' assessments. Finally, the viscoelastic and thermo-elastic effects will be compared using numerical simulations.

References

1. Menard, K.P.: Dynamic mechanical analysis: a practical introduction. Taylor & Francis, Texas (2008)
2. Seitz, J.T., Balazs, C.F.: Application of time-temperature superposition principle to long term engineering properties of plastic materials. Polym. Eng. Sci. **8**, 151–160 (1968)
3. Patel, M.: Viscoelastic properties of polystyrene using dynamic rheometry. Polym. Test. **23**(1), 107–112 (2004)
4. Ferry, J.D.: Viscoelastic properties of polymers. Wiley, New York (1980)
5. Zener, C.: Internal friction in solids I. Theory of internal friction in reeds. Phys. Rev. J. **52**, 230–235 (1937)
6. Chrysochoos, A.: Thermomechanical analysis of the cyclic behavior of materials. Procedia IUTAM. **4**, 15–26 (2012)
7. Lomellini, P.: Viscosity-temperature relationships of a polycarbonate melt: Williams-landel-ferry versus Arrhenius behaviour. Macromol. Chem. Phys. **193**(1), 69–79 (1992)
8. https://www.tainstruments.com/products/electroforce-mechanical-testers
9. Honorat, V., Moreau, S., Muracciole, J.M., Wattrisse, B., Chrysochoos, A.: Calorimetric analysis of polymer behaviour using a pixel calibration of an IRFPA camera. QIRT J. **2**(2), 153–171 (2012)
10. Capodagli, J., Lakes, R.: Isothermal viscoelastic properties of PMMA and LDPE over 11 decades of frequency and time: a test of time-temperature superposition. Rheological. Acta. **47**, 777–786 (2008)
11. Moreau, S., Chrysochoos, A., Muracciole, J.M., Wattrisse, B.: Analysis of thermoelastic effects accompanying the deformation of PMMA and PC polymers. Elsevier Masson. **333**(8), 648–653 (2005)
12. Chrysochoos, A., Louche, H.: An infrared image processing to analyse the calorific effects accompanying strain localisation. Int. J. Eng. Sci. **38**(16), 1759–1788 (2000)
13. Benaarbia, A., Chrysochoos, A., Robert, G.: Thermomechanical analysis of the onset of strain concentration zones in wet polyamide 6.6 subjected to cyclic loading. Mech. Mater. **99**, 9–25 (2016)

Chapter 5
Dynamic Response of Layered Functionally Graded Polyurethane Foam with Nonlinear Density Variation

Dennis Miller, Vijendra Gupta, and Addis Kidane

Abstract Polyurethane foam is most commonly used for its energy absorbing characteristics. The purpose of this study is to experimentally determine the energy absorbing of density graded foam subjected to dynamic loading. To define the energy absorption, the stress-strain relationship is developed under dynamic uniaxial compression via compressive Split-Pressure Hopkinson Bar apparatus; which is used in conjunction with DIC. SPHB yields the boundary stress where DIC is used to find the inertia stress term. Combining the boundary and inertia stress yields a full stress-strain response of the functionally graded foam material. Theoretically, it has been previously determined that for continuously graded foams with a nonlinearly increasing density has increased energy absorbing ability's. Our proposed experiments are used to validate the theoretical results and benchmark the ability of functionally graded foam to optimize the energy absorption of polyurethane foam. It has been found that the convex density gradient FGFM has a much higher normalized energy absorption when compared to that of a concave density gradient.

Keywords Dynamic loading · Polymeric foam · Digital image correlation · Energy absorption · Functional graded foam materials

Introduction

Polymeric foams are implemented for their ability to mitigate damage through their energy absorbing characteristics. These foams are often sought out for their high strength to weight ratio, where the energy absorption can then be optimized through density selection. The single most important property of foams is *relative density*, or the density of the foam compared to its base material's density. Where it is known that there is a correlation between relative density, strength, and energy absorption. This is attributed to the failure mechanism which governs foam deformations undergoing compressive loadings, progressive local crushing. As such, we seek to optimize and investigate the global response of polymeric foams which incorporate low and high density foams. These foams are known as FGFM (Functionally Graded Foam Materials) and are achieved by stacking discrete layers of varying densities. When these low and high densities are used in conjunction, the overall structure can take advantage of both the strength and weight saving properties. These FGFM have been the focus of numerous studies, however these studies have been mostly performed in a theoretical capacity. Experimentally, there have been few studies investigating the dynamic response of density-graded foams, where the studies that have been completed have focused on single phase, homogenous cellular materials. [1–3] Furthermore, foam structures whose density varies as a non-linear function, to the best of our knowledge, has only been investigated through finite element models. Ciu et al. [1] studied the effect of non-linear density gradation for varying density ranges and impact energies; it was concluded that FGFM can exhibit superior energy absorption over an equivalent density uniform foam, where convex gradients outperformed concave at low impact energies. Continuing his work with Kiernan and Gilchrist [2], a Split Hopkinson Pressure Bar (SHPB) model was created so an investigation of the stress wave propagation through FGFM could be identified. Koohbor et al. [3] experimentally analyzed the impact response of density gradation polyurethane foam through observing the compaction wave propagation using digital image correlation (DIC); the inertia stress distribution was determined from the acceleration field, where it was concluded that a variation of inertia stress is attributed to the compaction wave formed in the FGFM. Discretely layered and continuously graded foams were semi-analytically analyzed by Koohbor and Kidane [4] to further explore the density gradation by quantifying the relationships between continuously graded, linearly graded, and single-phase foams under quasi-static conditions. An analytical model for the continuously graded foam, governed by a power law

D. Miller (✉) · V. Gupta · A. Kidane
Department of Mechanical Engineering, University of South Carolina, Columbia, SC, USA
e-mail: Mille722@email.sc.edu

L. E. Lamberson (ed.), *Dynamic Behavior of Materials, Volume 1*, Conference Proceedings of the Society for Experimental Mechanics Series, https://doi.org/10.1007/978-3-030-30021-0_5

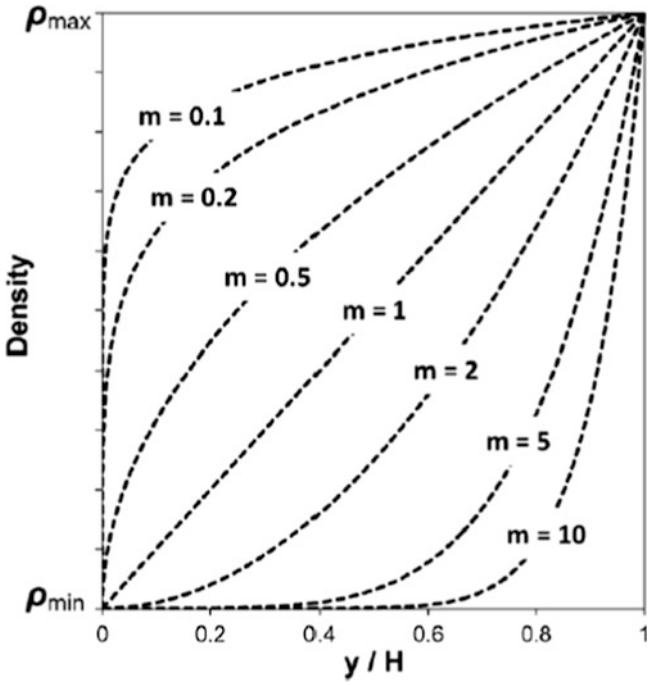

Fig. 5.1 Power-Law Function for normalized specimen length and density [4]

function, was implemented to produce a stress-strain curve which was compared to experimentally obtained stress-strain relations of an approximated continuously gradation via discrete layers, linearly graded, and single-phase foams. Liu, H. et al. [5] theoretically and analytically determined the dynamic performance of FGFM of nonlinear graduation, governed by a power-law function, to conclude the effect of positive and negative density variation, large and small power law exponents, and crushing wave initiation (Fig. 5.1).

The focus of this study is to experimentally verify the analytical and theoretical findings for the energy absorption and strength properties of dynamically loaded FGFM. Specifically, to characterize the energy absorption of a power-law density gradation FGFM for both nonlinear concave/convex and impact orientation. To achieve this end, the discretely layered foam samples were dynamically loaded via Split Hopkinson Pressure Bar (SHPB) which is used in conjunction with DIC so that the FGFM may be fully characterized.

Materials and Methods

Polyurethane foam (PU), purchased from General Plastics under the product name "Last-A-Foam® FR-7110 Rigid Polyurethane Foam", was used for the entirety of this study. This rigid, closed-cell polyurethane foam (PUR), is implemented in designs for its high strength to weight ratio. A total of four densities were selected to produce our samples: 160, 320, 480, and 640 kg/m^3. Each density was purchased in 5 mm thick sheets; to create the specimen's discrete layers, 25 × 200 × 5 mm^3 (*width* × *length* × *thickness*) strips were bonded together in the density arrangement desired using HH-66 Vinyl Cement, purchased from McMaster-Carr. The Vinyl Cement is necessary to ensure uniform and square samples where it is vital that the adhesive does not constrain out of plane deformation. HH-66 is selected for its flexibility where it should provide good layer bonding, while relatively, minimizing shear stress developed at the interface. From the bonded strips the samples were taken to ~17 mm × 17 mm on a vertical mill using a 3-insert carbide face mill rotating at high speed. The overall length of each sample is dependent on the density gradation being implemented and is shown in Table 5.1.

The samples were then polished using silicon carbide sand paper until a smooth surface finish was achieved. The smooth surface finish on the porous foam reduces the amount of white paint needed to uniformly cover the sample. Black speckles were applied using conventional spray painting methods.

Table 5.1 Specimen dimensions, density gradation, and apparent density

Sample gradation and dimensions				
FGFM	Discrete layer density (kg/m^3)	Layer thickness (mm)	Length (mm)	Apparent density (kg/m^3)
Power-law exponent				
Concave m = 2	160/160/160/320/320/320/480/640	5 & last layer 1.5	36.5	**317.31**
Convex m = 0.5	160/320/480/480/480/640/640/640	5 & first layer 1.5	36.5	**542.67**

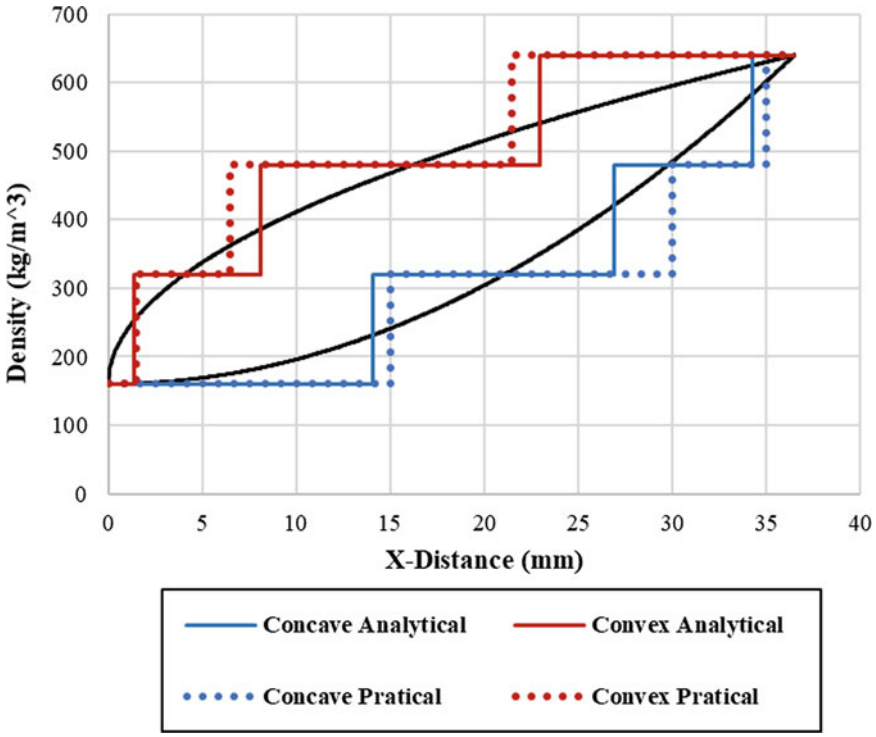

Fig. 5.2 Power-Law Function Approximation for concave and convex gradation

To characterize the properties of continuously graded polyurethane foam, an approximation of the non-linear gradation, described by a power law function operating on the exponential term "m", must be made through discrete layers. In Fig. 5.2, the effect of varying the exponential term in terms of density and normalized distance is demonstrated. When *m* is equal to 1, density is linearly increasing throughout the length; as *m* approaches 0 and infinity the length in which density varies approaches 0. To model the continuously graded power-law function, a value of *m* which yields a varying density, *while* being manufacturable, must be selected. Where at the same time, the density gradation should not emulate the linearly increasing $m = 1$. To determine the exponential terms that will be investigated, an optimization between available densities and overall specimen length is performed. Figure 5.2 shows the analytical discretization of the density gradient for $m = 0.5$ & 2; this resulted in layer thickness that could not be easily created, therefore, a practical approximation was implemented.

2-D DIC Approach

In order to fully characterize the FGFMs undergoing high strain rate deformation, it is necessary to obtain the boundary stress term and the inertial stress term. The boundary stress can be obtained from the strain gauges mounted on transmitted bar. The inertial stress term requires the quantification of the acceleration field which can be obtained by differentiating the displacement field. DIC is utilized to characterize these displacements, where it is important that the temporal resolution is selected so that we may have a sufficient number of data points.

As the FGFM being tested are of low-impedance, we use low-impedance bars to ensure discernable transmitted wave signal; in this case polycarbonate bars measuring approximately 5.5 ft. are used in conjunction with a polycarbonate striker

bar of 18 in. Two 350 Ω strain gages separated by 180° on both the incident and transmitter bar are used, where the incident bar gauges are also used for triggering. Two high speed cameras, HPV-X2 Shimadzu, are placed on either side of the SHPB where one camera will record the full field deformation at 400 k frames per second and the other camera will capture the beginning of deformation at a higher frame rate of 1 M frames per second. Both cameras were equipped with 100 mm Tokina macro lenses which yielded an optical resolution of 101 μm/pixel. To record at 1 M fps a 2000 W flash monolight from Photogenic Inc. was used, where a reflective bowl was used to redirect this light and illuminate the opposite side of the sample for the lower frame rate captures.

Results and Discussion

From Figs. 5.3 and 5.4, the strain evolution can be seen. As the load increases, axial strain is only seen to develop in the layers of lowest density. Axial strain is maximum in the lower density layers and minimum in the higher density layers. Interestingly, it can be seen that the failure mechanisms do not allow for uniform strain at a given location; instead, the strain propagates from a localized region ultimately causing uniform deformation across the layer.

Figure 5.5 shows the global stress-strain response for convex and concave density gradients. To achieve this plot the inertial stress term calculated from DIC is added to the boundary stress term measured using strain gauges. The initial hump in the stress strain response is seen and is attributed to the inertia of specimen.

From Fig. 5.6, upon comparison between the concave and convex samples at 10% strain, the convex absorbed ~4 times the energy of the concave specimen; this can be attribute to the increased apparent density of the convex sample. The energy absorbed was calculated by integrating the stress-strain curves using a trapezoidal approximation. Table 5.2 shows the normalized energy absorption with respect to mass. It can be concluded that the convex sample has increased energy absorption when compared to its concave counterpart.

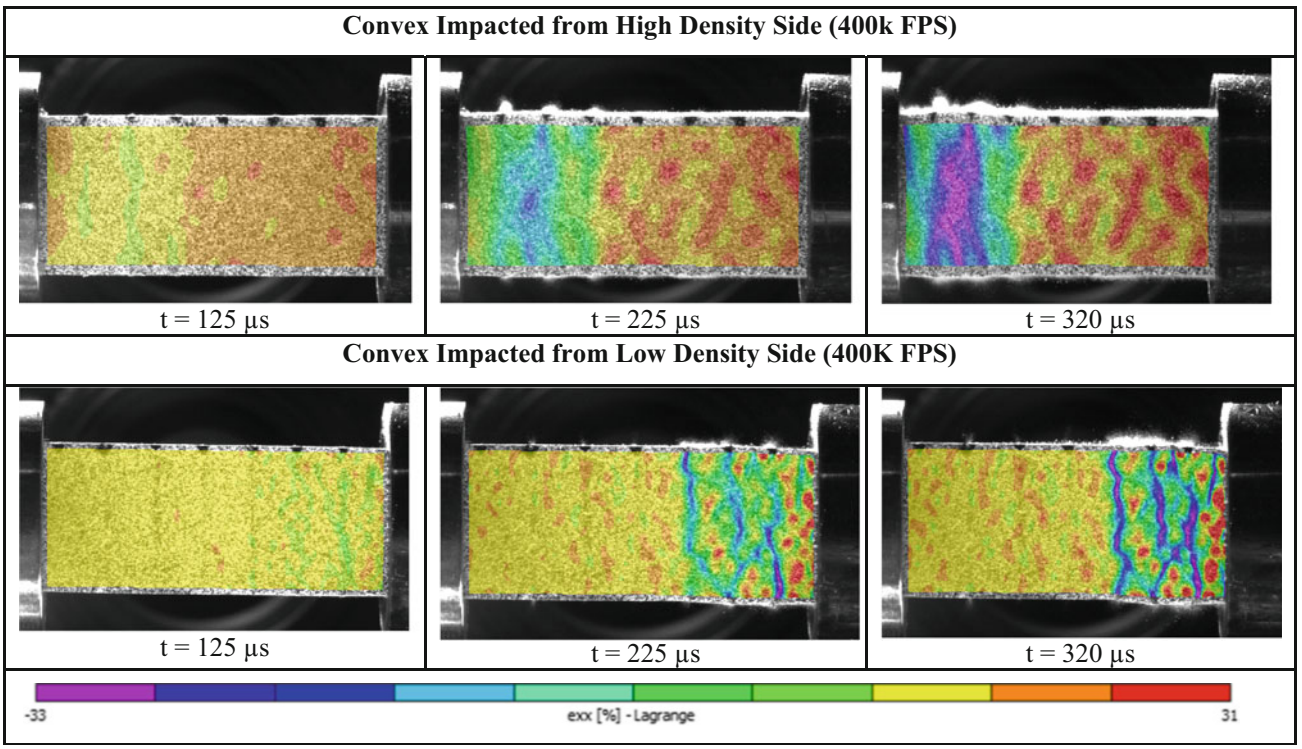

Fig. 5.3 Strain evolution of FGM foam with convex configuration

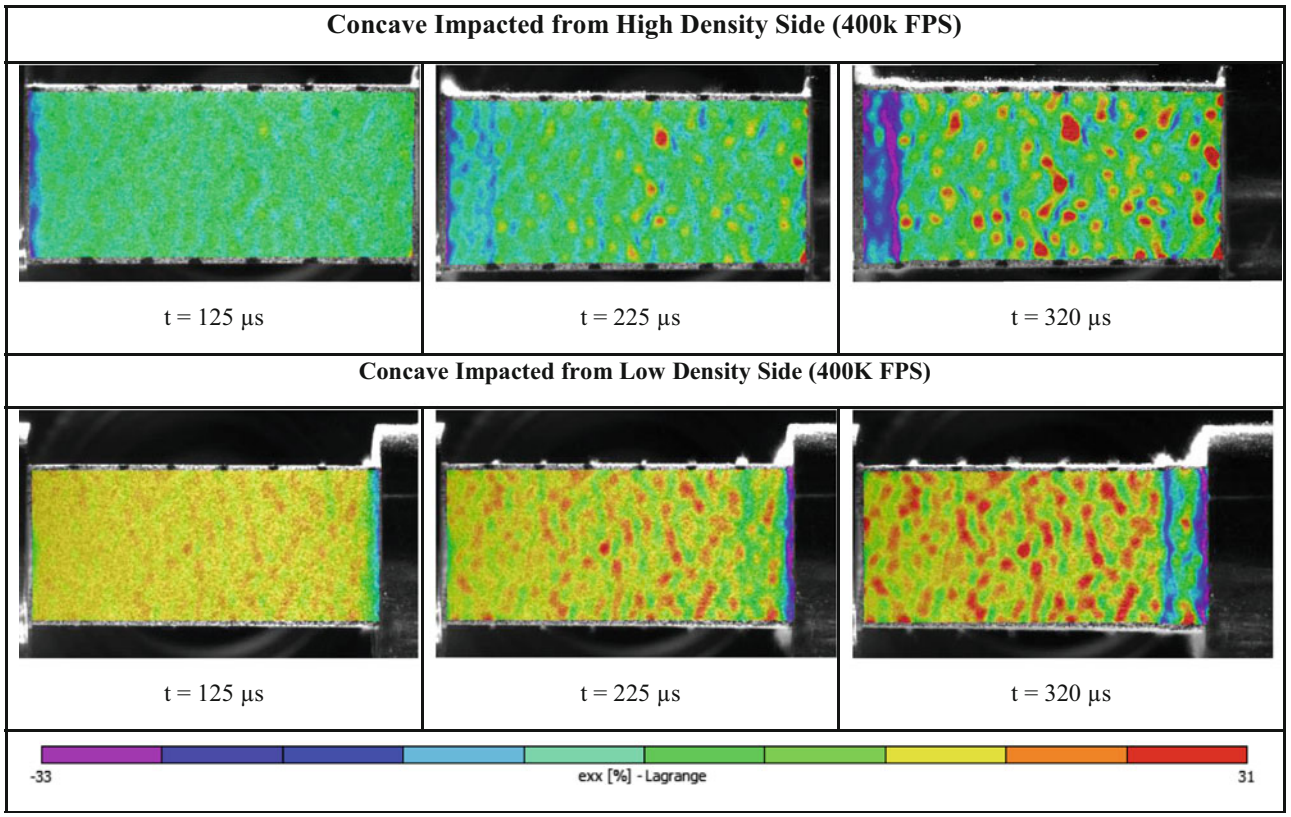

Fig. 5.4 Strain evolution of FGFM with concave density configuration

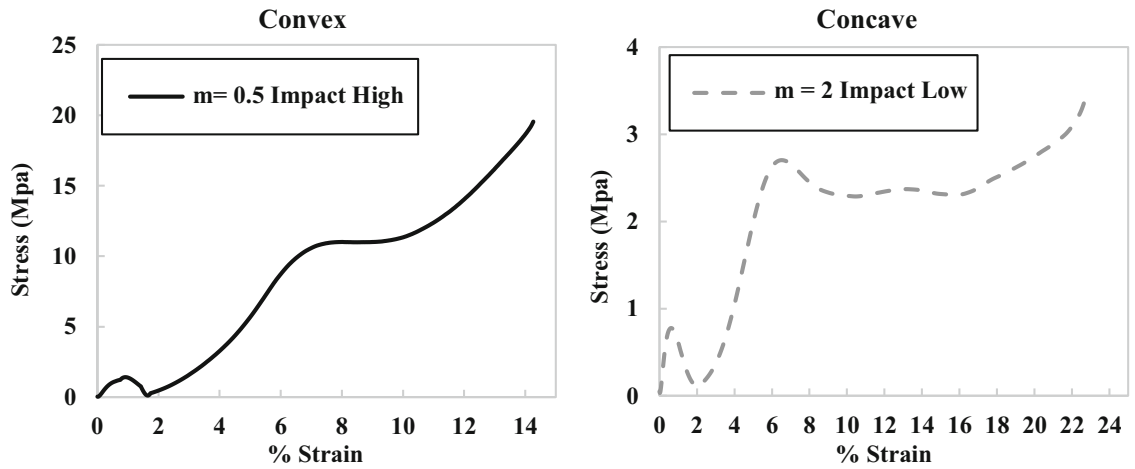

Fig. 5.5 Stress-strain curves for FGM with concave and convex nonlinear power-law approximation

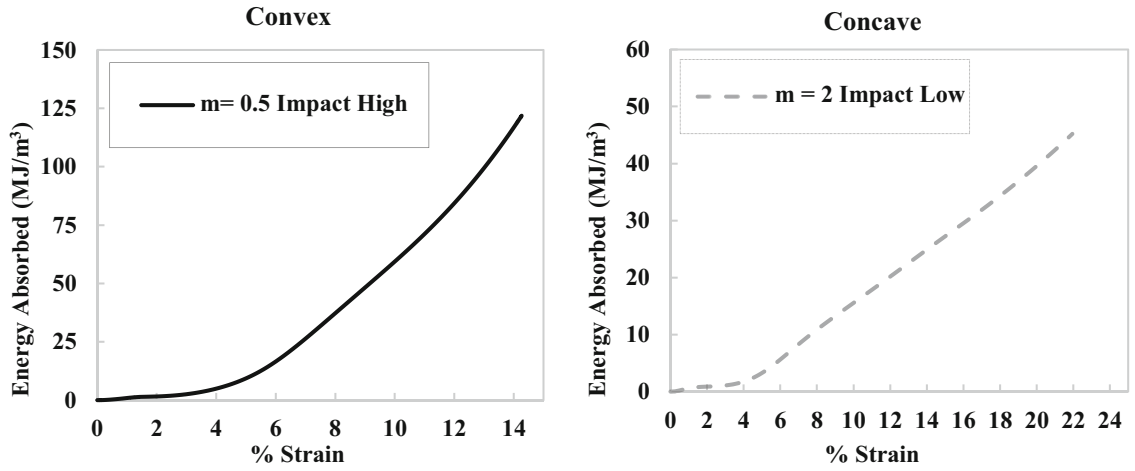

Fig. 5.6 Energy Absorption curves for concave and convex nonlinear power-law approximated FGFM

Table 5.2 Normalized energy absorption for both convex and concave specimens

Energy absorption comparison (10% strain)	
Convex	Concave
.1091 MJ/kg	.0489 MJ/kg

Summary

This work is a continuation of the analytical methods [1–4] previously implemented to characterize FGFMs. The energy absorption characteristics have been quantified for nonlinear density gradation of foam materials for both concave and convex functions experimentally. This required the use of SHPB to determine the boundary stress and DIC to determine the inertia stress; where once combined, the global dynamic response of the FGFM can be determined. The convex gradient is a more superior configuration than the concave, yielding double the amount of energy absorbed per kg. For future efforts, the investigation into the dynamic response of different density configurations for the optimization of energy absorption; as well as, the failure mechanisms that govern their deformation.

Acknowledgement The financial support of Us Army Research Office with grant number W911NF-17-S-0002 is greatly acknowledged.

References

1. Cui, L., Kiernan, S., Gilchrist, M.D.: Designing the energy absorption capacity of functionally graded foam materials. Mater. Sci. Eng. A. **507**(1–2), 215–225 (2009). https://doi.org/10.1016/j.msea.2008.12.011
2. Kiernan, S., Cui, L., Gilchrist, M.D.: Propagation of a stress wave through a virtual functionally graded foam. Int. J. Nonlin. Mech. **44**(5), 456–468 (2009). https://doi.org/10.1016/j.ijnonlinmec.2009.02.006
3. Koohbor, B., Ravindran, S., Kidane, A.: Impact response of density graded cellular polymers. In: Kimberley, J., Lamberson, L., Mates, S. (eds.) Dynamic Behavior of Materials, vol. 1, pp. 17–23. Cham, Springer International (2018)
4. Koohbor, B., Kidane, A.: Design optimization of continuously and discretely graded foam materials for efficient energy absorption. Mater. Des. **102**, 151–161 (2016). https://doi.org/10.1016/j.matdes.2016.04.031
5. Liu, H., Zhang, Z., Liu, H., Yang, J., Lin, H.: Theoretical investigation on impact resistance and energy absorption of foams with nonlinearly varying density. Compos. Part B. **116**, 76–88 (2017). https://doi.org/10.1016/j.compositesb.2017.02.012

Chapter 6
Numerical and Experimental Investigation of Density Graded Foams Subjected to Impact Loading

Vijendra Gupta, Dennis Miller, and Addis Kidane

Abstract Cellular materials offer many advantages due to their higher energy absorption capacity and strength for a given weight. The energy absorption performance is dependent on material density. Different density foams can be tailored and graded in a structure so that the merits of both low density and high density foams can be exploited. In this work, density graded polymeric foams with different configurations are examined, and their response to impact loading is studied both numerically and experimentally. Two-dimensional cell-based finite element model is developed for modeling the dynamic response of foams with different density gradation in Abaqus, a commercial finite element software. Three different types of foam structures are studied. Each of the foam structures is made up of three different density layers. The experimental investigation is also carried out on a gas gun setup incorporating high-speed imaging and is used to verify the numerical results. The stress-strain curves and the energy absorption characteristics of different graded foam structures are evaluated. It is found that the graded foam structure with higher density layer on the impact side absorbs more energy than the uniform foam structure at lower strains.

Keywords Graded foam · Impact loading · Energy absorption · Voronoi model · Digital image correlation

Introduction

Cellular foams are known to have excellent energy absorption ability and find applications wherever the effect of impact loading is desired to be mitigated [1]. The response of the solid foams depends mainly on the density. Lower density foams absorb more energy at lower stress levels, and higher density foams absorb more energy at higher stress levels. A superior energy absorption performance can be obtained if layers of different densities are united together.

There have been several numerical and experimental works on analysis of the mechanical response of solid foams. The effect of various microstructure irregularities in two-dimensional (2-D) foams has been studied at the quasi-static loading rate [2]. Wang et al. [3] investigated three-dimensional (3-D) foam subjected to high-velocity dynamic loading using a finite element model. Ajdari et al. [4] examined 2-D graded foam structure subjected to high rate dynamic loading. The quasi-static response of foam made up of discrete layers has been experimentally investigated [5].

In the present work, the response of the graded foam is studied under high impact velocity loading and compared to the foam having uniform density keeping the overall density same. The energy absorption performance of the foams is studied through both numerical models and experimental investigation. The numerical model is developed using cell-based finite element models in Abaqus. The model is generated by random 2-D Voronoi tessellation. 3-D models are closer to the real foams but are complex and computationally time intensive. Even though 2-D models do not capture the porosity of real foams in the third dimension, they are more straightforward and computationally more efficient. Thus, 2-D models were used for studying the dynamic behavior of foams. The foam structure is divided into discrete layers with different densities and its response is analyzed when subjected to dynamic loading. The numerical results are supported by the experimental investigation which is implemented using digital image correlation (DIC) along with high-speed imaging. The deformation of layered rigid polyurethane foam samples is analyzed under high-velocity impact loading.

V. Gupta (✉) · D. Miller · A. Kidane
Department of Mechanical Engineering, University of South Carolina, Columbia, SC, USA
e-mail: vijendra@email.sc.edu

L. E. Lamberson (ed.), *Dynamic Behavior of Materials, Volume 1*, Conference Proceedings of the Society for Experimental Mechanics Series, https://doi.org/10.1007/978-3-030-30021-0_6

Numerical Modeling

The finite element model is developed using Voronoi tessellation which is a common practice to model foams as it captures the nucleation and growth process observed in the cellular solids [6]. The Voronoi model, shown in Fig. 6.1, is an area of 15×15 mm^2 divided into three 5 mm thick layers. The finite element model is created in Abaqus environment. The material properties of rigid polyurethane are used for analysis. The parent material of the foam is assumed to be elastic-perfectly plastic with density of 1200 kg/m^3, Young's modulus of 1.6 GPa, Poisson's ratio of 0.33, and yield stress of 127 MPa. The cell walls are modeled by quadratic beam elements. The right end of the model is impacted by a rigid surface at 100 m/s, and the left end is supported by a rigid surface. The foam specimen is free to slide in traverse direction on rigid surfaces at both the ends. The coefficient of friction between the rigid surfaces and cell walls is set to be 0.1. The finite element model is solved using Abaqus/Explicit code.

By changing the wall thickness of the cell walls, the density of the foam in distinct layers can be controlled. Three types of foams based on different specified densities, as shown in Table 6.1, in the individual layers were studied. Foam A represents the uniform density foam with all the three layers having same density, while Foam B and Foam C are graded foam structures with linearly increasing and decreasing densities respectively. The overall density for all the foam structures is kept same to have an appropriate comparison of performance between them.

The stress-strain curves are obtained for the three types of foam structures. The stress-strain curves (up to 50% global strain) at the support side and the impact side are shown in the Fig. 6.2. The stresses on the impact end and the support end do not agree with each other since at high loading rates, the stress field is non-homogeneous. High stresses are observed on the impact end at low strains because of the inertia of the foam structure. The stresses become lower at higher strains. On the other hand, the stress at the support side is initially zero as the stress wave takes some time to reach the support end and the stress increases only after a certain point when the impact end has already seen some deformation.

The energy absorbed by the foam is extracted directly from the internal energy of the finite element model. The energy absorbed for each of the three specimens is shown in Fig. 6.3. The energy absorbed in Foam A increases approximately in a linear manner with the strain. On the other hand, the energy absorbed in Foam B increases rapidly at lower strains and does not increase much at higher strains. The energy absorption for Foam C is the least. The energy absorbed in Foam C increases slowly at lower strains and at higher strains it roughly increases at the same rate as that of Foam A.

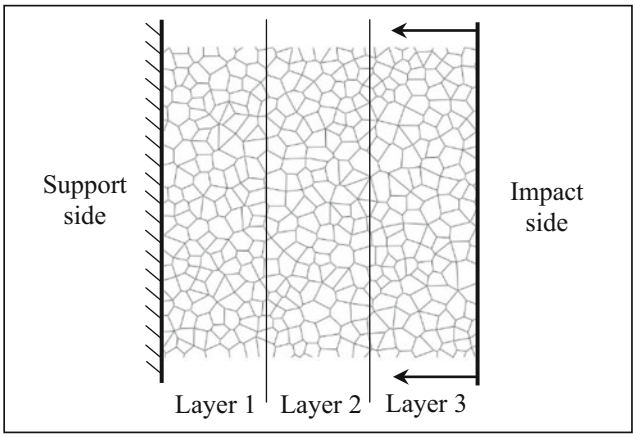

Fig. 6.1 2-D Voronoi model

Table 6.1 Density (in kg/m^3) for different layers

	Foam A	Foam B	Foam C
Layer 1	320	160	480
Layer 2	320	320	320
Layer 3	320	480	160

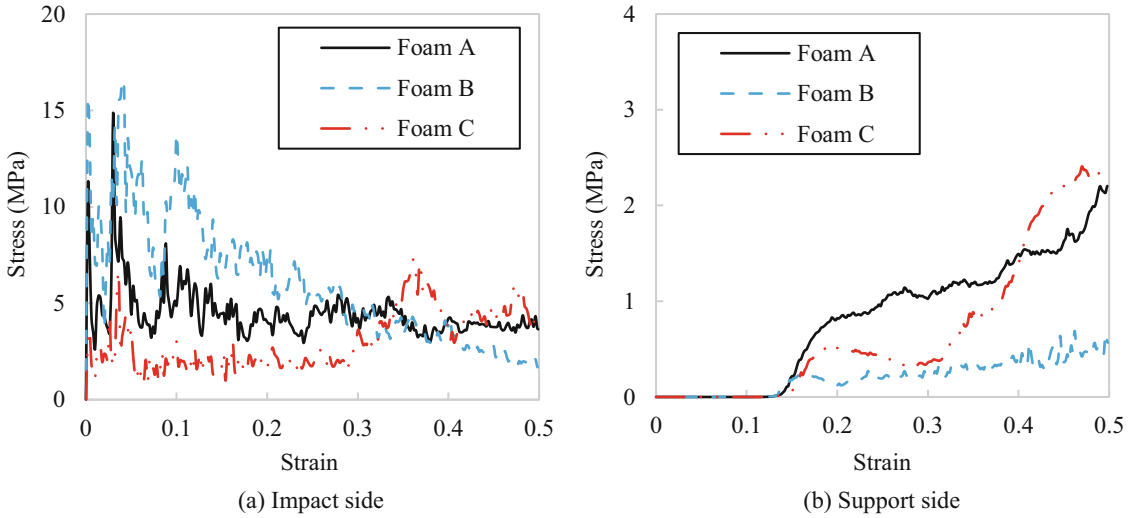

Fig. 6.2 Stress-strain curves for different foam structures

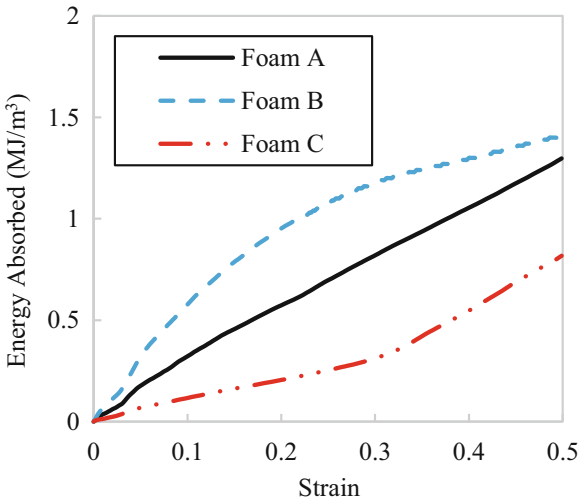

Fig. 6.3 Energy absorbed for different foam structures

Experimental Study

3-D rigid polyurethane foams are used for the experimental work. Similar to the numerical work, three different types of foam specimens are studied, and they are identified as Specimen A, Specimen B, and Specimen C. All the foam specimens are cubical samples of $15 \times 15 \times 15$ mm^3. Each of the foam specimens is made up of three 5 mm thick layers as shown in Fig. 6.4. The density of each of the layers is identical to the densities considered in numerical work as given in Table 6.1.

The left surface of the specimen is mounted on the load cell, which is fixed on a rigid support. The right surface of the specimen is impacted by a cylindrical polycarbonate projectile fired from a forward impact gas gun setup. The projectile is made to impact the specimen at approximately 100 m/s. HPV-X2 high-speed video camera is used to acquire images at 500 k fps. The experimental setup is shown in the Fig. 6.5.

The full-field stress and the strain in the specimen are calculated using digital image correlation [7]. VIC-2D, a commercial software by Correlated Solutions Inc. is used to post-process the digital images. The full-field stress is obtained from the inertial stress and boundary stress using the technique mentioned in [8]. The stress-strain curves for both the impact end and the support end in different specimens are shown in Fig. 6.6.

To determine the energy absorbed by the specimen, the full-field stress is spatially averaged and the area under the stress-strain curve is evaluated. The energy absorbed for each of the three specimens is shown in Fig. 6.7. Similar trends as found

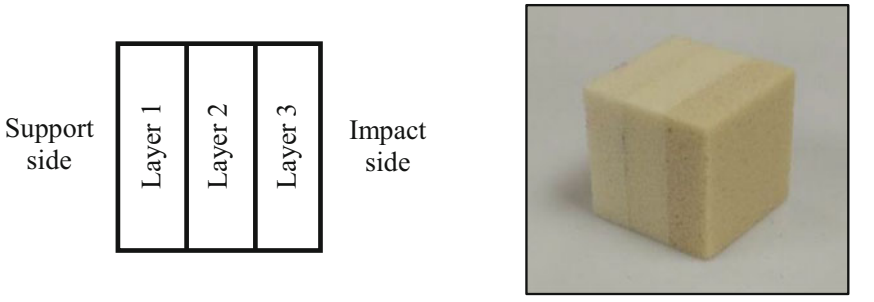

(a) Schematic of foam specimen (b) Actual graded foam specimen

Fig. 6.4 Foam specimen

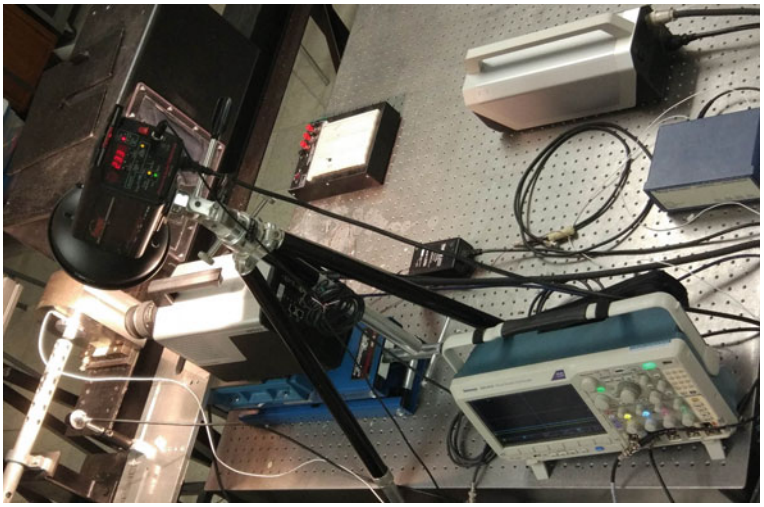

Fig. 6.5 Experimental setup

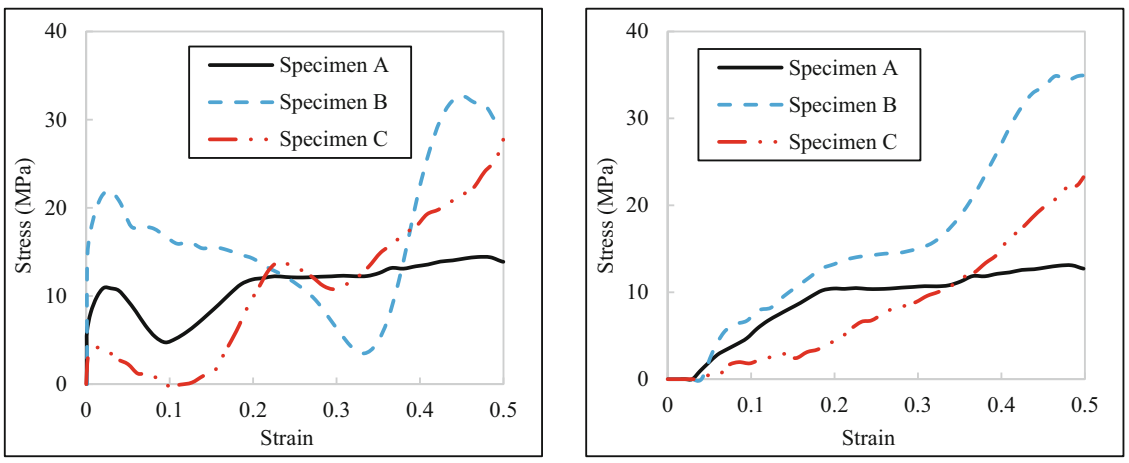

(a) Impact side (b) Support side

Fig. 6.6 Stress-strain curves for different specimens

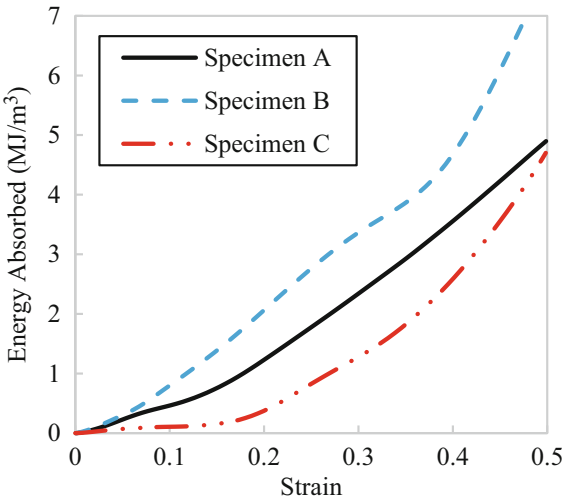

Fig. 6.7 Energy absorbed for different specimens

in the numerical work are observed here. The foam with higher density layer on the impact side performs better than the uniform density foams at lower strains. While the foam with lower density layer on the impact side performs worse than the uniform density foams.

Summary

The response of the graded foam structure is studied using numerical models and experimental observations. Cell-based finite element models are developed using Voronoi technique, while the experimental investigation is conducted using digital image correlation and high-speed imaging. The performance of graded foam structure with higher density layer towards the impact side is found to be better than the uniform density foam structure. Alternatively, the foam structure with lower density layer on the impact end is found to be underperforming. The graded foam structure looks attractive as it has the potential to absorb more energy if tailored in appropriate configuration. As a future scope of study, the optimal configuration of foam for maximizing the energy absorption can be explored.

Acknowledgment The financial support of US Army Research Office (grant number W911NF-17-S-0002) is greatly acknowledged.

References

1. Gibson, L.J., Ashby, M.F.: Cellular Solids: Structure and Properties, 2nd edn. Cambridge University Press, Cambridge (1997)
2. Alkhader, M., Vural, M.: Mechanical response of cellular solids: Role of cellular topology and microstructural irregularity. Int. J. Eng. Sci. **46**(10), 1035–1051 (2008)
3. Wang, S., Ding, Y., Wang, C., Zheng, Z., Yu, J.: Dynamic material parameters of closed-cell foams under high-velocity impact. Int. J. Impact Eng. **99**, 111–121 (2017)
4. Ajdari, A., Nayeb-Hashemi, H., Vaziri, A.: Dynamic crushing and energy absorption of regular, irregular and functionally graded cellular structures. Int. J. Solids Struct. **48**(3–4), 506–516 (2011)
5. Koohbor, B., Kidane, A.: Design optimization of continuously and discretely graded foam materials for efficient energy absorption. Mater. Des. **102**, 151–161 (2016)
6. Silva, M.J., Hayes, W.C., Gibson, L.J.: The effects of non-periodic microstructure on the elastic properties of two-dimensional cellular solids. Int. J. Mech. Sci. **37**(11), 1161–1177 (1995)
7. Sutton, M.A., Orteu, J.-J., Schreier, H.: Image Correlation for Shape, Motion and Deformation Measurements: Basic Concepts, Theory, and Applications, 1st edn. Springer, Berlin (2009)
8. Ravindran, S., Koohbor, B., Malchow, P., Kidane, A.: Experimental characterization of compaction wave propagation in cellular polymers. Int. J. Solids Struct. **139–140**, 270–282 (2018)

Chapter 7
Method for Characterizing Electric Current Effects on the Deformation of Metals

Christopher Rudolf, Wonmo Kang, and James Thomas

Abstract Traditional metal forming requires large forces and substantial tooling, high power, and large amounts of energy. Passing an electric current through the metal during forming has been shown to reduce the deformation energy and increase the materials' formability, leading to the possibility of increased formed-shape complexity. The primary challenge in characterizing electric current effects on plastic deformation has been decoupling the current and intrinsic Joule heating effects. Many of the experiments reported in the literature have specimen geometry and fixturing features that can lead to concentrations of stress, deformation, current, and/or temperature. The presence of one or more localized field concentrations in the specimen gage length can bias the observed deformation behavior and lead to erroneous conclusions. In this work, we addressed this challenge by conducting independent electro- and thermo-mechanical experiments for the current- and temperature-controlled characterizations, respectively. For the former, a novel cylindrical tensile specimen and grip design were developed to enable larger current densities with uniform deformations, currents, and temperature conditions in the gage section. Forced-air convection with vortex tube cooling was used to maintain uniform temperature conditions within the gage section. Non-contact video strain and infrared temperature measurements were employed, and test control and data acquisition were computer automated. A laboratory materials test system with an environmental chamber was used for tensile testing the cylindrical specimens under near-identical temperature histories as the applied current tests. These techniques were used to characterize the electro-deformation behavior of several pure metals, i.e., copper, iron, and titanium. The results convincingly demonstrated an electric current effect on the plastic deformation behavior of the titanium but not the copper and iron. Details of the experiments and methodology are described and discussed along with candidate mechanisms for current effects on the plastic deformation behavior of the titanium.

Keywords Electrically-assisted deformation · Microstructure · Titanium · Direct current · Constant current

Introduction

Electrically assisted deformation (EAD) is a technique by which electric current passage induces reductions in flow stress and ultimate strength for enhanced formability of metals. Despite its potential for manufacturing applications and many years of research, the role of the two key proposed mechanisms, intrinsically coupled electroplasticity (non-thermal effects) and resistive heating (thermal effects), has not been resolved. Passage of electric current in a metal produces temperature increases via Joule heating, which can affect thermally-activated deformation mechanisms such as thermal softening and expansion that mask possible non-thermal current effects. The different crystal structures (i.e., fcc, bcc, hcp) and multi-scale microstructural features (i.e., voids, dislocations, and grain boundaries) can also play a role in the activation of different deformation mechanisms.

The primary technical challenges impeding progress have been: (1) developing critical experiments (methodology and hardware) capable of clearly separating the contributions of electric current and Joule heating to the plastic deformation process; and (2) the inherent complexity of possible electric current interactions with the deformation processes occurring in metals under a diverse range of physical mechanisms, material properties, and microstructures. Many of the experiments reported in literature have specimen geometry and fixturing features that can produce stress, deformation, current, and/or

C. Rudolf (✉) · J. Thomas
Naval Research Laboratory, Washington, DC, USA
e-mail: christopher.rudolf@nrl.navy.mil

W. Kang
Leidos Inc., Arlington, VA, USA

L. E. Lamberson (ed.), *Dynamic Behavior of Materials, Volume 1*, Conference Proceedings of the Society for Experimental Mechanics Series, https://doi.org/10.1007/978-3-030-30021-0_7

temperature concentrations, and the presence of one or more localized field concentrations in the test specimen gage length can bias the deformation behavior and lead to erroneous conclusions.

In this work, the challenge was addressed by utilizing independent electro- and thermo-mechanical experiments for current- and temperature-controlled characterizations, respectively. The hardware and testing methodology developed in this research carefully addressed the issues leading to current and temperature hot-spots and strain gradients that may be responsible for many of the differing results reported for tests on the same material [1, 2]. In the sections below, details of the experiments and methodology will be described and discussed along with the test results for pure Cu, Fe, and Ti, and some candidate mechanisms for the observed current effects on the plastic deformation behavior of Ti.

Method

The critical design requirement for the test system was to achieve uniform current, temperature and strain conditions in the specimen gage section prior to specimen necking. Small specimen size provided greater temperature uniformity, however this meant that electric current had to be supplied to the specimen through the grips. Tensile loading offered the best possibility for achieving uniform conditions in the gage section with minimal effects from potential field concentrations at the specimen-grip interface.

Tensile experimentation at electric current densities of 10–100's A/mm^2 may require a large current (e.g., 80 A for 100 A/mm^2, test with a 1 mm diameter specimen), depending on specimen cross-section area, and this gives rise to safety concerns. Currents must be introduced into the specimen, sensitive components and instrumentation must be isolated from the current, and safe test operation must be guaranteed. Experimental design required consideration of the following:

1. Load-frame and gripping modifications to isolate the hot-side of the current and enable passage of large currents through the test specimen safely.
2. Specimen gripping hardware to achieve uniform strain, current density, and temperature conditions in the gage section.
3. Safe and accurate strain and temperature measurements along the gage length using non-contact methods.
4. Effective cooling to dissipate Joule heating in the gage section with potentially large (constant dc) current densities.
5. Time-synchronized data acquisition of signals from many different measurement sources.
6. Independent tensile experiments with zero current and ambient heating to achieve specimen temperature histories identical to those induced by Joule heating with electric current (i.e., thermal control experiments).

Test System

The methodology utilized two independent experimental setups (Fig. 7.1): an MTI SEMTester load-stage (MTI Instruments, Albany, NY) for tensile testing with applied electric currents, and an Instron ElectroPuls 3000 Test System (Instron, Norwood, MA) with an environmental chamber for tensile testing with controlled temperature histories to match those observed in the applied current tests. The zero-current, temperature history controlled tests with the Instron system provide a baseline for subtracting out thermal effects in the electric current test results to assess electroplasticity effects.

The SEMTester and tensile wedge-grip fixturing was modified to safely provide several hundred amps passing through the test specimen. The grip fixture with the positive current connection was electrically isolated from the load-frame and was capable of carrying the maximum tensile load (up to 8900 N). The (earth) grounded grip (load-cell side) was also electrically isolated to prevent any current from passing through the load cell. Numerous ground cables were added to the device for safety. The electrical isolation hardware for the wedge grips had to be mechanically robust enough to handle the maximum loads. The grips were modified to accommodate electrical isolation sleeves and washers made of polyimide and phenolic materials. The insulation hardware provided electrical isolation of the grips and specimen from the SEMTester device while allowing for transmission of tensile loads to the specimen.

The computer automated SEMTester load-stage, equipped with an 1100 N (250 lb) load cell, outputs load-displacement data via data-acquisition (DAQ) channels and analog-outputs (Fig. 7.2). A National Instruments (NI) DAQ system with a customized Labview code is employed to collect and synchronize data streams from multiple facility instruments. The system also provides control and monitoring of the electrical current supplied via an Agilent 6600C power supply (Agilent Technologies, Santa Clara, CA). The Instron ElectroPuls system was programmed and controlled using Bluehill Software and provided an analog output of the load which fed into the same NI DAQ to synchronize the load-displacement data with the data streams from the other instruments (video-extensometer and thermocouples).

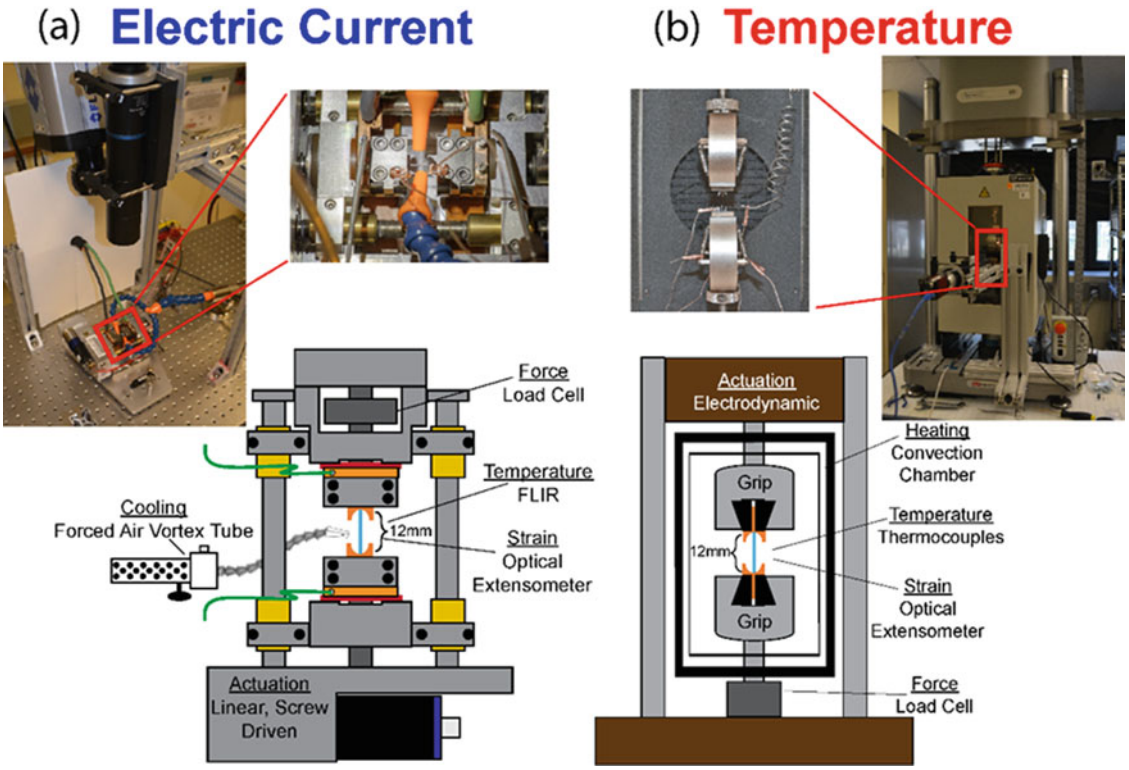

Fig. 7.1 Test methodology schematic for electric current tensile tests and corresponding temperature-history matched tests

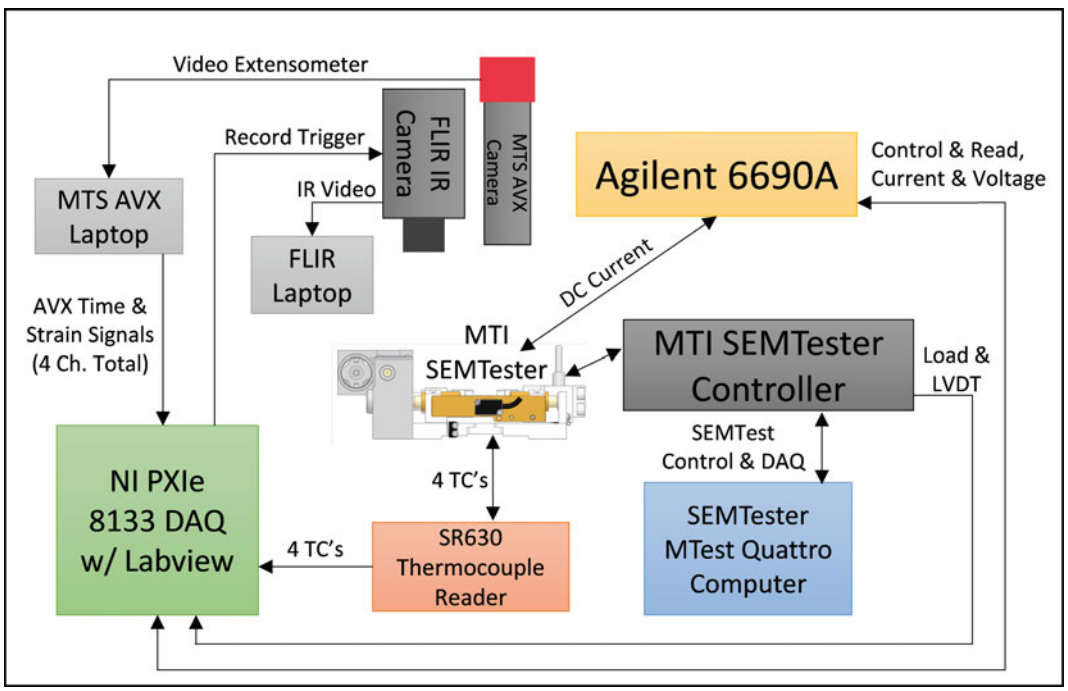

Fig. 7.2 Data flow diagram for applied electric current testing

Strain and Temperature Measurements

A FLIR IR camera (SC8300HD, FLIR Systems), equipped with a 100 mm lens and running at 15 Hz, was controlled by ResearchIR software (FLIR Systems). Points and lines along the specimen gage section were set up in the software prior to test start to read and record the real-time temperatures (±2 °C resolution). The IR video was also digitally recorded to allow for post-test analyses of the specimen temperature and gradients. Accurate measurement of the specimen temperature by IR required the surface emissivity to be equal to ~1. For this, a spray-on graphite coating (GRAPHIT 33, Kontakt Chemie/CRC Industries Group) was used.

An AVX video extensometer (Part No. 574281–04, MTS Systems Corporation, Eden Prairie, MN) was used for specimen strain measurements. The system employed a camera (Model Manta G146B ASG, Allied Vision Technologies) with attached lens (Sill Optics Correctal T/0,2D) with an f-stop setting of 11 and video capture frame rate of 5 Hz. The video extensometer could track the motion of up to 100 points in real time. The displacement measurements used a scaling factor of ~ 43 pixels/mm. Strains, displacements, rotations, etc. could be calculated as desired from the stored video data post-test. To generate marks for video strain tracking, a high-temperature white paint was speckle patterned onto the specimens using an air brush at low pressure (~0.035 MPa (~5 psi)) with a steady even stroke. Non-contact strain measurement enabled accurate strain data irrespective of potential slipping in the grips, grip-to-gage geometry transitions, and machine compliance effects.

Forced Air Cooling

The Instron environmental chamber has a maximum temperature of 250 °C. This placed an upper limit on the current densities that could be applied during the electric-current test; specimen temperatures with Joule heating were kept below 250 °C. A forced air cooling method was adopted to keep the gage section temperatures uniform and to enable an increase in applied current densities during testing (while remaining below 250 °C). A Frigid-X adjustable spot cooler (NueAir Engineered Products, Cincinnati, OH) provided convective cooling to the specimen with chilled, compressed air during electric current testing. With an input pressure of ~0.5 MPa (70 psi), about 500 L/min of flow resulted providing 360 W of cooling. The chilled air was split and flowed through two nozzles on two sides of the specimen. This cooling method minimized the specimen temperatures and gradients in the gage length. The resulting maximum current densities were: 200, 70, and 45 A/mm^2 with corresponding maximum temperatures at peak loading of: 112, 134, and 222 °C for the copper, iron, and titanium specimens, respectively. The specimen geometry, tabbed-gripping (described below), and convective cooling provided greater heat transfer with minimal thermal gradients compared with methods previously reported in literature [2–4].

Specimen Considerations and Design

Current densities, j, as high as several hundred A/mm^2 were desirable. The current, I, needed is dictated by the specimen cross-sectional area. For example, using a specimen cross-section of 25 mm^2 and assuming $j = 100$ A/mm^2 requires a 2500 A current. The load cell on the SEMTester also placed limits on the specimen cross-sectional area in order to be able to achieve ultimate failure stresses below capacity (1100 N). A design plot (Fig. 7.3) was made for resulting stresses and current densities corresponding to an applied 1100 N load and 10 A current as a function of the specimen cross-section area.

Initial dogbone specimens had a cross-section area of 2.5 mm^2, and for this size, the maximum possible applied stress at 1100 N was 445 MPa; the current density for 10 A current was 4 A/mm^2. This implied that the material under test should have an ultimate strength less than the 445 MPa, and 100 A/mm^2 current density would require 250 A of current. The maximum stress possible and the current levels needed for desired current density levels led to the decision to further reduce the gage cross-section. The dogbone design included outriggers (marked in red on Fig. 7.4) that were used for axial alignment and cut before testing.

Cylindrical (wire) specimens nominally 1 mm in diameter were selected for simplicity (no machining needed) and ample availability of high-purity materials in this configuration. For 1 mm diameter circular cross-sections, the maximum possible stress in the specimen at 1100 N load is 1410 MPa, which exceeds the ultimate strength of most pure and alloy metals. The corresponding current density at 10 A current is 12.7 A/mm^2, so a specimen current density of 100 A/mm^2 would require only ~80 A of current, a threefold reduction from previous dogbone specimens.

A key challenge in testing the 1 mm wire samples in tension was how to grip the wire to achieve tensile failure in the gage-section. The initial wire specimen holder design (holder 001, Fig. 7.5a) was a simple, one-sided v-groove tab holder

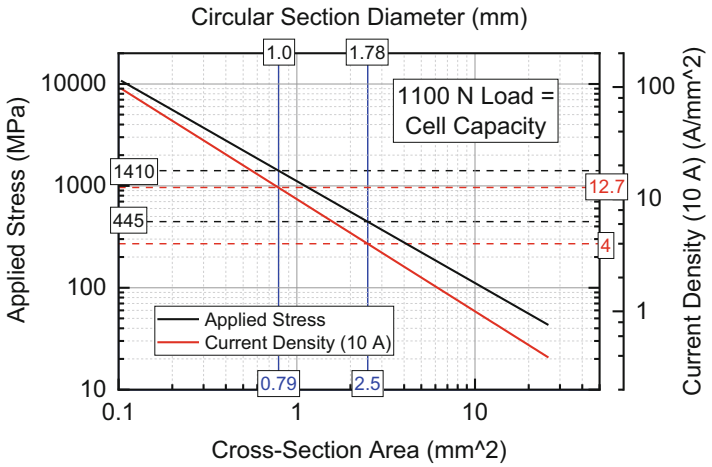

Fig. 7.3 Design plot for specimen sizing

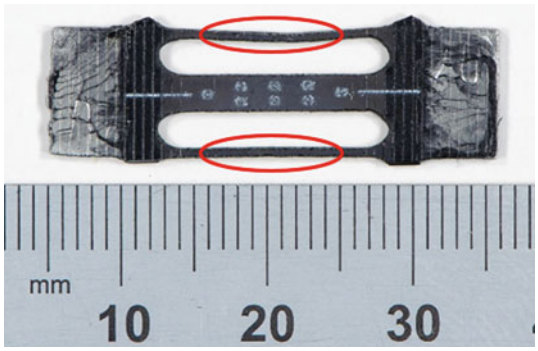

Fig. 7.4 Dogbone tensile specimen with high-emissivity graphite coating for IR temperature measurements and white circle targets for non-contact video strain measurements

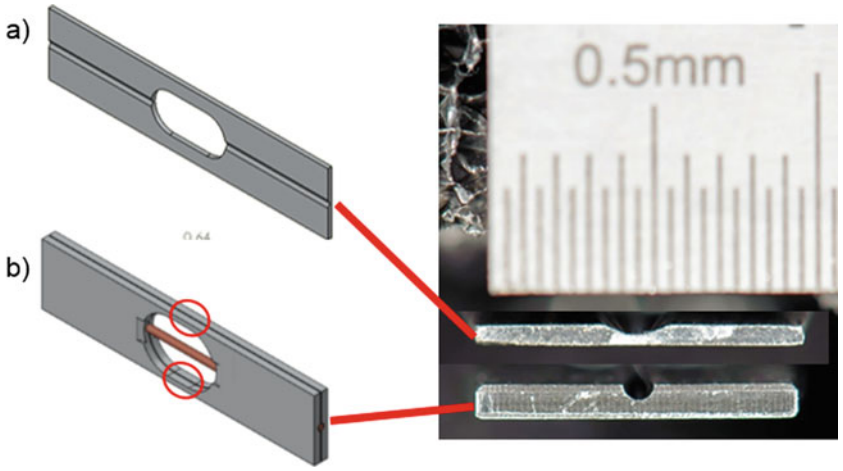

Fig. 7.5 CAD images and cross-sectional photos of (**a**) tab holder 001 and (**b**) tab holder 002

machined from aluminum. The wire was engaged by the wedge grips of the testing apparatus on top and the aluminum tab holder on the bottom. The wire tab holder also has "outriggers" for alignment during mounting, which are cut after mounting and prior to testing. This tab design led to many tensile failures in the grips, and high grip temperatures due to the large contact resistance between the grip wedges and the wire specimen.

A subsequent tab holder design (holder 002, Fig. 7.5b), utilized two tabs to sandwich the wire specimen with circular machined grooves ~2% larger in diameter than the wires, but with a slightly reduced depth. These tabs also had machined-in

taper features on the back-sides to provide a more gradual load-transition from gage section to grip, which performed well with specimen failures consistently occurring in the gage section rather than in or at the grips. This new design also provided better electrical and thermal contact between the grips and specimen compared to holder 001; Fig. 7.6 shows the new design produces a ~10 °C decrease in maximum temperature and lower gradients at a current density of 30 A/mm^2 on copper specimens. Additional schematic drawings of the tab holders can be found elsewhere [5].

The wire materials were supplied in wound-coil forms with significant residual stresses. To avoid adding significant plastic deformations during manually straightening, a stress-relief process was developed. Fixtures of identical materials (i.e., Cu bar for Cu wire, etc.) were machined with channels for straightening four lengths of wire (~1150 mm total) at a time. As shown in Fig. 7.7, each bar has four half-circle channels (1 mm diameter) for holding the wires straight when sandwiched between two bars. The assembly was bolted together to provide a clamping force and then oven heated in ambient air atmosphere at the temperatures and times listed in Table 7.1. The process produced straight wires, and subsequent metallurgical examinations showed that the stress-relief process had no effect on the "as-received" microstructures (grain sizes).

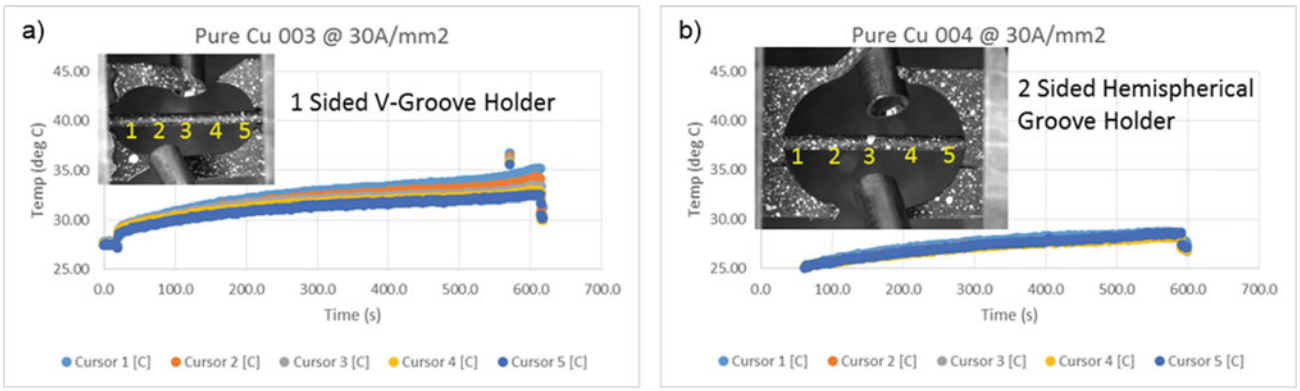

Fig. 7.6 Comparative plots of temperature across copper wire samples at a current density of 30 A/mm^2 for (**a**) holder 001 and (**b**) holder 002

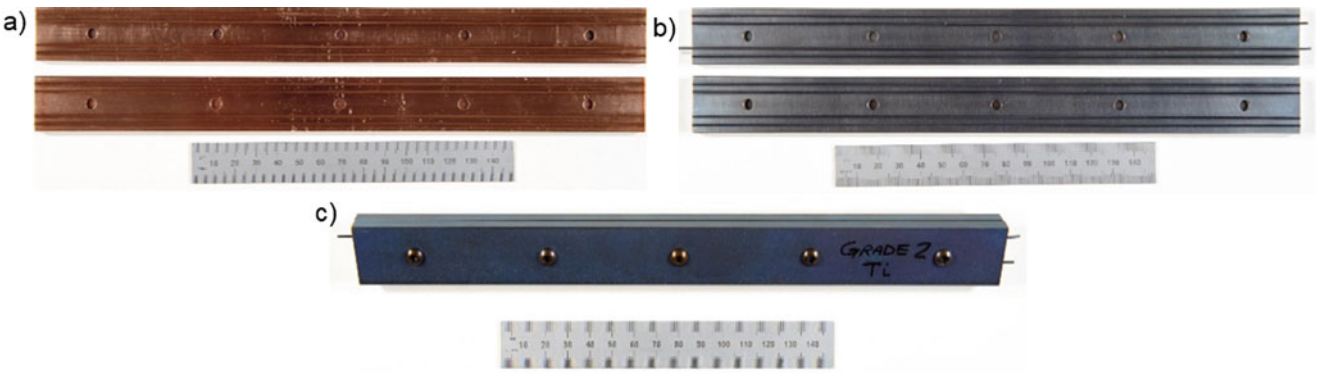

Fig. 7.7 Stress-relief fixtures for straightening the wire samples: (**a**) inside view of copper, (**b**) inside view of iron, and (**c**) assembled view of titanium

Table 7.1 Stress-relief parameters and grain sizes[a]

Material	Temperature (°C)	Time (hours)	Grain size (μm)
Copper (110)	190	2	3.3
Iron	425	2	5 and 10 bi-modal
Titanium (CP Grade 2)	500	2	9.0

[a]Grain sizes of the as-received and stress-relieved specimens were identical

Experimental

Zero-current baseline tensile tests were run using each system (SEMTester and Instron) at a cross-head displacement rate of 0.15 mm/min until break for matched comparison of stress-strain responses for each machine. As expected, they were identical. The following tests were conducted on each material (Cu, Fe, and Ti): zero-current baseline runs, non-zero current runs at two current densities for each material type, and temperature-history matched runs at zero-current in the Instron system. Preliminary tests were performed for each material type with SEMTester specimen-fixture cooling to determine the maximum current density levels possible while maintaining a gage-section temperature less than 200 °C (to ensure that the gage-section temperatures remained below the 250 °C at the ultimate load point of the test where the specimen temperature increases as a result of cross-section area decreases) and grip/fixture temperatures less than 50 °C to avoid possible damage to the load cell. The lower test level current densities were selected to be ~2/3 of the maximums. The Cu specimens were tested with constant dc current densities of: 0, 125, and 200 A/mm^2; the Fe specimens at: 0, 45, and 70 A/mm^2; and the Ti specimens at: 0, 25, and 40 A/mm^2. Multiple tests were performed (at least 3) for each material at each current density and at each temperature to assess repeatability. The results showed variations in ultimate strengths below 1.4% for the copper and iron specimens and 2.7% and 5% for titanium specimens at the low and high current densities, respectively. Average values for the multiple tests are reported.

Specimens were first tested at the desired current densities. The resulting thermal histories (averaged gage temperature versus time) were then programmed in the Instron environmental chamber to match the current-induced temperature history. This procedure differs from some reported in literature [2, 4] that use a single average or maximum temperature from the electric current test for the temperature control point in matching zero-current tests. Figure 7.8 shows averaged temperature histories for the three metals at the highest applied current densities. Prior to necking, the specimen temperatures increased by: 25, 50, and 35 °C respectively for the Cu, Fe, and Ti metals. After necking, a rapid increase in temperature occurs that cannot be simulated in the Instron environmental chamber. The results below are reported up to the ultimate load points (marked on the figure) where the temperature-history is accurately followed. The use of one constant temperature during the zero-current thermal baseline testing leads to unquantified experimental inaccuracies.

Results and Discussion

The test results for the pure Cu, Fe, and Ti materials are summarized in Table 7.2.

No discernable effects of current on the plastic deformation behavior of the pure Cu and Fe materials were detected beyond those due to temperature. Post-test examination of the Cu and Fe microstructures across the cross-section for all test

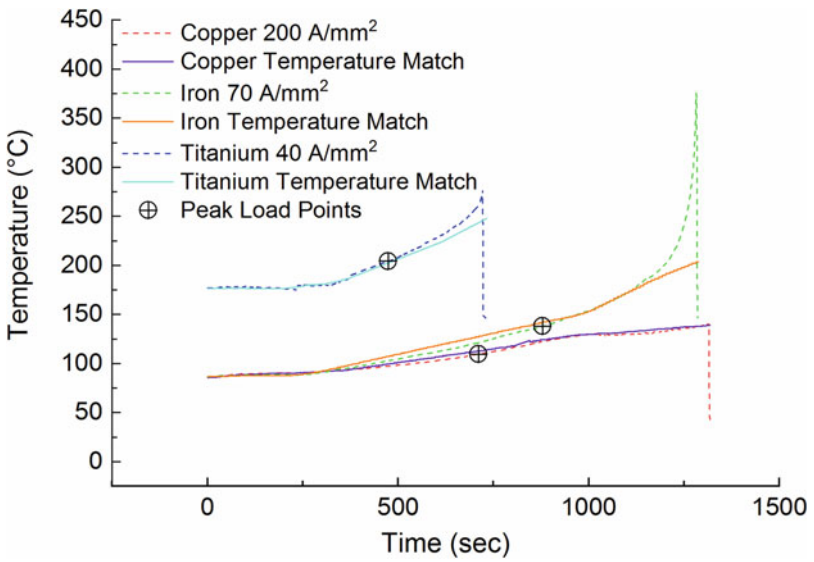

Fig. 7.8 Gage-section thermal histories from the electric current tests (averaged-dashed lines) and matching thermal histories from the zero-current tests (averaged-solid lines)

Table 7.2 Results from room temperature, applied electric current tests, and corresponding temperature-history matched zero-current tests for pure Cu, Fe, and Ti

Material	Current density (A/mm^2)	Temp. at ult. stress (°C)	Ultimate eng. stress (MPa)	% Change in eng. stress	Axial strain at ult. stress (% extension)	Yield strength (0.2% offset)	% Change in yield strength
Cu	RT	22.9	239.1	–	21.75	200.2	–
Cu	125	66.9	215.0	↓ 1.05%	16.50	193.6	↑ 1.26%
Cu	Temp. 125	–	218.3		15.70	191.2	
Cu	200	111.4	191.8	↓ 0.26%	9.00	180.3	↑ 0.28%
Cu	Temp. 200	–	192.3		7.50	179.8	
Fe	RT	21.2	323.9	–	20.53	257.2	–
Fe	45	53.9	311.7	↑ 0.52%	12.60	272.3	↑ 2.60%
Fe	Temp. 45	–	310.1		15.04	265.4	
Fe	70	136.3	275.7	↓ 0.58%	9.33	249.2	↓ 0.32%
Fe	Temp. 70	–	277.3		8.37	250.0	
Ti	RT	22.9	304.2	–	18.45	279.6	–
Ti	25	69.0	224.9	↓ 18.96%	8.88	214.3	↓ 19.13%
Ti	Temp. 25	–	277.5		13.12	265.0	
Ti	40	221.1	151.7	↓ 21.84%	3.20	150.4	↓ 20.25%
Ti	Temp. 40	–	194.1		7.88	188.6	

conditions showed no discernable grain growth. This was expected given that the maximum temperatures reached during testing were below the stress-relief temperatures, which did not produce microstructure changes. As the current densities increased, the flow stresses, ultimate strengths, and strains at the ultimate load were all reduced. Similar reductions occurred with the corresponding zero-current tests with matching temperature-histories. The results show that for Cu and Fe, electric current does not inherently affect the plastic deformation behavior (pre-necking) of these materials.

For Ti, the flow stresses, ultimate strengths, and strains at ultimate loads were all reduced with both applied current and elevated temperature, similar to the Cu and Fe specimens. However, the ultimate stresses were reduced by an additional ~19 and ~22% with applied electrical current versus that observed with matching temperature history! Post-test examination of the microstructure showed grain growth occurred in the deforming specimens with applied electric current (~35% and 64% for 25 and 40 A/mm^2, respectively) but not in the zero-current, temperature matched deforming specimens. More detailed microstructural analyses showed grain growth throughout the entirety of the specimen gage lengths and not just in the necking location. The observed grain growth was unexpected and surprising given that the maximum temperatures reached in testing were only 280 °C and 90 °C for the 40 A/mm^2 and 25 A/mm^2 current densities, respectively, well below the stress-relief temperature where no grain growth was observed.

Analysis of the possible mechanisms for the observed grain growth along with the resulting effect on the plastic deformation behavior is ongoing. It was found that grain growth only occurs with combined effects of mechanical deformation, electric current, and elevated temperatures. Additional experiments performed with passage of electric current without tensile deformation did not result in growth of the microstructure. It is possible that mechanical straining drives grain growth at temperatures lower than traditionally expected. Texture evolution in the microstructure could lead to localized, anisotropic electric resistivity that may potentially result in enhanced localized Joule heating at the grain boundaries. X-ray diffraction (XRD) and electron backscatter diffraction (EBSD) analyses are being utilized to provide greater insight. The further analysis of the mechanisms will be published elsewhere.

Conclusion

The use of independent electro- and thermo-mechanical testing systems enabled decoupling of the effect of elevated temperature caused by Joule heating on the metal's plastic deformation behavior from that caused by electric current passage. Initial baseline testing, use of the NI DAQ to synchronize all data, and use of the non-contact strain measurements removed any concern regarding differing machine compliance between the two test systems.

The experimental methodology followed in this work successfully removed any bias in the observed deformation behavior caused by inhomogeneity of the specimen gage-section that could have contributed to the differing conclusions reported in

literature. The symmetric geometry of the cylindrical wire specimens reduced the occurrence of stress and temperature concentrations that are traditionally observed in dogbone shaped tensile specimens. Higher constant dc current densities were facilitated by small specimen cross-sectional area, reduced contact resistance provided by the custom tab holders, and forced air convective cooling using a vortex air chiller. Both the tab holders and active cooling also reduced the temperature gradients over the gage section to <10 °C for all specimens and current densities tested. Off-axis deformation was negated by the design of the tab holders to include outriggers for precise alignment during the gripping of the specimens. This resulted in uniform, uniaxial straining. Lastly, what sets this work apart from previous methods was using the precise, history-matched temperature realized during the applied current testing for the zero-current temperature testing.

The meticulous experiments performed in this work unambiguously showed that the passage of electric current through pure Cu or Fe reduces the deformation forces, but the reductions are due to the increased temperature alone. The experiments with pure Ti discovered novel grain growth that only occurred with concurrent electric current (with accompanying temperature increases) and mechanical deformation. Mechanisms that might explain these findings are being explored and are expected to provide new insight on EAD of metals.

This work focused on three pure metals to reduce the complexity of the microstructure and better facilitate a definite understanding of the contributing factor (i.e., temperature or electric current) that causes the observed changes in plastic deformation behavior. It is evident from the initial Ti results that even after removing any bias caused by gage-section inhomogeneity, a full understanding of the mechanisms at play is nevertheless complex. There is an inherent coupling of electric current, mechanical deformation, temperature, and microstructure that will require complex modeling to fully decouple, especially when examining material systems that are more technologically relevant to complex manufacturing needs (i.e., alloys such as Ti-6Al-4V or 304 SS). Future research in this field should incorporate computational modeling with supplemented, methodical experimentation and microstructure characterization to better understand the underlying interaction of electric current on flow stress and deformation behavior.

Acknowledgements During this project, C.R. was supported by the ASEE-NRL fellowship. This work was supported by the Office of Naval Research (ONR) through the US Naval Research Laboratory's Basic Research Program.

References

1. Kinsey, B., Cullen, G., Jordan, A., Mates, S.: Investigation of electroplastic effect at high deformation rates for 304SS and Ti-6Al-4V. CIRP Ann. **62**(1), 279–282 (2013)
2. Ross, C.D., Kronenberger, T.J., Roth, J.T.: Effect of dc on the formability of Ti-6Al-4V. J. Eng. Mater. T. Asme. **131**(3), (2009)
3. Magargee, J., Morestin, F., Cao, J.: Characterization of flow stress for commercially pure titanium subjected to electrically assisted deformation. J. Eng. Mater. T. Asme. **135**(4), (2013)
4. Salandro, W.A., Bunget, C.J., Mears, L.: Several factors affecting the electroplastic effect during an electrically-assisted forming process. J. Manuf. Sci. E. T. ASME. **133**(6), (2011)
5. Rudolf, C., Kang, W., Kindle, C., Qidwai, S., Pande, C., and Thomas, J.: Influence of Electric Current on the Mechanical Deformation of Metals. In: NRL Memorandum Report, US Naval Research Laboratory (NRL) 2019

Chapter 8
Mechanical Properties of Transparent Laminates Fabricated Using Multi-Material Photopolymer Jetting

Michael Harr, Paul Moy, and Jian Yu

Abstract Additive manufacturing (AM), also known as 3D-printing, is already well established for its use in rapid prototyping. Increasingly, however, AM technology is being used for end use manufacturing. The ability to create multi-material and blended material components in a single process allows for unique properties and complex structures that are difficult or impossible to produce using traditional manufacturing techniques. In order to properly utilize these materials, it is necessary to quantify and understand the mechanical properties. In this study, a Stratasys PolyJet (J750) material jetting printer was used to fabricate transparent laminates with blends of a rigid, transparent polymer (VeroClear) and a rubber-like polymer (Agilus30). The rate of deformation as well as the thickness and numbers of layers in the material influence the material's strength and stiffness, with failure largely occurring at interfaces between the two materials. The experimental setup and results are discussed.

Keywords Digital image correlation · Additive manufacturing · Transparent laminates · Split-Hopkinson pressure bar · PolyJet 3D-printing

Introduction

Additive manufacturing provides for numerous potential benefits over more traditional manufacturing methods. Reduction in both the time and cost of manufacture can lead to an overall reduction of the product development cycle [1–4]. Additionally, objects may be printed with both a greater material complexity and a greater structural complexity. By directly printing complex part details, there is less need for elaborate machining, and structures that would normally not be possible, such as adding internal details without disassembling the object, can lead to advantages not just in time reduction, but also in enhanced material properties [1–5]. All of these advantages are leading to an increased interest in using AM for industrial end-use applications. Given the relative novelty of the additive manufacturing method and the myriad of still unexplored potential uses, it is necessary to investigate the properties of materials produced with these methods so that we can properly understand their advantages.

This study examines the usage of multi-material jetting using the Stratsys PolyJet technology. This technology operates utilizing multiple print heads which deposit liquid photopolymer through nozzles onto the print bed in a manner similar to that of an inkjet printer. An ultra violet light instantly cures the polymer. Support structures can be printed out of a gel-like material that can be removed with a high-pressure water jet [1, 3, 4]. The multiple print heads provide the main advantage of this process over some of the other types of additive manufacturing: the ability to print objects out of composites or multiple materials in a single print. An example of this type of material would be a transparent laminate where different layers can be printed as different materials as the job progresses. Potential applications for this type of material are helmet visors or bullet-resistant windows where optimizing properties such as impact absorption while maintaining the ability to be seen through are very important. The effects of build orientation, print speed, surface quality, and interfacial strength within multi-material

M. Harr (✉)
SURVICE Engineering, CCDC Army Research Laboratory, Aberdeen Proving Ground, Aberdeen, MD, USA

Materials Response and Design Branch, CCDC Army Research Laboratory, Aberdeen Proving Ground, Aberdeen, MD, USA
e-mail: michael.harr5.ctr@mail.mil

P. Moy
Materials Response and Design Branch, CCDC Army Research Laboratory, Aberdeen Proving Ground, Aberdeen, MD, USA

J. Yu
Manufacturing Science and Technology Branch, CCDC Army Research Laboratory, Aberdeen Proving Ground, Aberdeen, MD, USA

L. E. Lamberson (ed.), *Dynamic Behavior of Materials, Volume 1*, Conference Proceedings of the Society for Experimental Mechanics Series, https://doi.org/10.1007/978-3-030-30021-0_8

jetting AM have been previously examined [1, 2, 5, 6], however, there exists a lack of previous work specifically on properties of 3D-printed transparent laminates as a whole. Thus, an investigation into the mechanical properties of these 3D-printed laminates is of interest.

Materials

Two polymers were used to create the materials examined in this study. The first, VeroClear, is a polymethyl methacrylate (PMMA)-like photopolymer. The second material is translucent Agilus30, a rubber-like photopolymer. Both materials were sourced from Stratasys and printed using a Statasys J750 printer. The two materials were printed into five different types of specimens, all with a cylindrical geometry. Nominal dimensions are 12.5 mm in diameter (D) and 12.5 mm in length (L) to give a D/L ratio of one. The different formulations include monolithic VeroClear, monolithic Agilus30, and three laminates with alternating layers of the two monolithic materials. The laminates are differentiated by the number of layers in the 12.5 mm long specimen. The three different laminates have 39 (316 μm thick), 79 (158 μm thick), and 159 (79 μm thick) layers. Each specimen was printed with the harder material (VeroClear) as the first and last layer.

Methodology

Quasi-static and intermediate strain-rate compression experiments (10^{-3}/s–10^{0}/s) were performed using an electromechanical Instron 1123 axial load frame for the monolithic Agilus30 specimens and a servo-hydraulic Instron 1331 axial load frame along with a stainless steel compression test fixture from Wyoming Test Fixtures for the other four sets of specimens. High strain rate compression experiments (>10^{2}/s) were performed using a modified split-Hopkinson pressure bar setup with 6061 aluminum bars being use for the monolithic Agilus30 specimens and C300 maraging steel bars being used for the other four sample types. One dimensional wave theory and the other working principles behind the split-Hopkinson pressure bar are well documented [7, 8]. Copper pulse shapers, 0.25 in. in diameter and 0.02 in. thick, were used to achieve dynamic equilibrium in the specimen and a near-constant strain rate. For the aluminum bar, both the incident and transmission bar were 19 mm in diameter and 6.1 m in length. The steel bar consists of a 6.3 m incident bar and a 7.5 m transmission bar, 19 mm in diameter, both of which consist of two pieces joined in the center by a threaded coupling to provide a greater overall length. Full field strain was determined using stereo digital image correlation. Two FLIR 2.8 megapixel cameras were used for the 10^{-3}/s to 10^{-1}/s strain-rate experiments, two IDT Os5-4 K cameras were used for the 10^{0}/s strain-rate, and two Specialised Imaging Kirana high speed cameras were used for the high strain-rate experiments. High contrast black and white speckle patterns were used on the specimens for the low and intermediate strain-rates while a medium contrast pattern was used with the high strain-rate to reduce ghosting in the images on the high speed recordings.

Results and Discussion

Experiments were successfully performed on five formulations of additively manufactured photopolymers at low, intermediate, and high strain rates. In general, the materials exhibit an increase in both yield strength and elastic modulus as the strain-rate increases. A stress-strain plot, shown in Fig. 8.1, displays this trend in the 39 layer laminate specimens. Notably, no strain-hardening effect was observed. An unexpected result occurred, counter to the general trend, with the 79 layer and 159 layer laminates. While the properties do increase from 10^{-3}/s to 10^{-1}/s and 10^{0}/s to the high-rate Hopkinson bar experiments, the yield and modulus for the specimens does not increase from 10^{-1}/s to 10^{0}/s. For the 159 layer laminate the properties stay the same within their standard deviations, and for the 79 layer laminate the properties actually decrease. This suggests that with a decrease in the layer thickness, or an increase in the number of layers, the effect of changes in strain-rate lessen within the low to intermediate strain-rate range.

At higher strain-rates, all of the laminate specimens display a very similar stress-strain response. This is shown in Fig. 8.2, which shows the stress-strain response for each of the five sample types from the split-Hopkinson pressure bar experiments. It clearly shows how the response curves for the 39 layer, 79 layer, and 159 layer specimens all overlap. This suggest that at higher strain-rates, the thickness and number of layers does not have a strong effect on the response of the materials. An additional feature to note is that despite the peak stresses of the laminate specimens being approximately halfway between the

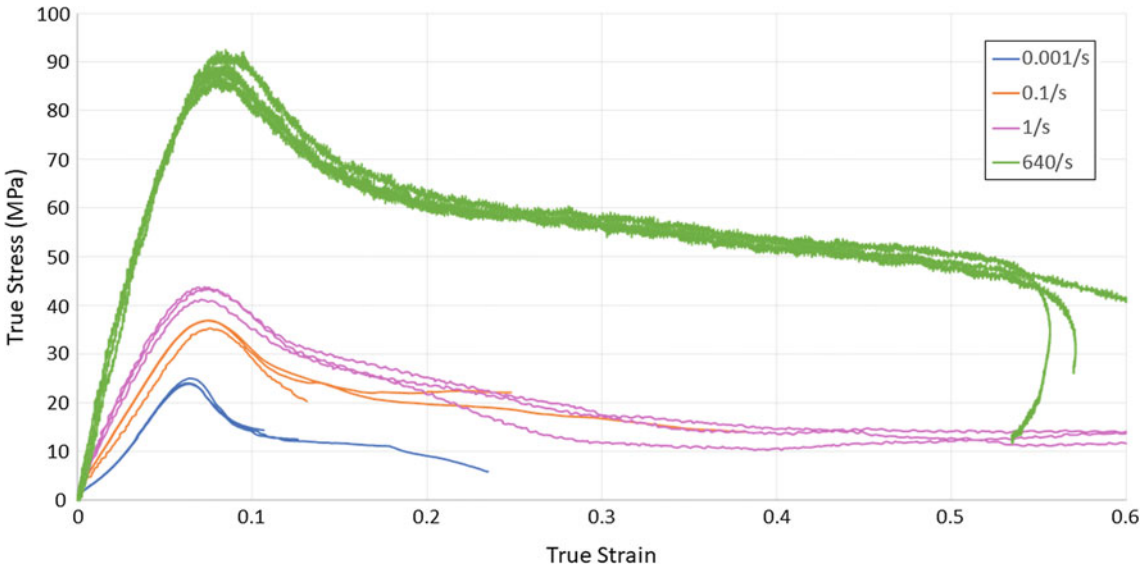

Fig. 8.1 True stress as a function of true strain for 39 layer VeroClear/Agilus30 laminate across a range of strain rates

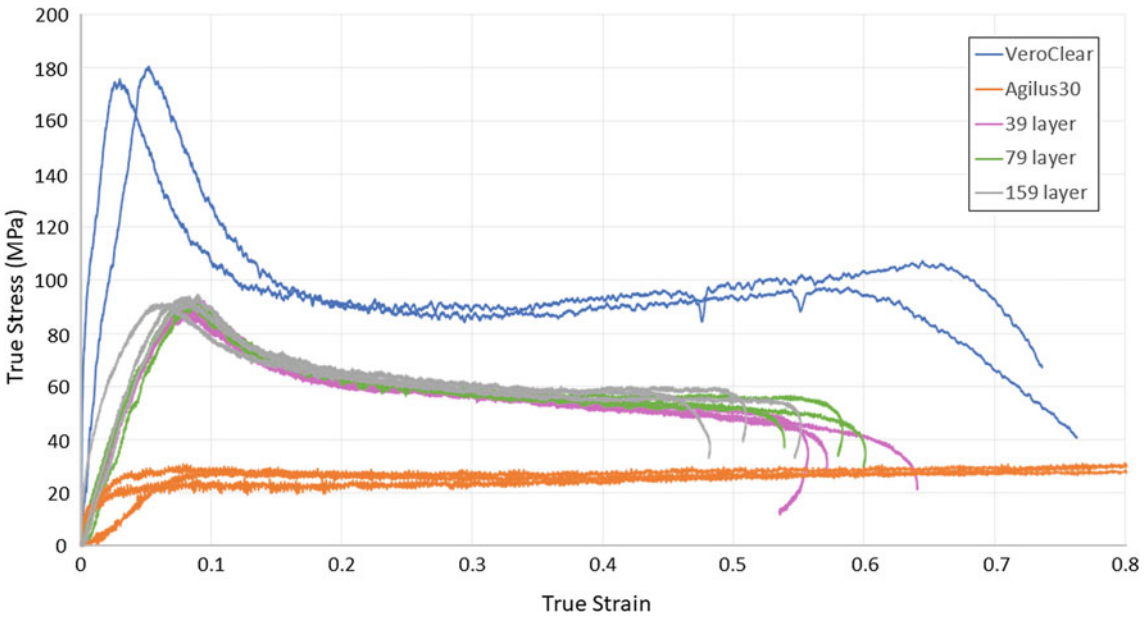

Fig. 8.2 True stress as a function of true strain for all five materials at a high strain-rate

two monolithic materials, the latter portion of the curves lies much closer to the VeroClear response. Thus, while combining the two materials into a laminate reduces the yield stress, the laminates show a greater potential for absorbing energy by maintaining a higher stress relative to the yield value in the post-yield region.

All five sample materials exhibited recovery at all strain-rates. The higher strain-rate experiments displayed significantly more recovery than the low and intermediate-rate experiments, however the only specimens to fully recover were the monolithic Agilus30 specimens. An interesting phenomenon is observed during failure of the laminate specimens. Figure 8.3 shows selected frames from a 1/s experiment (a–c) and a high-rate (651/s) experiment (d–f) of the 159 layer laminate. The quasistatic experiments exhibit failure where the material slides against itself along an area close to the midsection of the specimen. This suggests the failure occurs either within the Agilus30 layers, or at an interface of the two materials. This is in contrast to the high-rate experiments which exhibited barreling, and the material yields as a whole instead of failing at singular locations. All three laminate materials exhibited the same failure mode at quasistatic rates. Both of the monolithic materials exhibited barreling at all strain-rates. Additionally of note, despite the quasistatic laminate specimens often splitting

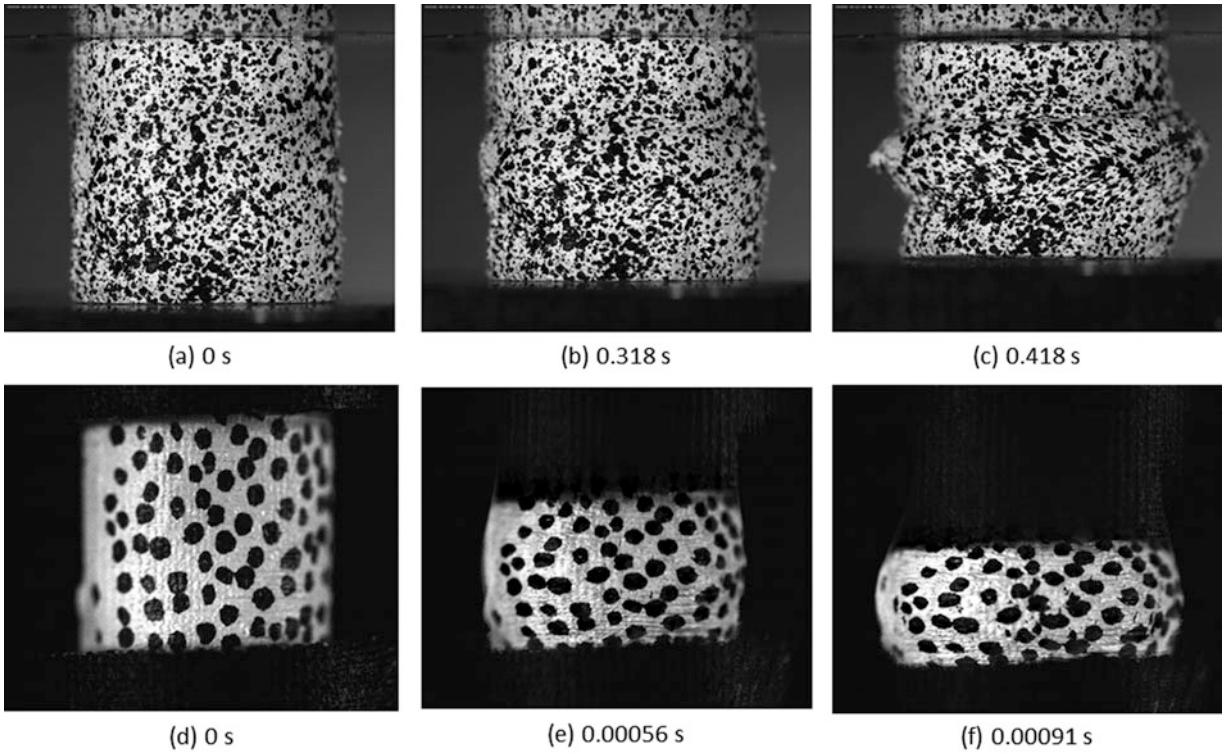

Fig. 8.3 Images showing a 1/s experiment (**a**–**c**) and 651/s experiment (**d**–**f**) for the 159 layer laminate

through the layer in which they failed, they would remain a singular piece as opposed to breaking into two or more pieces. This phenomenon could possibly be explained by the heat generated during deformation causing the photopolymer to activate and self-repair.

Further Work

Additional experiments utilizing specimens with different dimensions could help determine whether the number of layers in a specimen have an effect or whether the driving factor is simply the layer thicknesses (i.e. use a shorter specimen with less layers but the same assortment of thicknesses as previous experiments.) Additionally, despite the high printing surface resolution when printing with PolyJet, edge effects from the printing process are still a possibility. By printing larger specimens and machining to size, as opposed to printing net-shape specimens, this effect could be completely eliminated. Furthermore, the ability to mix the materials as they are printed could allow for grading of the laminate materials, starting with the rigid material at one end and grading the material to the elastomer at the other end. This could open up more ways to manipulate the material properties and is also of interest.

Acknowledgements The research reported in this document was performed in connection with contract/instrument W911QX-16-D-0014 with the U.S. Army Research Laboratory. The views and conclusions contained in this document are those of SURVICE Engineering and the U.S. Army Research Laboratory. Citation of manufacturer's or trade names does not constitute an official endorsement or approval of the use thereof. The U.S. Government is authorized to reproduce and distribute reprints for Government purposes notwithstanding any copyright notation hereon.

References

1. Das, S.C., Ranganathan, R.: Effect of build orientation on the strength and cost of PolyJet 3D printed parts. Rapid Prototyp. J. **24**, 832–839 (2018)
2. Vu, I., Bass, L., Meisel, N., Orler, B., Williams, C.B., Dillard, D.A., Characterization of Multi-Material Interfaces in PolyJet Additive Manufacturing. Solid Freeform Fabrication Symposium. 959–982 (2015)

3. Dizon, J.R., Espera, A.H., Chen, Q., Advincula, R.C.: Mechanical characterization of 3D-printed polymers. Addit. Manuf. **20**, 44–67 (2018)
4. Vu, I.Q., Bass, L.B., Williams, C.B., Dillard, D.A.: Characterizing the effect of print orientation on interface integrity of multi-material jetting additive manufacturing. Addit. Manuf. **22**, 447–461 (2018)
5. Gay, P., Blanco, D., Pelayo, F., Noriega, A., Fernandez, P.: Analysis of factors influencing the mechanical properties of flat PolyJet manufactured parts. Procedia Eng. **132**, 70–77 (2015)
6. Tsouknidas, A., Pantazopoulos, M., Katsoulis, I., Fasnakis, D., Maropouls, S., Michailidis, N.: Impact absorption capacity of 3D-printed components fabricated by fused deposition modeling. Mater. Des. **102**, 41–44 (2016)
7. Chen, W., Lu, F., Zhou, B.: A quartz-crystal-embedded split Hopkinson pressure bar for soft materials. Exp. Mech. **40**(1), 1–6 (2000)
8. Chen, W., Song, B.: Split Hopkinson (Kolsky) Bar Design, Testing, and Applications. Springer, Berlin (2011)

Chapter 9
Structural Intensity Assessment on Shells via the Projection of Experimental Data on a Finite-Element Mesh

F. Pires, S. Avril, S. Vanlanduit, and J. Dirckx

Abstract The computation of the structural intensity on the basis of measured displacement fields is an approach that permits the visualization of energy paths taking place on thin structures. The development of such an analysis is made feasible when the sample is assumed to behave in accordance with the Kirchhoff-Love postulates. This permits the generalized forces within the structure to be estimated through the differentiation of displacement data, which in turn are the inputs to assess the vibrational energy flow. Such an analysis is widely documented in cases, which the sample is either a plate or a shell-like structure with simple geometrical configurations. However, it is from the author's knowledge that such an analysis has not yet been performed on arbitrary geometries, such as doubly curved shells. This work proposes a method that allows the structural intensity of an arbitrary geometry to be computed on the basis of measured displacement fields and spatial coordinates from a sample's outer-surface. After measuring these fields via a Digital Image Correlation set-up, it is assumed that the geometrical data can be represented as an assembly of flat plates. The elements of this assembly overlap with the sample's spatial coordinates and are treated as the constituents of a finite element mesh. Afterwards, the experimental displacement fields are projected on the nodes of that mesh via a global least-squares minimization approach, which in turn enables the nodal deformations to be differentiated with proper finite element shape functions. By assuming that the elements of the mesh behave in accordance with the Kirchhoff-plate theory, it is feasible to estimate the generalized forces on the sample's mid-surface and to assess the structural intensity vector field. By treating the geometrical spatial coordinates as a finite element mesh and the displacement data as projected degrees of freedom, the presented method has shown itself to be a reliable tool to extract the vibrational energy taking place on arbitrary shells.

Keywords Structural intensity · Shell · Finite element method · Digital image correlation · Kirchhoff-love plate model

Introduction and Background

The analysis of energy transmission paths taking place on plate-like structures is a subject that is well documented in literature [1, 2]. Usually, the strategy to assess the vibrational energy is by assuming that the analyzed sample obeys the Kirchhoff-Love postulates. This simplification allows the computation of the Structural Intensity (SI) to be done only via the spatial derivatives of a sample's out-of-plane displacement and a knowledge of its material properties. However, shell-like structures require additional data processing, since the in-plane displacements also play an important role in the SI analysis. Apart from its importance, the spatial derivatives of these displacements along specified local and tangent coordinates of the shell should also be taken into account. Examples of studies related on shells have already been reported and the presented geometries

F. Pires (✉)
Department of Physics, University of Antwerp, Antwerp, Belgium

Department of Mechanical Engineering, Vrije Universiteit Brussel, Brussels, Belgium
e-mail: felipe.pires@uantwerpen.be

S. Avril
Mines de Saint-Étienne, Université Lyon, Saint-Étienne, France

S. Vanlanduit
Department of Mechanical Engineering, Vrije Universiteit Brussel, Brussels, Belgium

Department of Electromechanical Engineering, University of Antwerp, Antwerp, Belgium

J. Dirckx
Department of Physics, University of Antwerp, Antwerp, Belgium

L. E. Lamberson (ed.), *Dynamic Behavior of Materials, Volume 1*, Conference Proceedings of the Society for Experimental Mechanics Series, https://doi.org/10.1007/978-3-030-30021-0_9

have local and tangent coordinates that are aligned with analytical coordinate systems, such as the cylindrical or spherical ones [3, 4].

This work proposes an alternative method; which computes the SI from shells of arbitrary shapes. The main assumption from which the equations are developed is that the studied sample behaves in accordance with the Kirchhoff-Love plate model [5]. Due to this, it is admitted that the geometry can be simplified to a Finite Element (FE) mesh with flat elements, each of which the Kirchhoff plate theory is invoked. The displacement fields stored at the nodes of this mesh are computed via a projection of experimental displacements, which can be interpreted as a global least-squares minimization problem [6]. By creating an orthogonal set of local coordinates, the required spatial derivatives of the rotations and displacement fields are computed by differentiating predefined quadratic shape functions. Since it is accepted that the in-plane displacements and strains vary linearly with respect to the sample's through-thickness coordinate, the inputs related to the sample's mid-surface could be estimated from what was regularized from its outer-surface. At this point, all terms related to the SI would be available and the estimated energy paths could be studied.

To test this method, a thin membrane with a localized damper on its center was used as a sample and the displacement and shape data were acquired on the basis of the Digital Image Correlation (DIC) [7] technique. By processing the measured data with the proposed method, the SI result was estimated and a strong energy flow convergence to the region were the damper was installed could be identified. These primal results have indicated that the assumptions present the in Kirchhoff-Love plate model in combination with the experimental data projection on a FE mesh is a reliable strategy to analyze vibrational energy taking place on thin shells.

Theory and Methods

This work presents a method that extracts the SI on irregular shells with the assumptions that the sample's outer-surface is the only region, where the shape and displacements can be measured from. If the shell is considered to behave in accordance with the Kirchhoff-Love postulates and by using curvilinear coordinates to represent the in-plane directions of the sample [8], it holds that the time-averaged and active SI taking place on the sample's mid-surface is

$$\mathbf{I} = \begin{Bmatrix} I_1 \\ I_2 \\ I_3 \end{Bmatrix} = -(\pi f) \begin{Bmatrix} \mathrm{Im}\left\{ Q_1 u_3^* + M_{11}\theta_1^* + M_{12}\theta_2^* + N_{11}u_1^* + N_{12}u_2^* \right\} \\ \mathrm{Im}\left\{ Q_2 u_3^* + M_{21}\theta_1^* + M_{22}\theta_2^* + N_{21}u_1^* + N_{22}u_2^* \right\} \\ 0 \end{Bmatrix}, \tag{9.1}$$

being the subscripts "1" to "3" indications of an orthonormal and local basis: the subscripts "1" and "2" refer to terms pointing at the shell's in-plane local coordinates, while the subscript "3" indicates a term, whose direction is normal to the sample's surface. The "Im{}" term is an indication that just the imaginary unit should be taken into account, f is the excitation frequency response, the superscript "*" refers to the term's complex conjugate, the terms Q, M and N are the components of the shear force $\mathbf{Q}$, bending moment $\mathbf{M}$ and membrane force $\mathbf{N}$, respectively; the u's are the terms of the displacement vector of the mid-surface ($\mathbf{u}$) and the θ's are the terms of the rotation ($\boldsymbol{\theta}$). The displacement and rotation vector can be represented with

$$\mathbf{u} = \begin{Bmatrix} u_1 \\ u_2 \\ u_3 \end{Bmatrix}, \qquad \boldsymbol{\theta} = \begin{Bmatrix} \theta_1 \\ \theta_2 \\ 0 \end{Bmatrix}. \tag{9.2}$$

The terms $\mathbf{N}$, $\mathbf{M}$, $\mathbf{Q}$, $\mathbf{u}$ and $\boldsymbol{\theta}$ are defined in the shell's mid-surface. However, it is assumed that it is only possible to measure displacement and shape information from the outer-surface of a shell and that these very data are defined along a pre-defined Cartesian coordinate system ($\mathbf{e}_x$, $\mathbf{e}_y$, $\mathbf{e}_z$). Not just the transformation of coordinates [from ($\mathbf{e}_x$, $\mathbf{e}_y$, $\mathbf{e}_z$) to ($\mathbf{e}_1$, $\mathbf{e}_2$, $\mathbf{e}_3$)] should take place before the data processing, but the estimation of the terms shown in Eq. (9.1) should be carried out exclusively from measured terms related to a sample's outer-surface. These issues were solved by assuming that the studied shell behaves as a Kirchhoff-Love plate model [5], i.e., that it could be described as an assembly of flat elements, each of which would follow the Kirchhoff plate theory.

By choosing this approach, it was decided to project the dense point cloud of experimental displacement fields on the nodes of a FE mesh with quadratic and triangular elements and which is achieved via a least-squares inversion on the basis of the element's shape functions [6]. By considering $\boldsymbol{\Phi}$ to be the assembled matrix of these shape functions evaluated at the experimental data points and $\mathbf{U}_{exp}$ to be the experimental displacement data, the projected displacement fields on the mesh's

nodes can be represented with

$$\mathbf{U}^{h/2} = \left[\mathbf{\Phi}^T \mathbf{\Phi}\right]^{-1} \mathbf{\Phi}^T \mathbf{U}_{exp}, \tag{9.3}$$

being h the shell's thickness, the superscript "$h/2$" indicates that the term refers to the displacements on the outer-surface and $\mathbf{U}^{h/2}$ is the global displacement vector field, i.e., the sample's displacement represented by the coordinates ($\mathbf{e}_x$, $\mathbf{e}_y$, $\mathbf{e}_z$). With the mesh and the displacements at hand and since the shear strains are neglected, the global rotations $\mathbf{\Theta}$ are acquired by subtracting the normal directions $\mathbf{e}_3$ of the deformed geometry with the reference mesh. Lastly, the fields in $\mathbf{U}^{h/2}$ and $\mathbf{\Theta}$ are transformed, so its components are referenced with respect to the local coordinates ($\mathbf{e}_1$, $\mathbf{e}_2$, $\mathbf{e}_3$). With this operation, the local displacement of the outer-surface $\mathbf{u}^{h/2}$ and rotation $\boldsymbol{\theta}$ are obtained. To estimate the displacement on the mid-surface $\mathbf{u}$ via the terms $\mathbf{u}^{h/2}$ and $\boldsymbol{\theta}$, the assumption referring to the in-displacements varying linearly with respect to the sample's thickness is used with the following equation:

$$\mathbf{u} = \mathbf{u}^{h/2} - \frac{h}{2}\boldsymbol{\theta}. \tag{9.4}$$

Since each element of the mesh follows the Kirchhoff plate theory, the generalized forces can be computed with the following equations for each element:

$$\mathbf{N} = \begin{Bmatrix} N_{11} \\ N_{22} \\ N_{12} \end{Bmatrix} = h\mathbf{C}\boldsymbol{\gamma}, \qquad \mathbf{M} = \begin{Bmatrix} M_{11} \\ M_{22} \\ M_{12} \end{Bmatrix} = \frac{h^3}{12}\mathbf{C}\boldsymbol{\chi}, \qquad \mathbf{Q} = \begin{Bmatrix} Q_1 \\ Q_2 \end{Bmatrix} = \begin{Bmatrix} M_{11,1} + M_{12,2} \\ M_{12,1} + M_{22,2} \end{Bmatrix}, \tag{9.5}$$

where the subscripts ",1" and ",2" indicate a spatial derivative of the referred term along the directions "1" and "2", respectively; $\mathbf{C}$ is the stiffness matrix, $\boldsymbol{\gamma}$ is the membrane strain on the shell's mid-surface and $\boldsymbol{\chi}$ is the bending strain. The individual terms present in the stiffness matrix and the strains are

$$\mathbf{C} = \frac{E}{1-\nu^2}\begin{bmatrix} 1 & \nu & 0 \\ \nu & 1 & 0 \\ 0 & 0 & 1-\nu \end{bmatrix}, \qquad \boldsymbol{\gamma} = \begin{Bmatrix} \gamma_{11} \\ \gamma_{22} \\ \gamma_{12} \end{Bmatrix}, \qquad \boldsymbol{\chi} = \begin{Bmatrix} \chi_{11} \\ \chi_{22} \\ \chi_{12} \end{Bmatrix}, \tag{9.6}$$

being E the Young's modulus and ν is the Poisson's coefficient. As it is the case for the displacement, the strains also vary linearly along the direction $\mathbf{e}_3$. Therefore, it holds that

$$\boldsymbol{\gamma} = \boldsymbol{\varepsilon}^{h/2} - \frac{h}{2}\boldsymbol{\chi}, \tag{9.7}$$

where $\boldsymbol{\varepsilon}^{h/2}$ is the strain on the shell's outer-surface. Lastly, by considering these strains to be small, the right-handed terms of Eq. (9.7) can be directly estimated with the displacement's and rotation's spatial derivatives shown in Eq. (9.8):

$$\varepsilon_{ij}^{h/2} = \frac{1}{2}\left(u_{i,j}^{h/2} + u_{j,i}^{h/2}\right), \qquad \chi_{ij} = \frac{1}{2}\left(\theta_{i,j} + \theta_{j,i}\right), \qquad \text{for } i,\, j = \{1, 2\}. \tag{9.8}$$

Since the elements are quadratic triangles, the required spatial derivatives shown in Eqs. (9.5 and 9.8) are carried out by differentiating the elements' shape functions. With the equations shown so far and by assuming that both the stiffness matrix and the sample's thickness are known, one needs to project the displacement field of the outer-surface on a FE mesh with Eq. (9.3), compute the global rotation $\mathbf{\Theta}$, transform these data to a set of a local coordinate system, estimate the necessary spatial derivatives [Eqs. (9.5 and 9.8)] and compute the terms related to the mid-surface [Eqs. (9.4 and 9.7)]. Lastly, one has all the necessary inputs to visualize the SI [Eq. (9.1)].

Materials and Results

The chosen subject to test this approach was a thin and soft circular membrane with a diameter of 12 cm and a thickness of 1 mm (see Fig. 9.1). The same figure also shows that the clamping of the membrane was provided by a closed chamber. At the other side of this very device, a loudspeaker was installed and was set to provide single-sine excitations. Since the space inside the chamber was sealed, it was ensured that most of the loudspeaker's power would be received by the membrane. Lastly, a strip of a viscous damper was used as the material that would absorb power from the excited membrane. One end of this strip was installed at the center of the membrane, while the other was fixed at the chamber's other end.

The loudspeaker was set to transmit pressure waves at 150 Hz. Since the frequency is considered to be low, it was safe to assume that the pressure exciting the membrane was uniform over its surface. Moreover, the setup's configuration allowed the viscous damper to be moved from inside the chamber. By pulling it from the inside, the membrane acquired a concaved and curved-conical configuration. The last step of the set-up's preparation was to paint the membrane with a fine speckle pattern, since its displacement fields would be recorded by means of the Digital Image Correlation (DIC) [7]. The recording of the displacement fields was made with two high-speed cameras and the image correlation of the excited membrane was computed with the Istra4D software.

By the time the displacement fields and the membrane's spatial point cloud were correlated, a FE mesh made of quadratic and triangular elements could be developed. The shape of its elements overlapped with the measured point cloud and the displacement fields were interpolated to the mesh's nodes by means of a least-squares inversion [6] (Fig. 9.2a). Moreover, the in-plane local coordinates of the FE mesh were defined to be its principal curvature directions of the curved membrane (Fig. 9.2b, c).

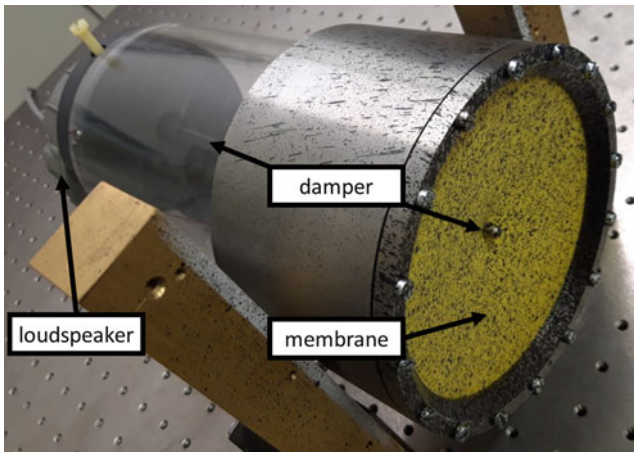

Fig. 9.1 Set-up

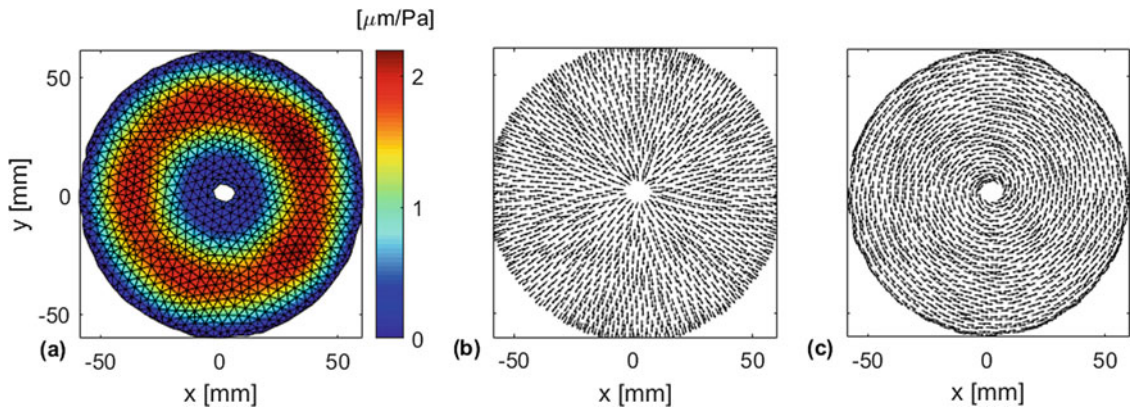

Fig. 9.2 Absolute value of $\mathbf{U}^{h/2}$ [see Eq. (9.1)] on the developed mesh (**a**); and in-plane directions $\mathbf{e}_1$ (**b**) and $\mathbf{e}_2$ (**c**), which are equivalent to the principal curvature directions of the studied geometry

With the displacements located at the mesh's nodes and by assuming that the mesh behaves as if it was a Kirchhoff-Love plate model, the rotation $\boldsymbol{\Theta}$ was estimated. Both displacement $\mathbf{U}^{h/2}$ and rotation $\boldsymbol{\Theta}$ of the membrane were available at this point and a coordinate transformation could take place and $\mathbf{u}^{h/2}$ and $\boldsymbol{\theta}$ were obtained. After transforming the referred terms from the Cartesian coordinates ($\mathbf{e}_x$, $\mathbf{e}_y$, $\mathbf{e}_z$) and representing them on the basis of the local coordinates [see Fig. 9.2b, c], their necessary spatial derivatives could be computed with Eq. (9.8). Lastly, since the thickness is known, Eqs. (9.4 and 9.7) were used to estimate the in-plane displacement and membrane strain on the sample's mid-surface. Figure 9.3 displays the three normalized terms of Eq. (9.7) that are aligned with the direction $\mathbf{e}_1$. Since all right-handed terms of Eq. (9.1) are available at this point, the SI vector field could be finally computed. Figure 9.4 displays the energy path transmission of the membrane.

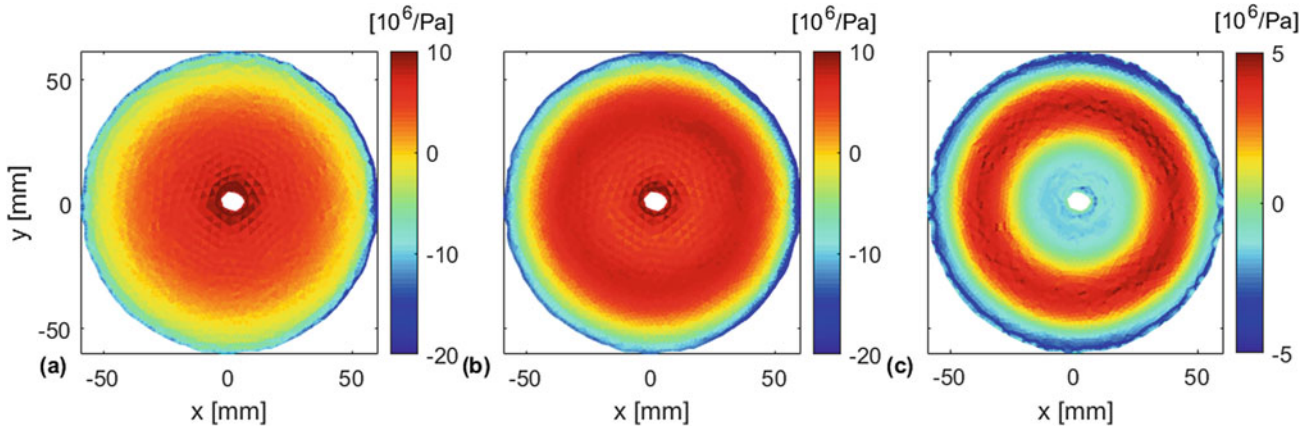

Fig. 9.3 Representation of the strains γ_{11} (**a**), $\varepsilon_{11}^{h/2}$(**b**) and $\frac{h}{2}\chi_{11}$ (**c**) at time $t = 0$ s and normalized with respect to the applied pressure

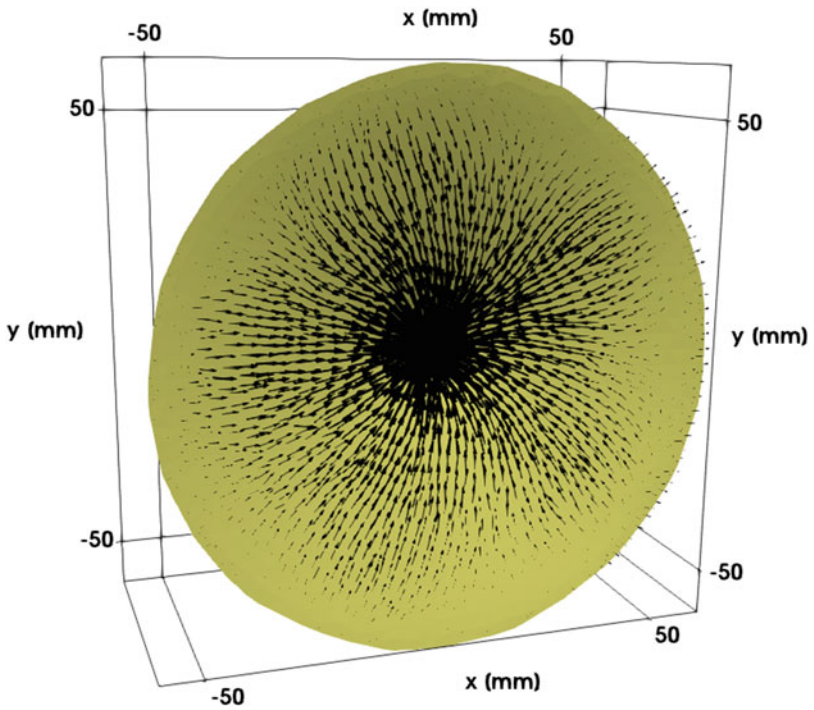

Fig. 9.4 Computed structural intensity vector field [Eq. (9.1)] of the membrane at 150 Hz

Discussion and Conclusion

The energy transmission paths shown in Fig. 9.4 provided vector fields, whose directions were pointing at the damped region, i.e., the center of the membrane and where the strip of viscous damper was installed. The proposed method has shown a SI result that was in accordance with what was expected from the built set-up.

Moreover, it should be noted that the most well-documented approaches to estimate the SI are by means of the finite-difference-method or by processing the displacement data on the wavenumber domain [9, 10]. It is also to the author's knowledge that the results presented so far were displayed in samples, whose local coordinates were aligned with analytical coordinate systems [3, 4]. These requirements are absent in the proposed method: it takes advantage of the local differentiation of FE triangular elements by differentiating the shape functions and the in-plane local directions are no longer restrained with well-defined coordinates. Due to the preliminary results related to the SI vector fields, which were in accordance with what was excepted from the built set-up and by considering the relatively simple data processing to compute the strains and, in turn, the generalized forces, the proposed method has shown itself to be another alternative to process and estimate the energy flow on shell structures.

Acknowledgement Financial support for this work was supplied by the Research Foundation of Flanders (FWO), (grant No. G049414N).

References

1. Semperlotti, F., Conlon, S.C.: Structural damage identification in plates via nonlinear structural intensity maps. J. Acoust. Soc. Am. **127**(2), EL48–EL53 (2010)
2. Roozen, N.B., Guyader, J.L., Glorieux, C.: Measurement-based determination of the irrotational part of the structural intensity by means of test functional series expansion. J. Sound Vib. **356**, 168–180 (2015)
3. Williams, E.G.: Structural intensity in thin cylindrical shells. J. Acoust. Soc. Am. **89**(4), 1615–1622 (1991)
4. Saijyou, K., Yoshikawa, S.: Structural intensity measurement of cylindrical shell based on NAH technique and influences of a rib on the acoustic energy flow. J. Acoust. Soc. Jpn. E. **20**(2), 125–136 (1999)
5. Chapelle, D., Bathe, K.J.: The finite element analysis of shells - Fundamentals. Springer Science, Berlin (2010)
6. Avril, S., Feissel, P., Pierron, F., Villon, P.: Comparison of two approaches for differentiating full-field data in solid mechanics. Meas. Sci. Technol. **21**(1), 015703 (2009)
7. Schreier, H., Orteu, J.J., Sutton, M.A.: Image correlation for shape, motion and deformation measurements. Springer, US (2009)
8. Gavrić, L., Pavić, G.: A finite element method for computation of structural intensity by the normal mode approach. J. Sound Vib. **164**(1), 29–43 (1993)
9. Arruda, J.R.F., Mas, P.: Localizing energy sources and sinks in plates using power flow maps computed from laser vibrometer measurements. Shock. Vib. **5**(4), 235–253 (1998)
10. Morikawa, R., Ueha, S., Nakamura, K.: Error evaluation of the structural intensity measured with a scanning laser Doppler vibrometer and a k-space signal processing. J. Acoust. Soc. Am. **99**(5), 2913–2921 (1996)

Chapter 10
Dynamic Compressive Response of Carbon Fibre Laminar Composite and Carbon Fibre Corrugated Sandwich Panel

W. X. Huang and L. Tsai

Abstract Carbon fiber composite is widely used in aero industries and on automobile body panel due to its high strength and light weight. In order to achieve even better fuel economy, various sandwich panels with different core structures are being studied.

In this study, Split Hopkinson Pressure Bar (SHPB) is utilized to conduct high strain rate compression tests on carbon fiber panel and carbon fiber sandwich panel. The fused deposition modeling method is utilized to manufacture corrugated cores which are glued onto carbon fiber face panels with epoxy resin. The main goal of the experiment is to discuss the specific strength and energy absorption differences of monolithic material and corrugated sandwich with same thickness.

Keywords Split Hopkinson pressure bar · Carbon fiber · Corrugated structure · Dynamic compression test · Fused deposition modeling

Introduction

Composite material is made of two or more different materials. It can be divided into three main categories by its structure: fibrous (matrix mix with fibers), laminar (layers of different materials), particulate (matrix mix with particles) [1].

Carbon fiber composites are widely used in aero industry, military applications, and automobile industry due to its high strength, high modules, and low density [2]. Carbon fiber composites can be divided by its ply orientation into three main categories: (1) Woven (2) Unidirectional piles (3) Cross-ply [3]. When unidirectional carbon fiber composite subjected to out of plane compression, the ultimate strength of dynamic compression is 37% higher than that of quasi-static compression; when subjected to in-plane compression, the strength and ultimate strain of dynamic compression are 79% and 74% higher than those of static compression respectively. When cross-ply carbon fiber composite subjected to in-plane compression, the strength and ultimate strain of dynamic compression are 67% and 57% higher than those of static compression respectively [4].

Sandwich structures are composed of a relatively low density core material combines with rigid face panel [5]. These structures are often used in vehicle industries, ship manufacturing, and civilian engineering. Due to their higher bending rigidity and strength compare to monolithic materials with same weight [6].

Fused deposition modeling (FDM) allows us to model corrugated cores with more complex structures; fast specimens manufacturing speed is also one of its advantages. Different printing directions may have some influences on mechanical properties of specimens, thus cores with same structure will be printed with two different printing paths to discuss the difference.

W. X. Huang · L. Tsai (✉)
Department of Mechanical Engineering, National Kaohsiung University of Science and Technology, Kaohsiung City, Taiwan
e-mail: liren@nkust.edu.tw

L. E. Lamberson (ed.), *Dynamic Behavior of Materials, Volume 1*, Conference Proceedings of the Society for Experimental Mechanics Series, https://doi.org/10.1007/978-3-030-30021-0_10

Fig. 10.1 Dynamic responses of carbon fiber composites

Experiment Layout

Split Hopkinson Pressure Bar

Split-Hopkinson pressure bar is composed of striker bar, Incident bar, and transmitter bar. The length of striker bar, incident bar, and transmitter bar are 600 mm, 2000 mm, 1600 mm respectively. The diameter of all bars is 25.4 mm. The main working principle of SHPB is that a compressive wave is generated when striker bar impacts incident bar, the compressive wave is transmitted to specimen by incident bar. A portion of initial wave is transmitted through specimen to transmitter bar, the remaining portion of the wave is reflected back to incident bar due to the impedance difference between bars and specimen. Split Hopkinson Pressure Bar can generate strain rate of 200~10^4 s^{-1} [7] (Fig. 10.1) .

Specimen Manufacturing

The carbon fiber specimens are made from unidirectional B10037K carbon epoxy pre-preg provided by Advanced International Multitech Co., Ltd. The stack sequence is $[0/90_{(x)}]_S$, due to different specimen thickness, the number X varies. Once stacking is completed, the specimen is pressurized at 120 psi in steel mold and heated in high-temperature oven at 190 °C for 2 h. After epoxy cured, specimens were cut into cylinders with diameter of 6 mm with waterjet. Three different thickness (6 mm, 3 mm, 2 mm) are manufactured.

The corrugated core is manufactured with fused deposition modeling method (3D printing). The core will be sandwiched between two 2 mm cylindrical carbon fiber face panel. The total thickness of the specimen is 6 mm.

Result and Discussion

Carbon Fiber Composites under out of Plane Dynamic Compression

Figure 10.2 shows the stress-strain responses of specimens with thickness and diameter of 6 mm under out of plane dynamic compression. It is clear that peak stress increases as strain rate increases for all of specimens. The peak stress of 300 s^{-1}, 600 s^{-1}, 900 s^{-1}, 1170^{-1} are 248, 578, 937, 1010 MPa, respectively. It is clear that peak stress increases as strain rate increases, which indicates that carbon fiber composites are strain rate sensitive.

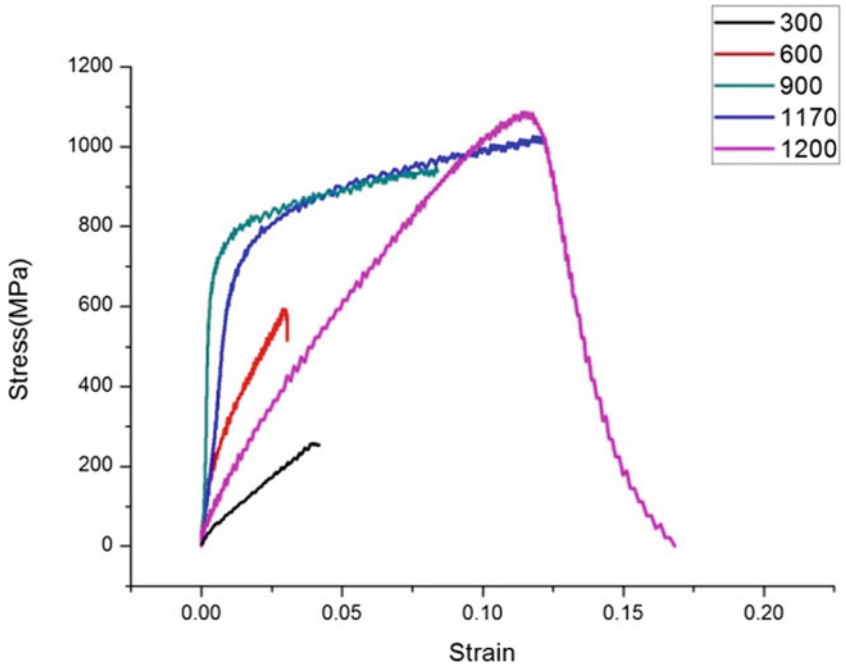

Fig. 10.2 Dynamic responses of carbon fiber composites

Conclusion

Dynamic compression tests on carbon fiber composites are conducted in this study. Strain rates ranging from 300 s^{-1} to 1200 s^{-1}. The result shows that carbon fiber is strain rate sensitive, the peak stress increases considerably comparing 1170s^{-1} to 300 s^{-1}, which indicates that it has potentials to be utilized in high strain rate environment. Further study on different material stacking and corrugated sandwich will be conducted in the future.

Acknowledgement Appreciate lab M305 of National Kaohsiung University of Science and Technology for providing all the resources and help.

References

1. Lubin, G.: Handbook of Composites. Springer Science, Berlin (2013)
2. Chung, D.D.L., Chung, D.: Carbon Fiber Composites. Elsevier, Amsterdam (2012)
3. Wen, J., Xia, Z., Choy, F.: Damage detection of carbon fiber reinforced polymer composites via electrical resistance measurement. Compos. Part B. **42**(1), 77–86 (2011)
4. Hsiao, H.M., Daniel, I.M.: Strain rate behavior of composite materials. Compos. Part B. **29**(5), 521–533 (1998)
5. Haldar, A.K., et al.: The compressive properties of sandwich structures based on an egg-box core design. Compos. Part B. **144**, 143–152 (2018)
6. Rejab, M.R.M., Cantwell, W.J.: The mechanical behaviour of corrugated-core sandwich panels. Compos. Part B. **47**, 267–277 (2013)
7. Gama, B.A., Lopatnikov, S.L., Gillespie, J.W.: Hopkinson bar experimental technique: a critical review. Appl. Mech. Rev. **57**(4), 223–250 (2004)

Chapter 11
Strain Rate Dependence of Stabilized, Nanocrystalline Cu Alloy

S. A. Turnage, M. Rajagopalan, K. A. Darling, C. Kale, B. C. Hornbuckle, C. L. Williams, and K. N. Solanki

Abstract The effect of mechanical loading, particularly at dynamic strain rates, on nanocrystalline (NC) materials has eluded researchers owing to the inherent instability of the NC structure. However, a recently developed NC Cu-10 at.%Ta alloy has exhibited an ability to maintain a NC structure at temperatures up to 873 K. Here, NC Cu-10 at.%Ta is tested under compressive strain rates ranging from 10^{-3} s^{-1} up to 10^{5} s^{-1} and at temperatures from 298 K up to 1073 K. Typical materials show a sharp increase in flow stress occurring around 10^{3} s^{-1} as deformation mechanisms shift away from thermal activation mechanisms; however, at 298 K, NC Cu-10 at.%Ta observes only a limited increase in flow stress indicating that typical thermally activated mechanisms still apply up to strain rates of 10^{5} s^{-1}. Post deformation analyses indicate a shift from nucleation of full dislocations to increased nucleation of partial dislocations at 298 K. However, as temperature increases, thermal activation mechanisms give way to viscous effects and the high density of nucleated full dislocations leads to a dramatic increase in flow stress.

Keywords Nanocrystalline · Stabilized · Dynamic behavior · Flow stress upturn · Strain rate

Introduction

Nanocrystalline materials have been shown to exhibit high strength and ductility making them desirable candidates for applications requiring structural resilience as well as high strength to weight ratios. However, as strain rates and temperatures increase, the mechanical performance of traditional nanocrystalline materials rapidly degrades. Typically, nanocrystalline materials undergo rapid grain growth resulting from thermal and mechanical loading leading to a loss of the mechanical benefits of the reduced grain size following intense loading procedures such as observed in forming processes [1, 2].

The benefits of nanocrystalline grain size can be maintained, however, through either thermal or kinetic stabilization methods [3, 4]. In particular, the work of Darling et al. [5] indicates that Cu with Ta addition can maintain a stable nanostructure up to temperatures of 873 K while the yield stress of the nanocrystalline Cu based material remains significantly higher than that of pure, polycrystalline Cu.

Materials/Methods

Powder metallurgy provides the ability to combine immiscible elements such as Cu and Ta into a powdered alloy with nanometer grain size. Here, 10 at.% Ta is added to Cu powder and milled at cryogenic temperature for 4 h. All powder handling was performed under Ar atmosphere to reduce oxygen contamination. Following cryogenic milling, equal channel angular extrusion is used to consolidate the powdered alloy into a fully dense bulk material where the severe plastic deformation aids to maintain a nanometer grain size. Here, the alloyed powder is loaded under Ar atmosphere into Ni cans which are extruded through a 90° angle at 700 °C to produce a final grain size of ~50 nm.

Samples from the extruded billet are machined through wire electrical discharge machining (EDM) into cylindrical specimens of 3 mm diameter by 3 mm height. These samples are used for both quasi-static and dynamic compression.

S. A. Turnage (✉) · K. A. Darling · B. C. Hornbuckle · C. L. Williams
U. S. Army Research Laboratory, Aberdeen Proving Grounds, Aberdeen, MD, USA
e-mail: scott.a.turnage.ctr@mail.mil

M. Rajagopalan · C. Kale · K. N. Solanki
School for Engineering of Matter, Transport, and Energy, Arizona State University, Tempe, AZ, USA

L. E. Lamberson (ed.), *Dynamic Behavior of Materials, Volume 1*, Conference Proceedings of the Society for Experimental Mechanics Series, https://doi.org/10.1007/978-3-030-30021-0_11

Quasi-static compression from 10^{-3} to 1 s^{-1} is performed with a 5900 series Instron mechanical tester equipped with a furnace capable of reaching temperatures as high as 1473 K. Dynamic testing is performed using a Kolsky bar capable of reaching strain rates from 10^2 to 10^4 s^{-1} on such small specimens. A tube furnace capable of heating a sample to 1073 K is fitted to the Kolsky bar for high temperature testing. As the tube furnace also heats the ends of the Inconel Kolsky bar, a correction is applied in the form of

$$\varepsilon = \frac{4c_T E\left(\varepsilon_i - \varepsilon_t\right)}{\left(E_T + \sqrt{E * E_T}\right) l_s}$$

$$\sigma = \frac{\varepsilon_t E_T A_b}{A_s}$$

where ε and σ are the engineering strain and stress in the specimen, c_T and E_T are the wavespeed and Young's modulus of the bar at temperature, E is the Young's modulus in the bar at room temperatrure, ε_i and ε_t are the measured strains in the incident and transmitted bars, l_s is the specimen length, and A_b and A_s are the cross-sectional areas of the bar and specimen.

Results

As received material shows a high density of Ta nano-dispersions and a few twins throughout the material. The average Cu grain size is approximately 50 nm while Ta particles exist in a binary grouping of particle sizes. Ta nano-dispersions average 3.2 ± 0.9 nm in diameter while larger Ta particles average 32 ± 8 nm in diameter. The initial microstructure is shown in Fig. 11.1.

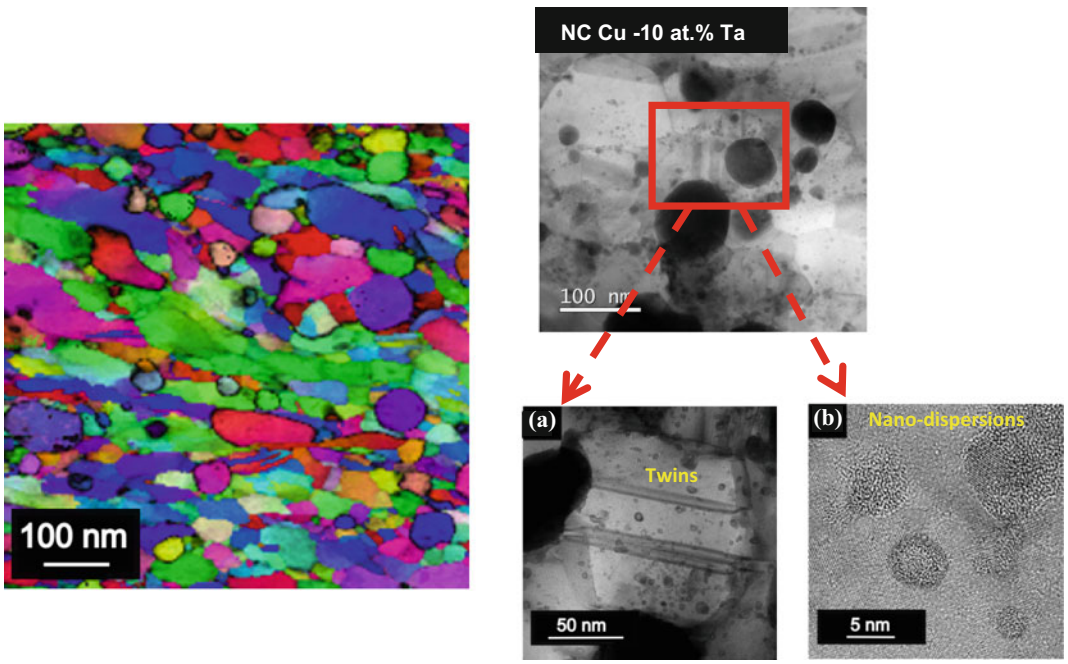

Fig. 11.1 Initial microstructure of NC-Cu-10 at.%Ta. (left) Precession diffraction image showing randomized texture of the alloy. (right) TEM images revealing (**a**) twins and (**b**) nano-dispersions in the as-extruded material

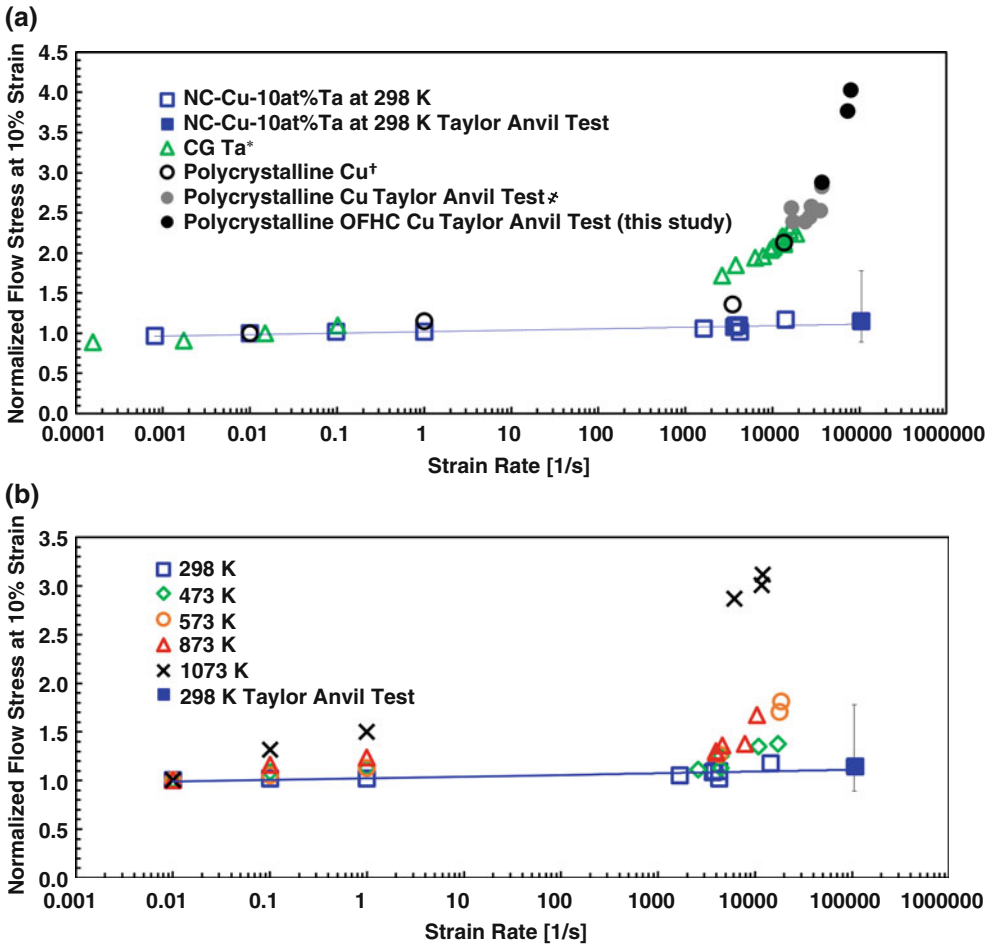

Fig. 11.2 Normalized flow stress as a function of strain rate. (**a**) Comparison of NC-Cu-10 at.%Ta with pure polycrystalline OFHC Cu and pure polyrystalline Ta. (**b**) Comparison of NC-Cu-10 at.%Ta data at elevated temperatures

Mechanical behavior is probed with quasi-static compression for strain rates below 1 s^{-1}, Kolsky bar methods are employed for strain rates from 10^3 to 10^4 s^{-1}, and a Taylor anvil test probes the mechanical behavior up to 10^5 s^{-1}. As Fig. 11.2 reveals, room temperature compression tests show only limited strain rate effects up to 10^5 s^{-1}. As temperatures and strain rates increase, the flow stress begins a steep rise which is commonly associated with viscous material behavior as lattice vibrations begin to have an effect on the dislocation motion. This is a common effect in polycrystalline materials; however, the effect is observed in polycrystalline OFHC Cu at room temperature and strain rates as low as 10^3 s^{-1}.

Microstructural characterization in Fig. 11.3 reveals increased twin density with limited dislocation formation at room temperature and strain rates above 10^3 s^{-1}. At elevated temperatures, dislocation clusters become more apparent. At all temperatures, nano-clusters maintain nanometer spacing and grain size remains below 100 nm up to 873 K as shown in Fig. 11.4.

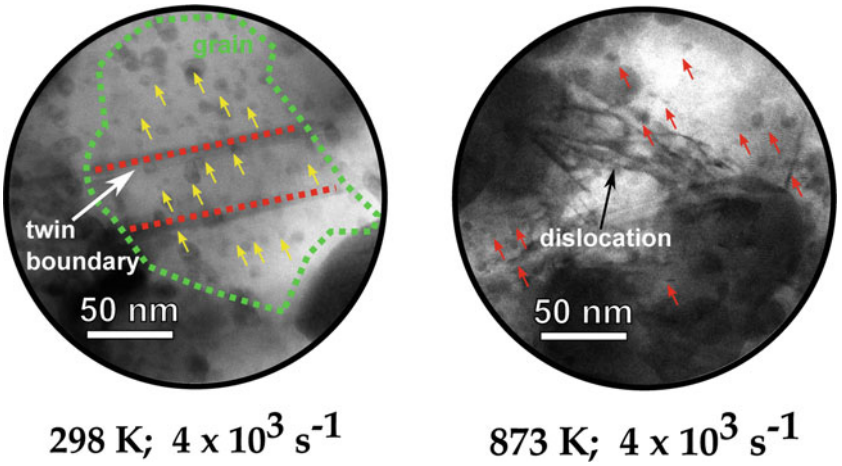

Fig. 11.3 Comparison of microstructures after high rate deformation at (left) room temperature and (right) 873 K

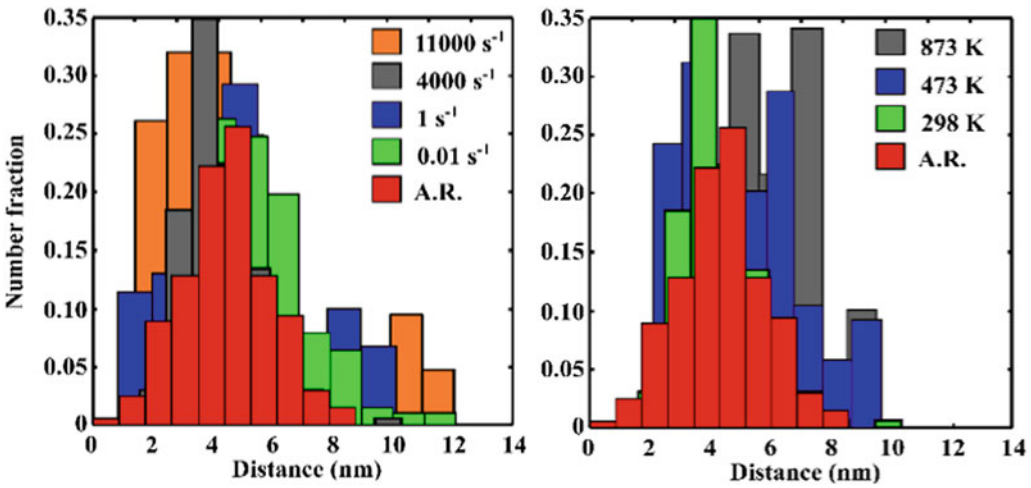

Fig. 11.4 Spacing of Ta nano-dispersions as a function of (left) strain rate and (right) temperature

Discussions

The stable mechanical properties observed in Fig. 11.2 are the result of the stabilized microstructure of the nanocrystalline alloy. As further discussed in [6], the low length scale between dislocation pinning defects such as grain boundaries and Ta nano-dispersions results in both a lower density of mobile dislocations and an inability for the dislocations to achieve an average velocity high enough for interaction with lattice vibrations. As a result, the deformation of nanocrystalline Cu-10 at.%Ta at room temperature is dependent on the thermal activation processes of nucleation of partial dislocations which are almost immediately pinned by defects as well as the thermal activation of partial dislocations to overcome such barriers.

At elevated temperatures, the thermal energy available to activate dislocations is higher resulting in a higher density of mobile dislocations. Further, the lattice vibrations are increased, so viscous effects can be more pronounced as strain rates increase despite the stability of the Ta nano-dispersion spacing, i.e., the stable spacing of dislocation barriers. These factors contribute to the rapid increase in flow stress observed in Fig. 11.2 at temperatures above 473 K.

Conclusion

Here, the dynamic behavior of a stable, nanocrystalline alloy is explored at strain rates ranging from 10^{-3} to 10^{5} s^{-1} and temperatures from 298 K to 1073 K. The presence and stability of Ta nano-clusters results in a stability of flow stress values not seen in other nanocrystalline materials at high strain rates and temperatures. However, as the temperature rises, a rapid

flow stress increase is observed at strain rates above 10^3 s^{-1} resulting from the increased thermal energy available for full dislocations to overcome dislocation barriers.

References

1. Dalla Torre, F., Van Swygenhoven, H., Victoria, M.: Nanocrystalline electrodeposited Ni: microstructure and tensile properties. Acta Mater. **50**, 3957–3970 (2002)
2. Dalla Torre, F., Van Swygenhoven, H., Schaublin, R., Spatig, P., Victoria, M.: Mechanical behaviour of nanocrystalline electrodeposited Ni above room temperature. Scr. Mater. **53**, 23–27 (2005)
3. Kalidindi, A.R., Schuh, C.A.: Stability criteria for nanocrystalline alloys. Acta Mater. **132**, 128–137 (2017)
4. Purja Pun, G.P., Darling, K.A., Kecskes, L.J., Mishin, Y.: Angular-dependent interatomic potential for the Cu-Ta system and its application to structural stability of nano-crystalline alloys. Acta Mater. **100**, 377–391 (2015)
5. Darling, K.A., Huskins, E.L., Schuster, B.E., Wei, Q., Kecskes, L.J.: Mechanical properties of a high strength Cu-Ta composite at elevated temperature. Mater. Sci. Eng. A. **638**, 322–328 (2015)
6. Turnage, S.A., Rajagopalan, M., Darling, K.A., Garg, P., Kale, C., Bazehhour, B.G., Adlakha, I., Hornbuckle, B.C., Williams, C.L., Peralta, P., Solanki, K.N.: Anomalous mechanical behavior of nanocrystalline binary alloys under extreme conditions. Nat. Commun. **9**, (2018)

Chapter 12
Designing Future Materials with Desired Properties Using Numerical Analysis

Constantine (Costas) G. Fountzoulas and Jian H. Yu

Abstract The swift advancement of the computer power and the recent advances in the numerical techniques, and improved strength and failure material models, resulted in accurate simulation of manufacturing processes and events, such as stress optimization during lamination process of polymers and impact into multi-layer opaque and transparent armor configurations. Parametric analysis of materials of known material models can contribute to the development of future materials. The systematic numerical analysis of the effect of material properties, such as modulus of elasticity, yield strength and ultimate tensile strength, on the performance of various systems can provide researchers and manufacturers crucial design information for the technologies of the future. This paper presents the modeling efforts at U.S. Army Research Laboratory (ARL) to develop a correlation between failure mechanisms and the material properties obtained experimentally leading to future materials technologies for personnel protection.

Keywords Future materials design · Modeling · Numerical analysis · X-ray tomography · Properties · Technologies

Introduction

Software

To study in depth the response of materials in diverse loading environments, various commercial and specialized software for numerical analysis is used at ARL, such as ANSYS/WORKBENCH, which includes AUTODYN, COMSOL, LSDYNA EPIC and THERMOCALC. In particular, LSDYNA, AUTODYN and EPIC are used for the dynamic characterization of materials, while THERMOCALC is used for construction of phase diagrams and sintering processing. The effect of defects, such as cracks, and the crack propagation in the failure mechanism of ceramics has being studied for the past few decades. For example, the effect of defect clustering, almost impossible to introduce in a transparent material experimentally for validation of the modeling results, with respect to distance from the line of impact, defect density, and defect shape on the damage propagation in the ceramic hard face of the laminate was studied (Fig. 12.1) [1].

Experimental Characterization

X-ray Computed Tomography

The need for production of material strength and failure models that can be used at the multiscale modeling requires advanced nondestructive characterization techniques, such as Digital Image Correlation (DIC) and X-ray Computed Tomography (XCT) [2]. X-ray tomography is a non-destructive technique which provides 3D information of materials. Therefore, it is very attractive in materials science and engineering since the relation between macroscopic properties and the microstructure of a material is very frequently required. X-ray radiography is the basis of X-ray tomography: an X-ray beam is sent on a sample and the transmitted beam is recorded on a detector. According to Beer–Lambert law, the ratio of the number of transmitted to incident photons is related to the integral of the absorption coefficient of the material μ along the path that the photons follow through the sample. Currently, the presence of cracks and porosity, in materials such aluminum and high

C. G. Fountzoulas (✉) · J. H. Yu
U.S. Army Research Laboratory, WMRD, Aberdeen Proving Ground, Aberdeen, MD, USA
e-mail: Constantine.fountzoulas.civ@mail.mil; jian.h.yu.civ@mail.mil

L. E. Lamberson (ed.), *Dynamic Behavior of Materials, Volume 1*, Conference Proceedings of the Society for Experimental Mechanics Series, https://doi.org/10.1007/978-3-030-30021-0_12

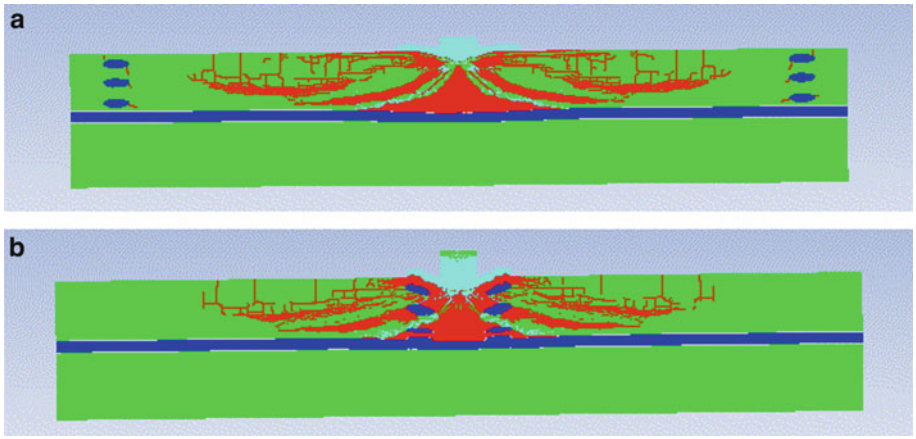

Fig. 12.1 Damage propagation after 30 μs for elliptical defects with the minor axis parallel to line of impact; (**a**) 5 mm and (**b**) 65 mm from the target edge

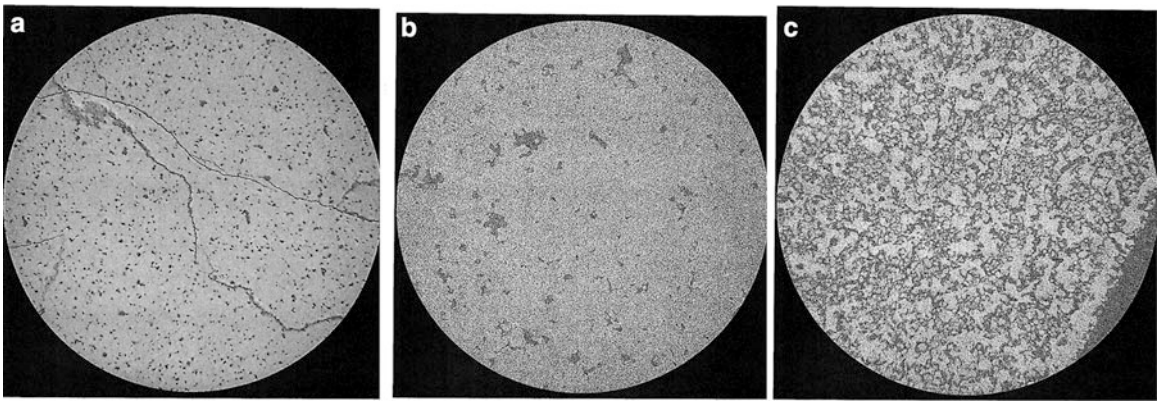

Fig. 12.2 XCT slices: (**a**) cracks in aluminum (resolution 2 μm), (**b**, **c**) void density in the polymer with different stoichiometry of ceramic particles (resolution, 4.7 μm)

melting temperature polymer with ceramic particles as processing aid in selective laser sintering [2] was studied by XCT using the in-house ZEISS Xradia 520 Versa microscope [3, 4], a nondestructive technique for visualizing interior features within solid objects, and for obtaining digital information on their 3-D geometries and properties (Fig. 12.2). The findings of these studies will be used for the production of strength and failure models of new materials or for the optimization of existing ones.

Discussion

ANSYS/WORKBENCH, COMSOL EPIC and Thermocalc is the software used for our numerical analysis. To date, our efforts have been focused mainly on duplicating the main cracks of metals such as aluminum, as the ones which are shown on Fig. 12.2a. Next step will be the introduction in our models of circular cross section defects in selected polymer samples and study their effect on the failure mechanism during impact. Optimization of materials performance will be studied by modifying the physical properties of existing materials aiming toward the synthesis of future materials. Moreover, defects will be strategically placed in these materials to study possible mass minimization without compromising their performance to external loading.

References

1. Fountzoulas, C.G., Sands, J.M.: Proceeding of 26th International Symposium of Ballistics, Miami, FL, USA, September 12–16, 2011
2. Yu, J.H, et al.: Private communication (2018)
3. Carl ZEISS X-Ray Microscopy, Inc., Pleasanton, CA
4. Salvo, L., et al.: Nucl. Instrum. Methods Phys. Res. **200**, 273–286 (2003)

Chapter 13
Kolsky Bar Testing of Pressure Sensitive Adhesives

Evan L. Breedlove, David Lindeman, and Chaodi Li

Abstract Pressure sensitive adhesives (PSAs) are highly viscoelastic rubber-like materials which are widely employed to bond a range of materials. They typically exhibit rubbery-plateau shear moduli on the order of 1 MPa and glass-plateau shear moduli on the order of 1 GPa with variable levels of strain-rate sensitivity within each rheological plateau. PSAs are frequently employed in applications which can result in high rate and large deformation loading; however, characterization frequently emphasizes small-strain viscoelastic properties as measured by dynamic mechanical analysis (DMA) with time-temperature superposition. Kolsky bar (split-Hopkinson pressure bar) testing can provide direct measurement of the high-rate, finite strain properties; however, the experimental challenges to obtain reliable data are well documented for soft materials. Specifically, soft material testing is sensitive to issues with sample stress equilibrium, radial inertia effects, and poor signal to noise ratio. These challenges are compounded in PSAs, which are apt to adhere to the bar surfaces and can chemically interact with typical lubricants, thus changing the properties.

In this work, we detail the development of appropriate test conditions to obtain high rate mechanical properties of PSAs. Two commercially available materials are evaluated at a range of strain rates in a series of three systematic studies of test conditions. First, the effect of sample geometry is considered. Several thickness to diameter ratios were evaluated as well as annular specimens. Results indicate that annular specimens are not necessary to manage radial inertia effects for this class of materials, and a range of different thickness and diameter choices provide various tradeoffs in signal to noise ratio versus maximum measurable strain. Next, the effect of lubricant is presented for three commercially available lubricants; furthermore, the effect of contact time between the lubricant and the PSA is explored. Finally, we explore the selection of pulse shaper to obtain stress equilibrium. Several conventional copper pulse shaping methods are considered alongside paper, polymeric, and elastomeric pulse shapers.

As a final validation of the presented test methods, measurements were compared to finite element predictions based on a constitutive model derived from quasistatic uniaxial tests combined with DMA. Good agreement was obtained, indicating that the presented Kolsky bar method yields mechanical properties consistent with other modes of testing.

Keywords Pressure sensitive adhesive · Kolsky bar · Viscoelasticity · Impact compression · Pulse shaping

Introduction

Pressure sensitive adhesives (PSAs) are highly viscoelastic rubber-like materials which are widely employed to bond a range of materials. They typically exhibit rubbery-plateau shear moduli on the order of 1 MPa and glass-plateau shear moduli on the order of 1 GPa with variable levels of strain-rate sensitivity within each rheological plateau. Bulk moduli are typically on the order of a few GPa with little rate sensitivity, rendering them nearly incompressible over a wide range of rates. PSAs are frequently employed in applications which can result in high strain rate and large deformation loading. Nevertheless, PSA mechanical characterization frequently emphasizes small-strain viscoelastic properties, as measured by dynamic mechanical analysis (DMA) with time-temperature superposition, as well as phenomenological failure tests, such as peel and shear-creep debonding. These test methods do not robustly measure the high-rate, finite strain mechanical properties. Mechanical design increasingly relies on computational modeling, which means effective integration of PSAs into mechanical design requires accurate constitutive and failure models, which in turn must be based on relevant mechanical property measurements.

Kolsky bar (split-Hopkinson pressure bar) testing can provide these direct measurements. In a typical Kolsky bar compression experiment, a cylindrical specimen is placed between two long bars made of an elastic material. These bars

E. L. Breedlove (✉) · D. Lindeman · C. Li
Corporate Research Laboratory, 3M Company, Maplewood, MN, USA
e-mail: elbreedlove@mmm.com

L. E. Lamberson (ed.), *Dynamic Behavior of Materials, Volume 1*, Conference Proceedings of the Society for Experimental Mechanics Series, https://doi.org/10.1007/978-3-030-30021-0_13

serve as one-dimensional waveguides, and stress wave propagation may be inspected by means of strain gages. To perform the experiment, the incident bar is impacted, typically by firing a striker bar from a gas gun. The resulting incident pulse travels toward the sample. At the sample interface, some portion of the wave reflects, and the rest is transmitted into the sample and ultimately into the transmission bar on the other side of the sample. Various data reduction methods exist, but the majority infer the uniaxial, compressive strain and stress in the specimen through inspection of these waves. A common feature of Kolsky bar test methods is that they rely on experimental assumptions regarding stress equilibrium, radial inertia, friction, and adequate signal-to-noise ratio [1]. Soft materials pose challenges to these assumptions, and care must be taken in the selection of experimental conditions to ensure that the resulting stress-strain response is valid [2].

The purpose, therefore, of this work was to determine appropriate experimental conditions for Kolsky bar compression testing of PSAs. Furthermore, this work aimed to explore the sensitivity of the material response to the selected conditions. To that end, three systematic studies were conducted examining the effect of specimen geometry, pulse shaping, and lubrication. Each section examines these factors independently and builds toward a recommended experimental procedure which yields consistant and valid test results. Finally, finite element modeling results are presented which demonstrate consistency between measured material response and behavior based on other test methods.

General Methods

All tests were conducted on a pair of PSAs manufactured by 3M Company which will be referred to as the stiff and the soft adhesive. The two adhesives bracket common properties of industrially-relevant PSAs.

Tests were conducted on an aluminum Kolsky bar apparatus with properties summarized in Table 13.1. Bar moduli and wave speeds were computed from the measured wave speed in blank shots. The bars were gaged at mid-length using traditional strain gages (Omega Engineering Inc.; Norwalk, CT). Bridge completion and amplification were provided by Vishay 2310b amplifiers (Micro-Measurements; Wendell, NC) and signals were recorded with a PicoScope 4824 digital oscilloscope (Pico Technology; Cambridgeshire, UK) at a rate of 80 MHz. Strain measurements were calibrated by applying a known shunt load. The striker was fired from a commercially available gas gun (REL Inc.; Marquette, MI). Proper alignment and motion of the bars were verified by firing blank shots and assuring undistorted transmission of the pulse along the length of both bars with no reflection from the interface. Previous testing using opposed gages also confirmed that bending was not observed.

All data were processed using one-wave methods based on the incident, reflected, and transmitted bar strains [1]. Assuming sample stress equilibrium, the strain rate in the sample was determined as

$$\dot{\epsilon} = -2\frac{C}{t}\epsilon_r \tag{13.1}$$

where C is the longitudinal wave speed in the bar, t is the sample thickness, and ϵ_r is the reflected bar strain. Sample strain is determined from numerical integration. The stress in the sample is determined as

$$\sigma = \frac{A_b}{A_s}E_b\epsilon_t \tag{13.2}$$

where A_b is the cross-sectional area of the bar, A_s is the cross-sectional area of the sample, E_b is the bar modulus, and ϵ_t is the transmission bar strain. Initial post-processing was conducted using the open-source SurePulse software [3]. This software provides an interface for strain gage voltages to bar strains, selecting pulses, associating other essential test data with raw oscilloscope measurements, and visualization of computed results. Incident and transmitted pulses were selected manually, and the reflected pulse was determined from the measured wave speed and known position of the incident bar gage, consistent with the method of Lifshitz and Leber [4]. Additional post-processing was conducted in a custom program

Table 13.1 Properties of the Kolsky bar apparatus

Bar	Material	Diameter (mm)	Length (m)	Density (gcc)	Modulus (GPa)	Wave speed (m/s)
Striker	Al 7075	19	0.3	2.77	73.33	5145.2
Incident	Al 7075	19	3.66	2.77	73.33	5145.2
Transmission	Al 7075	19	3.66	2.77	73.25	5142.4

implemented in Python 3.7. All final processing was conducted after down sampling data to 4 MHz and passing through an eighth order Chebyshev type I filter. Because the wave speed of the samples is not well-characterized and strain-dependent, the sliding window method of Lifshitz and Leber was not fully feasible. Instead, the starting and ending times of pulses was optimized from the initial manual selection by minimizing both the equilibrium error between the front and back face forces [5] as well as minimizing the error in the equation

$$\epsilon_i = \epsilon_t + \epsilon_r \tag{13.3}$$

The front and back face forces were computed as

$$F_f = A_b \left(\epsilon_i + \epsilon_r\right) \tag{13.4}$$

$$F_b = A_b \epsilon_t \tag{13.5}$$

This pulse selection method draws elements from Lifshitz-Leber's sliding pulse windows and the Zhao-Gary approach of iteratively modulating the selection to ensure optimal self-consistency of the pulse selections [6].

Sample Geometry Study

A study was conducted to determine appropriate sample geometry. Sample dimensions are especially important in soft material testing due to the competing issues of friction, signal-to-noise ratio, stress equilibrium, and radial inertia [2, 7]. Smaller diameters minimize friction and radial inertia, but they also increase the impedance mismatch between the bars and sample and reduce transmitted signal amplitude, which can lead to noisy stress measurements and failure to achieve constant strain rate [8]. Thick samples attenuate transmitted signal and may not reach stress equilibrium [9].

All experiments in this section were conducted using peanut oil lubrication and a silicone pulse shaper (OD = 6 mm, t = 1.6 mm, 60A durometer). Sample geometries are given in Table 13.2. For each geometry, samples were tested at "slow" and "fast" strain rates based on gun pressures of 69 and 138 kPa, respectively. Three replicate tests were conducted for each condition.

Comparable plateau strain rates of approximately 5000/s and 7500/s were generated for the slow and fast conditions in both PSAs (Figs. 13.1 and 13.2). Resulting stress-strain curves were also similar among all test conditions (Figs. 13.3 and 13.4). Notably, the 6 mm outer-diameter sample yielded larger variance compared with other sample geometries. This is consistent with a drop in the transmitted signal amplitude. Annular samples did not result in measurably different material response for most test conditions, suggesting that radial inertia is not a significant issue. The annular specimen did result in systematically lower stresses for the soft PSA under the fast condition, perhaps indicating insipient radial inertial effects that could become problematic at higher rates; however, these differences were not observed for the slow rate (Fig. 13.4). Additionally, thick samples yielded results consistent with other sample geometries while maintaining low levels of error in the stress response, indicating that additional signal attenuation was not a significant issue.

While results appeared to be largely insensitive to sample geometry, several practical considerations indicate that the 10 mm outer diameter samples with a thickness on the order of 2 mm were the optimal choice. First, larger diameters yield better stress signal-to-noise ratio. Second, annular samples require additional sample preparation and are subject to errors in the concentricity of the inner cutout. Finally, the thicker samples limit achievable strain rates since rates are halved for

Table 13.2 Sample dimensions evaluated in sample geometry study. All samples were cylindrical

Sample	OD (mm)	ID (mm)	Thickness (mm)
Soft	6	0	2.6
	10	0	2.6
	10	0	4.3
	10	4	2.6
Stiff	6	0	2.1
	10	0	2.1
	10	0	3.8
	10	4	2.1

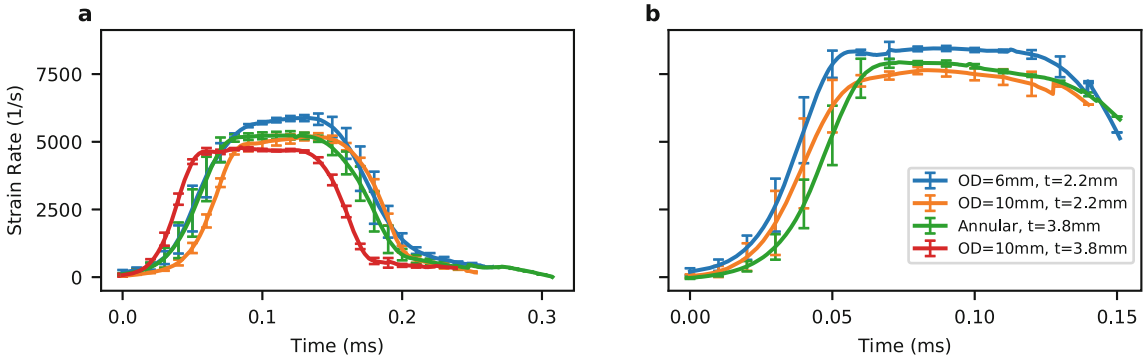

Fig. 13.1 Stiff PSA strain rates for (**a**) slow and (**b**) fast conditions

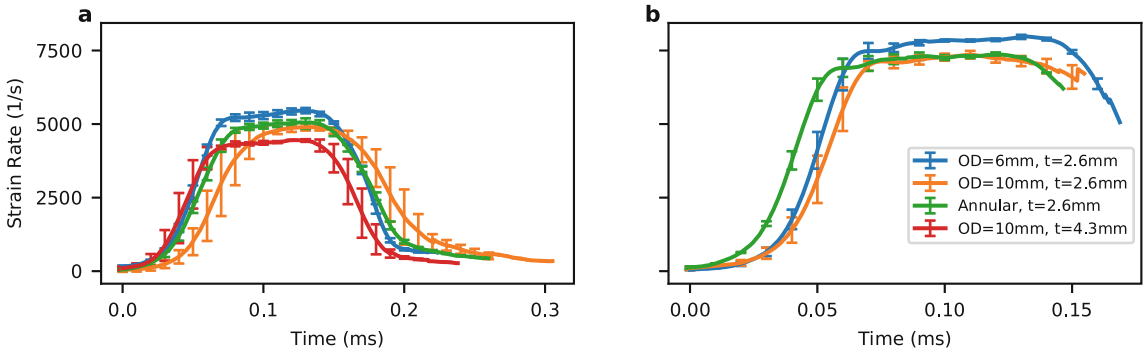

Fig. 13.2 Soft PSA strain rates for (**a**) slow and (**b**) fast conditions

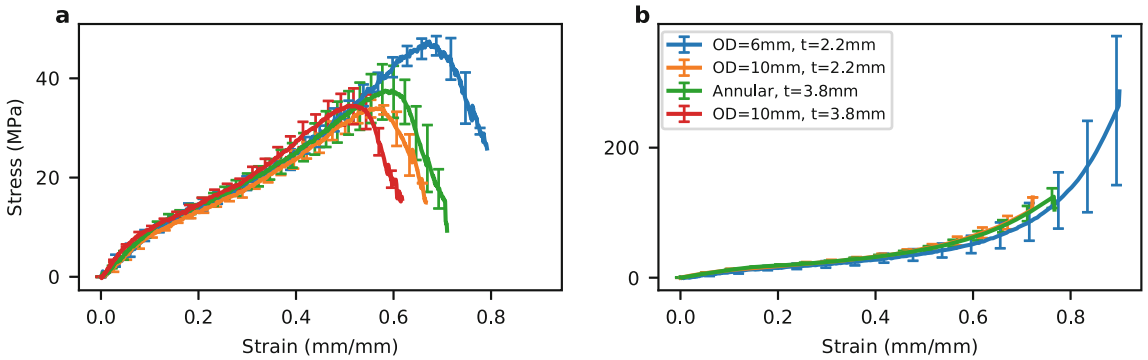

Fig. 13.3 Stiff PSA stress-strain curves for (**a**) slow and (**b**) fast conditions. Minimal dimension effect was observed, though standard deviations were larger for the OD = 6 mm geometry

equivalent striker bar velocities (i.e., thick samples which were tested under the slow condition were tested with the gas gun set to 138 kPa). In view of these results, the 10 mm outer diameter specimen with the ~2 mm thickness were selected for all remaining tests.

Pulse Shaping Study

Stress equilibrium is a significant concern in soft materials since the wave velocity within the sample is substantially lower than the wave velocity within the bars. This leads to two practical issues. First, the sample may become significantly deformed before stress equilibrium is achieved [9]. Second, determination of stress equilibrium is challenging because the front-face force is determined from the difference between the incident and reflected wave amplitudes as shown in Eq. (13.4).

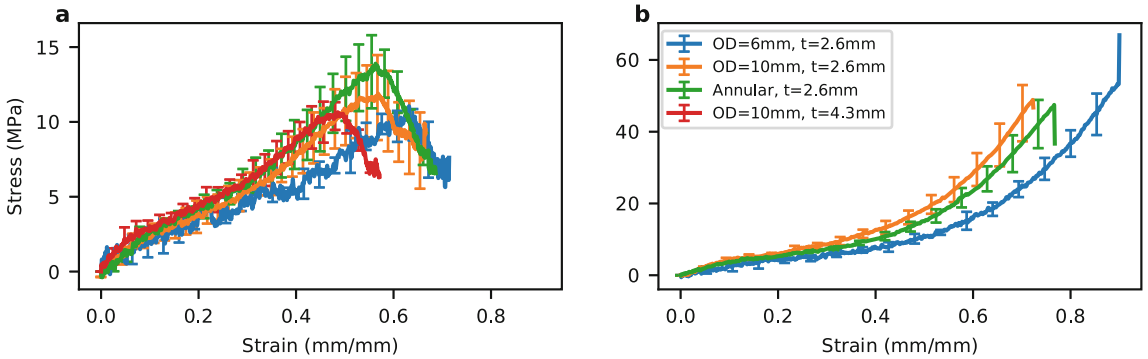

Fig. 13.4 Soft PSA stress-strain curves for (**a**) slow and (**b**) fast conditions. Minimal dimension effect was observed, though standard deviations were larger for the OD = 6 mm geometry, and the smaller geometry also systematically registered lower stresses

Table 13.3 Evaluated pulse shapers

Material	OD (mm)	Thickness (mm)	Other info
Silicone	6.0	1.60	60A Durometer
PET	6.0	0.12	
Paperboard	6.0	1.25	
Copper (Cu)	6.4	0.41	

The large impedance mismatch causes the amplitude of the reflected wave to be large compared with the incident wave; therefore, the difference between these pulses amplifies noise and dispersion effects leading to poor signal-to-noise ratio in the front face force [10]. While these issues may be addressed through the use of polymeric bars, this strategy comes with its own challenges related to heat dissipation in the strain gages and analysis of wave propagation in a viscoealstic medium. Alternatively, the use of an appropriate pulse shaper can mitigate both of these issues [2]. Several pulse shapers were evaluated (Table 13.3), and the effectiveness of each was evaluated by comparing front and back face forces and stress-strain curves. Each PSA was tested at slow and fast conditions, and three replicates were collected for each condition.

Significant differences in face force equilibrium were observed among the four pulse shapers (Figs. 13.5, 13.6, 13.7 and 13.8). In general, the PET pulse shaper resulted in large oscillations observed early in the compression pulse with a corresponding rapid rise time (Figs. 13.9 and 13.10). The paperboard pulse shaper yielded low levels of oscillation at slow speeds but not under the fast condition. It also resulted in a slow rise time, with a knee in the rise appearing for the slow condition with the soft PSA (Fig. 13.10a). The copper pulse shaper resulted in relatively low oscillations, and it achieved this result while maintaining a relatively quick rise time, meaning constant strain rate was achieved at lower strains. The amplitude of the front face oscillations was larger for the soft adhesive. The silicone pulse shaper consistently yielded the lowest front face force oscillations and slow rise time. Sample equilibrium for the silicone pulse shaper was also apparent through visual inspection of the deformation (Fig. 13.15).

The effect of the different pulse shapers on the resulting stress and strain was minimal, with standard deviations on the order of 10% for each test condition and overlap of the measured response for the different shapers (Figs. 13.11 and 13.12). The paperboard resulted in larger errors under all conditions, and one test for the soft adhesive, fast condition deviated substantially from the other two replicates. It is believed that this difference arose from inconsistencies in the friction between the striker and paperboard. The PET shaper yielded results similar to copper and silicone; however, greater ripple in the stress signal was observed, consistent with the larger oscillations observed in the face forces (Figs. 13.5, 13.6, 13.7 and 13.8).

In view of these results, silicone and copper appear to be the most appropriate pulse shapers for PSA testing. The silicone pulse shaper yielded better measured force equilibrium at the expense of a slower rise time. In contrast, copper resulted in more significant front face oscillations for the soft PSA, making assessment of stress equilibrium more challenging. Therefore, silicone may be the more versatile pulse shaper for PSA testing, but both should be considered on a case-by-case basis.

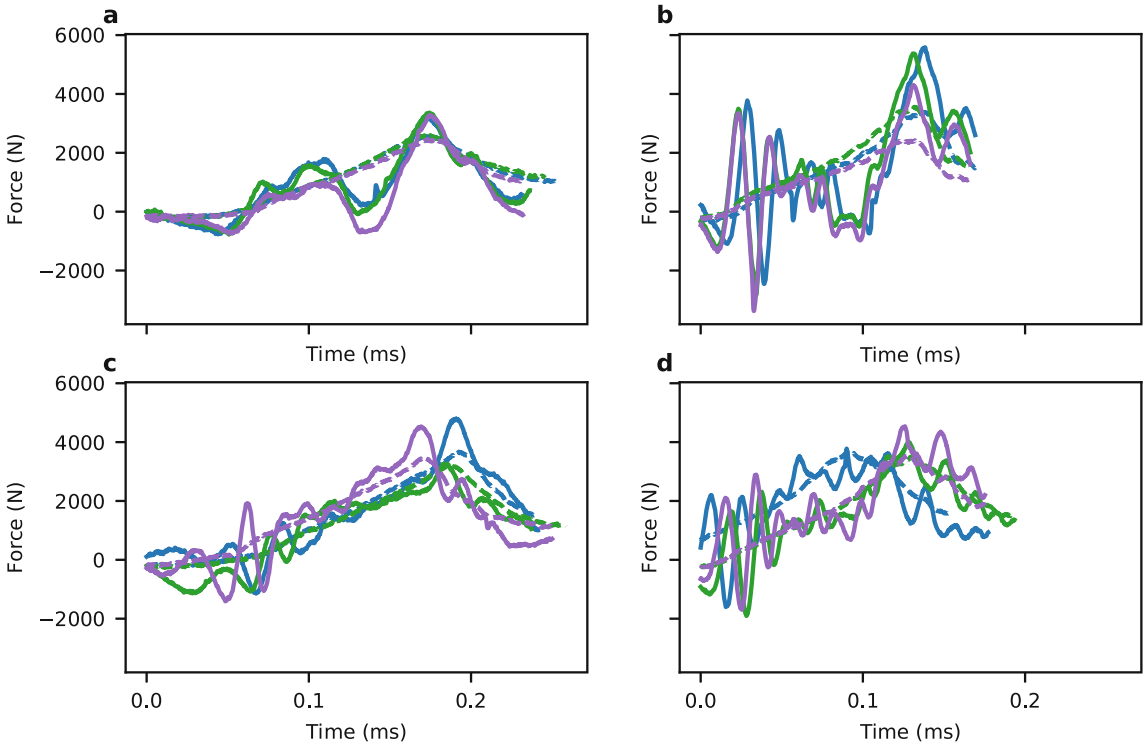

Fig. 13.5 Stiff PSA face equilibrium for slow condition using (**a**) silicone, (**b**) PET, (**c**) Paper, and (**d**) copper pulse shapers. Solid (-) lines represent the front face and dashed (−) lines represent the back face, with matched colors showing a single replicate

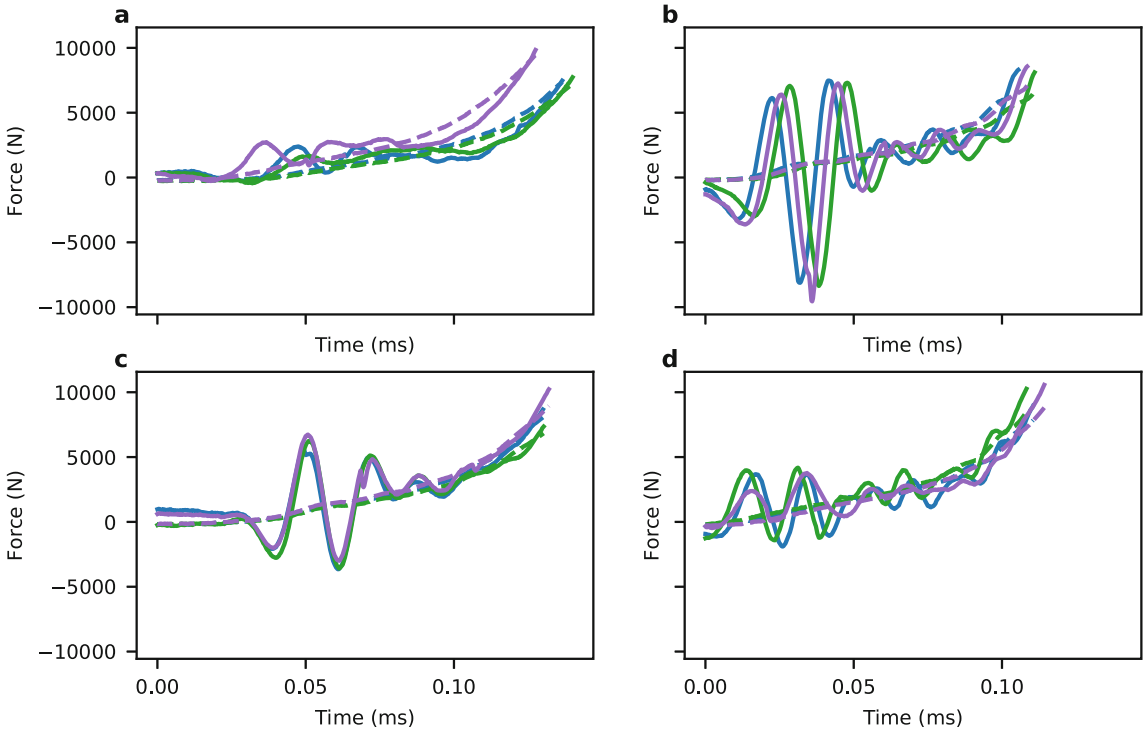

Fig. 13.6 Stiff PSA face equilibrium for fast condition using (**a**) silicone, (**b**) PET, (**c**) Paper, and (**d**) copper pulse shapers. Solid (-) lines represent the front face and dashed (−) lines represent the back face, with matched colors showing a single replicate

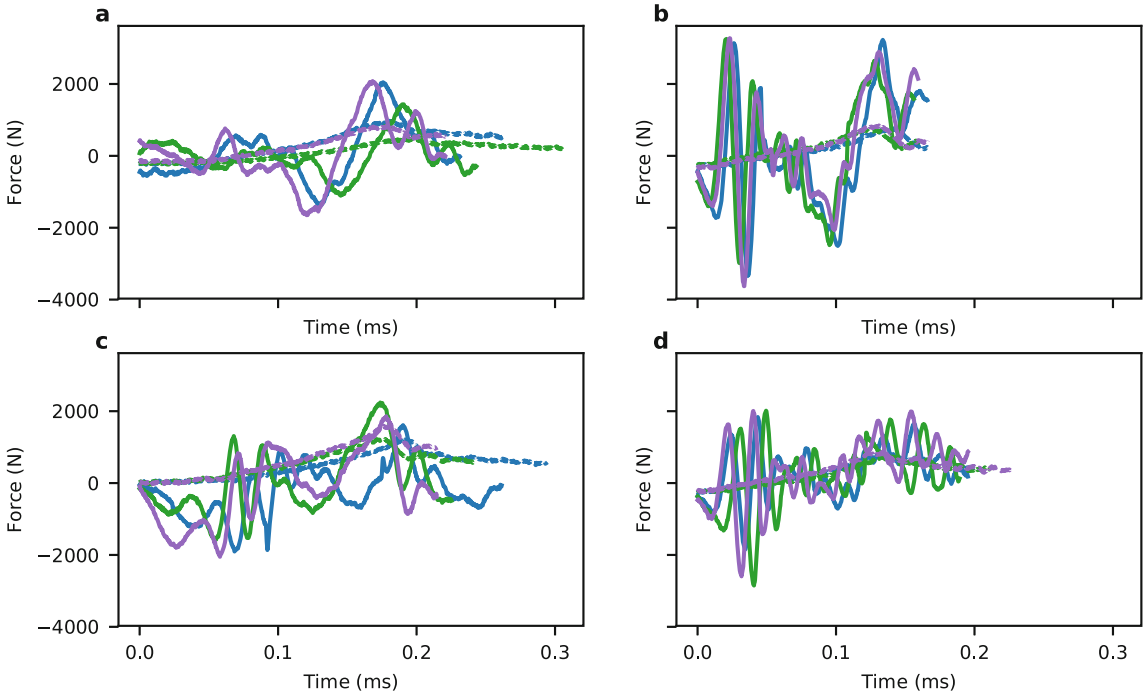

Fig. 13.7 Soft PSA face equilibrium for slow condition using (**a**) silicone, (**b**) PET, (**c**) Paper, and (**d**) copper pulse shapers. Solid (-) lines represent the front face and dashed (–) lines represent the back face, with matched colors showing a single replicate

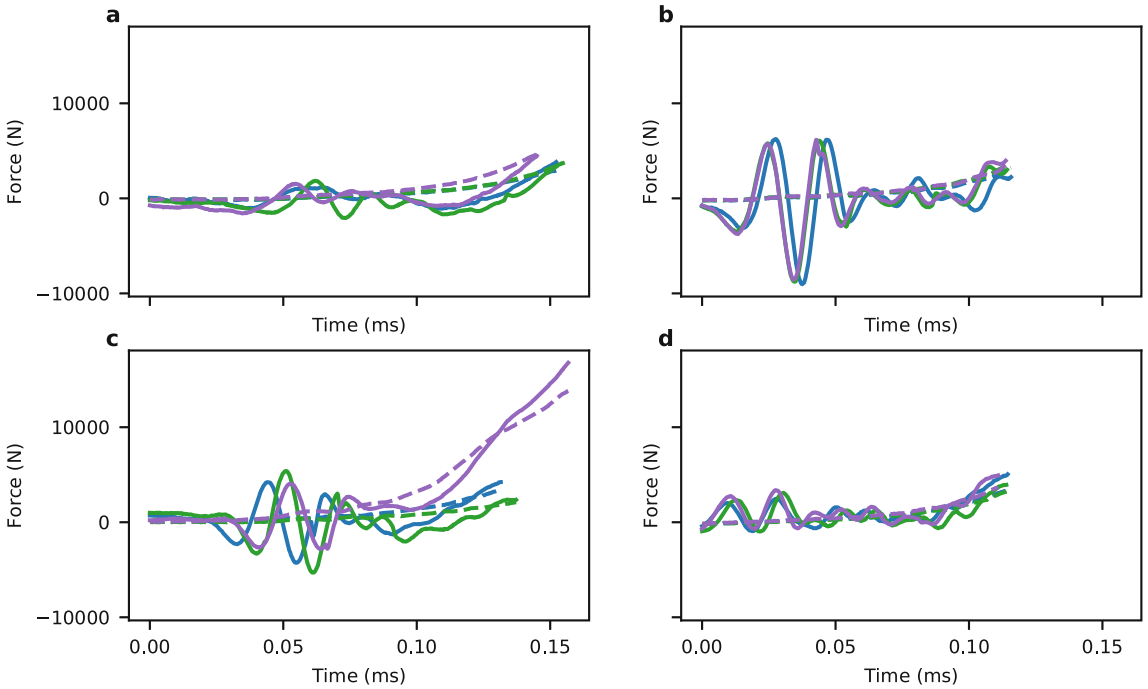

Fig. 13.8 Stiff PSA face equilibrium for fast condition using (**a**) silicone, (**b**) PET, (**c**) Paper, and (**d**) copper pulse shapers. Solid (-) lines represent the front face and dashed (–) lines represent the back face, with matched colors showing a single replicate

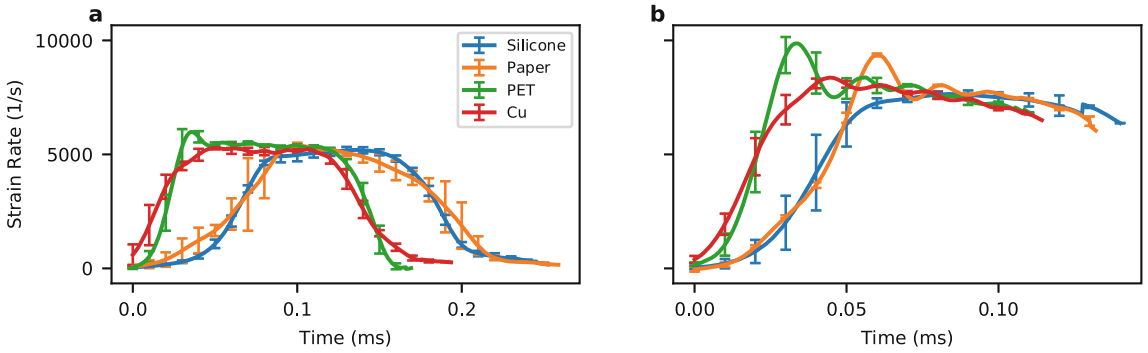

Fig. 13.9 Stiff PSA strain rates for pulse shaper study under (**a**) slow and (**b**) fast conditions

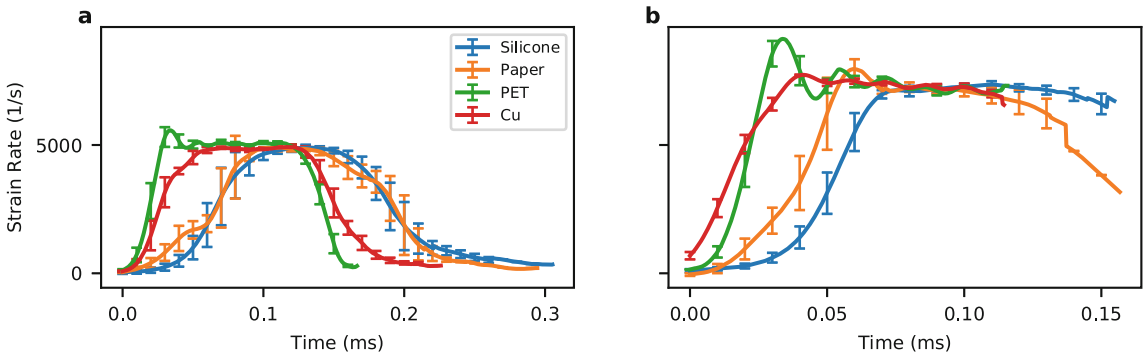

Fig. 13.10 Soft PSA strain rates for pulse shaper study under (**a**) slow and (**b**) fast conditions

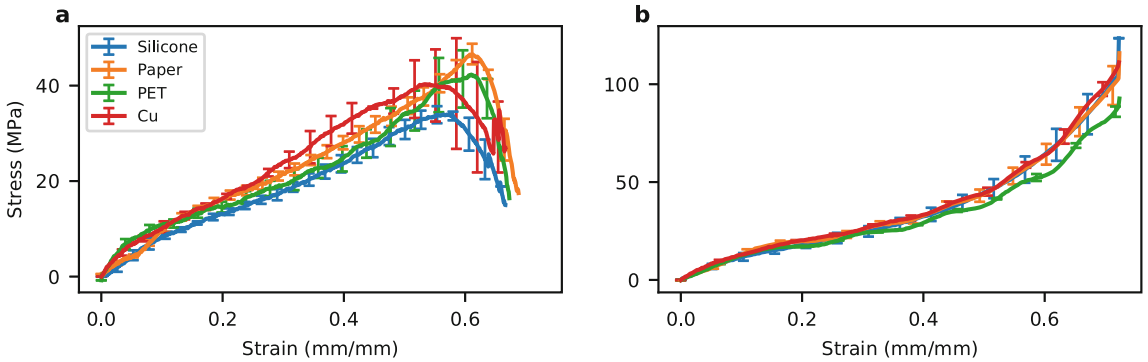

Fig. 13.11 Stiff PSA stress-strain response for the pulse shaper study under (**a**) slow and (**b**) fast conditions

Lubrication Study

Sample lubrication is critical, especially for PSAs which are tacky, to minimize friction and ensure a one-dimensional state of stress. Lubricants such as petroleum jelly, vegetable oil, and peanut oil are often chosen [1]; however, the chemical structure of PSAs raises concerns that lubricants could swell or plasticize the adhesive and change their material properties. This study evaluated the effects of lubricant selection on the resulting stress-strain response. For each adhesive and speed, the traditional peanut oil was compared to Krytox fluorinated grease (Chemours Company; Wilmington, DE) and dry powdered zinc lubricant. The zinc was selected because it is not chemically reactive with PSAs and would provide an ideal lubricant if effective. Two additional tests were conducted with oil and Krytox at the fast speed in which the samples were lubricated and then allowed to sit for 1 h. In all cases the lubricant visibly soaked into the adhesives. These soaked samples were then re-lubricated and immediately tested. In all other cases samples were tested immediately after lubricating.

Zinc resulted in stiffer sample response at both speeds for the stiff PSA and at the high speed for the soft PSA, indicating that it is not a suitable lubricant (Figs. 13.13 and 13.14). Oil and Krytox yielded similar results at the high speed; however,

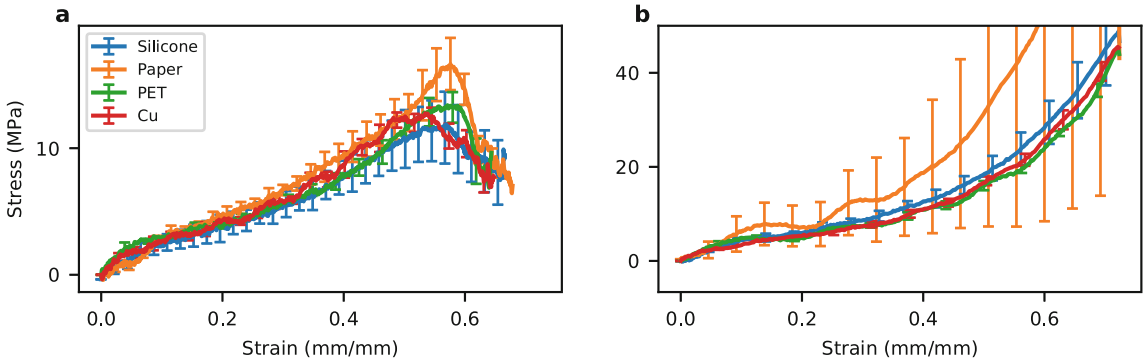

Fig. 13.12 Soft PSA stress-strain response for the pulse shaper study under (**a**) slow and (**b**) fast conditions

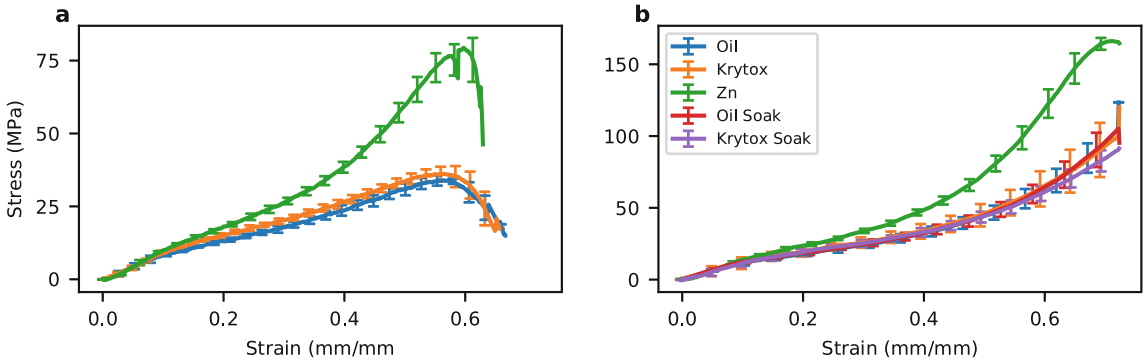

Fig. 13.13 Stiff PSA stress-strain curves for the lubrication study at (**a**) slow and (**b**) fast conditions

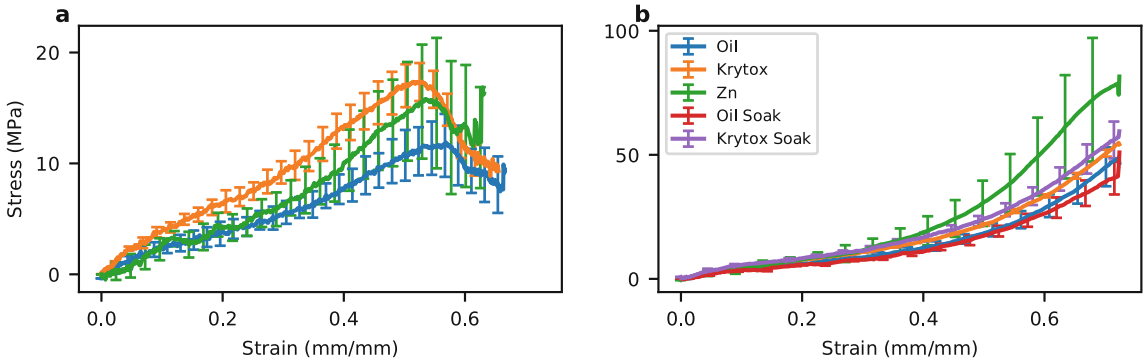

Fig. 13.14 Soft PSA stress-strain curves for the lubrication study at (**a**) slow and (**b**) fast conditions

Krytox appeared to result in a stiffer response at slow speeds. This may reflect the rheology of the Krytox grease, which exhibits shear thinning behavior and may yield insufficient lubrication levels at lower test speeds. It is notable that soaking had no measurable effect; therefore, despite both Krytox and oil soaking into the PSA, mechanical behavior was not substantially altered. This result may not hold for other PSAs; however, results appear to indicate that oil is reasonable lubricant choice provided significant time does not pass before the sample is tested.

Lubricant performance was also assessed visually using high speed video (1,000,000 fps; Shimadzu HPV-X2). Clear barreling was evident with zinc lubricant, while symmetric deformation is observed for both Krytox and oil lubricants (Fig. 13.15). These images also indicate an additional challenge of PSA Kolsky bar testing: samples distort when they are die cut, and creating of truly perpendicular and straight lateral faces can be difficult (see Fig. 13.15a). This difficulty is exacerbated for thicker samples, further justifying the selection of thinner sample dimensions.

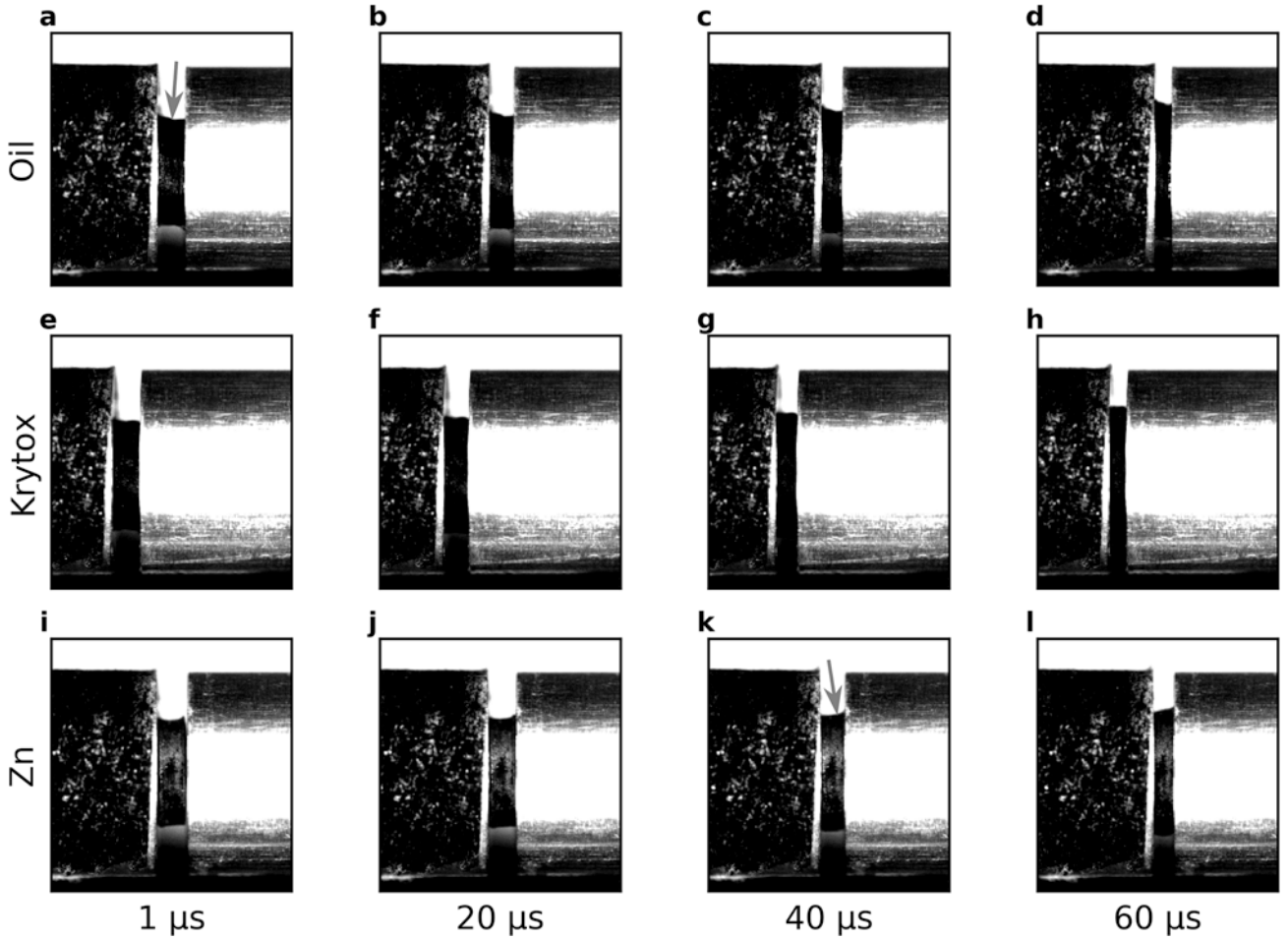

Fig. 13.15 Deformation at times throughout the deformation for (**a**–**d**) oil, (**e**–**h**) Krytox, and (**i**–**l**) zinc lubricants. The arrow in (**a**) indicates that the sample was slightly distorted at zero strain, and the deformation retained that distortion throughout all times without evidence of barreling. In contrast, the zinc lubricant resulted in noticeable barreling as indicated by the arrow in (**k**)

Simulation

The recommended test conditions were validated by comparing Kolsky bar test results to a previously developed constitutive model for a soft PSA related to the soft PSA considered above [11]. The prepared sample had a diameter of 10 mm and a thickness of approximately 2 mm. The sample was lubricated with peanut oil, and a silicone pulse shaper was used. To simulate the expected response, the measured incident pulse was applied to a full system model of the bar and sample implemented in Abaqus (Dassault Systemes; France) and described in greater detail elsewhere [11]. The resulting reflected and transmitted pulses were measured at locations corresponding to the strain gages on the actual apparatus and compared to measured response (Fig. 13.16). Results show good agreement between the predicted and measured behavior, suggesting that the characterized stress and strain due indeed reflect the high-rate, uniaxial compressive properties.

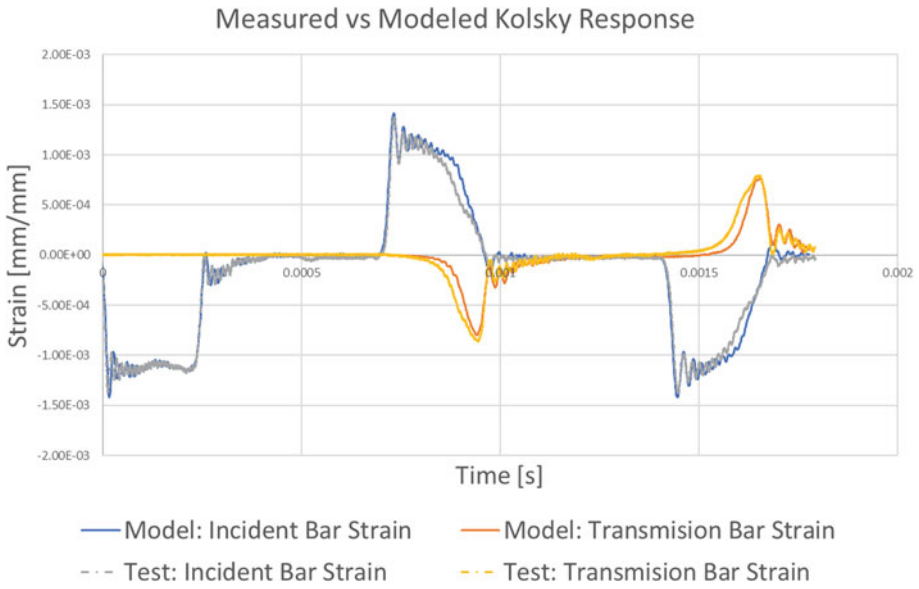

Fig. 13.16 Comparison of simulated and measured pulses for dynamic compression of a soft PSA whose constitutive model was based on quasistatic uniaxial tension and compression as well as shear DMA. Simulation results agree well with measured pulses, indicating that measured properties are consistent with expected behavior

Conclusion

This work presents a systematic study of sample geometry, pulse shaping, and lubrication for Kolsky bar compression testing of pressure sensitive adhesives. These materials exhibit mechanical properties between conventional silicone rubbers and the extreme softness of biological tissue, meaning that many of the soft-material testing challenges are exhibited. Despite their industrial importance in applications where high-rate mechanics are important, no evidence of characterization of PSAs by Kolsky bar was found in the literature. Therefore, this foundational work was necessary to establish suitable test conditions for PSA testing and to assess the relative sensitivity in measured mechanical properties.

Tests indicate that key Kolsky bar assumptions of uniaxial stress state and stress equilibrium can be achieved with suitable selection of lubrication and pulse shaper. Specifically, peanut oil was identified as an effective lubricant and silicone was selected as a pulse shaper. Fortunately, little sensitivity to specimen geometry was identified despite the expected issues with radial inertia and friction.

The Kolsky bar method is valuable for the calibration and validation of constitutive models for PSAs. Comparison of test results with predicted response provides direct evaluation of the ability of a constitutive model to correctly predict the high-rate, finite deformation behavior of the PSA. Compared to the complex system dynamics of alternative test methods, the Kolsky bar has the desirable quality that the success or failure of the model to predict the measurement may be attributed to the quality of the model and does not reflect issues with the measurement itself.

Future improvements in testing could be achieved through the use of semiconductor strain gages [2] and inertia-compensated quartz force sensors as described by Casem et al. [10]. Future work should also consider intermediate strain rates, which may require further method development. Finally, a round-robin study similar to the one conducted for metallic materials [12] would provide better measures of the robustness of these measurements and would improve industrial relevance.

Acknowledgement Thank you to Michael Kennedy for his tireless assistance with this work.

References

1. Chen, W., Song, B.: Split Hopkinson (Kolsky) Bar. Springer Science, New York (2011)
2. Chen, W.W.: Experimental methods for characterizing dynamic response of soft materials. J. Dyn. Behav. Mater. **2**, 2–14 (2016)
3. Inc. R. SURE-Pulse, GitHub (2015)

4. Lifshitz, J., Leber, H.: Data processing in the split Hopkinson pressure bar tests. Int. J. Impact Eng. **15**, 723–733 (1994)
5. Follansbee, P.S., Frantz, C.: Wave propagation in the split Hopkinson pressure bar. J. Eng. Mater. Technol. **105**, 61–66 (1983)
6. Zhao, H., Gary, G.: On the use of SHPB techniques to determine the dynamic behavior of materials in the range of small strains. Int. J. Solids Struct. **33**, 3363–3375 (1996)
7. Song, B., Ge, Y., Chen, W.W., Weerasooriya, T.: Radial inertia effects in Kolsky bar testing of extra-soft specimens. Exp. Mech. **47**, 659 (2007)
8. Liao, H., Chen, W.W.: Specimen-bar impedance mismatch effects on equilibrium and rate constancy for Kolsky bar experiments. Exp Mech. **58**(9), 1439–1449
9. Chen, W., Lu, F., Frew, D.J., Forrestal, M.J.: Dynamic compression testing of soft materials. J. Appl. Mech. **69**, 214 (2002)
10. Casem, D., Weerasooriya, T., Moy, P.: Inertial effects of quartz force transducers embedded in a split Hopkinson pressure bar. Exp. Mech. **45**, 368–376 (2005)
11. Breedlove, E. L., Lindeman, D,, Li, C., Xia, Y., Wald, M., Hedegaard, A., Clark, B.: High rate mechanical characterization of PSAs and consistency with linear viscoelastic behavior, Proceedings of the Adhesion Society (2019)
12. Kariem, M.A., Santiago, R.C., Govender, R., Shu, D.W., Ruan, D., Nurick, G., Alves, M., Lu, G., Langdon, G.: Round-Robin test of split Hopkinson pressure bar. Int. J. Impact Eng. **126**, 62–75 (2018)

Chapter 14
Full-Field Mechanical and Thermal Strain-Rate Dependence of CFRP Laminates

Brian Smith, Amos Gilat, and Jeremy Seidt

Abstract The aim of the project is to characterize the strain rate dependence of a representative carbon fiber reinforced polymer unidirectional laminate for thermal and mechanical properties. Digital image correlation is used to obtain full-field deformation and thermal effects of CFRP samples at strain rates of 0.001 s^{-1}, 1 s^{-1}, 100 s^{-1}, and 1000 s^{-1}. A combination of hydraulic load frame and split-hopkinson bar tests are used to load samples while optical and IR imaging is used to obtain deformation and thermal footage. Strain rate dependence is known to occur in the clear-cast polymer material, and is not prevalent in the carbon fiber material. Therefore, the strain rate dependence of the CFRP at varying orientations and loading conditions including tension, compression, and shear are of interest. Initial results show strong strain rate dependence in the polymer-dominated 90° orientation and clear-cast specimens.

Keywords Composites · Strain-rate dependence · Laminates · Full-field measurement · Tension

Introduction

Material behavior of composite materials are both exceptionally difficult and important to accurately model. Additionally, many applications of laminate composites undergo high-strain rate loading conditions, including aerospace and automotive applications. Composites in these applications are typically thin laminate geometries which are most accurately and efficiently modeled in shell element formulations. Accurate data for material deformation parameters and failure properties is valuable for material model development.

LS-DYNA is a commonly implemented numerical simulation software used in the aerospace and automotive industry. The software is tailored for dynamic simulations involving wave propagation and rate-dependent material models. Currently in development is the material model MAT 213, a tabulated model designed with dynamic orthotropic materials in mind. The motivation of this research project is to obtain accurate thin laminate composite data for use in development of a shell element formulation for LS-DYNA material model MAT 213.

The split hopkinson pressure bar (SHB) is an effective option for precise high-rate characterization testing. A pressure gun or pre-tensioned cable segment releases a rapid loading pulse in tension or compression that travels through the apparatus, loading the specimen at a prescribed strain rate. Strain gages located on the bar are used to calculate the forces incident on the specimen as well as provide crosshead strains across the entire specimen. Any high-frequency strain recording device can be used to record the specimen strain, including Digital Image Correlation (DIC).

Background

Laminate CFRP materials pose several challenges with characterization testing. Brittle behavior requires sensitive strain recording equipment to handle the failure strains of less than 1%. For DIC strain measurement, measures must be taken to accurately record surface deformation. Increased spatial resolution increases the correlation accuracy, allowing for more accurate strain measurements. Particularly for higher rate testing, the specimen should efficiently fill up as much of the camera frame as possible. For most cameras, increasing resolution requires decreasing recording frame rates, therefore increasing test difficulty by requiring accurate triggering systems for image capture and lighting.

B. Smith (✉) · A. Gilat · J. Seidt
Department of Mechanical and Aerospace Engineering, College of Engineering, The Ohio State University, Columbus, OH, USA
e-mail: smith.11937@buckeyemail.osu.edu

L. E. Lamberson (ed.), *Dynamic Behavior of Materials, Volume 1*, Conference Proceedings of the Society for Experimental Mechanics Series, https://doi.org/10.1007/978-3-030-30021-0_14

Unidirectional (UD) laminates such as the subject material for this research, are highly sensitive to misalignment. Off-axis loading can cause significantly reduced ultimate strengths and requires precise implementation of loading fixtures [1]. To mitigate off-axis loading, universal joints are employed for the hydraulic frame loading. Universal joints are not used for the high-rate testing, as there is no effective way to maintain clean wave propagation through the joints in a SHB apparatus.

Tensile fixtures for laminate composite testing must be designed to maximize grip strength while minimizing grip pressure. Particularly for the longitudinal direction, the failure stresses are very large relative to the failure stress in the through-thickness direction. For low-force orientations such as the transverse direction, simple adhesives are adequate for tensile testing. As the forces required to fail the specimen increase, tabs are used to increase the maximum gripping pressure that can be applied. Adhesives are used for high-force tensile configurations to additionally increase the maximum grip forces achievable.

Analysis

Initial testing has been conducted on the available material. Tensile tests have successfully been performed on epoxy-only and 90° samples at 0.001 and 1 s^{-1}, as well as tests on 45° samples at 0.001 s^{-1}. The samples are of dogbone geometry as shown in Fig. 14.1 and are designed to be used in both hydraulic load frames and SHB devices with minimal changes to geometry. All tests were performed on a hydraulic load frame with universal joints for reduced off-axis loading. 2D DIC is used to obtain strain values, which are compared to crosshead displacements and paired with loading values from the hydraulic load frame. The resulting stress-strain curves are shown in Fig. 14.2.

Significant strain rate dependent hardening occurs in the epoxy-only samples as well as the epoxy-dominated 90° samples. The ultimate tensile strengths of the epoxy and the 90° oriented CFRP are similar, with the epoxy exhibiting ductile behavior and the CFRP exhibiting brittle behavior. Fiber-dominated orientations exhibit higher ultimate tensile strengths and more ductility as expected from laminate composite theory. Brittle behavior poses a challenge to the DIC correlation due to the small strains present. Therefore, high resolution is prioritized over high temporal resolution to increase the correlation accuracy.

Limited infrared imaging was performed for justification during testing. An infrared camera, synchronized to record at integer multiples of the optical camera, imaged the reverse side of the specimen during testing to measure temperature increase during loading. As expected, brittle material in tension did not exhibit much plastic deformation, and therefore did not show any measurable thermal rise during testing.

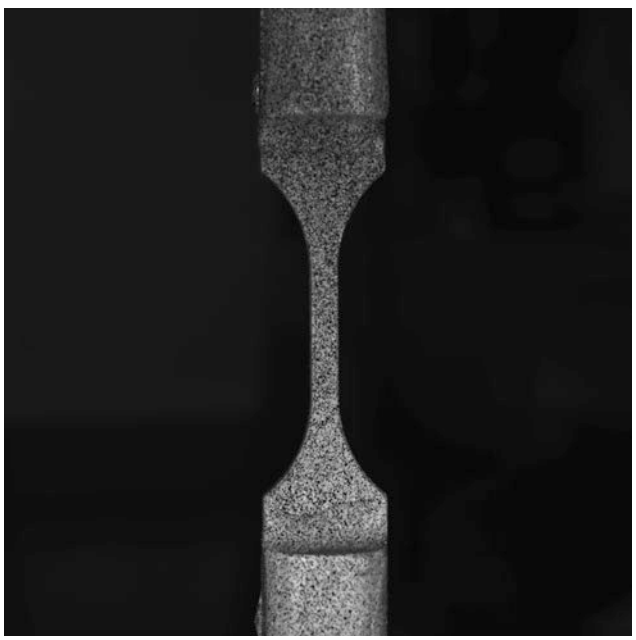

Fig. 14.1 DIC image of CFRP dogbone sample

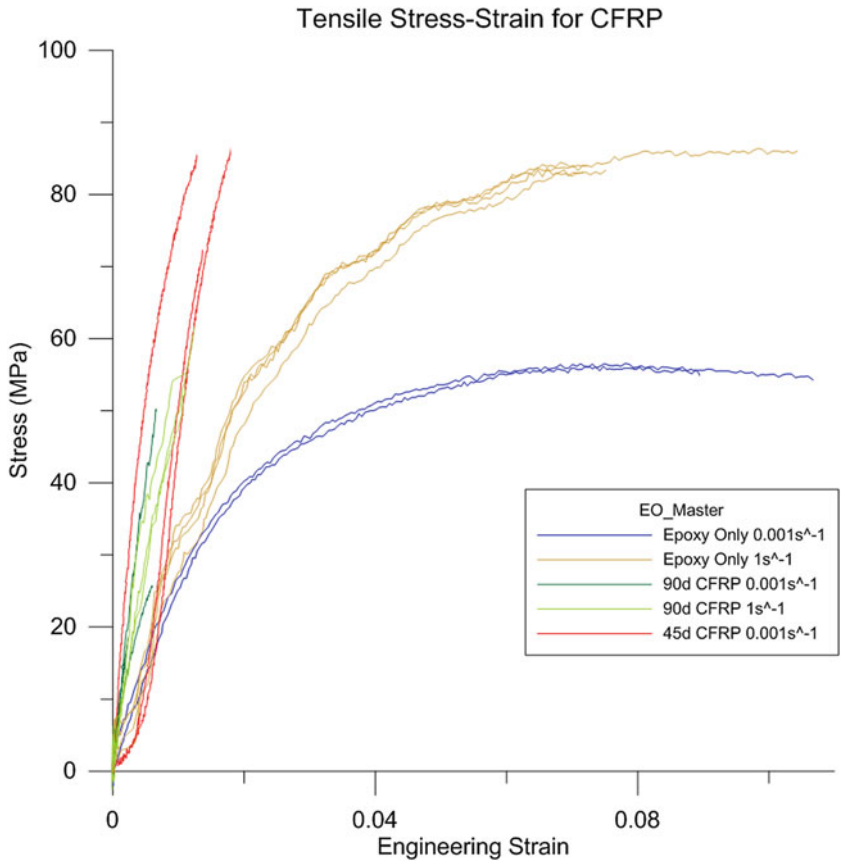

Fig. 14.2 Tensile stress-strain plots for epoxy only & CFRP

Conclusion

Testing of epoxy and UD CFRP samples are tested in tension at 0.001 s^{-1} and 1 s^{-1}. Strain rate effects are shown in the epoxy-dominated specimens, with brittle behavior shown for composite specimens. DIC is used to obtain full-field strain measurements, and is paired with crosshead displacements and load cell outputs to obtain stress-strain data. IR imaging is used to sync thermal measurements with displacement, justifying the lack of thermal effects during the brittle tensile loading. Further testing is planned to characterize additional strain rates and orientations.

Acknowledgement Thanks to the support of the fellow graduate students and professional researchers in the Dynamic Mechanics of Materials Lab at The Ohio State University for their support and guidance.

Reference

1. Kyriakides, S., Arseculeratne, R., Perry, E.J., Liechti, K.M.: On the compressive failure of fiber reinforced composites. Int. J. Solids Struct. **32**(6–7), 689–738. ISSN 0020-7683 (1995)

Chapter 15
Enhanced Energy Absorption Performance of Liquid Nanofoam-Filled Thin-Walled Tubes under Dynamic Impact

Mingzhe Li, Saeed Barbat, Ridha Baccouche, Jamel Belwafa, and Weiyi Lu

Abstract Thin-walled structures have been widely used among other energy absorbing structures in automotive, aerospace and other industries, due to their high energy absorption capacity and light weight. In some cases, these structural components were filled with metallic foams to further improve their energy absorption performance and capacity. This may lead to an increase in the structural component weight. In this study, a highly compressible liquid filler, i.e. liquid nanofoam (LN), has been introduced into the thin-walled tubes. We have characterized the mechanical response of these LN-filled tubes (LNFTs) by using quasi-static compression tests and dynamic impacts. The quasi-static compression tests are conducted by an MTS system. Results show that the energy absorption capacity of LNFTs is 45% higher than that of identical empty tubes. The dynamic behavior of LNFTs is characterized by using a gas gun apparatus at impact speed of 6.7 m/s. It is found that the energy absorption capacity of LNFTs is 76% higher than that of identical empty tubes. Importantly, by increasing the strain rate from quasi-static condition (10^{-2} s^{-1}) to intermediate range (10^{2} s^{-1}), the energy absorption capacity of LNFTs is increased by 54% without increasing the working pressure of the system. The strain rate sensitive behavior of LNFTs suggests that LNFTs can be used as advanced energy absorber whose impact mitigation capability is adaptive to the impact energy levels. These findings warrant future considerations of these new liquid nanofoam filled thin-walled structures for vehicle crashworthiness and infrastructure protection.

Keywords Thin-walled structures · Liquid nanofoam · Impact · Vehicle crashworthiness · Energy absorption

Introduction

Over recent decades, enormous efforts have been made to develop Advanced Energy Absorption Materials and Structures (AEAMS) [1]. AEAMS can mitigate the kinetic and strain energies associated with the impact when subjected to external loadings, and thus mitigate personnel injuries or key facilities damages. Among many other AEAMS, thin-walled structures, e.g. thin-walled metallic tubes, have been widely used as conventional energy absorbing devices due to their light weight and high energy absorption capacity [2, 3]. The axial folding of the tube wall is known as the main working mechanism. However, the tube wall buckling initiation requires a relatively large stress, after which the average stress of post-buckling plateau drops abruptly. The specific energy absorption of empty tube is dominated by the post-buckling stress. Therefore, the specific energy absorption is much lower than the theoretical limit which is proportional to the initial buckling stress. In past years, extensive research has been focused on metallic foam-filled thin-walled tubes and it has been demonstrated that filler-tube interaction can effectively improve the energy absorption and mechanical properties of the resulted hybrid tube under both quasi-static [4–6] and dynamic [7, 8] conditions. However, due to the imperfect bonding between the metallic filler and tube wall, delamination of filler and tube wall occurs at large deformation [9]. Therefore, the interaction effect between filler and tube wall is weakened, leading to a reduced energy absorption capacity.

Recently, a highly compressible liquid system, liquid nanofoam (LN) [10–13], have been employed as an advanced filler to improve the energy absorption performance of thin-walled tubes [14–16]. LN composes of hydrophobic nanoporous materials and a non-wettable liquid. Due to capillary effect, the liquid stays outside the nanopores at ambient condition. As an external load is applied, the liquid is forced into the nanopores and tremendous amount of energy is dissipated [17]. Since LN is in liquid form, it can always fit well with the tube wall; that is, an "perfect bonding" can be created between LN and tube

M. Li (✉) · W. Lu
Department of Civil & Environmental Engineering, Michigan State University, East Lansing, MI, USA
e-mail: limingzh@egr.msu.edu

S. Barbat · R. Baccouche · J. Belwafa
Ford Motor Company, Dearborn, MI, USA

L. E. Lamberson (ed.), *Dynamic Behavior of Materials, Volume 1*, Conference Proceedings of the Society for Experimental Mechanics Series, https://doi.org/10.1007/978-3-030-30021-0_15

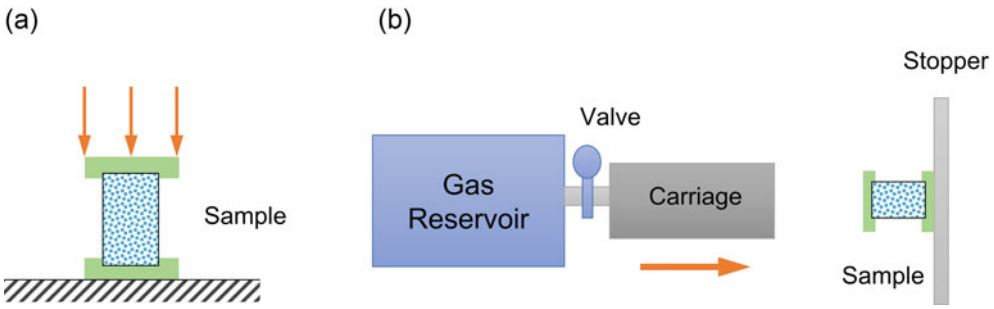

Fig. 15.1 Schematic of the experimental set-up of (**a**) quasi-static compression tests (**b**) dynamic impact tests

wall, leading to a better interaction effect. Previous studies on liquid nanofoam filled tubes (LNFTs) have demonstrated that the specific energy absorption of empty tube under both quasi-static compression and dynamic impact can be improved by the LN filler [18, 19] and the dominant reinforcing mechanism, e.g. filler-tube wall interaction, has been extensively studied in [15]. However, those studies are limited to small-scale demonstration and the incident energy is relatively low. This study focuses on the mechanical response of large-scale LNFTs subjected to external impact with relatively high incident energy. Results show that the energy absorption performance is considerably increased, especially under dynamic conditions.

Methods

The thin-walled aluminum (Al 6061) tube was purchased from McMaster (Product No. 9056 k85). The outer diameter, wall thickness and height of the Al tube were $R = 38.1$ mm, $t = 1.63$ mm and $h_0 = 101.6$ mm, respectively. The thin-walled Al tube was then filled with LN. The empty Al tube was used as reference. The Al tubes were then sealed by attaching both ends with two metal caps equipped with O-rings. The effective height of the tube is $h = 81.3$ mm. During all experimental process, no liquid leakage was observed at the sealing part of the Al tubes. The LN contained a nanoporous silica from Sigma-Aldrich (Product No. 60759) and 15 wt% ethanol aqueous solution. The as-received nanoporous silica had C8 modified surface, which was non-wettable to the aqueous solution.

The quasi-static infiltration behavior of the LN was characterized by quasi-static pressure-induced infiltration tests by an Instron 5982 universal tester at a constant loading rate of 2 mm/min. The LN specimen was sealed in a stainless-steel testing cell. The applied force was gradually increased from 0 kN to 6.3 kN, after which the Instron crosshead was moved back at the same speed.

The mechanical behavior of empty and LN filled Al tubes were characterized by a series of quasi-static compression and gas gun impact tests. The experimental setups are shown in Fig. 15.1. The quasi-static compression tests were conducted by using an MTS system at a constant loading rate of 2 mm/s. The dynamic behavior of the Al tubes was characterized by a gas gun apparatus at Ford facility. The incident speed and carriage weight of gas gun tests were 6.7 m/s and 181.55 kg, respectively.

Results

Figure 15.2 shows typical quasi-static pressure induced infiltration behavior of the LN. As the LN was compressed, the LN system volume decreased slowly when the applied external pressure was relatively low. When the pressure increased to about 5 MPa, the slope of the curve decreased remarkably and an infiltration plateau was observed. The plateau indicated that the capillary effect of the hydrophobic nanopore was overcome and the liquid molecules were compressed to the nanopores. As the external pressure reached around 15 MPa, the infiltration plateau ended. Therefore, the working pressure of LN ranged from 5 MPa to 15 MPa. The effective pore volume, which was the volume change during liquid infiltration, was around 450 mm^3/g. Upon unloading, the pressure dropped abruptly, leading to a highly hysteretic behavior of the LN system.

The typical stress-strain curves of tube samples under quasi-static compression are shown in Fig. 15.3. The empty tube wall buckling was initiated at 25 MPa, after which the stress level dropped to around 10 MPa and a wide stress plateau was formed. As the tube was filled by LN, the buckling initiation was not affected. The stress drop after buckling initiation resulted from the small amount of air bubbles trapped in the LN. At strain of 0.2, the LN filler started to take effect and

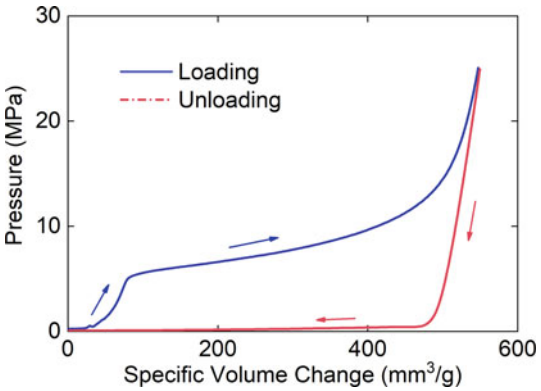

Fig. 15.2 Mechanical behavior of the LN

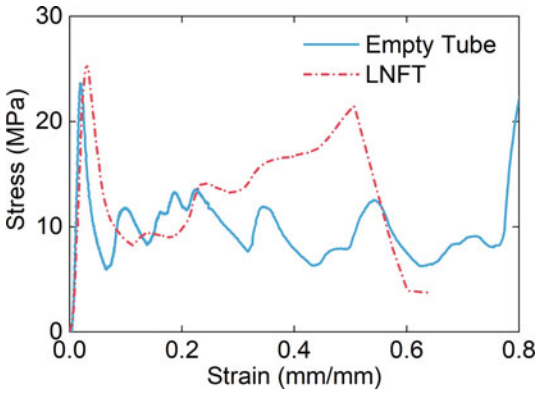

Fig. 15.3 Typical stress-strain curves of Al tubes under quasi-static compression

Table 15.1 Performance of empty and LN filled tubes under quasi-static compression and dynamic impact

	Quasi-static		Dynamic	
	Strain at burst	Energy absorption capacity (J)	Strain at burst	Energy absorption capacity (J)
Empty tube	N/A	1843	N/A	2349
LNFT	0.5	2678	N/A	4130

the nominal stress increased to about 13 MPa. The system then became highly compressible and an enhanced post-buckling stress plateau was observed. The width of the stress plateau was around 30% of the effective height of the LN tube. As the nominal stress increased to 20 MPa, the tube wall cracked, which led to leakage of the LN. From this point, the behavior of the LN-filled tube was similar to that of the empty tube as the solid-liquid interaction was nearly zero. As shown in Table 15.1, the energy absorption capacity of empty tube at total strain of 0.6 was 1843 J, while the value of LNFTs was 2678 J. Therefore, the energy absorption capacity was improved by 45%. The increase of energy absorption capacity of LNFTs is due to the enhanced liquid-solid interaction between LN and tube wall as well as the high compressibility of LN.

Figure 15.4a shows the dynamic stress-strain curves of empty Al tubes. As the empty tube was impacted, the average stress of the post-buckling plateau was close to that in quasi-static compression tests. Figure 15.4b shows typical dynamic stress-strain curves of LNFTs. All the incident energy was absorbed by the LNFT at a strain of 0.6 and the tube did not burst. The average stress of the post-buckling plateau was promoted to 20 MPa, which was 25% higher than that in quasi-static compression tests. The energy absorption capacity of LNFTs under dynamic impact was 4130 J, which was 54% higher than that in quasi-static compression tests. The strain rate sensitivity is related to the initiation of higher buckling mode or new energy absorption mechanism such as energy capture [20, 21] at higher strain rate.

Figure 15.5 shows the snapshots of the Al tubes under dynamic impact. The empty Al tube buckled in diamond mode (Fig. 15.5a), while the LNFT buckled in a concertina mode (Fig. 15.5b).

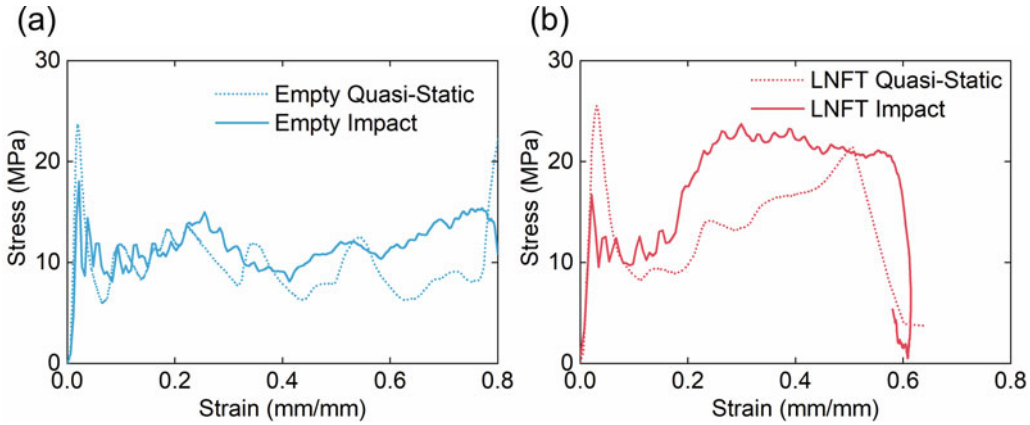

Fig. 15.4 Typical stress-strain curves of Al tubes under dynamic impact (**a**) Empty tube (**b**) LNFT

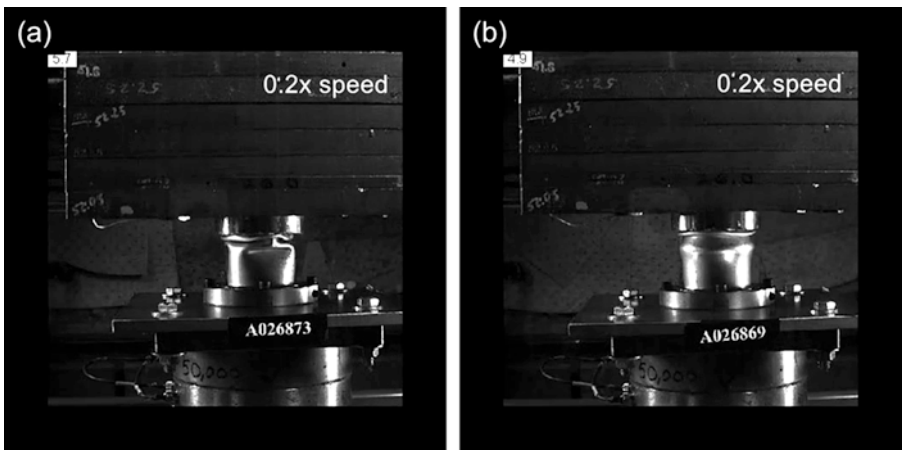

Fig. 15.5 Snapshots of Al tubes under dynamic impact (**a**) Empty tube and (**b**) LNFT

Conclusion

In this study, the energy absorption performance of large-scale LNFTs under dynamic impact test were experimentally investigated. Based on the comparison of energy absorption capacity of LNFTs and empty tubes, we have demonstrated that by adding LN as a filler, the thin-walled tubes can be reinforced remarkably. Importantly, the mechanical response of LNFTs shows high strain rate sensitivity, revealing that LNFTs have better energy absorption performance at high strain rates. These findings can shed light on the design of AEAMS for vehicle crashworthiness and infrastructure protection.

Acknowledgement This work was financially supported by Ford-MSU Alliance program.

References

1. Lu, G., Yu, T.X.: Energy Absorption of Structures and Materials. CRC Press, Boca Raton (2003)
2. Wierzbicki, T., Abramowicz, W.: On the crushing mechanics of thin-walled structures. J. Appl. Mech. **50**(4a), 727 (1983)
3. Chen, W., Wierzbicki, T.: Relative merits of single-cell, multi-cell and foam-filled thin-walled structures in energy absorption. Thin-Walled Struct. **39**(4), 287–306 (2001)
4. Zarei, H.R., Kröger, M.: Optimization of the foam-filled aluminum tubes for crush box application. Thin-Walled Struct. **46**(2), 214–221 (2008)
5. Hangai, Y., Saito, M., Utsunomiya, T., Kitahara, S., Kuwazuru, O., Yoshikawa, N.: Fabrication of aluminum foam-filled thin-wall steel tube by friction welding and its compression properties. Materials. **6**(9), 6796–6810 (2014)
6. Taherishargh, M., Vesenjak, M., Belova, I.V., Krstulović-Opara, L., Murch, G.E., Fiedler, T.: In situ manufacturing and mechanical properties of syntactic foam filled tubes. Mater. Des. **99**, 356–368 (2016)

7. Rajendran, R., Prem Sai, K., Chandrasekar, B., Gokhale, A., Basu, S.: Impact energy absorption of aluminium foam fitted AISI 304L stainless steel tube. Mater. Des. **30**(5), 1777–1784 (2009)
8. Hanssen, A.G., Langseth, M., Hopperstad, O.S.: Static and dynamic crushing of circular aluminium extrusions with aluminium foam filler. Int. J. Impact Eng. **24**(5), 475–507 (2000)
9. Bonaccorsi, L., Proverbio, E., Raffaele, N.: Effect of the interface bonding on the mechanical response of aluminium foam reinforced steel tubes. J. Mater. Sci. **45**(6), 1514–1522 (2010)
10. Chen, X., Qiao, Y.: Science and prospects of using nanoporous materials for energy absorption. MRS Proc. **1041**, (2007)
11. Li, M., Lu, W.: Liquid marble: a novel liquid nanofoam structure for energy absorption. AIP Adv. **7**(5), 055312 (2017)
12. Zhang, Y., Li, M., Gao, Y., Xu, B., Lu, W.: Compressing liquid nanofoam system: liquid infiltration or nanopore deformation? Nanoscale. (2018)
13. Li, M., Xu, L., Lu, W.: Nanopore size effect on critical infiltration depth of liquid nanofoam as a reusable energy absorber. J. Appl. Phys. **125**(4), 044303 (2019)
14. Sun, Y., Li, Y., Zhao, C., Wang, M., Lu, W., Qiao, Y.: Crushing of circular steel tubes filled with nanoporous-materials-functionalized liquid. Int. J. Damage Mech. **0**(0), 1–12 (2016)
15. Li, M., Li, J., Barbat, S., Baccouche, R., Lu, W.: Enhanced filler-tube wall interaction in liquid nanofoam-filled thin-walled tubes. Compos. Struct. **200**, 120–126 (2018)
16. Liu, Y., Schaedler, T.A., Jacobsen, A.J., Lu, W., Qiao, Y., Chen, X.: Quasi-static crush behavior of hollow microtruss filled with NMF liquid. Compos. Struct. **115**(1), 29–40 (2014)
17. Lu, W., Han, A., Kim, T., Chow, B.J., Qiao, Y.: Endcapping treatment of inner surfaces of a hexagonal mesoporous silica. J. Adhes. Sci. Technol. **26**(12–17), 2135–2141 (2012)
18. Chen, X., Surani, F.B., Kong, X., Punyamurtula, V.K., Qiao, Y.: Energy absorption performance of steel tubes enhanced by a nanoporous material functionalized liquid. Appl. Phys. Lett. **89**(24), 1–3 (2006)
19. Sun, Y., Xu, J., Zhao, C., Li, P., Li, Y.: Exploring a new candidate of energy absorber: thin-walled tube structures filled with nanoporous material functionalized liquid. IRCOBI Conference. **2014**, 578–586 (2014)
20. Xu, B., Chen, X., Lu, W., Zhao, C., Qiao, Y.: Non-dissipative energy capture of confined liquid in nanopores. Appl. Phys. Lett. **104**(20), 2012–2016 (2014)
21. Lu, W.: Novel Protection Mechanism of Blast and Impact Waves by Using Nanoporous Materials, *Dynamic Behavior of Materials*, vol. 1, pp. 177–183. Springer International Publishing, Berlin (2016)

Chapter 16
Effect of Heat-Treatment on Rock Fragmentation Using Dynamic Ball Compression Test

Ying Xu, Wei Yao, and Kaiwen Xia

Abstract Rock fragmentation is mainly induced by dynamic mechanical loading in mining and rock engineering. Heat-treatment is one of the rock pre-treatment methods to optimize the rock fragmentation. It is therefore important to investigate the effect of heat-treatment on the outcome of rock fragmentation. This study is concerned with the rock fragmentation in crushing, which is experimentally studied utilizing the dynamic ball compression test conducted by the spilt Hopkinson pressure bar (SHPB) system with a high-speed camera. The spherical specimens made of Laurentian granite (LG) heat-treated under various temperatures (250, 450, 600 and 850 °C) are first characterized by the X-ray micro-computed tomography (CT) method. The damage variable derived from the CT value is used to quantify the thermal damage. The dynamic indirect tensile strength of LG increases with the loading rate under a given heat-treatment temperature. The energy dissipation in crushing is obtained at five fixed input energy levels for all specimens. The energy efficiency (energy dissipation/input energy) of crushing varies with the input energy and the heat-treatment temperature.

Keywords Fragmentation · Heat-treatment temperature · SHPB · CT · Energy efficiency

Introduction

Rock fragmentation in many geotechnical engineering applications (rock crushing) is a dynamic process in which energy is consumed to create new fracture surfaces. The understanding of rock fragmentation in crushing is therefore critical to the reduction of the energy consumption. Over years, heat-treatment has been proposed as a pre-condition method to facilitate rock fragmentation in crushing by weakening the rocks through thermal damage so as to reduce the energy consumption in fragmentation. The effect of heat-treatment temperature on the mechanical and physical properties of rocks has been extensively studied for decades. Furthermore, the controlled single particle tests have been suggested to establish the relationship between the input mechanical energy and size reduction in crushing, and further to better understand the crushing mechanism [1]. However, the energy absorbed by rock particles during crushing is difficult to quantify in these tests. In a spilt Hopkinson pressure bar (SHPB) system, the energy dissipation can be easily determined from stress waves and the single pulse loading can be achieved using the momentum-trap technique. Thus, the relation between damage and energy consumed for fragmentation can be accurately established. As a result, the dynamic ball compression test is utilized in this work to investigate the effect of heat-treatment temperature on the dynamic rock fragmentation by using the SHPB system.

Experiment

Five groups of Laurentian granite (LG) spherical specimens (with the diameter of 21 ± 0.1 mm) were prepared: room temperature (25 °C), and thermally treated for 2 h under 250 °C, 450 °C, 600 °C, and 850 °C (Fig. 16.1a). In Fig. 16.1b, there is no visible difference between the CT images of specimens from 25 °C to 250 °C. When the temperature reaches 600 °C, several cracks appear in the CT image. The crack density increases with the temperature. We resort to the CT

Y. Xu
State Key Laboratory of Hydraulic Engineering Simulation and Safety, School of Civil Engineering, Tianjin University, Tianjin, China

W. Yao · K. Xia (✉)
Department of Civil and Mineral Engineering, University of Toronto, Toronto, ON, Canada
e-mail: kaiwen.xia@utoronto.ca

L. E. Lamberson (ed.), *Dynamic Behavior of Materials, Volume 1*, Conference Proceedings of the Society for Experimental Mechanics Series, https://doi.org/10.1007/978-3-030-30021-0_16

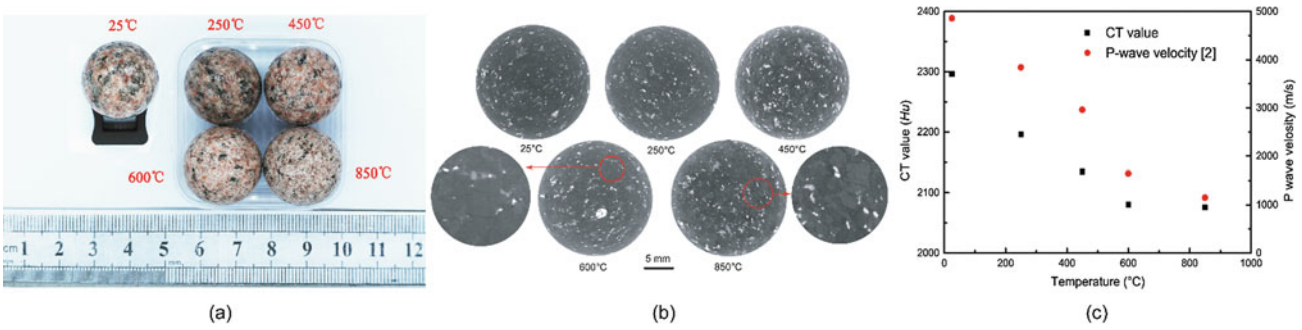

Fig. 16.1 (**a**) Rock ball specimens after heat-treatment, (**b**) Typical CT images of LG specimens after heat-treatment, (**c**) Variation of CT value and P-wave velocity with the treatment temperature

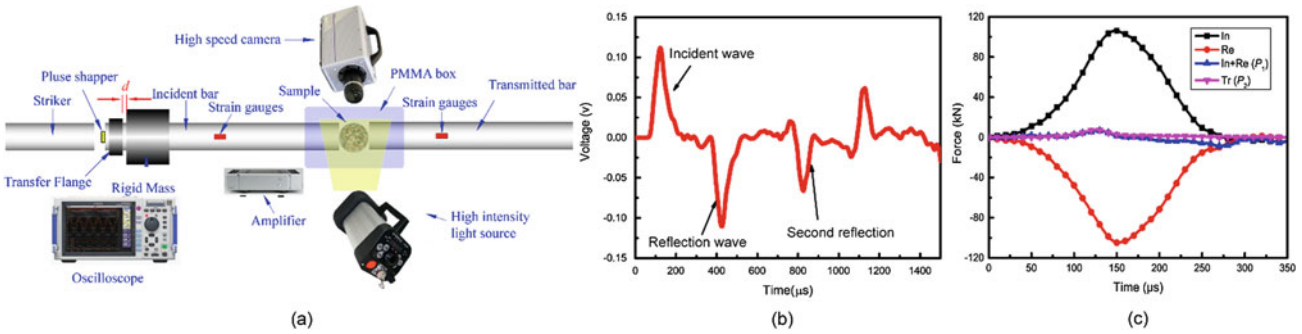

Fig. 16.2 (**a**) The SHPB system and monitoring system, (**b**) Typical oscilloscope signal on the incident bar with the momentum-trap, (**c**) Dynamic force history of a typical dynamic ball test

value (i.e. Hounsfield radiological density) to estimate the thermally-induced damage. Figure 16.1c shows that the CT values decrease with the temperature. The reduction of the CT value is mainly caused by the increase of the number and size of cracks due to thermal stresses and the transition from α to β quartz at 573 °C. Also, both the CT value and the P-wave velocity of LG measured by Yin et al. [2] show similar trend with the temperature in Fig. 16.1c.

The SHPB system combined with a high-speed camera and a momentum-trap system was adopted to conduct the dynamic rock ball compression test (Fig. 16.2a). With the momentum-trap, the second reflected tensile stress pulse (Fig. 16.2b) would detach the specimen from the incident bar in actual dynamic tests, resulting in the single pulse loading on the specimen [3]. A box was designed to recover the fragments while allowing us to monitor the fragmentation process with high speed photography. The pulse-shaping technology was used to facilitate the dynamic force balance ($P(t) = P_1(t) = P_2(t)$) in ball specimens (Fig. 16.2c). Since the spherical specimen fails in tension along the diametrical compressive loading direction, the dynamic tensile stress at the center of the ball is $\sigma(t) = (0.7 \times P(t))/(\pi \times r^2)$, where r is the radius of the specimen. The peak value of $\sigma(t)$ is the dynamic tensile strength of the ball specimen. Further, the loading rate for the ball compression test is determined as the slope of the roughly linear portion of the tensile stress history before the failure.

Analysis

Each group of heat-treated specimens was impacted under five striker velocities, which are achieved by five air pressures in the air gun: 5 psi, 7 psi, 10 psi, 15 psi and 21 psi. Due to the single impact loading on the ball specimens, all the fragments of the specimens were softly recovered after the dynamic tests (Fig. 16.3a). After dynamic compressive loading, there are two failure modes in the ball specimens: fragmentation and pulverization. The fragmentation is defined as the maximum length of fragment is larger than the ball specimen radius. Otherwise, the failure mode is pulverization. In Fig. 16.3b, the dynamic tensile strength of LG exhibits significant rate dependency for a given heat-treatment temperature and decrease with the temperature. The change of the dynamic tensile strengths of LG with the temperature is caused by the thermally induced damage due to micro-cracking and chemical reactions [2]. Due to the single pulse impact on the ball specimen, the total energy absorbed by the rock ball specimen ΔW is partially used to generate the new fracture surfaces (W_f), and the

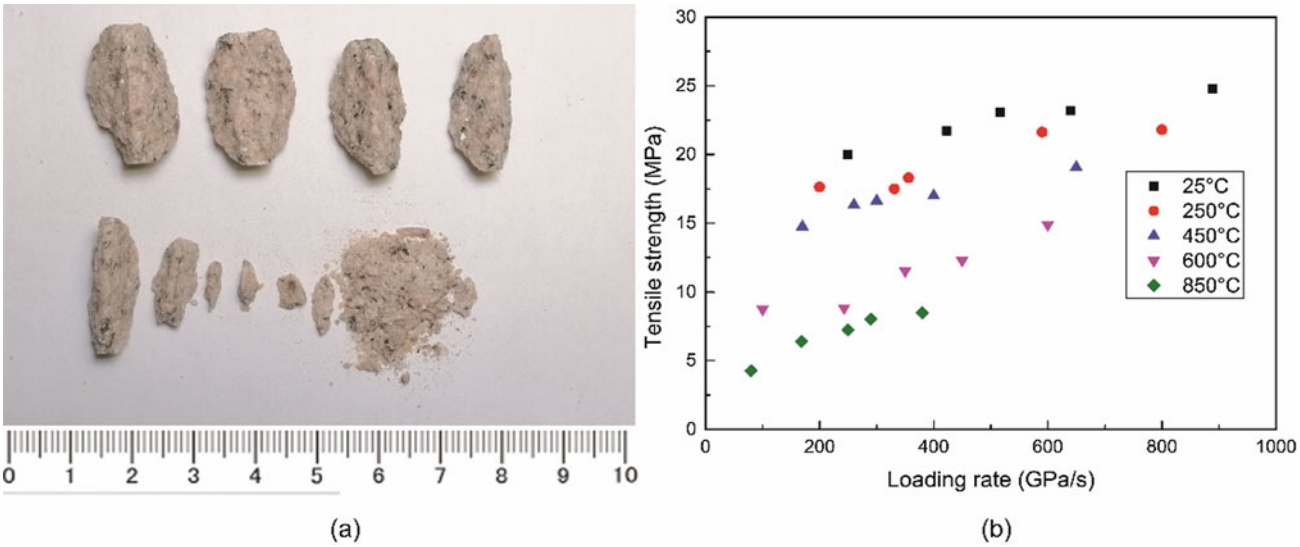

Fig. 16.3 (**a**) The recovered fragments for a typical dynamic ball specimen, (**b**) Dynamic tensile strength under various temperatures

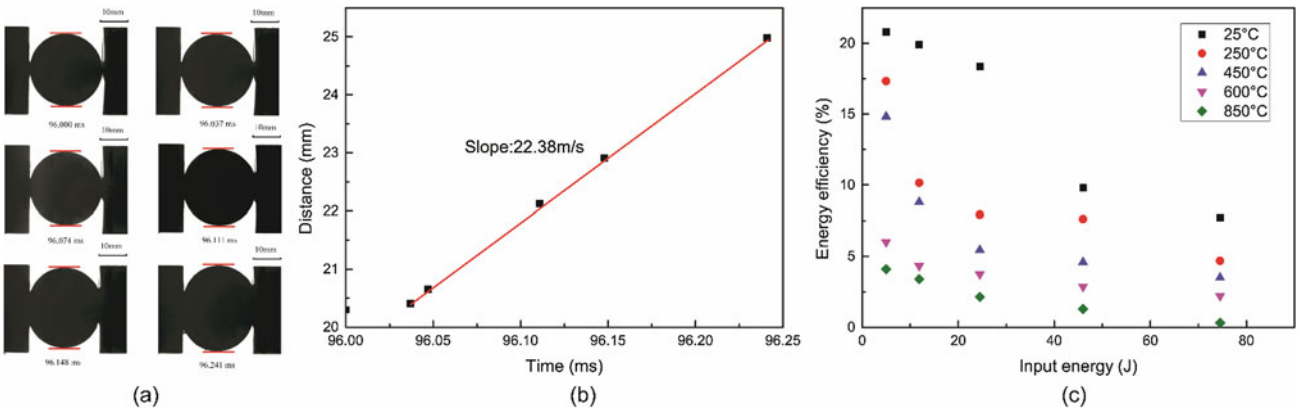

Fig. 16.4 (**a**) The movement of fragments for a test from high-speed frames, (**b**) The distance between two solid red lines vs. time, (**c**) Variation of energy efficiency with the input energy W_i

remainder is transferred into the kinetic energy of the fragments (K) and other forms (e.g., heat, sound). Since other forms of energy is negligible, the fracture energy $W_f = \Delta W\text{-}K$. The kinetic energy of the fragments was estimated by using the high-speed images. The solid red lines in each high-speed frame in Fig. 16.4a indicate the top and bottom boundaries of the fragments. Here, we assume that all fragments fly from the loading axis with the same velocity. Thus, the velocity of fragments can be estimated through the variation of the distance between the top and bottom boundary lines. The distance between two lines almost linearly increases and the half of slope of the linear fitting line is defined as the velocity (v) of fragments (Fig. 16.4b). As the mass of the ball specimen m_t was obtained before each dynamic test, the kinetic energy ($K = m_t v^2/2$) of fragments can be calculated for each dynamic test.

The useful work done in the dynamic ball compression tests is the energy for creating the new fracture surfaces. Thereby, the energy efficiency (e_e) is defined as W_f / W_i (i.e., input energy). As shown in Fig. 16.4c, the energy efficiency of the ball specimens generally decreases with both the input energy and the temperature. This trend is caused by the increase of the thermally induced micro-cracks, which reduces the energy for creating the new fractures during the dynamic loading.

Conclusion

The LG spherical specimens heat-treated under five temperatures were characterized via the CT values. The dynamic ball compression test was conducted at five input energy levels. The results indicate that the dynamic indirect tensile strength increases with the loading rate for a given temperature. The failure mode of specimen can be categorized as fragmentation and pulverization. Moreover, the energy efficiency of each group of ball specimens generally decreases with the input energy.

Acknowledgement The current work was funded by the Natural Science Foundation of China (NSFC) under Grant Nos. 51704211, 51879184.

References

1. Tavares, L.M.: Breakage of single particles: Quasi-Static. In: Salman, A.D., Ghadiri, M., Hounslow, M. (eds.) Handbook of Powder Technoloy, pp. 3–68. Elsevier, Amsterdam (2007)
2. Yin, T., Li, X., Xia, K., Huang, S.: Effect of thermal treatment on the dynamic fracture toughness of laurentian granite. Rock Mech. Rock. Eng. **45**(6), 1087–1094 (2012)
3. Song, B., Chen, W.: Loading and unloading split Hopkinson pressure bar pulse-shaping techniques for dynamic hysteretic loops. Exp. Mech. **44**(6), 622–627 (2004)

Chapter 17
Effect of Confining Pressure on the Dynamic Mode II Fracture Toughness of Rocks

Wei Yao, Tony Zhang, and Kaiwen Xia

Abstract The dynamic shear failure of rocks with confinements is important in rock engineering and it is thus desirable to quantify the dynamic Mode II fracture toughness of rocks under confining conditions. This paper presents a punch-through shear (PTS) method to measure such material parameter of rocks under different confining pressures. A split Hopkinson pressure bar system with a Hoek cell is used to exert the dynamic PTS tests. The dynamic PTS specimen is a 50 mm diameter and 30 mm long cylinder with two 10 mm-deep circular notches at both ends. The finite element method is used to obtain equations calculating Mode II fracture toughness. The validity and applicability of the proposed method are demonstrated via the dynamic PTS tests of an isotropic and fine-grained Fangshan marble (FM) under five confining pressures. The PTS specimens are punched into a short rod and a hollow cylinder. The dynamic Mode II fracture pattern of the recovered FM are analyzed using the X-ray micro-CT technique. The results show that the rock specimen failure is shear dominant and the Mode II fracture toughness of FM increases with the loading rate under a certain confining pressure and increases with the lateral confinement at a given loading rate.

Keywords Mode II fracture toughness · Punch-through shear method · SHPB · Confinement · FEM

Introduction

Shear fracturing and mixed mode failure often occur in rock structures, resulting from the complicated mutual effect between tensile and shear fractures. Further, in many underground rock engineering applications, e.g., deep rock excavation and geothermal exploitation, rocks with high in-situ stresses may be dynamically failed. Hence, it is necessary to determinate the dynamic Mode II fracture toughness K_{IIC} of rocks over different confinement levels. Many investigations have revealed that the static K_{IIC} of rocks is intensely dependent on the confinement. To our best knowledge, there is only one experimental study in the open literature that has been conducted on the determination of the dynamic K_{IIC} of rocks with confining pressures [1]. Among the methods for measuring the K_{IIC}, the punch-through shear (PTS) test is currently popular since the failure in PTS specimen is shown to be dominant in mode II [2]. As a result, the International Society for Rock Mechanics and Rock Engineering (ISRM) has recently accepted the PTS method as the suggested method for measuring the static K_{IIC} of rocks [2]. Another important merit of the PTS specimen is that it facilitates in the measurement of the K_{IIC} with confinements. Therefore, this work introduces a modified PTS method to measure the dynamic K_{IIC} of rocks with lateral confining pressure.

Experimental Methodology

Fangshan marble (FM) from Beijing, China is selected in this study to conduct the proposed dynamic PTS tests with confinement because it has fine grains and homogeneous. According to the ISRM recommended static PTS approach for mode II fracture [2], a valid dynamic PTS specimen geometry has been proposed in our previous study for dynamic tests without confinement [3]. Hence, the same PTS specimen geometry is designed in this study for the dynamic tests with confinement except for the outer diameter, as shown in Fig. 17.1a, b. To fit the inner diameter of the Hoek cell used for applying confinement pressure, the outer diameter of the PTS specimen in this study is changed into 54 mm, which is 4 mm

W. Yao · T. Zhang · K. Xia (✉)
Department of Civil and Mineral Engineering, University of Toronto, Toronto, ON, Canada
e-mail: kaiwen.xia@utoronto.ca

L. E. Lamberson (ed.), *Dynamic Behavior of Materials, Volume 1*, Conference Proceedings of the Society for Experimental Mechanics Series, https://doi.org/10.1007/978-3-030-30021-0_17

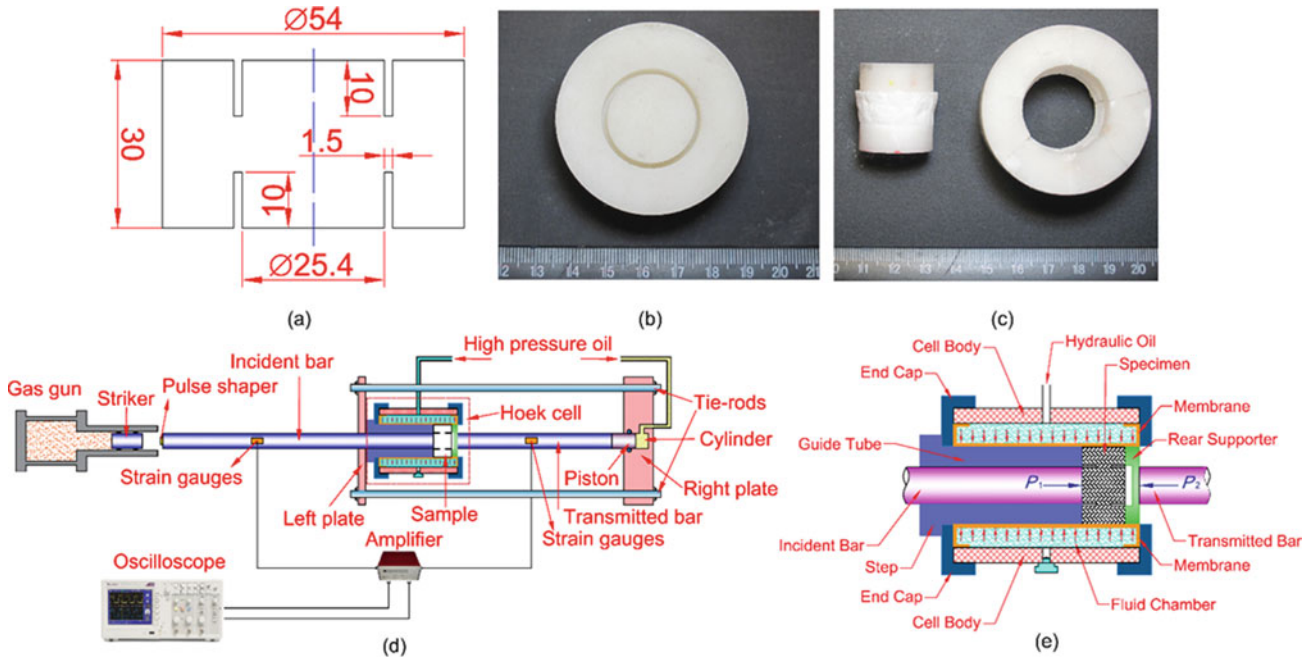

Fig. 17.1 (**a**) The dimensions of the dynamic PTS specimen and a typical (**b**) original and (**c**) tested PTS specimen; (**d**) The triaxial-SHPB system and (**e**) the specimen holder and Hoek cell for dynamic PTS tests with confinement

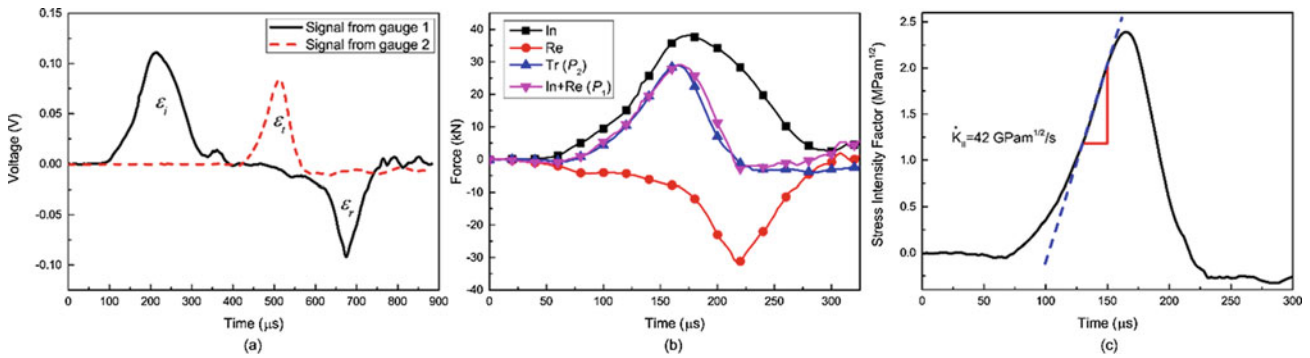

Fig. 17.2 (**a**) original three waves, (**b**) dynamic force history and (**c**) SIF-time curve for a typical dynamic PTS experiment

bigger than that of both the static [2] and previous dynamic [3] PTS specimen. A slight increment of outer diameter is reasonable for a valid K_{IIC} measurement in the dynamic PTS tests because it has been proven that the K_{IIC} obtained from the PTS test is almost independent of the outer diameter when other dimensions of the PTS specimen are constant [2]. As a further investigation of the dynamic PTS method without confinement, the split Hopkinson pressure bar (SHPB) system (Fig. 17.1d) was modified to obtain the dynamic K_{IIC} of rocks in this study [3]. The confining pressure is uniformly acted on the side surface of the PTS specimen by using a Hoek cell. The axial compressive pre-stress is acted on the outer ring part of the dynamic PTS specimen to ensure that the sample assembly maintains intact when the high pressure is applied through the Hoek cell. The small contact area between the rear supporter and the membrane of the rear supporter (Fig. 17.1e) is necessary to diminish the frictional effect. Further, the incident bar can move freely, providing dynamic loading to the PTS specimen.

With the pulse shaping technique [4], the non-dispersive sinusoidal pulse is obtained in Fig. 17.2a. The dynamic force equilibrium ($P_1 \approx P_2$) on two ends of the PTS samples with the confinement (Fig. 17.2b) is effectively attained before the peak of these two forces, which is also synchronized with the failure point of the PTS specimen [3]. It further approves that the design for the dynamic PTS tests with confinement successfully minimizes the friction between the sample and the membrane in this study. The dynamic stress intensity factor (SIF) K_{II} (MPa $m^{1/2}$) can be derived by $K_{II}(t) = \eta\, P(t) + \lambda\, p_c$, where $P(t)$ is the axial dynamic loading history (MPa), p_c is the confining stress (MPa). The geometry parameters η and λ are determined via the displacement extrapolation technique (DET) along with a finite element analysis (FEA) [2]. In this

study, $\eta = 0.04192\ \mathrm{m}^{1/2}$ and $\lambda = -5.6 \times 10^{-3}\ \mathrm{m}^{1/2}$ for the new dynamic FM PTS specimen geometry. The maximum value of K_{II} is the dynamic K_{IIC} of the PTS specimen and the loading rate for the PTS specimens is calculated through the slope (the dashed line in Fig. 17.2c) of the nearly linear increasing region in the SIF-time curve during the dynamic loading period.

Analysis

Figure 17.1c shows the soft-recovered PTS specimen, which is broken in a short bar and a hollow cylinder with few visible radial cracks. The fracture patterns inside the recovered dynamic PTS specimens from the micro-CT images are shown in Fig. 17.3. Since the main facture always commences from the upper notch, the "doughnut fracture" sometimes formed at the lower notch has negligible impact to the SIF of the main fracture commencement. Moreover, the wing crack is initiated from the inner upper notch and finally ceases at the shear zone [2]. Therefore, the main fracture in the dynamic PTS test with the confinement is a primary mode II fracture. Further, the wing cracks are vanishing and the "doughnut fractures" appear as the confining pressure increases. This phenomenon may be caused by the different static stress states around the notch tips due to the increasing confining pressures. Moreover, the correlation between the dynamic K_{IIC} of FM and loading rates under confining pressures is demonstrated in Fig. 17.4. It shows that, under a given lateral confinement, the K_{IIC} increases with the loading rates, showing that the K_{IIC} of FM has strong loading rate dependence. Another important observation is that at a specified loading rate, the K_{IIC} enhances as the lateral confinement. This trend is also observed about the static K_{IIC} of other rocks under confining pressures [2].

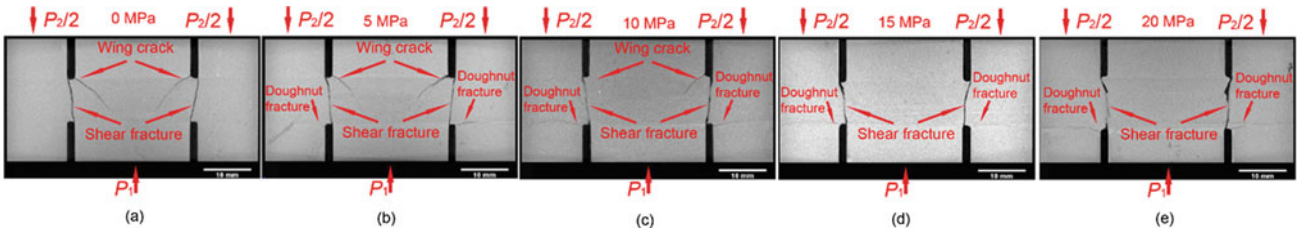

Fig. 17.3 The fractures in the specimen over the similar loading rates and different confining pressures

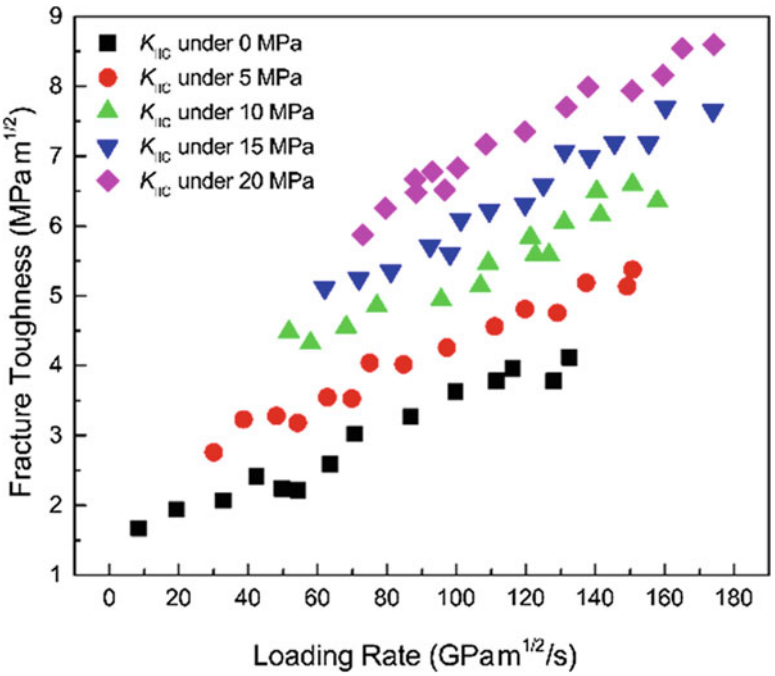

Fig. 17.4 Dynamic fracture toughness for FM with various confining pressures

Conclusion

The dynamic Mode II fracture toughness of rocks over various confining pressures was investigated through a dynamic punch-through shear method. The rock specimen was punched and broke into a short bar and a hollow cylinder. The wing cracks are vanishing and the "doughnut fractures" appear with the increment of confining pressure. Moreover, the main fracture is primarily a Mode II fracture. The K_{IIC} of Fangshan marble at a specified confining pressure rises as the loading rate. Another important observation is that the K_{IIC} at a given loading rate rises as the lateral confining pressure.

Acknowledgment Funding was provided by the Natural Sciences and Engineering Research Council of Canada (NSERC) through the Discovery Grant No. 72031326.

References

1. Lukić, B., Forquin, P.: Experimental characterization of the punch through shear strength of an ultra-high performance concrete. Int. J. Impact Eng. **91**, 34–45 (2016)
2. Backers, T., Stephansson, O.: ISRM Suggested Method for the Determination of Mode II Fracture Toughness. In: Ulusay, R. (ed.) The ISRM Suggested Methods for Rock Characterization, Testing and Monitoring: 2007–2014 [S], pp. 45–56. Springer International, New York City (2015)
3. Yao, W., Xu, Y., Yu, C., Xia, K.: A dynamic punch-through shear method for determining dynamic Mode II fracture toughness of rocks. Eng. Fract. Mech. **176**, 161–177 (2017)
4. Zhou, Y.X., Xia, K., Li, X.B., Li, H.B., Ma, G.W., Zhao, J., Zhou, Z.L., Dai, F.: Suggested methods for determining the dynamic strength parameters and mode-I fracture toughness of rock materials. Int. J. Rock Mech. Min. Sci. **49**, 105–112 (2012)

Chapter 18
A Viscoelastic-Viscoplastic Characterization with Time Temperature Superposition for Polymer Under Large Strain Rates

V. Dorleans, F. Lauro, R. Delille, D. Notta-Cuvier, and E. Michau

Abstract In the sectors of activity such as the automotive industry, polymers are definitively present into the different components of the vehicle. These materials may be subjected to high loads such as crash impact. Therefore, they have to meet strong requirements in terms of safety regulations. It is so important to know and to anticipate the behavior of the material in a wide strain rate and temperature range in order to predict the risk of failure.

In this paper, some results of experimental research are proposed about the dependence between the strain rate and the temperature for viscoelastic and viscoplastic behavior in the perspective to build an efficient experimental procedure of behavior characterization. The studied material is a 15 wt% mineral (talc) filled and impact modified copolymer propylene ethylene.

Keywords Polymer · Strain rate dependence · Time temperature superposition

Introduction

This study focuses on a copolymer propylene ethylene, which is 15% mineral (talc) filled and impact modified. (P/E-MD15 impact modified). This material is used in the design of injection-moulded top covers of dashboard. To characterize this material in a wide strain rate range (from 10^{-5} to 300 s^{-1}) and at different temperatures (from −30 °C to +85 °C), which corresponds to the severe loads imposed to the material during the airbag deployment, an important test campaign is needed. The final objective is to predict the failure behavior of the material by taking into account its fragile or ductile behavior following to static and dynamics loadings for different temperatures. The aim of this work is then to reduce the experimental test campaign of characterization by coupling the adequate polymer model to the time temperature superposition principle.

The different experimental tests carried out on this material have shown a viscoelastic-viscoplastic behavior, sensitive to the hydrostatic pressure, possibly affected by damage but also strongly temperature dependent. In order to take all observed behaviors specificities into account into accurate numerical simulations, the model developed by Balieu [1, 2] is used. This model allows taking the viscoelasticity-viscoplasticity behavior with a non-associative approach and a non-local damage model at room temperature into account. The identification of all the parameters of the model is carried out mainly thanks to direct procedure with specific method developed by Epee [3, 4].

In this paper, the influence of the coupling between the strain rate and the temperature on the material behavior is highlighted and validated experimentally by using the time temperature superposition principle for small and large deformations. A modified Balieu's model is then implemented with these results and allows the definition of a new experimental procedure with a reduced test campaign.

V. Dorleans
University Polytechnic Hauts de France, LAMIH, UMR CNRS 8201, Valenciennes, France

Faurecia Interior System, Méru, France

F. Lauro (✉) · R. Delille · D. Notta-Cuvier
University Polytechnic Hauts de France, LAMIH, UMR CNRS 8201, Valenciennes, France
e-mail: franck.lauro@uphf.fr

E. Michau
Faurecia Interior System, Méru, France

L. E. Lamberson (ed.), *Dynamic Behavior of Materials, Volume 1*, Conference Proceedings of the Society for Experimental Mechanics Series, https://doi.org/10.1007/978-3-030-30021-0_18

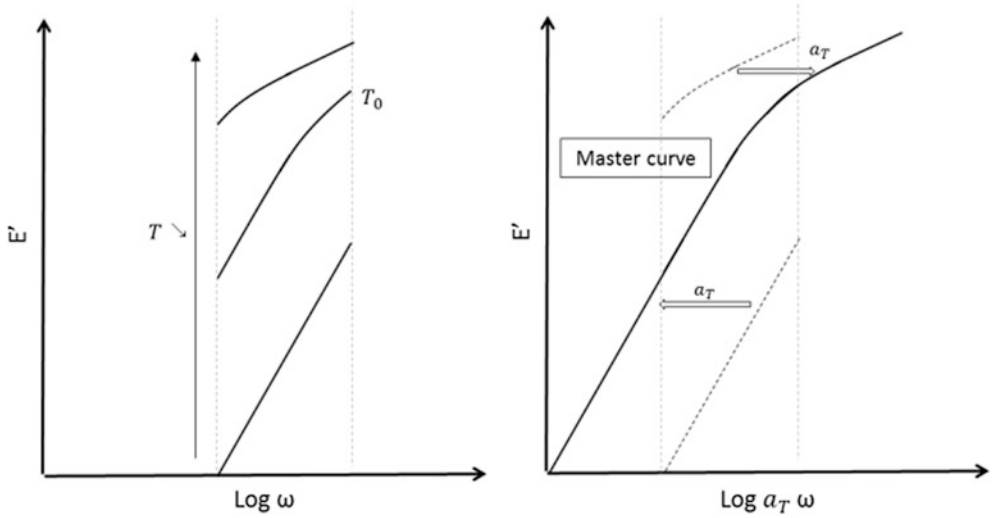

Fig. 18.1 Frequency sweep for polymer

Time Temperature Superposition

The time temperature superposition is based on a relation between the strain rate and the temperature for viscoelasticity domain for polymers. Nowadays, it has been verified for PA [5, 6], PMMA [7] or PP [8], e.g., A master curve giving the storage modulus versus the frequency (related to strain rate) is obtained by applying a shift factor determined by dynamic mechanical analysis (Fig. 18.1) and a mathematical model like Williams-Landel-Ferry, Vogel or Arrhenius [8–12].

Experiments

The viscoelastic properties of the P/E-MD15 impact modified, are obtained by using an Instron Electropulse E3000 machine in a frequency range 0.05 to 30 Hz at different temperatures from −30 °C to +80 °C and by applying a sinusoidal displacement (loading/unloading tensile cycles).

The following figure shows the evolution of the storage modulus versus the frequency for temperatures steps of 10 °C (Fig. 18.2).

In the frequency range studied, the storage modulus increases linearly of 300 MPa whatever the temperature. The influence of the strain rate on material viscoelastic properties is therefore independent of the temperature.

The reference temperature (T_{ref}) chosen is 23 °C. Then for each temperature, a shift factor is defined in order to build the master curve that leads to results exposed in Fig. 18.3.

The shape of the master curve is linear. It is thus easy to define a mathematical relation between the shift factors and the temperatures. It is presented in the following form.

$$a_T(T) = \exp(-C(T - T_{ref})) \tag{18.1}$$

T is the current temperature and T_{ref} the reference temperature. C is a mathematical constant, here identified at 0.25.

In addition to DMA, some elastic modulus measurements have been done on tensile specimens. As the loss modulus is low, the Young modulus is directly compared to the storage modulus and the results (Fig. 18.4) highlight the efficiency of the time temperature equivalence principle for this material into the viscoelastic domain.

The time temperature equivalence is now extended to the viscoplastic domain by keeping the same shift factor as the one determined in the viscoelastic domain. To validate this approach some uniaxial tensile tests are carried out at different strain rates (from $5e^{-3}s^{-1}$ to $30s^{-1}$) in a temperature range between −30 °C and +85 °C.

For the quasi-static loadings, the test device used is the same as the DMA tests: the electromagnetic device (Instron E3000) with a 3 kN cell force. A hydraulic high speed device (Instron VHS) is used for the dynamic loadings with a 5 kN cell force.

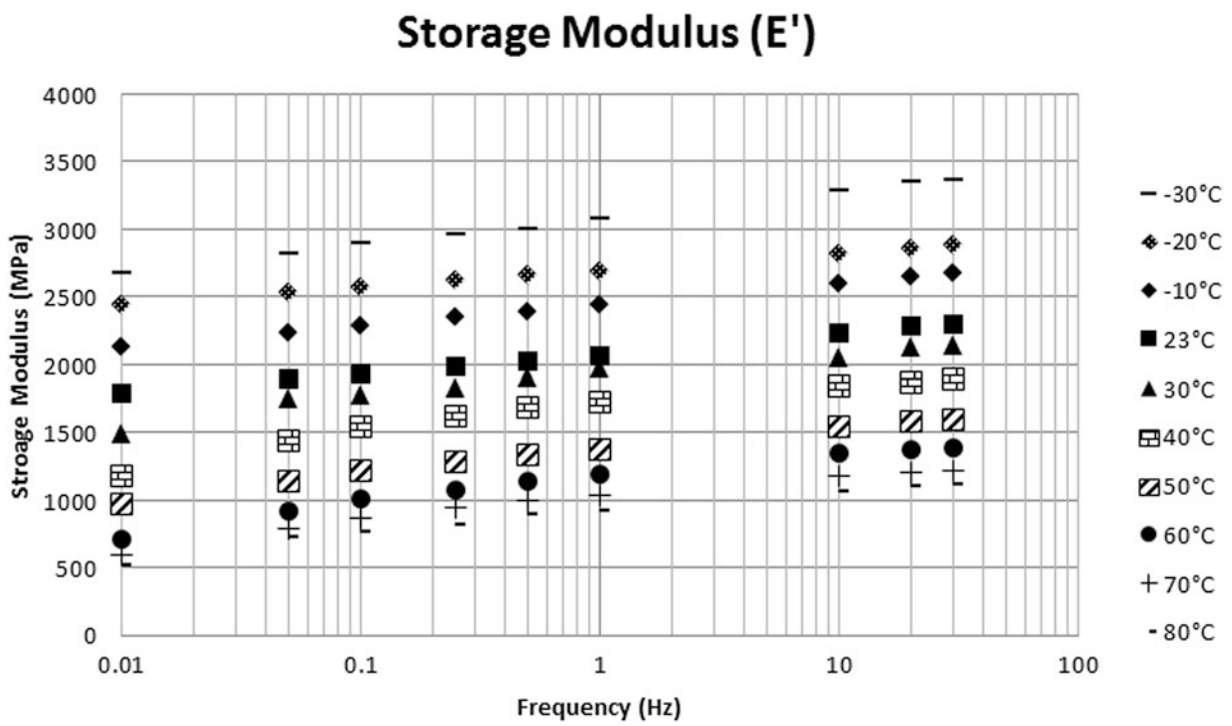

Fig. 18.2 Storage modulus at different temperatures versus frequency

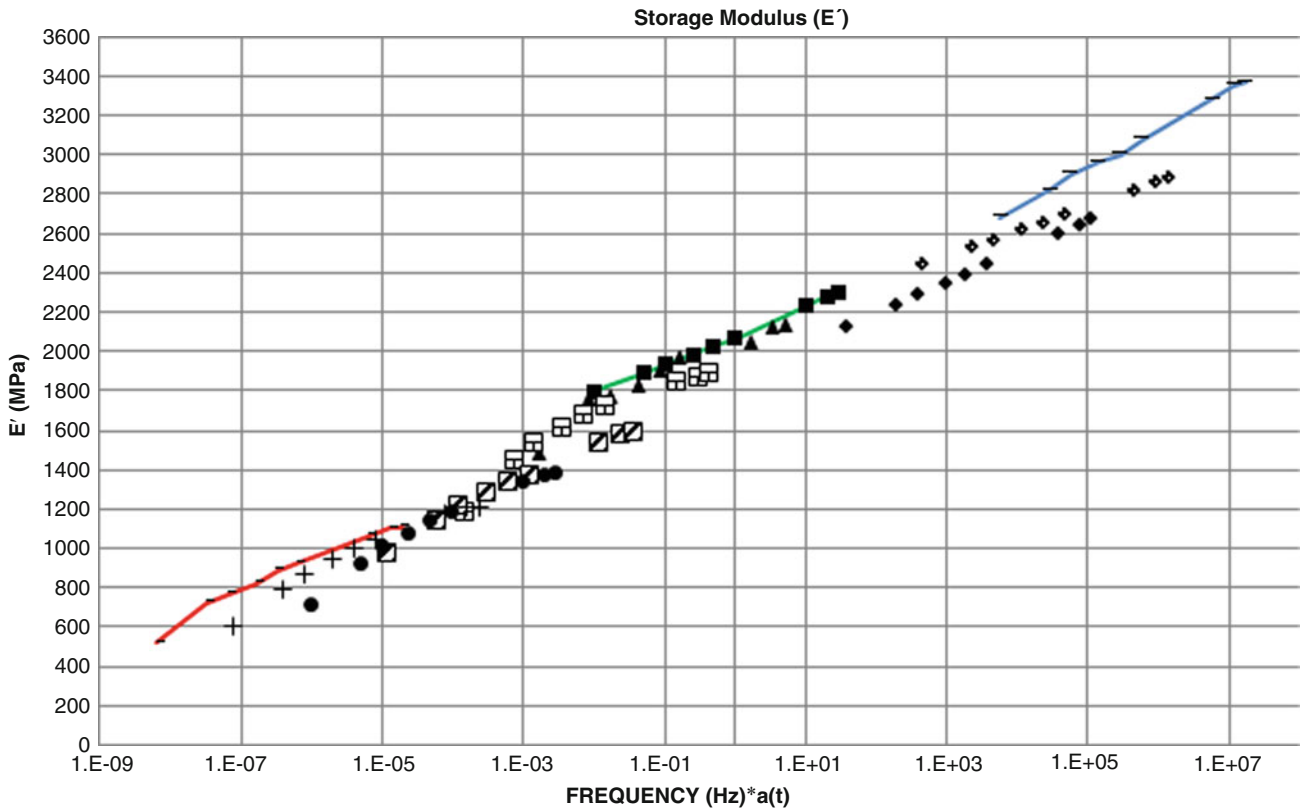

Fig. 18.3 Storage modulus of the master curve versus frequency range*shift factors

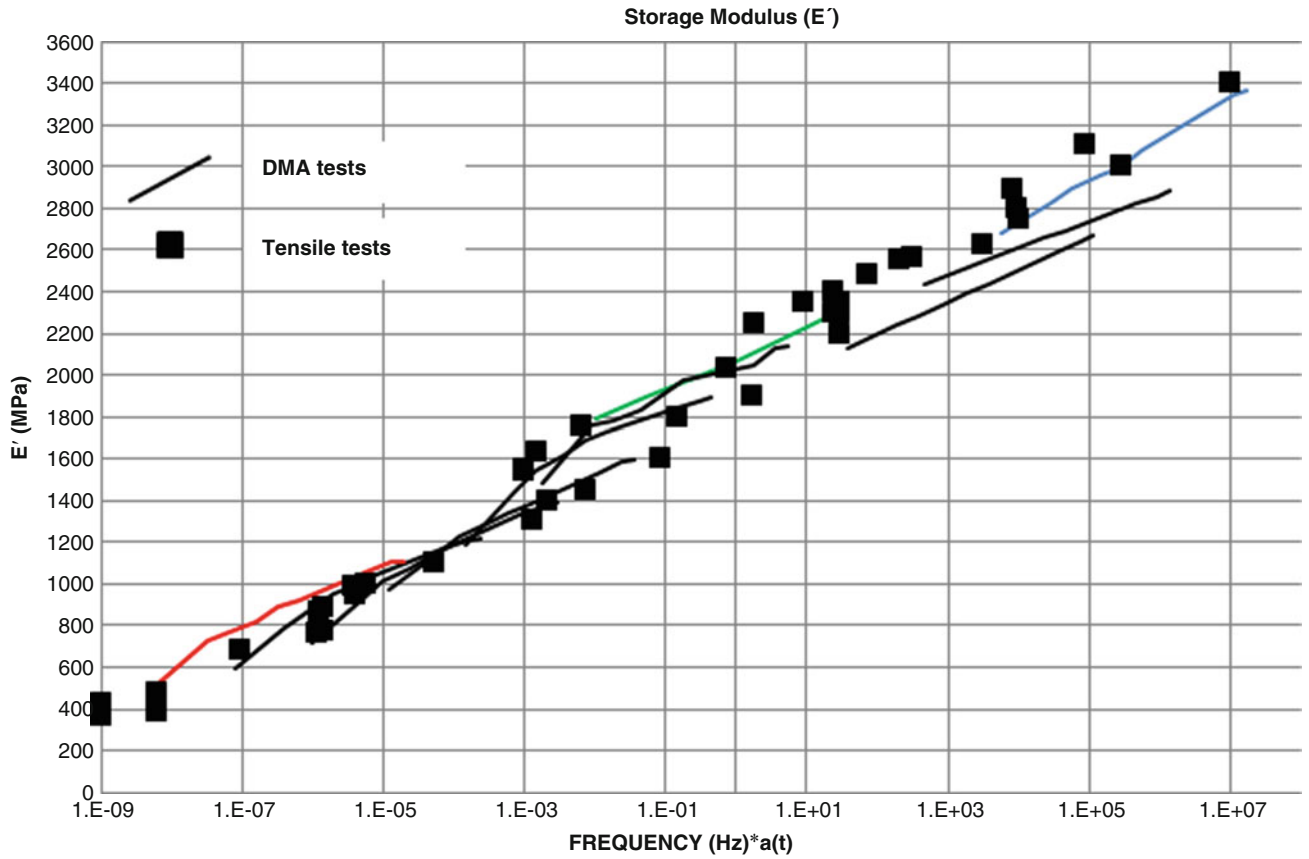

Fig. 18.4 Evaluation of the elastic modulus from two test methods: DMA and tensile tests

To measure the displacements fields on the specimen, the 2D digital image correlation technique is employed with a high speed camera (Photron APX 3000) and also specific technics for patterns building (black and white paint for quasi-static/dynamic and hot temperatures and grease with alumina balls for the cold temperatures).

The results of uniaxial tensile tests for the mini and maxi of the temperature range (−30 °C and 85 °C) at various strain rates are shown above (Figs. 18.5 and 18.6).

The stress increases non linearly with the strain rate and the temperature. At high temperature (+85 °C), the material shows highly ductile behavior. At low strain rate, the deformation level can exceed 100% of plastic strain. The presence of elastomer in the compound of the material is responsible for this high capability of deformation. However at low temperature (−30 °C), the material is brittle. At high strain the level of plastic strain doesn't exceed 7%. Concerning the hardening slope, is it relatively similar for all the loadings.

To characterize the viscoplastic behavior of the material, the SEE method is used [3]. This method allows building a behaviour surface: true stress versus true strain versus strain rate from uniaxial tensile tests. By cutting the surface obtained at the desired strain rate, the behavior law at constant strain rate is obtained. The time temperature equivalence is then carried out to introduce the results of all the tests in the SEE method by using the viscoelastic shift factor (Fig. 18.7).

The viscous behaviour law which best describes current material behavior is the modified G'Sell-Jonas model one (Eq. 18.3) [13]. σ_t is the initial yield stress, $\dot{\kappa_0}$ is the initial strain rate reference, κ is equivalent plastic strain, and n a material parameter,

$$\sigma_y^v = (\sigma_t + R(\kappa)) \left(\frac{\dot{\kappa}}{\dot{\kappa_0}}\right)^n \tag{18.2}$$

where the hardening variable $R(\kappa)$ is defined by:

$$R = Q_1\kappa \quad \exp(-b_1\kappa) + Q_2(1 - \exp(-b_2\kappa)) + b_3\kappa^3 + b_4\kappa^2 + b_5\kappa \tag{18.3}$$

with Q_i and b_i material parameters,$\forall_i$.

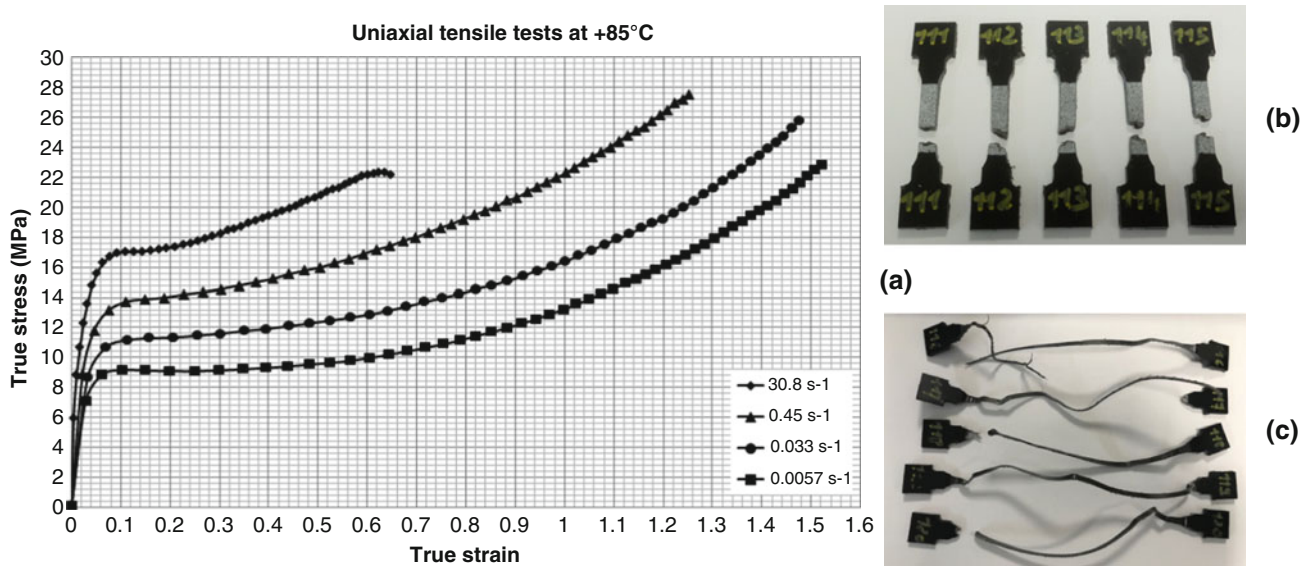

Fig. 18.5 Uniaxial tensile tests at +85 °C (**a**). Samples after tests at 0.45 s^{-1} (**b**). Samples after tests at 30.8 s^{-1} (**c**)

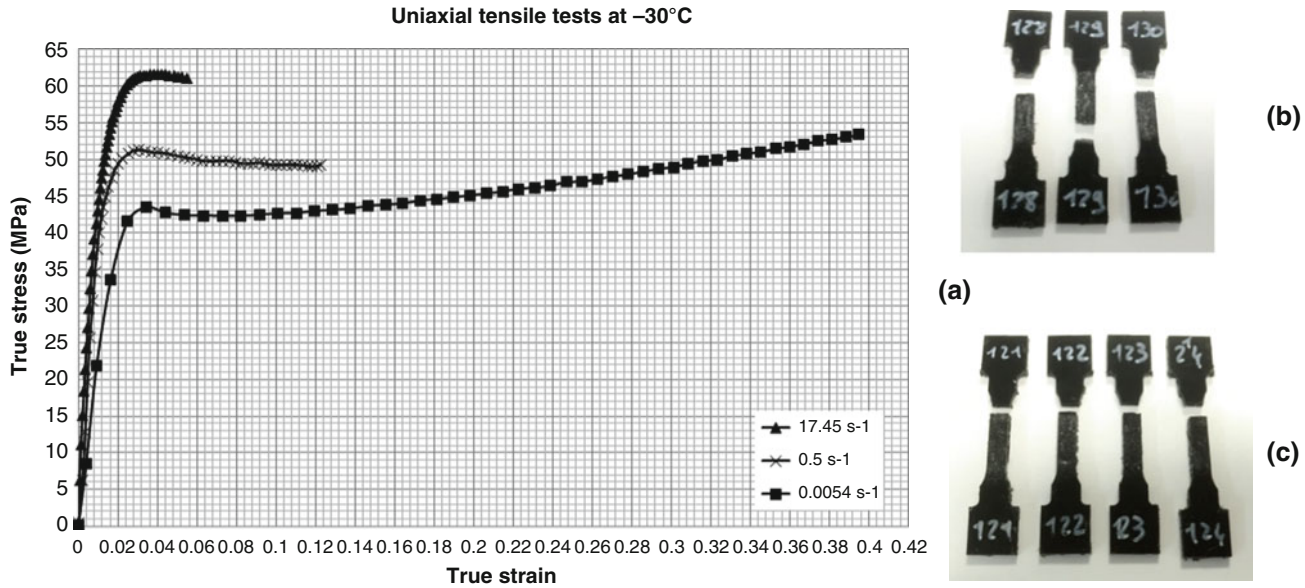

Fig. 18.6 Uniaxial tensile tests at −30 °C (**a**). Samples after tests at 0.62 s^{-1} (**b**). Samples after tests at 0.024 s^{-1} (**c**)

The 3D surface presented on the graph below describes the complete behaviour of the P/E-MD15 impact modified in the temperature range between −30 °C and +85 °C at different strain rates. The identification of the parameters for the behavior model has been done through an optimization process with Matlab tool.

To validate the extension of the time temperature principle on the viscoplastic domain for this large range of temperature and strain rate, some temperature/strain rate couples are chosen as examples for numerical simulations and results are compared to experimental data obtain by uniaxial tensile tests (Figs. 18.8 and 18.9).

The different tested couples clearly show that the time temperature superposition is also validated for viscoplasticity with the same coefficient as viscoelasticity. A tensile test done at high strain rate at room temperature gives the same result than a tensile test at low strain rate at low temperature. The phenomenon is also observed between room temperature and hot temperature.

From these results an interesting experimental procedure is then defined. The whole viscoelastic and viscoplastic behavior law for such polymer could therefore be determined by using DMA to identify the viscoelastic behavior and the shift parameter and a single tensile test at room temperature. The experimental campaign is then consequently strongly reduced.

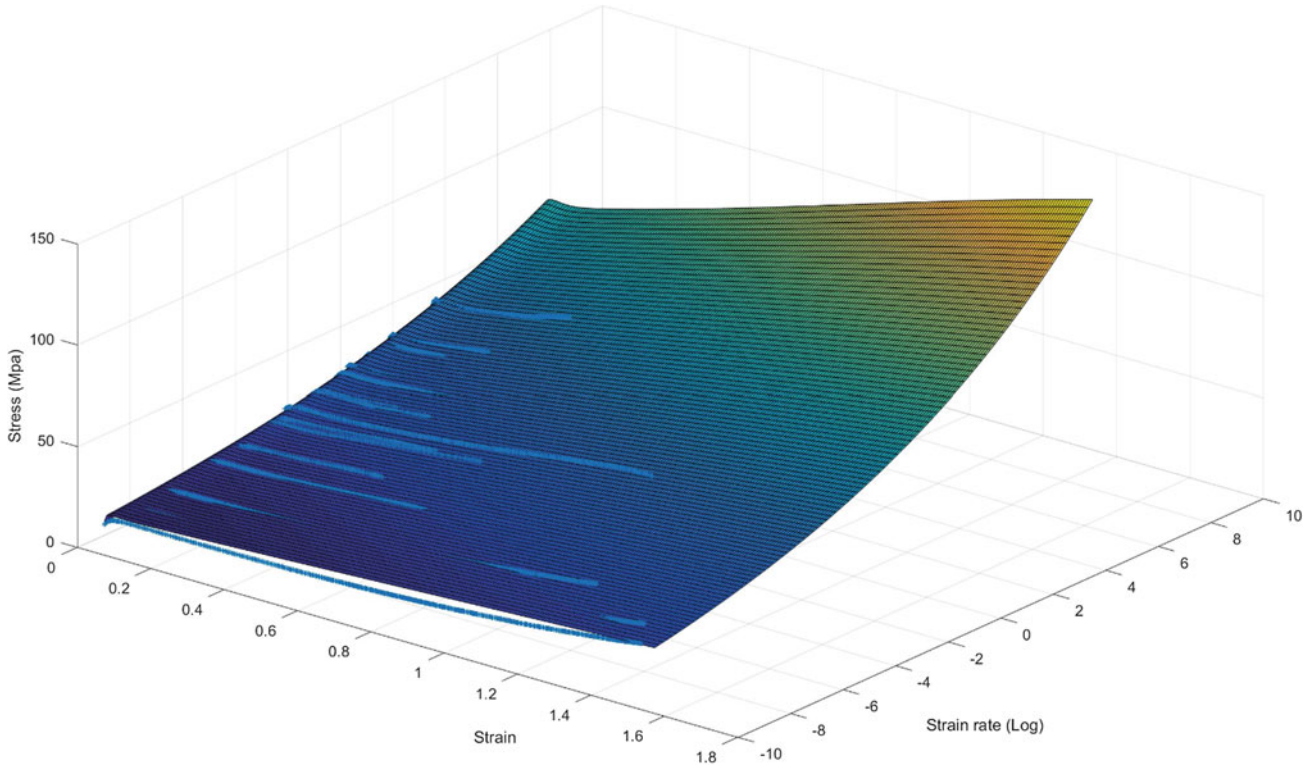

Fig. 18.7 3D behavior surface of the P/E-MD15 impact modified

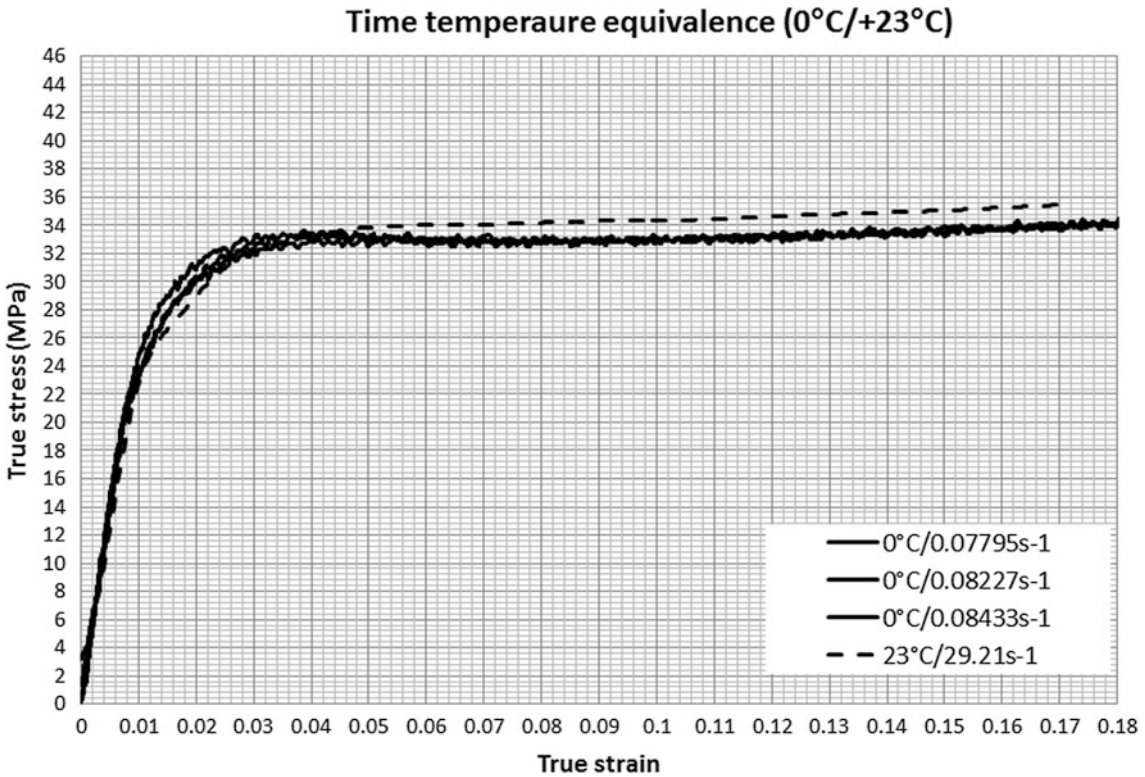

Fig. 18.8 Couple tested at 0° and +23 °C

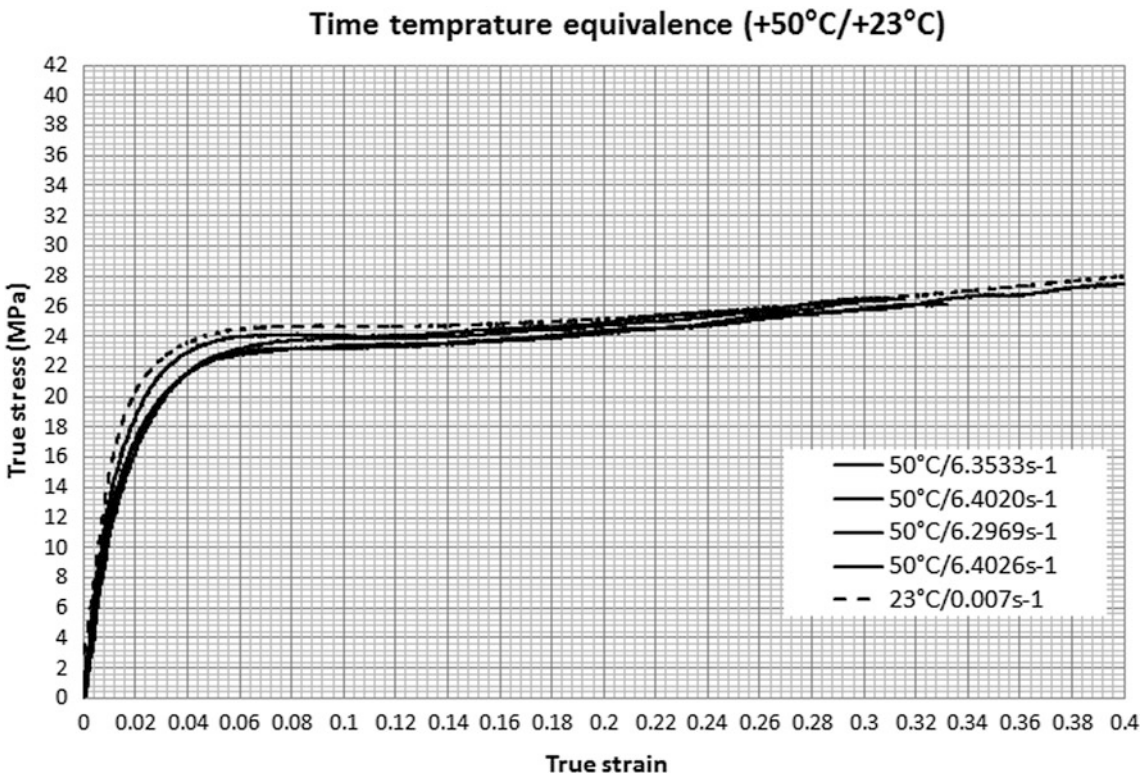

Fig. 18.9 Couple tested at +50° and +23 °C

Conclusion

In this paper we have shown that the principle of time temperature superposition is applicable for the complete behaviour of the studied material. On the basis of DMA, a coefficient C has been identified and used for viscoplasticity modelling. The key advantage of this method is to reduce significantly the number of tests for material characterization in a wide temperature and strain-rate range. It allows reaching in numerical predictions some temperatures or strain rates sometimes that can not be achieved by classical test devices.

Endly it will be interesting to investigate if the time temperature superposition can be also applied for failure prediction.

Acknowledgements The present work has been supported by the LAMIH UMR CNRS 8201, the research department of the University Polytechnic Hauts-de-France and the Faurecia Interior System Company. I would like to express my sincere gratitude to all of them.

References

1. Balieu, R., Lauro, F., Bennani, B., Delille, R., Matsumoto, T., Mottola, E.: A fully coupled elastoviscoplastic damage model at finite strains for mineral filled semi-crystalline polymer. Int. J. Plast. **51**, 241–270 (2013)
2. Balieu, R., Lauro, F., Bennani, B., Matsumoto, T., Mottola, E.: Non-associated viscoplasticity coupled with an integral-type non local damage model for mineral filled semi- crystalline polymers. Comput. Struct. **134**, 18–31 (2014)
3. Lauro, F., Bennani, B., Morin, D., Epee, A.: The SEE method for determination of behaviour laws for strain rate dependant material: Application to polymer material. Int. J. Impact Eng. **37**, 715–722 (2010). impact Loading of Lightweight Structures
4. Epee, A., Lauro, F., Bennani, B., Bourel, B.: Constitutive model for a semi-crystalline polymer under dynamic loading. Int. J. Solids Struct. **48**, 1590–1599 (2011)
5. Aurelien, M.-P., Erwan, B., Jerome, B., Jean-Luc, B., Noëlle, B.: A thermo-mechanical large deformation constitutive model for polymers based on material network description: Application to a semi-crystalline polyamide 66. Int. J. Plast. **67**, 102–126 (2015)
6. Noëlle, B.: New constitutive modeling for time-dependent mechanical behavior of polymers close to glass transition: Fundamentals and experimental validation. J. Appl. Polym. Sci. **125**(6), 4390–4401 (2012)
7. Wortmann, F.-J., Schulz, K.V.: Stress relaxation and time/temperature superposition of polypropylene fibres. Polymer. **36**(2), 315–321 (1995)

8. Armelle, R.: Ph.D. thesis. Étude de la modification des propriétés rhéologiques linéaires et non linéaires par ingénierie moléculaire. Vers le contrôle des propriétés adhésives de matériaux autocollants.www.theses.fr. Submitted on 12 Dec 2011
9. Li, R.: Time-temperature superposition method for glass transition temperature of plastic materials. Mater. Sci. Eng. **A278**, 36–45 (2000)
10. Williams, M.L., Landel, R.F., Ferry, J.D.: The Temperature Dependence of Relaxation Mechanisms in Amorphous Polymers and Other Glass-forming Liquids. Temperature dependence of relaxation mechanisms 3701 [Contribution from the department of chemistry, University of Wisconsin]. (1955)
11. Ljubic, D., Stamenovic, M., Smithson, C., Nujkic, M., Medo, B., Putic, S.: Time—temperature superposition principle—Application of WLF equation in polymer analysis and composites. Scientific paper. UDC:629.179.13:678.06
12. Pesce, J.J.: Influence de l'orientation moléculaire d'un polymère fondu en écoulement sur l'anisotropie induite des propriétés à l'état solide
13. G'Sell, C., Jonas, J.: Determination of the plastic behaviour of solid polymers at constant true strain rate. J. Mater. Sci. **14**, 583–591 (1979)

Chapter 19
Tensile Hopkinson Bar Analysis of Additively Manufactured Maraging Steel

Nicholas E. Taylor, David M. Williamson, Christopher H. Braithwaite, and Sarah J. Ward

Abstract Maraging steel is a hard, tough steel. These properties make it desirable in mechanically demanding applications. However, it is also expensive and difficult to work. Additive manufacture is therefore attractive: it reduces both the amount of material required, and the amount of machining required, to construct a given object. Additively manufactured maraging steel is commercially available, but the selective laser melting technique used to produce it may affect the material's mechanical properties.

The tensile Hopkinson bar is a useful system for applying a well-defined tensile loading pulse at a strain rate of order 1000 per second. Calibration and data analysis for the system are not straightforward, however.

This work presents the design, calibration and analysis used to recover stress and strain data for maraging steel loaded to failure using a tensile Hopkinson bar. Conventional wrought maraging steel, additively manufactured maraging steel and other materials were studied.

Keywords Tensile failure · High speed video · Dynamic failure · Strain extraction · Necking

Introduction

The mechanical properties of materials vary with deformation rate [1]. The high-rate deformation and failure behavior of materials are often relevant to system design. High-rate materials testing is a useful input to modelling at those rates. The experimental techniques described here have already been used to inform a rate-dependent model of maraging steel [2].

High-rate materials testing presents a few challenges that quasi-static testing avoids. Most notably, it can be difficult to discriminate between the dynamic response of the testing equipment and that of the material under test. One testing apparatus that overcomes this problem is the split Hopkinson pressure bar (SHPB), also known as the Kolsky bar [3]. In this system, the well-characterized apparatus is dynamically loaded. This transmits a well-defined loading pulse to the sample, and the sample response can be measured.

In compressive loading, the SHPB is a mature technique; subject to some reasonable assumptions, the output of strain gauges on the bars can be easily transformed into the stress and strain experienced by the sample. Tensile loading in an SHPB presents some difficulties, both mechanical and analytical. Here we address those difficulties.

Design

The first problem to be solved is that of sample mounting. In a compressive SHPB the sample rests in contact with the bars. This arrangement has the appealing feature that, to good approximation, the sample/system interface is planar. Measuring the bar strain, and hence the displacement of the bar ends, gives the sample length directly. This sample mount cannot, however, support tensile loading. A threaded sample, with a thin gauge section between the threads, was therefore used. This added its own complications: the transfer of strain from the bar to the threaded section, and thence to the gauge section of the sample, is not trivial. Figure 19.1 shows a typical compressive SHPB sample, compared with the tensile SHPB sample used in this work.

N. E. Taylor (✉) · D. M. Williamson · C. H. Braithwaite · S. J. Ward
Department of Physics, University of Cambridge, Cambridge, UK
e-mail: net20@cam.ac.uk

L. E. Lamberson (ed.), *Dynamic Behavior of Materials, Volume 1*, Conference Proceedings of the Society for Experimental Mechanics Series, https://doi.org/10.1007/978-3-030-30021-0_19

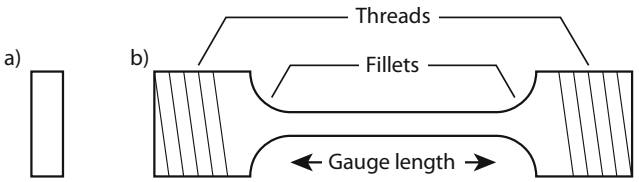

Fig. 19.1 Schematic of samples for (**a**) compressive and (**b**) tensile SHPB

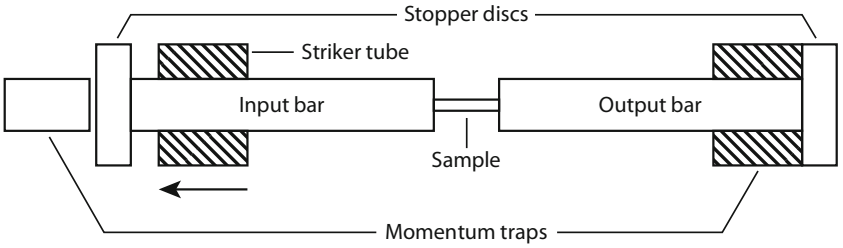

Fig. 19.2 Schematic of tensile split Hopkinson pressure bar. Gun omitted for clarity. Not to scale: actual length to diameter ratio of input and output bars approximately 150:1

The next problem is one of strain localization. While strain can localize in compression (see for example [4], or in a strict sense the entirety of dislocation theory) this is typically a microstructural effect: a scalar longitudinal strain can meaningfully be assigned to the whole sample. In tension, it is very common for strain to localize in a single "neck" region. This means that, even if the problem of strain transfer from the bar to the gauge section is solved, the overall strain of the gauge section is a poor indicator of the strain in the failing section.

The last problem is that of force equilibrium in the sample. The gauge region needs a high length-to-diameter ratio to achieve nearly uniform stress. Consequently, the wave travel time through the gauge region is of order microseconds. In practice for ductile metals failure is slow enough that force equilibrium is established before failure. This lack of equilibrium could present a problem for brittle samples, though.

The tensile SHPB itself is conceptually very similar to a compressive SHPB, except that the striker bar and momentum trap are tubes, and the striker bar is launched by an annular gun. Figure 19.2 shows a schematic of the system. One challenge with testing maraging steel was that its yield stress was approximately 2.5 times that of the grade 5 titanium[1] bars. To test a representative sample of the maraging steel the gauge diameter could not be smaller than 2.5 mm. The force required to yield such a sample in tension was close to that required to strip the threads in the input and output bars. Spiralock® threads were used to reduce stress localization in the bars [5].

Calibration

The elastic strain in the bars was measured using resistive semiconductor strain gauges. These gauges have suitable time and force resolution, but individual gauges vary significantly in their properties. It is therefore necessary to calibrate them. In a compressive SHPB, it is straightforward to apply a known impulse to the system and use this for calibration. The stopper discs complicate the mechanics so that we had no confidence in our ability to apply a known impulse. Therefore we used a photon Doppler velocimeter (PDV) [6] alongside strain gauges in experiments with no sample loaded. The time resolution of the PDV was inadequate for experiments on samples, but provided a known bar strain against which to calibrate the strain gauges.

Analysis

High-speed photography was used to image the sample's deformation. The camera used, a Vision Research Phantom v1610, was able to record 16 gigapixels per second. This meant that reducing pixel resolution directly increased frame rate, and hence temporal resolution of strain measurements. We therefore used two analysis techniques, with different camera configurations.

[1] 6% aluminum, 4% vanadium, balance titanium

The first imaged the entire gauge length and tracked the evolution of necking as the sample failed. This provided useful information for developing a constitutive model, but was not especially novel [7].

The second used a significantly reduced field of view to increase the camera's frame rate. The technique resembles that of [8], significantly modified to account for the camera's low resolution. While still imaging the entire length of the gauge section, the camera's vertical field of view was set to 32 pixels, the smallest possible. By careful lighting, small irregularities in the sample surface were highlighted. Vertically averaging the field of view then produced a streak image of the sample surface over time. Figure 19.3 illustrates these images.

Tracing streaks on this image using a zero-normalized sum-squared-differences system provided sample surface longitudinal displacement u as a function of position x and time t. In principle strain ε could be calculated using $\varepsilon = \frac{\mathrm{d}u}{\mathrm{d}x}$. However, in practice this was unacceptably noisy, and any filter broad enough to eliminate the noise also eliminated any strain localization. Instead a functional form of

$$\varepsilon = \ln\left\{m + \exp\left[-\left(\frac{x-\mu}{s}\right)^2\right]\right\}$$

for localized strain was chosen and fitted to the measured displacements. This gave acceptable results; Fig. 19.4 gives an example. Uncertainty was assessed by bootstrapping [9].

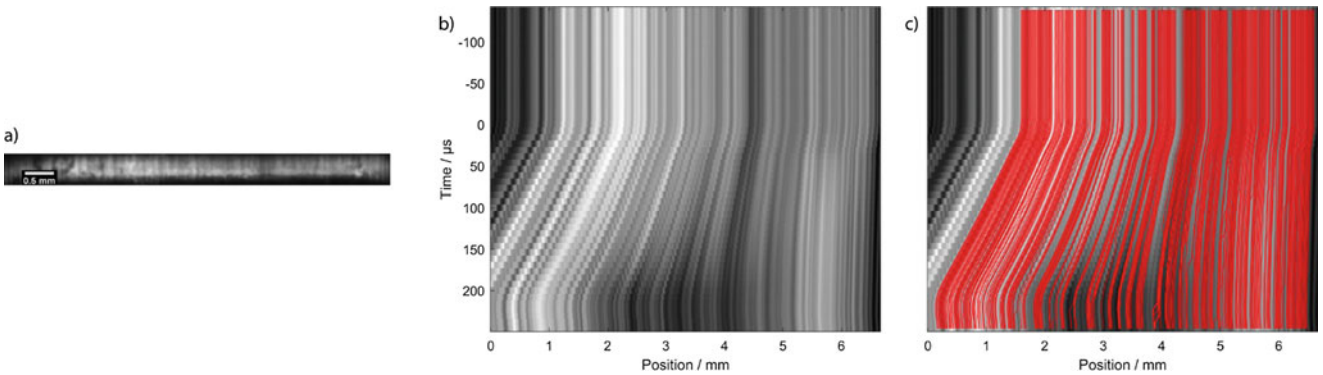

Fig. 19.3 Illustration of image processing on oxygen free high conductivity copper C103. (**a**) Camera field of view, (**b**) Streak image, (**c**) Streak image with traced flow lines

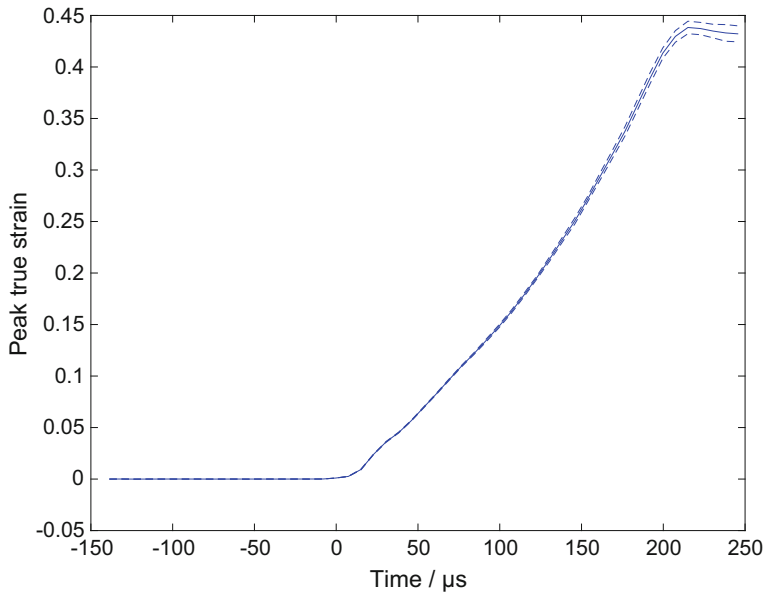

Fig. 19.4 Maximum true strain for C103 copper experiment shown in Fig. 19.3

Conclusion

A tensile split Hopkinson pressure bar can give useful quantitative information on the failure of metals in high-rate tension.

Acknowledgement This research was funded by QinetiQ. Peter Gould, Phil Church and Michael Lytwyn of QinetiQ are thanked for several helpful discussions.

References

1. Gray, G.T.: High-strain-rate deformation: mechanical behavior and deformation substructures induced. Annu. Rev. Mater. Res. **42**, 285–303 (2012). https://doi.org/10.1146/annurev-matsci-070511-155034
2. Church, P., Reynolds, M., Gould, P., Oakley, R., Harrison, N., Williamson, D., Braithwaite, C., Taylor, N.: Tensile properties of AM maraging steel. EPJ Web of Conferences. **183**, 01058 (2018). https://doi.org/10.1051/epjconf/201818301058
3. Gray, G.T.: Classic split Hopkinson pressure bar testing. In: Kuhn, H., Medlin, D. (eds.) *Mechanical Testing and Evaluation*, volume 8 of *ASM Handbook*, pp. 402–476. ASM International, Materials Park, OH (2000)
4. Timothy, S.P.: The structure of adiabatic shear bands in metals: a critical review. Acta Metall. **35**(2), 301–306 (1987). https://doi.org/10.1016/0001-6160(87)90238-0
5. Tremsin, A.S., Yau, T.Y., Kockelmann, W.: Non-destructive examination of loads in regular and self-locking Spiralock® threads through energy-resolved neutron imaging. Strain. **52**(6), 548–558 (2016). https://doi.org/10.1111/str.12201
6. Lea, L.J., Jardine, A.P.: Application of photon Doppler velocimetry to direct impact Hopkinson pressure bars. Rev. Sci. Instrum. **87**, 023101 (2016). https://doi.org/10.1063/1.4940935
7. Noble, J.P., Goldthorpe, B.D., Church, P., Harding, J.: The use of the Hopkinson bar to validate constitutive relations at high rates of strain. J. Mech. Phys. Solids. **47**, 1187–1206 (1999). https://doi.org/10.1016/S0022-5096(97)00090-2
8. Arthington, M.R., Siviour, C.R., Petrinic, N., Elliott, B.C.F.: Optical surface profile tracking for high-resolution strain measurement. Meas. Sci. Technol. **22**, 025304 (2011). https://doi.org/10.1088/0957-0233/22/2/025304
9. Press, W.H., Teukolsky, S.A., Vetterling, W.T., Flannery, B.P.: Numerical Recipes in C, 2nd edn. Cambridge University Press, New York (1992)., section 15.6

Chapter 20
Large-Diameter Triaxial Kolsky Bar for Evaluating Very-High-Strength Concrete

Brett Williams, William Heard, Bradley Martin, Colin Loeffler, and Xu Nie

Abstract The U.S. Army Engineer Research and Development Center (ERDC) uses quasi-static triaxial compression experiments as a basis to adjust its constitutive models to predict full-scale penetration events on hardened concrete structures. However, there is a fundamental knowledge gap between quasi-static and dynamic characterization of concrete specimens under complex stress states. Although triaxial Kolsky bars have been used previously for brittle materials, the bar diameter is typically in the range of 12–19 mm. In some cases, specimen sizes are much smaller than the bar such that dynamic failure is achieved. The inherent nature of concretes is such that they have substantial heterogeneity at this length scale; therefore, a larger diameter bar must be used to acquire bulk properties. To alleviate this problem, a state-of-the-art 50-mm-diameter triaxial Kolsky bar that operates with a maximum confining pressure of 200 MPa was used to perform initial experiments on a very-high-strength concrete (f_c' ~ 130 MPa). The focus of our current stage of study is to optimize specimen preparation techniques while establishing standard operating procedures for the large-diameter triaxial Kolsky bar.

Keywords Very-high-strength concrete · Kolsky bar · Triaxial loading · Dynamic increase factor · Hardened structures

Introduction

The Army relies heavily on hardened structures to protect critical personnel and infrastructure. The ERDC has developed modeling and simulation capabilities to provide reasonable predictions for penetration events into concrete structures. However, a fundamental knowledge gap still exists when trying to understand how loading rate and confinement effects are coupled during extreme loading events. Through the use of a novel large-diameter (50 mm) triaxial Kolsky bar at the ERDC, concrete response can be investigated with various combinations of strain rates and complex stress states.

Background

Dynamic triaxial experiments were pioneered in the 1970s [1, 2], with substantial improvements being made in 2010 as noted on a 12.7-mm-diameter triaxial Kolsky bar designed by Frew to characterize limestone specimens [3]. Frew's design was also implemented on a 19.0-mm triaxial Kolsky bar to assess dynamic confined properties of sand [4] and glass [5]. A limited study was performed on ultra-high performance concrete (UHPC) with a maximum particle size <600 μm [6]. However, a larger diameter bar is necessary for capturing bulk material response for cementitious materials with heterogeneities at larger length scales. The ERDC has recently acquired a 50-mm-diameter triaxial Kolsky bar for the purpose of quantifying the

B. Williams (✉)
U.S. Army Engineer Research and Development Center, Vicksburg, MS, USA

Department of Mechanical Engineering, Southern Methodist University, Dallas, TX, USA
e-mail: Brett.A.Williams@usace.army.mil

W. Heard
U.S. Army Engineer Research and Development Center, Vicksburg, MS, USA

B. Martin
Air Force Research Laboratory (RW), Eglin AFB, FL, USA

C. Loeffler · X. Nie
Department of Mechanical Engineering, Southern Methodist University, Dallas, TX, USA

L. E. Lamberson (ed.), *Dynamic Behavior of Materials, Volume 1*, Conference Proceedings of the Society for Experimental Mechanics Series, https://doi.org/10.1007/978-3-030-30021-0_20

dynamic behavior of high-strength concretes under triaxial loading conditions. Experiments in this preliminary study were all performed on BBR9, which has an unconfined compressive strength of 130 MPa for cast cylindrical specimens with a diameter of 75 mm and a height of 150 mm [7] and 140 MPa for cored cylindrical specimens with a diameter of 50 mm and a height of 114 mm [8].

Analysis

In quasi-static experiments on BBR9, brittle, quasi-brittle and ductile failure modes were observed under confinement pressures of 10 MPa, 50 MPa, and 100 MPa, respectively. Therefore, these pressures were also selected for investigations on the triaxial Kolsky bar. All tests were conducted on cored cylindrical BBR9 concrete specimens with a diameter and height of 25 mm.

Since the triaxial Kolsky bar experiments presented here utilize pressurized fluid (kerosene) to provide hydrostatic confinement pressure, it is of the utmost importance that the specimen can be sealed from the surrounding fluid. This can be quite challenging since there is a sharp corner where the 25-mm-diameter specimen meets the 50-mm-diameter bar. In a previous study on borosilicate and soda-lime glass, a heat shrink tubing with a coat of J-B WaterWeld epoxy was used to surround the entire specimen, therefore providing the required sealing [5]. However, as the failure mode in concrete becomes more ductile, it was suspected that the rigidity of epoxy could skew experimental results. Therefore, the specimens in this study were prepared in four distinct steps as shown in Fig. 20.1: (1) Specimen is positioned and then seated with an axial prestress of 5 MPa, (2) a thin line of WaterWeld epoxy is applied at the sharp corner of the specimen/bar interfaces and then shaped into a small radius, (3) a translucent latex triaxial membrane is stretched over the specimen while overlapping the initial epoxy application, and (4) an additional layer of epoxy starts at the edge of the bar surface and extends over the latex membrane. This method allows the majority of the specimen to only be covered by the flexible latex layer. Additionally, tests were performed while the epoxy was still malleable (prior to full set).

Experimental data were collected using strain gauges with a Wheatstone bridge circuit and recorded on an oscilloscope. An example loading pulse is shown in Fig. 20.2 for a test conducted with a preloaded hydrostatic pressure at 50 MPa. For this experiment, an annular annealed copper pulse shaper was used with a thickness of 1.1 mm and outer and inner diameters of 19.0 mm and 6.3 mm, respectively. An additional annular PTFE pulse shaper with a thickness of 0.26 mm and outer and inner diameters of 11.1 mm and 9.5 mm, respectively, was added to further smooth the loading pulse. Specimen stress was calculated at the front and back face verifying that dynamic stress equilibrium was achieved. However, the strain rate was increasing slightly as the specimen failed. Additional pulse shaping is required for future experiments to ensure that a constant strain rate can be achieved at each specified level of confining pressure.

The experimental data was processed using the methods described by Chen and Song [9] for triaxial Kolsky bar experiments where the offset in static preload is shifted back to zero for dynamic analysis. The resulting stress and strain data are presented in terms of principal stress difference and axial strain as shown in Fig. 20.3. For clarification, principal stress difference refers to the difference between axial stress (σ_1) and radial stress (σ_2) where $\sigma_1 = \sigma_2$ during the hydrostatic loading phase. Note that σ_2 is assumed to remain constant throughout the duration of dynamic loading. As the confinement pressure

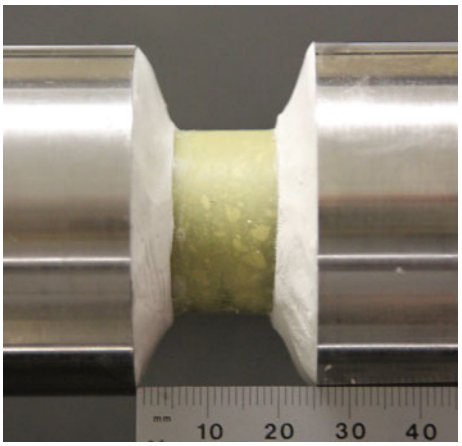

Fig. 20.1 Triaxial Kolsky bar specimen sealed with a translucent latex triaxial membrane and layering of WaterWeld epoxy

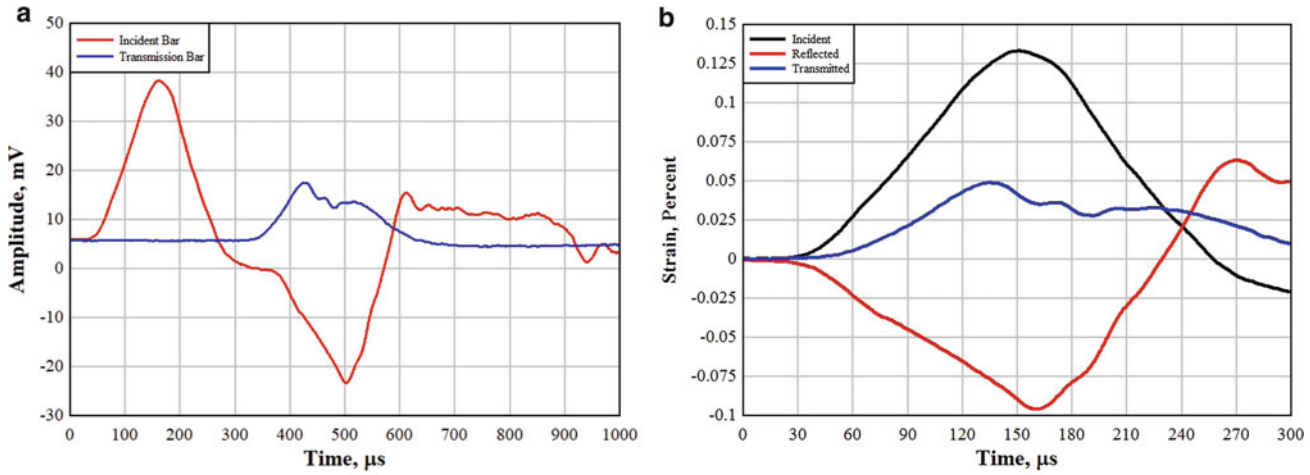

Fig. 20.2 (**a**) Output voltage showing incident wave and transmitted wave and (**b**) shifted strain pulses for three-wave analysis

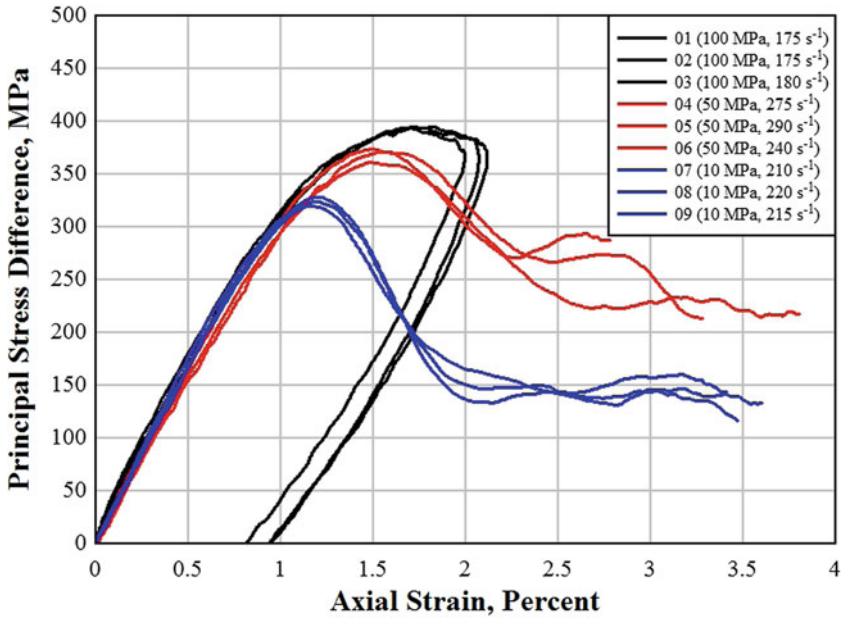

Fig. 20.3 Compressive stress-strain data for triaxial Kolsky bar experiments with confinement pressures of 10 MPa, 50 MPa, and 100 MPa

increases, the concrete failure mode begins to transition from brittle to ductile. Although strain rates were not constant for all experiments, approximate strain rates at peak stress are noted in the legend of Fig. 20.3 with a range of 175–290 s^{-1}.

Conclusion

A new method of specimen preparation was developed to provide a means of sealing a dynamic triaxial specimen from confining fluid for cases where the specimen is smaller than the Kolsky bar. With this method the majority of the specimen is only restricted by a flexible latex membrane with the specimen ends sealed to the bar using WaterWeld. Dynamic triaxial compressive response for BBR9 concrete presented in this study exhibited a clear brittle-to-ductile transition similar to what has been observed under quasi-static loading. However, further work is needed to tailor the loading pulses so that constant strain rate is achieved. Future work will focus on improving the quality of dynamic triaxial data, increasing confinement

pressures up to the design limit of 200 MPa for the ERDC's 50 mm triaxial Kolsky bar, and finalizing quasi-static triaxial experiments on the same specimen geometry to isolate rate effects for the purpose of calculating dynamic increase factors (DIFs).

Acknowledgements The work described in this document was funded under the US Army Basic Research Program under PE 61102, Project T22, Task 02 "Material Modeling for Force Protection" and was managed and executed at the US Army ERDC. Permission to publish was granted by the Director, Geotechnical and Structures Laboratory.

References

1. Christensen, R.J., Swanson, S.R., Brown, W.S.: Split-Hopkinson-bar Tests on Rock under Confining Pressure. Exp. Mech. **12**(11), 508–513 (1972)
2. Lindholm, U.S., Yeakley, L.M., Nagy, A.: The dynamic strength and fracture properties of dresser basalt. Int. J. Rock Mech. Min. Sci. Geomech. Abstr. **11**(5), 181–191 (1974)
3. Frew, D.J., Akers, S.A., Chen, W.W., Green, M.L.: Development of a dynamic triaxial Kolsky bar. Meas. Sci. Technol. **21**(10), 105704 (2010)
4. Martin, B.E., Kabir, M.E., Chen, W.W.: Undrained high-pressure and high strain-rate response of dry sand under triaxial loading. Int. J. Impact Eng. **54**, 51–63 (2013)
5. Chojnacki, J.T., Chen, W.W.: Mechanical response of borosilicate and soda-lime glass under dynamic triaxial compression. J. Dyn. Behav. Mater. **2**(2), 251–258 (2016)
6. Mondal, A.B., Chen, W.W., Martin, B.E., Heard, W.F.: Dynamic triaxial compression experiments on cor-tuf specimens. Dyn. Behav. Mater. **1**, 245–249 (2013)
7. Williams, B.A., Heard, W.F., Graham, S.S., Martin, B.E., Loeffler, C.M., Nie, X.: Mechanical response and damage evolution of high-strength concrete under triaxial loading. Dyn. Behav. Mater. **815**(9), 69–71 (2019)
8. Vankirk, G., Heard, W.F., Frank, A., Hammons, M., Roth, M.J.: Residual structural capacity of a high-performance concrete. Dyn. Behav. Mater. **815**(42), 233–236 (2019)
9. Chen, W.W., Song, B.: Split Hopkinson (Kolsky) Bar. Springer, Berlin (2010)

Chapter 21
Dynamic Compressive Tests of Alumina Dumbbells Using a Spherical Joint

Steven Mates, Richard Rhorer, and George Quinn

Abstract The dynamic compressive strength of ceramic armor materials is difficult to obtain experimentally due to the sensitivity of fracture strength to small misalignments, end effects, and surface effects. In this work we introduce a spherical joint into a compression Kolsky bar to investigate whether the joint can alleviate bending stresses due to minor misalignment in compression tests on alumina dumbbell specimens. Tests are conducted both with and without the spherical joint, and high-speed (75,000 frames/s) three-dimensional Digital Image Correlation (3D DIC) is used to measure both the strain field on the dumbbell specimen and motion, if any, in the spherical joint. Results indicate that the spherical joint is extremely sensitive to eccentric loading and in most cases increases rather than decreases the bending stresses in the test, leading to lower apparent fracture strengths.

Keywords Kolsky bar · Dynamic fracture strength · Dumbbell specimens · 3D DIC · High-speed video

Introduction

The design of ceramic armor systems requires precise knowledge of the dynamic mechanical behavior of the ceramic armor materials, including dynamic compressive fracture strength, which is typically measured using a Split Hopkinson Pressure Bar, or Kolsky Bar [1]. The fracture strength of brittle materials is very difficult to measure accurately because of the extreme sensitivity of the test results to mechanical alignment, end effects, and surface effects. Researchers at the U.S. Army Research, Development and Engineering Command (RDECOM) have developed a dumbbell-shaped specimen to avoid premature fracture from end splitting due to tensile stresses developed during elastic punching, lateral strain mismatches, and/or friction that can occur when simple cylindrical specimens are used. As part of this research effort, the U.S. Army RDECOM organized a limited round robin test effort involving three laboratories. In this paper we report on the testing performed at the National Institute of Standards and Technology (NIST) as part of the limited round robin.

Because dumbbell specimens often have much larger aspect ratios compared to usually short cylindrical or cubic specimens used for dynamic testing, they might be susceptible to premature failure from bending. Alignment of the Kolsky bar interface is therefore crucial if bending is to be minimized during dynamic compression testing of dumbbell specimens. Alignment quality is usually checked by doing Kolsky bar tests with no sample and with the bar ends pressed tightly together. Perfect alignment results in complete transmission of the elastic loading pulse and no reflected pulse. While this condition is achievable in practice, in the present study we investigated whether bending stresses caused by small misalignment of the interface could allow large axial loads to be transmitted while minimizing bending in a dynamic compression test of a ceramic dumbbell specimen.

The present study compares fracture strength experiments performed with and without a spherical joint. The joint consists of a precisely-machined spherical interface placed on the transmission side of the specimen in Kolsky bar test. High-speed, three-dimensional digital image correlation (3D DIC) is used to measure the motion of the specimen and the platens during testing. From these measurements, specimen rotation is measured by comparing displacement vectors of the cylindrical ends of the dumbbell specimens with the original specimen axis. If the specimen rotates during the test, bending stresses are likely. The rotation observed in the DIC data are correlated to the apparent fracture strengths. Finally, the effect of the spherical

S. Mates (✉) · G. Quinn
National Institute of Standards and Technology, Gaithersburg, MD, USA
e-mail: smates@nist.gov

R. Rhorer
Rhorer Precision Engineering, Gaithersburg, MD, USA

L. E. Lamberson (ed.), *Dynamic Behavior of Materials, Volume 1*, Conference Proceedings of the Society for Experimental Mechanics Series, https://doi.org/10.1007/978-3-030-30021-0_21

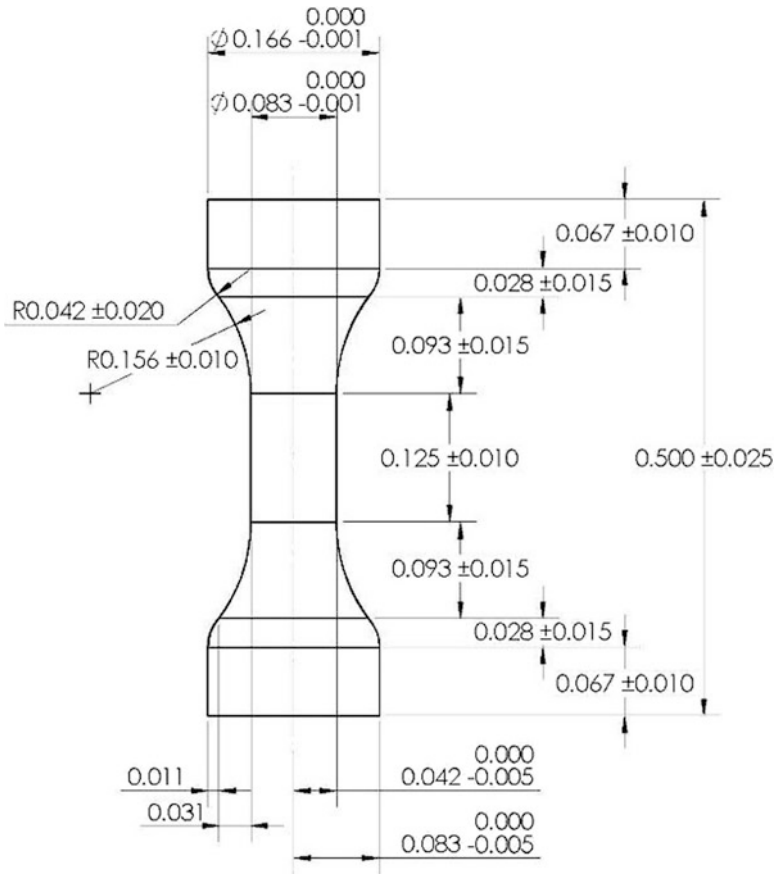

Fig. 21.1 Fabrication drawing for alumina dumbbell compression specimens. Dimensions in inches

joint on both rotation and apparent fracture stress is determined by comparing the results against similar experiments without the spherical joint.

Experimental

Specimens provided by the U.S. Army RDECOM were manufactured according to the specifications shown in Fig. 21.1. The test material was Coorstek[1] CAP3 alumina with a nominal Young's modulus of 370 GPa and a nominal compressive fracture strength of 5 GPa.

The NIST compression Kolsky Bar is pictured in Fig. 21.2 along with the results of a bar-to-bar test showing a small first reflection, indicative of imperfect interface alignment. Dimensions of the NIST Kolsky bar are given in Table 21.1 along with bar material properties and the longitudinal elastic wave speed in the bars. The Kolsky bar test was designed to fracture the samples in a single strike with a constant strain rate. For test design purposes, the breaking stress of this material was assumed to be 5 GPa, such that the fracture load of the specimens is estimated to be 17.8 kN. The fracture strain is estimated to be 0.0135 based on this fracture load and the nominal Young's modulus of 370 GPa. To break the sample, the striker length and impact velocity is selected to exceed both the peak load and the fracture strain. Based on a limited number of trials, a 203 mm long maraging steel striker bar (15 mm diameter) with an impact velocity of 9.9 m/s ± 0.1 m/s (± here is 2 standard deviations) were found to produce an adequate loading pulse. To achieve a constant strain rate, a ramped input pulse is created, following the recommendation in [1], with an annealed copper pulse shaper measuring 4.64 mm in diameter

[1] Certain commercial equipment, instruments, or materials are identified in this paper to specify the experimental procedure adequately. Such identification is not intended to imply recommendation or endorsement by the National Institute of Standards and Technology, nor is it intended to imply that the materials or equipment identified are necessarily the best available for the purpose.

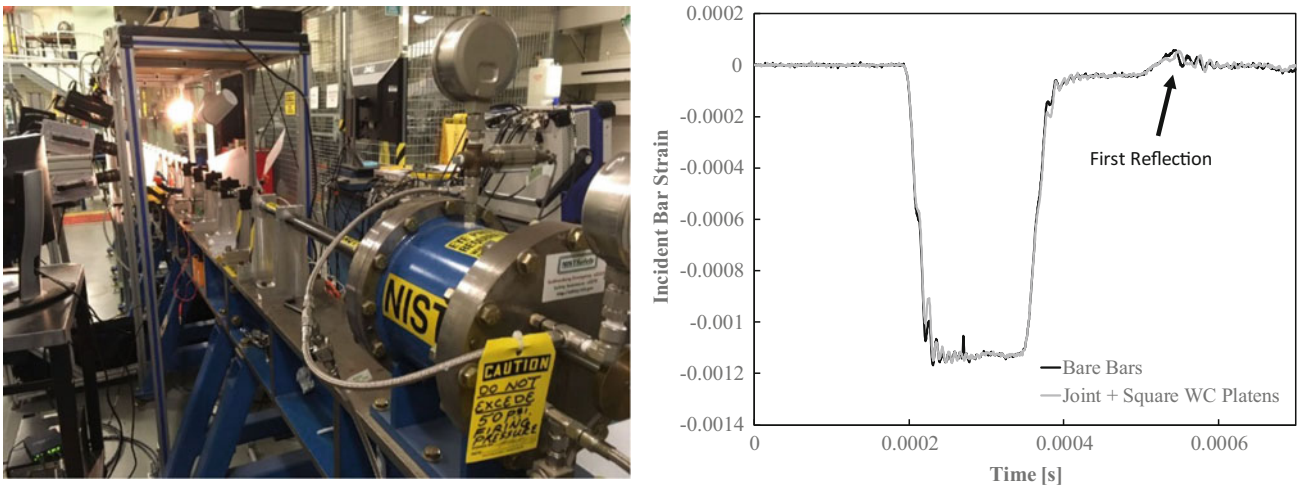

Fig. 21.2 Picture of the NIST compression Kolsky bar (left) and bar-to-bar test showing small first reflection indicative of imperfect interface alignment (right)

Table 21.1 NIST Kolsky bar dimensions and materials

Element	Quantity	Unit
Incident and transmission bar length	1.5	m
Incident, transmission & striker bar diameter	0.015	m
Striker bar length	0.203	m
Bar material	Maraging steel (un-hardened)	
Bar modulus	170	GPa
Bar wave speed	4600	m/s

and 1.59 mm thick. Kolsky bar strain pulses are measured using dual 1000 Ω metal foil strain gages, one pair on each bar, located approximately midway along each bar. The strain gage bridge circuits are powered by a 24 V battery and the output is recorded at 2 MHz with a (14-bit) storage oscilloscope.

To protect the maraging steel bar ends from being damaged by ceramic fracture debris, square-shaped tungsten-carbide (WC) tool inserts (12 mm square by 3.22 mm thick) were placed on either side of the specimen as sacrificial protective elements. The WC tool inserts provided flat, hard surfaces that were well matched to the bar diameter. In some tests, round WC platens with stainless steel confining rings (12 mm diameter by 3 mm thick, impedance matched to the bars), leftover from previous studies, were used instead.

The spherical joint was constructed of 15 mm OD maraging steel. The mating surfaces, which were well matched and polished, had a radius of curvature of 17 mm, and the thickness of each piece was approximately 3 mm. The joint was placed directly behind the WC platen on the transmission side of the sample. The setup involving the spherical joints and a combination of square and round WC plates is shown in Fig. 21.3(a). Interfaces between the bars and the spherical joint and WC platens were lubricated with heavy grease and the assembly was kept aligned with a small compressive force provided by elastic bands fixed between the bar and the bearing holders using capstan-style connectors.

The imaging setup is pictured in Fig. 21.3(a). Twin Photron SA1 high speed digital cameras with 90 mm macro lenses were used for 3D DIC measurements as well as to determine when and where the sample fails by videography. The lens apertures were set to the lowest setting (f/32) to maximize the image depth-of-field. The frame rate was 75,000 frames per second with a pixel resolution of 128 pixels by 352 pixels, and the exposure time was reduced to 1.76 μs using an electronic shutter on the cameras to eliminate motion blur prior to fracture. The geometric field of view was approximately 7.8 mm by 21.4 mm (about 16 pixels per mm), and the minimum object resolution, determined by the 1951 Air Force target method, was determined to be 0.0625 mm, indicating sharp focus. Illumination was provided by a single Photogenic PL2500 DR flash unit (871 W-s output over 0.001 s) positioned above the camera pair. A semi-circular diffuse reflector was added to improve illumination on the bottom side of the specimen and to provide a light background for the high-speed movies.

A sample DIC image is shown in Fig. 21.3(b). Black speckles are produced on the white alumina sample using a fine, disperse spray of flat black spray paint. The included angle of the DIC cameras was 24° ± 2°, and the working distance was 250 mm ± 25 mm. DIC measurements were obtained using Vic-3D from Correlated Solutions, with 15 pixel (0.94 mm)

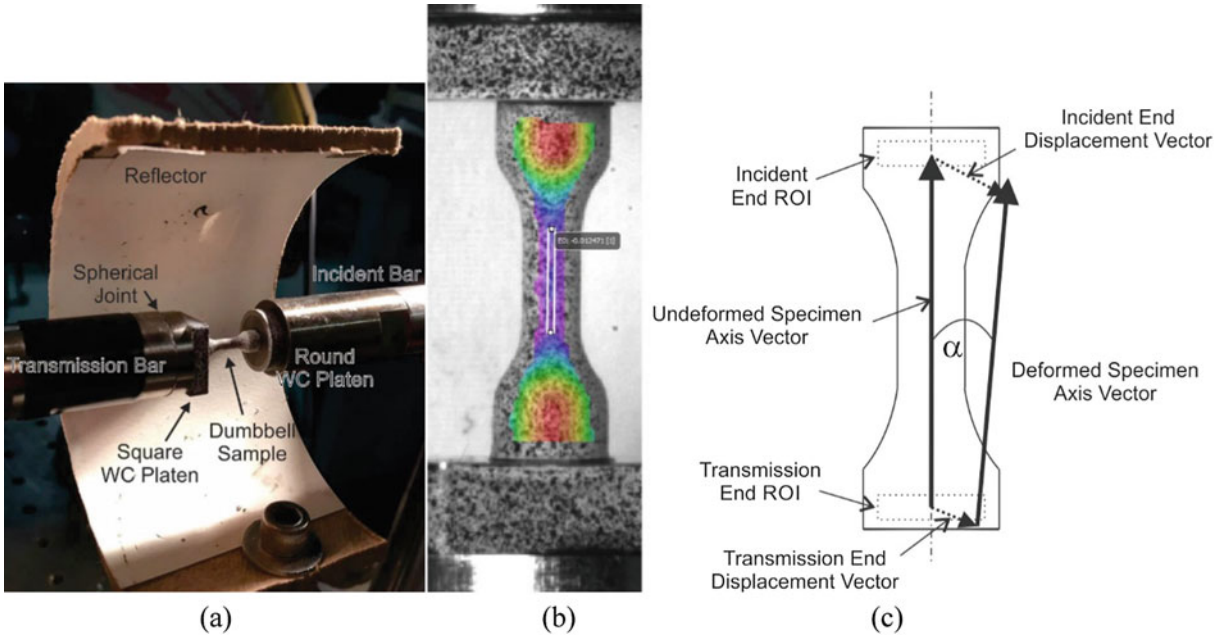

Fig. 21.3 Sample, WC platens, spherical joint and reflector (**a**), DIC image of ceramic dumbbell showing correlation region and virtual gage used for strain measurement (color represents out-of-plane dimensional coordinate) (**b**), and vector definitions for axis misorientation angle measurements (**c**)

correlation windows (subsets) and a 3 pixel (0.19 mm) overlap. Correlations were determined using Gaussian subset weights with an optimized 6 tap interpolation scheme with normalized squared differences as the correlation criterion, according to the software settings. As this figure shows, the correlation region on the gage region is quite narrow, due to the high curvature of the specimen. Because of the limited number of DIC subsets available in the gage section, DIC measurements of sample strain in the gage section were obtained using the "virtual strain gage" method available in Vic-3D, which simply measures the relative displacement between two correlated subsets chosen along the gage section. The virtual gage is superimposed on the DIC image in Fig. 21.3(b). The gage length in this example is 3.18 mm (51 pixels). The noise error for DIC displacement measurements, based on a set of 12 consecutive still images obtained under conditions identical to the real measurements, is a maximum of 1 μm and is dominated by the out-of-plane displacement component. The noise is quite small compared to the typical maximum displacement measured prior to fracture (300 μm for the incident bell end, 160 μm for the trans bell end). Possible bias errors were not explored but are assumed to be small. The DIC parameters reported here are in partial fulfillment of the requirements laid out in the DIC Good Practice Guide [2].

Results

Spherical Joint Tests with Ductile Metals

Experiments were conducted to ensure that the spherical joint and the WC protective platens did not introduce significant disturbance of the strain waves that might influence the data analysis in compression tests performed on actual samples. Previously, it was shown in bar-to-bar tests that the spherical joint and platens did not alter the wave transmission compared to tests without it (Fig. 21.2, right). Compression tests with and without the spherical joint and platens were conducted on samples of a brass alloy (26000) and on Ti-6Al-4 V. Results of these tests are shown in Fig. 21.4. The results show that the presence of the additional elements does not change the stress-strain result for either material. We note that in these tests, the striker bar length and velocities were not identical, which caused the difference in total strains during the tests as evident in the figure. Regardless, the data agree quite well where they overlap in strain, indicating no significant disturbance of the waves through the joint and platens.

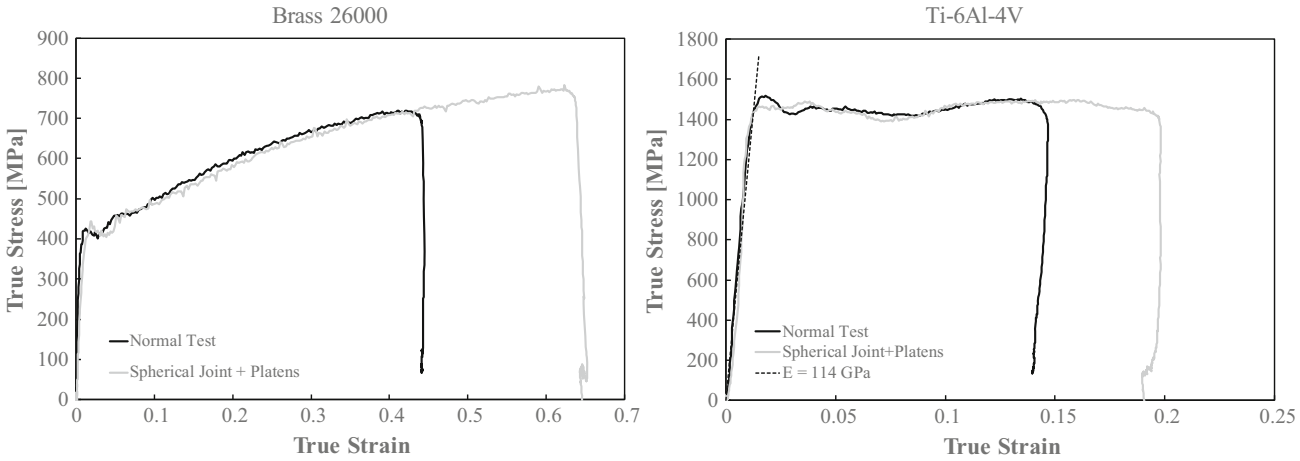

Fig. 21.4 Brass 26,000 (left) and Ti-6Al-4 V (right) measurements with and without spherical joint and WC platens. A nominal value of Young's Modulus (E) is plotted for Ti-6Al-4 V for comparison with the data

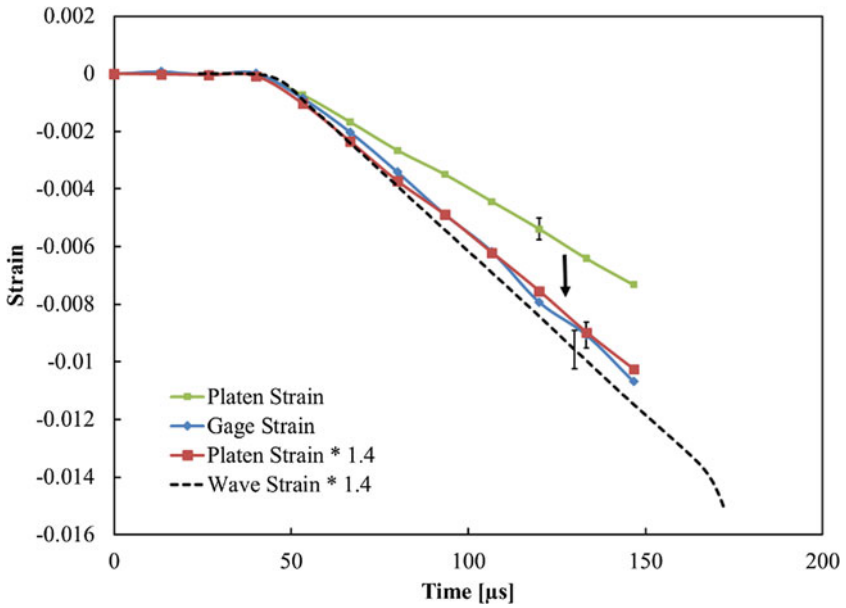

Fig. 21.5 Comparison of DIC Gage Strain (using the virtual gage method) with the overall strain of the dumbbell (Platen Strain from DIC-measured platen displacements), and the resulting correction factor of 1.4 applied to the Platen Strain data and the Wave Strain data. Error bars are determined using random error propagation and represent a coverage factor of 1

Alumina Dumbbell Compression Tests

The dynamic stress-strain response of the dumbbell samples is determined from the usual Kolsky bar strain wave analysis technique but with an adjustment to account for the strain concentration in the gage section of the dumbbell due to the reduced cross-sectional area there. Figure 21.5 compares the strain-time data obtained from the adjusted wave analysis with DIC measurements directly on the gage section. Also shown in the figure is the platen strain, which is the overall dumbbell strain as determined from the measured displacements of the WC platens from DIC data. The DIC measurements indicated the gage strain is 1.4 times higher than the overall dumbbell strain due to the reduced cross-sectional area. In the case shown in Fig. 21.5, the adjusted wave strain is slightly higher than the adjusted platen strain, but the difference is within experimental uncertainty.

Kolsky bar strain wave data showing the raw strain waves, equilibrium, strain-rate versus time and the stress-strain response for a dumbbell compression test that is considered valid (little obvious rotation observed from videography) are

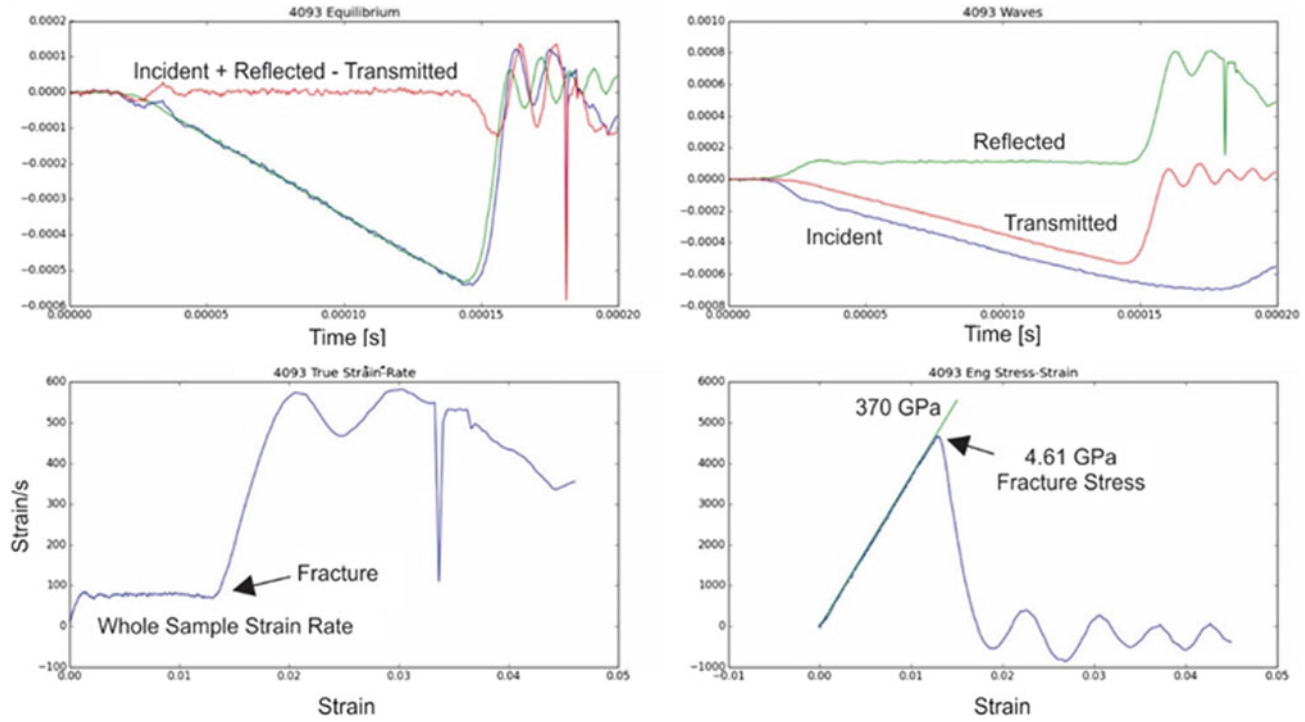

Fig. 21.6 Strain wave data from a dumbbell test that is considered valid. Upper left: comparison of incident, reflected and transmitted waves as a function of time. Upper right: raw incident, reflected and transmitted waves. Ordinate values of both plots in volts. Lower left: strain rate versus strain of the whole dumbbell sample, which is lower than the strain rate in the gage section by a factor of 1.4. Lower right: engineering stress-strain curve up to fracture (ordinate values in MPa)

Table 21.2 Uncertainty budget for fracture stress

Quantity	Uncertainty (coverage factor = 1)
$\delta A_{bar}/A_{bar}$	0.007
$\delta E_{bar}/E_{bar}$	0.012
$\delta \varepsilon_{frac}/\varepsilon_{frac}$	0.013
$\delta D_{gage}/D_{gage}$	0.004
$\delta \sigma_{frac}/\sigma_{frac}$	0.02

Coverage factor = 1. δ denotes uncertainty

shown in Fig. 21.6. The apparent fracture stress, σ_{frac}, is determined from the peak load obtained from the Kolsky bar transmitted strain (ε_{frac}), and is determined from the following equation:

$$\sigma_{frac} = \frac{P_{frac}}{A_{gage}} = \frac{A_{bar} E_{bar} \varepsilon_{frac}}{\frac{\pi}{4} D_{gage}^2} \tag{21.1}$$

P is load, E is Young's modulus, A is area. Subscript *gage* denotes dumbbell gage section properties, and *bar* denotes Kolsky bar properties. The uncertainty budget for the measurement of apparent fracture stress is given in Table 21.2, with the last entry being the calculated fractional uncertainty of the apparent fracture stress, considering independent, random error propagation. We note the apparent fracture stress uses the original cross-sectional area of the specimen, so it does not account for lateral expansion of the gage section due to Poisson effects.

Table 21.3 lists the results of the eight experiments where DIC data were available. Four tests used the spherical joint with WC platens and four tests used only WC platens. As the table shows, the apparent fracture stresses are generally lower when the spherical joint was employed, indicating that, rather than improving the test quality, the spherical joint actually makes things worse. Visual inspection of the high-speed movies revealed that the spherical joint appears to cause more significant rotation (bending) in the sample because of rotation in the joint. Fracture strains, determined from the wave strain at fracture adjusted by the factor 1.4, are also listed in Table 21.3. A bias error in these strains is likely due to possible bending in the

Table 21.3 Test conditions and results[a]

Test ID number	Ambient temp [°C]	Ambient relative humidity (%)	Strain rate [1/s] ± 5	Fracture stress [MPa] ± 2%	Fracture strain ± 1.0%	Spherical joint?	α [Deg] ± 0.002
4085	23	18	115	3700	0.014	Y	0.130
4086	23	18	115	3530	0.013	Y	0.071
4087	23	18	122	3790	0.014	Y	0.260
4088	23	18	126	4460	0.013	N	0.050
4090	24	32	111	4040	0.013	Y	0.102
4091	24	32	112	4550	0.013	N	0.050
4092	24	32	109	4250	0.013	N	0.130
4093	24	32	113	4610	0.013	N	0.025

[a]Uncertainty estimates are determined with random error propagation techniques with a coverage factor = 1

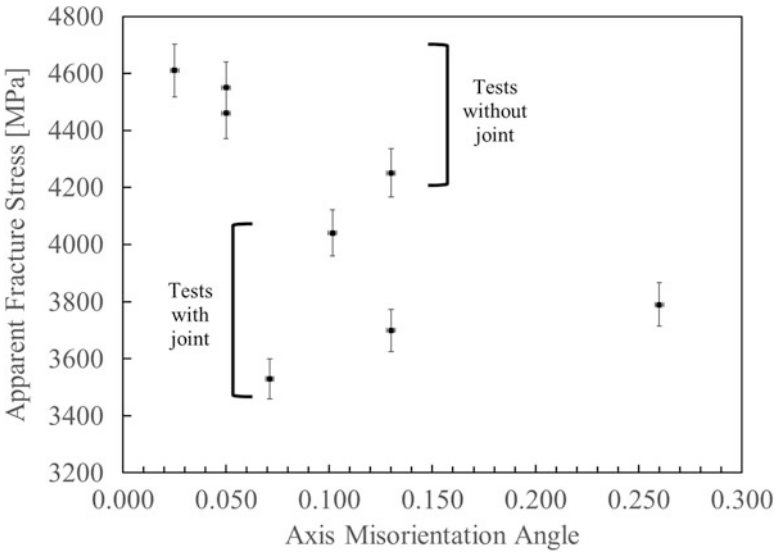

Fig. 21.7 Influence of measured axis misorientation angle just prior to fracture on apparent fracture stress in dynamic compression tests of brittle dumbbell specimens. Error bars reflect quantities given in Table 21.3

dumbbells during loading. Angles of rotation α are determined from DIC displacement data are also listed in Table 21.3, and their calculation is described below.

DIC measurements were used to quantify the deviation from uni-axial kinematics by measuring a misorientation angle, α, between the initial specimen axis and its axis just before fracture, as defined in Fig. 21.3(c) and computed from the dot product of the two position vectors. Kinematically, in a uni-axial compression test of a dumbbell specimen, the axis of the dumbbell should remain parallel to the initial axis. If this is not the case, then the specimen is rotating and/or bending. Because the specimen is quite stiff, the amount of rotation and bending will be very small, even if bending stresses are high. As such, measuring rotation and/or bending requires very sensitive DIC displacement measurements. To examine whether rotation can be detected in our data, we compare the misorientation angle α to the apparent fracture stress, with the hypothesis being that the more the specimen rotates during the test, the larger the bending stress is likely to be, so that fracture strength should show a negative correlation with α (higher fracture stresses for lower misorientation angles). In addition, we expect, based on the visual assessment, that α will be larger for tests with the spherical joint compared to tests without the joint.

Misorientation angles are reported in Table 21.3 just prior to fracture. The angles are quite small, as expected due to the high stiffness of the specimen and the Kolsky bar. While a random error analysis indicates that the uncertainty of the misorientation angle measurement is about two thousandths of a degree in the present case (based on the measured displacement noise components), bias errors have not been investigated, and a more thorough evaluation of the uncertainty magnitude is needed, for example using a very precise rotation stage. However, the results show larger misorientation angles when the spherical joint is used, confirming the earlier qualitative videography results. Further, as Fig. 21.7 shows, the apparent fracture stress increases as the misorientation angle decreases, which is also in-line with expectations. These results suggest that sensitive 3D DIC measurements may be able to provide useful information about the quality of a dynamic ceramic dumbbell compression test by measuring the degree of misorientation (bending) during the test. The simple

misorientation analysis used here was motivated by the limited spatial and temporal resolution of the cameras on-hand; more advanced high-speed cameras with greater resolution at higher frame rates could provide other means to quantify bending, including a more accurate measure of the distortion of the dumbbell during loading and a more detailed measurement of the state of surface strain in the gage section. If bias sources can be more thoroughly quantified, a more definitive outlook on the usefulness of 3D DIC for improving the accuracy of dynamic compressive strength measurements of ceramic dumbbells can be made. The advantage of 3D DIC is rooted in the ability to measure out-of-plane displacements, which 2D DIC cannot provide. This capability could be used to guide the alignment of the Kolsky bar interface with dumbbell tests taken not quite to fracture, so allowing one to measure misorientation under load, saving valuable specimens until the bending is reduced to acceptable levels (possibly zero). The technique could also identify which fracture tests suffer from significant bending and should be discarded from the data set. Previously, the use of multiple gage-mounted strain gages has been suggested to monitor bending in dynamic compression tests on ceramics [1], although laboratories that already have access to very high-speed 3D DIC systems may consider using this optical method instead.

Conclusions

NIST's participation in a mini round robin involving dynamic fracture tests on dumbbell-shaped ceramic specimens has been described. A spherical joint was placed on the transmission side of the specimen to reduce bending loads on the specimen due to minor bar misalignment and thereby obtain more accurate fracture data. Instead, the joint resulted in lower apparent fracture strengths compared to tests performed without a joint. 3D DIC measurements of the specimen motion during testing showed a correlation between the amount of deviation from uni-axial kinematics and fracture strength, pointing to the possible usefulness of 3D DIC to monitor dynamic fracture test quality and improve overall test results by identifying invalid tests.

Acknowledgement Dr. Jeffrey Swab, U.S. Army RDECOM, for inviting us to participate in the round robin and for valuable discussions.

References

1. Chen, W., Song, B.: Split Hopkinson (Kolsky) Bar: Design, Testing and Applications, p. 2011, New York (2011). ISSN 0941-5122
2. Jones, E.M.C., Iadicola, M.A.: A Good Practices Guide for Digital Image Correlation. s.l. International Digital Image Correlation Society (2018)

Chapter 22
Experimental Method for Mode I Dynamic Fracture Toughness of Composite Laminates Using Double Cantilever Beam Specimens

G. Portemont, T. Fourest, and R. De Coninck

Abstract To perform predictive crash simulations on composite structures, it is necessary to provide reliable input data for the cohesive material models often used to describe delamination processes in composite materials. For quasi-static loadings, the mode I fracture toughness measurement has been standardized. However, for high-rate of loading, additional challenges arise. Consequently, no test standard has yet been defined for the mode I fracture toughness evaluation under high rates of loading. Therefore, this research aims at developing an experimental procedure to characterize the dynamic fracture toughness of a fast running crack in carbon fiber-reinforced epoxy matrix composite T700/M21. The dynamic fracture toughness is characterized using the Double Cantilever Beam test under several loading rates up to 17 m.s^{-1}. An experimental protocol has been developed to identify the dynamic energy release rate G_{ID} for the mode I crack opening with various crack speeds å.

Keywords High loading rate · Fracture toughness · Double cantilever beam · Split Hopkinson Pressure Bar

Introduction

Impact loadings on laminated composite materials may damage the interlaminar phase and initiate the delamination process. Ideally, the material constituting the interlaminar phase must ensure overall cohesion and resist crack propagation. However, large decohesion may critically compromise the integrity of CFRPs lightweight structures. The capacity of the material to resist crack propagation is classically modelled by the energy release rate G which stands for the energy per unit area dissipated to form new crack surfaces [1]. For a mode I crack opening, the critical energy release rate G_{IC} refers to the initiation, and the dynamic energy release rate G_{ID} is dedicated to the propagation stage. The interlaminar fracture energy is not a material property of the matrix because it depends on the thickness of the interlaminar phase and for on the substrate material [2]. For mode I opening, the initiation value of the interlaminar fracture energy for CFRPs is classically determined by a Double Cantilever Beam (DCB) quasi-static test defined in ISO standard [3]. However, dynamic effects associated with fast crack propagations produce sharp oscillations in the recorded load, making it unrepresentative of the instant crack growth [4]. Consequently, no test standard has yet been defined for the mode I fracture toughness evaluation under high rates of loading. The general purpose of the present research is the definition of an experimental procedure to characterize the dynamic fracture toughness dependency on the crack velocity G_{ID}(å) for carbon fiber-reinforced epoxy matrix composite. This work focuses on the description of the experimental protocol and the evaluation of the energy release rate without monitoring the crack tip.

Development of an Innovative Experimental Protocol

The present work is focused on the analysis of the loading rate effect on the mode I fracture of laminate carbon fiber-reinforced epoxy matrix composite T700/M21. The mode I is classically characterized using a DCB configuration tests [5]. Uniaxial dynamic loading have been performed using a Tensile Split Hopkinson Bar for opening rates between 4 m.s^{-1}

G. Portemont (✉) · T. Fourest · R. De Coninck
DMAS, ONERA, Lille, France
e-mail: gerald.portemont@onera.fr

L. E. Lamberson (ed.), *Dynamic Behavior of Materials, Volume 1*, Conference Proceedings of the Society for Experimental Mechanics Series, https://doi.org/10.1007/978-3-030-30021-0_22

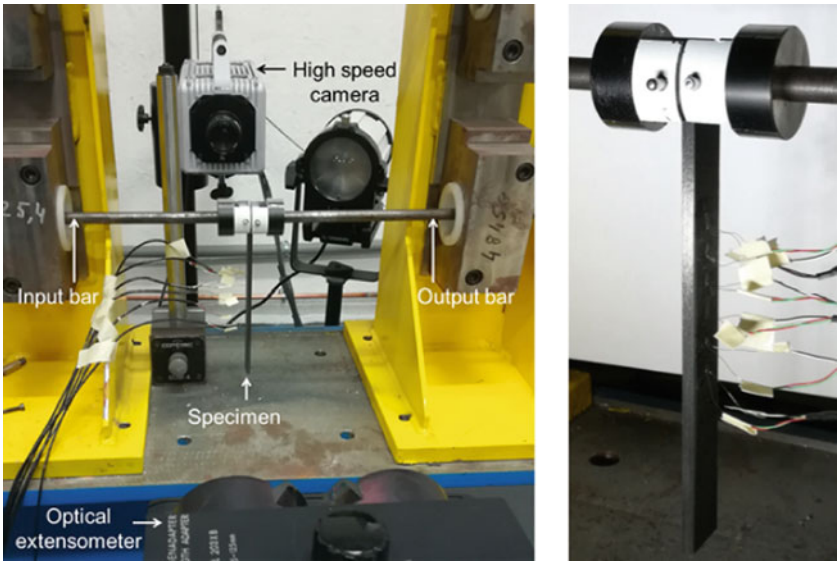

Fig. 22.1 Experimental setup and closed view of the DCB specimen

and 17 m.s^{-1}. The opening displacement with respect to the loading axis was measured using an optical extensometer. The measurement is based on the tracking of a black-and-white target. The input and output bars are equipped with strain gauges to measure the tensile strain applied on the bars in order to evaluate the transmitted forces in the specimen. To measure the strain on the outer skin of the specimen, five strain gauges have been glued on each specimen spaced 10 mm apart. The kinematic field has been measured using 2D Digital Image Correlation (DIC) technique on the edge of the specimens. The images are captured by a high speed camera (Photron SA-X). Figure 22.1 illustrates the experimental setup.

To process the experimental results, the energy release rate G_{IC} is expressed using the Linear Elastic Fracture Mechanics (LEFM) theory. However in this approach, the determination of G_{IC} is very sensitive to the crack length measurement. Indeed, due to its singularity, the crack tip is intrinsically difficult to measure experimentally, especially for high loading rates for which the camera resolution is low with respect to those usually obtained for quasi-static tests. Therefore, in the present work, an analytic approach is proposed to locate the crack tip. This method consists in extending the Corrected Beam Theory with Effective crack length method to the crack propagation stage. The crack propagation stage is estimated using only the load and the opening displacement measurements. In this study, the energy release rate is expressed by the energy dissipation mechanism [6]:

$$\frac{d\left(W_{ext} - U_{el} - U_{kin}\right)}{bda} = G - \frac{dU_{kin}}{bda}.$$

where W_{ext} is the external work, U_{el} is the elastic energy and U_{kin} is the kinetic energy. The crack is assumed to have a straight front of width b and an extension da of the crack length a is considered. This new approach allows the evaluation of the energy release rate G_{ID} and the crash velocity (å) without monitoring the crack tip. Consequently, each energy terms was determined experimentally thanks to the measurement of the specimen displacement using Digital Image Correlation (Fig. 22.2), strain gauges measurements and the opening loading. An assessment of the proposed technique by comparison with ASTM standard approach applied to the low loading rates has been performed.

Conclusion

An experimental protocol has been developed to identify the dynamic energy release rate for delamination processes in composite materials in mode I. Double Cantilever Beam specimens were selected and tested on tensile Split Hopkinson Pressure Bars for several loading rates up to 17 m.s^{-1}. A new analysis method was developed using strain measurements and displacement fields evaluated with the Digital Image Correlation method on the edges of the sample.

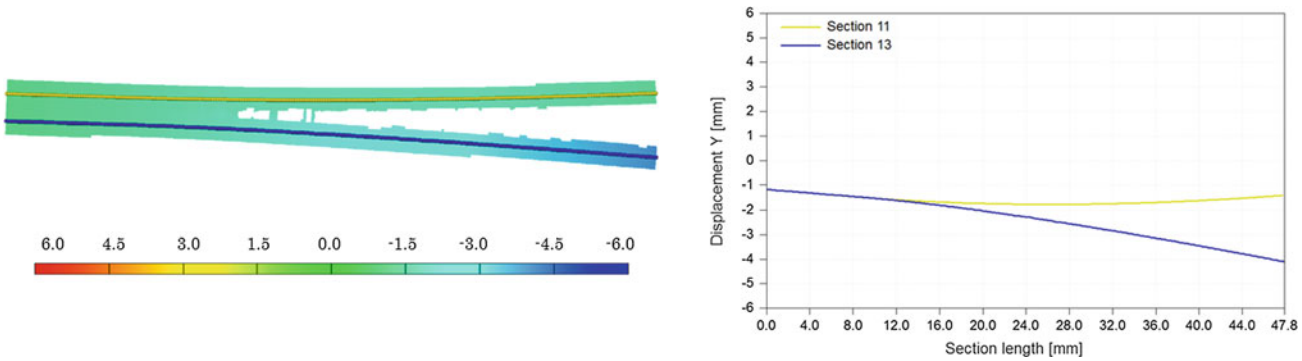

Fig. 22.2 Measurement of the displacement field along the loading axis

Acknowledgements The works presented in the communication have been funded by the Physafe project under the Directorate General of Civil Aviation (DGAC). The authors are also grateful to the French Ministry of Defense, the Elsat2020, the FEDER and the Région Haut de France for their financial support.

References

1. Griffith, A.A.: The phenomena of rupture and ow in solids. Philosophical Transactions of the Royal. Soc. Lond. **221**, 163–198 (1921)
2. Blackman, B.R.K., Kinloch, A.J., Paraschi, M., Teo, W.S.: Measuring the mode I adhesive fracture energy GIC of structural adhesive joints: the results of an international round-robin. Int. J. Adhes. Adhes. **23**, 293–305 (2003)
3. ISO: Fibre-reinforced plastic composites | Determination of mode I interlaminar fracture toughness GIC for unidirectionally reinforced materials. (2001). ISO 15024:2001(E)
4. Blackman, B.R.K., Dear, J.P., Kinloch, A.J., Macgillivray, H., Wang, Y., Williams, J.G., et al.: The failure of fibre composites and adhesively bonded fibre composites under high rates of test,Part I : Mode I loading experimental studies. J. Mater. Sci. **30**, 5885–5900 (1995)
5. ASTM D5528–13: Standard test method for mode I interlaminar fracture toughness of unidirectional fiber polymer matrix composites. (2013)
6. Hashemi, S., Kinloch, A.J., Williams, J.M.: The analysis of interlaminar fracture in uniaxial fibre-polymer composites. Proc. R. Soc. Lond. A. **427**(1872), 173–199 (1990)
7. Isakova, M., Maya, M., Hahna, P., Paula, H., Nishib, M.: Fracture toughness measurement without force data – Application to high rate DCB on CFRP. Comp. Part A. **119**, 176–184 (2019)

Chapter 23
Numerical Study of Ring Fragmentation

Brady Aydelotte

Abstract The fragmentation of rings and shells is a topic of enduring interest both because of the interesting dynamic conditions under which it takes places and the practical importance of fragmentation to various military and industrial applications. Fragmentation is a complex process in which potential fracture sites interact with one another in a deforming body to form a population of fragments. The details of this process are important, and realistic models need to capture the essential features of this process in order to make accurate predictions.

In this work, computational modeling of fragmentation experiments involving Al 6061-0 rings is explored and compared with experimental data. The effect of the mesh description and resolution on modeling the fragmentation process will be examined. The effect of defect population and the manner in which it is applied in the model will also be explored.

Keywords Cone crack · Impact · Indentation · Ceramic · Damage

Introduction

Fragmentation has been of practical and theoretical interest for decades. Seminal work by Mott [1] discerned the fundamental physics that governs the fragmentation process; fragments are formed by a competition between the formation and growth of fractures and the formation and growth of stress relieved areas created by completed fractures. There is a large and rich literature on the topic of fragmentation and many researchers have contributed to it (see for example works by Gurney [2], Gurney and Sarmousakis [3], Grady [4], Grady and Kipp [5], Glenn and Chudnovsky [6], and Grady's excellent book [7]).

Much of the experimental work on fragmentation has utilized high explosives to provide the loading required to initiate fragmentation. As an alternative which is somewhat more amenable to optical diagnostics, some experimenters have used RLC circuits to electromagnetically impart a load to uniformly expand and fragment sample rings of various materials. Niordsen [8] appears to have been the first, followed by Walling and Forrestal [9], and Grady and Benson [10]. Gourdin et al. [11] and Gourdin [12] also helped popularize the technique.

Excellent work was published by Zhang and Ravi-Chandar [13, 14] on expanding ring fragmentation. Their work provided high speed photography and detailed analysis of their experiments, which included materials such as 6061-O aluminum, 1100-H14 aluminum, and OFHC copper. Published fragmentation data, particularly that mentioned here, offer rich data sets to work with in studying the fragmentation process or the behavior of numerical modeling tools.

Modeling fracture and fragmentation has widespread value to military and safety applications where failure experiments are cost prohibitive or difficult to perform. Han and Tvergaard [15] conducted finite element simulations of ring fragmentation wherein they introduced small imperfections into their model and observed that these strongly influenced the necking process. Pandolfi et al. [16] performed simulations of 1100-O rings being fragmented. They used a fully Lagrangian approach which included a traction separation law to account for fracture and a flow model based on J2 plasicity. The meshing tool introduced small variations in geometry that contribute to necking. Becker [17] performed simulations of U-6Ni rings. He employed a Gurson constitutive model and two different failure criterion and either random perturbation of the initial void fraction or geometric variations; Becker reported good agreement between simulated and experimental results. Moxnes and Børve [18] used an SPH methodology; they reported that their SPH code was capable of capturing fragment distributions, but it was somewhat sensitive to the resolution and method of discretizing the computational domain. They applied the methodology of Meyer and Brannon [19] to impose a Weibull distribution on the first two parameters of the Johnson Cook [20] fracture model.

B. Aydelotte (✉)
US Army Research Laboratory, Aberdeen Proving Ground, Aberdeen, MD, USA

L. E. Lamberson (ed.), *Dynamic Behavior of Materials, Volume 1*, Conference Proceedings of the Society for Experimental Mechanics Series, https://doi.org/10.1007/978-3-030-30021-0_23

The approaches above all utilized Lagrangian analysis of one sort or another. Eulerian approaches for high strain rate and large deformation problems are also very popular and have met with a variety of outcomes in modeling this problem. Meulbroek et al. [21] computationally examined the experiments of Zhang and Ravi-Chandar [13] using the popular hydrocode CTH. Meulbroek et al. [21] did not introduce defects or non-deterministic material properties and Meulbroek et al. [21] found it difficult to obtain good agreement between the simulated and experimental results. They found that both the fragment sizes and the distributions were strongly dependent on the grid resolution and some of the basic details of the failure process such as neck formation were not well captured. Barton [22] published a novel Eulerian approach to modeling the ring fragmentation data that Becker [17] studied. Of interest here is that he used a method published by Vitali and Benson [23] to advect initial material properties, which were randomly perturbed, in a way that prevents their being smeared by the advection algorithm. This combined with the level set method employed by Barton [22] to track fracture interfaces led to good agreement with experimental data.

In this work, I simulated an experiment published by Zhang and Ravi-Chandar [13], the expansion and fragmentation of an 6061-O ring at an average velocity of approximately 200 m/s; experiment D in their paper. I examine the effects of statistically perturbing model parameters and the effect of Lagrangian versus Eulerian mesh descriptions.

Simulation Setup

The arbitrary Eulerian-Lagrangian hydocode ALEGRA [24] was used for the modeling work presented here. It is capable of fully Lagrangian, fully Eulerian, or arbitrary Eulerian-Lagrangian mesh descriptions. ALEGRA can impose uniform random, Weibull, Minimum Order Statistic, and/or Karhunen-Loéve distributions as well as volume scaling upon virtually any initial material property [24].

As pointed out by Vitali and Benson [23] and Barton [22], any initial perturbation of material properties would be reduced to the mean values in short order by the advection algorithm in an Eulerian simulation, but ALEGRA contains a method for preventing advection smearing. ALEGRA is able to push constitutive material properties and the deformation gradient onto mass-less tracking particles which are stationary with respect to the material. These particles, termed Lagrangian Material Tracking particles, are advected with the mass; the material states are updated using constitutive data from the particles. In this way, the evolving material state as well as its initial condition is retained with minimal losses due to advection [24].

I simulated radial ring expansion for a ring 1.0 mm tall, 0.5 mm thick and 15.5 mm mean radius. At this stage of the work, I elected not to model the electromagnetic loading; instead I imposed an initial radial velocity of 270 m/s. This yields an approximate average velocity of 200 m/s which is what was reported for test D in [13].

For the Lagrangian simulations, the smallest ring dimension, 0.5 mm, was discretized into 10, 15, or 20 linear hexahedral elements. This yields element sizes (edge lengths) of 0.05, 0.033, and 0.025 mm. These same mesh resolutions were used in the Eulerian simulations, making the Eulerian simulations very large.

The fragmentation process is influenced by features which exist at length scales which cannot be resolved in these simulations, such as surface finish, voids, inclusions, and crystallographic texture. One way that sub-scale information reveals itself at the larger length scale is that material properties are statistically distributed rather than deterministic. This is essentially the approach taken by much of the previous work cited in the Introduction.

I elected to study the perturbation of both the strength and strain to failure properties. I have chosen to impose a Weibull distribution on the quantity D1+D2 from the Johnson Cook fracture model following Meyer and Brannon [19] or on the A parameter (the initial yield strength) from the Johnson Cook strength model. Mott [1] concluded that variation in strain to failure drove the fragment statistics, but variation in yield strength may also play a role and was examined.

Using published Johnson-Cook material parameters for 6061-T6 aluminum [25] and stress strain data for 6061-O published by Zhang and Ravi-Chandar [13], I developed a parameterization for the Johnson-Cook constitutive model and fracture model for 6061-O aluminum.

Results and Discussion

Mesh resolution studies for the Lagrangian simulations show that the fracture behavior was very similar across all three resolutions as shown in Fig. 23.1. The necking and fracture behavior produced by the Lagrangian simulations appears qualitatively reasonable and similar for all three resolutions. This suggests that all three mesh resolutions provided an adequately converged mechanical response. For zero volume scaling and the same Weibull modulus, the highest and lowest

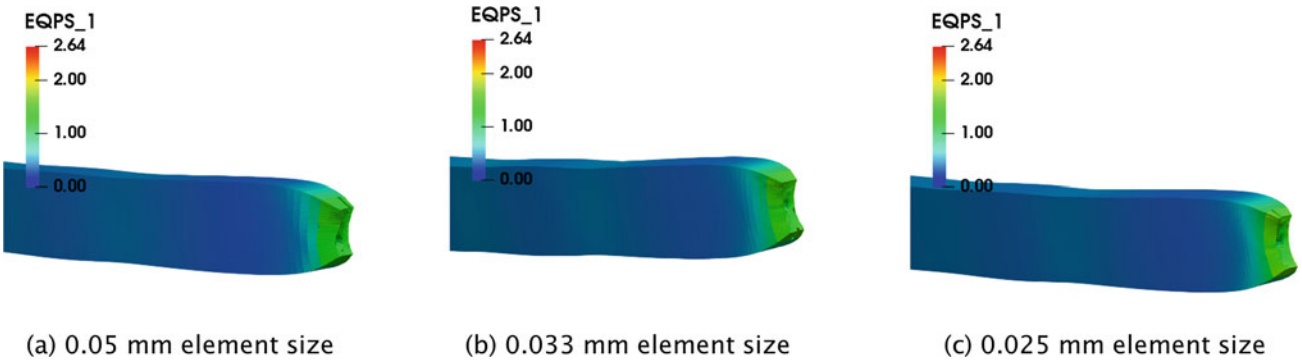

Fig. 23.1 Results of the mesh resolution study for Lagrangian ring fragmentation for three different resolutions. The failed ends from each resolution have similar features: similar maximum strain values, necked regions with similar shapes and extents, and dimpled fracture surfaces. This suggests that all three resolutions provide a converged mechanical response

Table 23.1 Summary of Lagrangian numerical modeling results

Mesh	Resolution	Property	Modulus	Volume exponent	Reference volume (m^3)	Fragments
Lagrangian	10	D1+D2	10	0.0	1.25E−13	20
Lagrangian	20	D1+D2	10	0.0	1.25E−13	18
Lagrangian	10	D1+D2	10	0.6	1.25E−13	20
Lagrangian	20	D1+D2	10	0.6	1.25E−13	15
Lagrangian	10	D1+D2	10	0.0	2.00E−08	20
Lagrangian	20	D1+D2	10	0.0	2.00E−08	18
Lagrangian	10	D1+D2	10	0.6	2.00E−08	9
Lagrangian	15	D1+D2	10	0.6	2.00E−08	5
Lagrangian	20	D1+D2	10	0.6	2.00E−08	1
Lagrangian	10	None	NA	0.6	2.00E−08	11
Lagrangian	10	D1+D2	10	0.6	2.00E−08	9
Lagrangian	10	D1+D2	20	0.6	2.00E−08	6
Lagrangian	10	D1+D2	30	0.6	2.00E−08	6
Lagrangian	10	A	10	0.6	2.00E−08	18
Lagrangian	10	A	20	0.6	2.00E−08	17
Lagrangian	10	A	30	0.6	2.00E−08	18

mesh resolutions produced reasonably comparable fragment numbers, 18 versus 20 respectively. A summary of the results is shown in Table 23.1.

Perturbing the strain to failure (D1+D2) in the Johnson-Cook fracture model, following Meyer and Brannon [19], produced reasonable looking fracture and fragmentation seen in Fig. 23.2a. Zhang and Ravi-Chandar [13] reported 14 fragments being produced for experiment D while simulations produced 6–9 fragments for a Weibull modulus of 30 to 10 respectively for a fixed volume scaling factor. With no volume scaling, the fragment number increased to 20.

Statistically distributing the yield strength, A in the Johnson-Cook strength model, tended to produce more fragments. At fixed volume scaling, this produced 17–18 fragments for the coarsest resolution.

The fragment number was quite sensitive to volume scaling when statistically distributing the strain to failure. By using a reference volume consistent with the gauge section of a tensile sample (Zhang and Ravi-Chandar [13] didn't indicate exactly what the sample size was, only that it matched the aspect ratio of the ring and that it complied with ASTM E8M-04. I assumed a gauge region size of $10 \times 2 \times 1$ mm for convenience. The results aren't sensitive to this value because it is much larger than the element size) the scale factor $\left(\frac{V_{ref}}{V_{element}}\right)^k$ becomes very large due to the small element sizes and grows very rapidly with reductions in element size. This causes the finer mesh resolutions to have much lower fragment numbers. This is due to the increased strain to failure, D1+D2. If the reference volume is set to the volume of the coarsest element size I used, in this case 0.05 mm edge length or a volume of 1.25e−04 mm^3, the change in fragment number is still apparently significant in the simulations with element sizes of 0.025 mm.

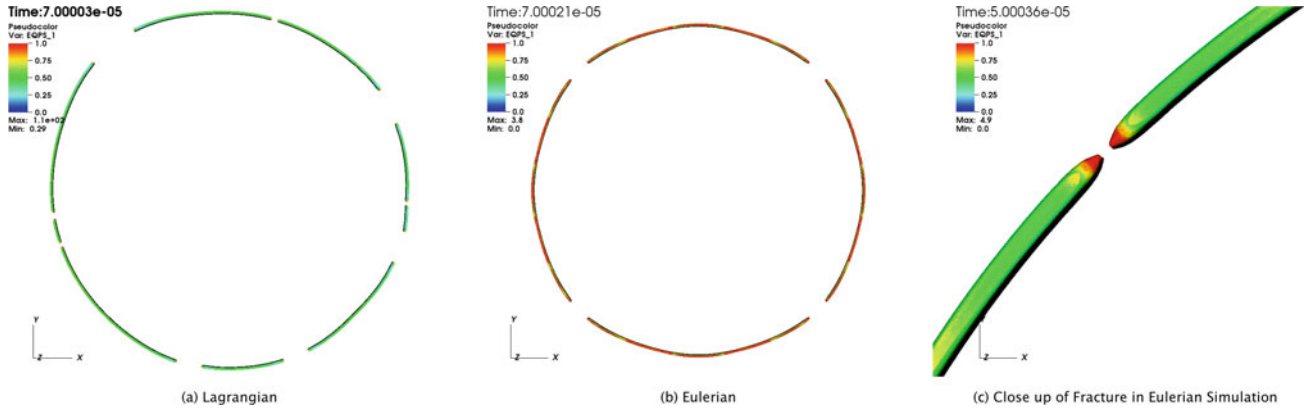

Fig. 23.2 A comparison of Lagrangian and Eulerian simulations with the strain to failure perturbed and the same Weibull modulus and volume scaling. (**a**) Lagrangian simulation after fragmentation. (**b**) An Eulerian simulation showing the effects of the Cartesian mesh. (**c**) A fracture in the Eulerian simulation with reasonable looking necking behavior

At the time of submission, the Eulerian simulations are not complete. They are very large due to the high resolution which must be maintained over a large region due to the deformation of the ring prior to fracture. However, some preliminary results are available for discussion.

A comparison of a Lagrangian and an Eulerian simulation are shown in Fig. 23.2. The Lagrangian simulations fragmented into different sizes in a manner that was influenced by the initial defect population rather than solely by the mesh discretization as shown in Fig. 23.2a. Even when using Lagrangian Material Tracking, there is still a strong mesh effect visible in Fig. 23.2b. The ring failed simultaneously in the $+/-$ 45° directions from the ring center, along mesh diagonals. This may suggest that the advection algorithm plays a role in initiating material instabilities despite the use of Lagrangian Material Tracking. However the necking and fracture itself still appears reasonable.

Conclusions

ALEGRA was used successfully to model expanding ring fragmentation with several different materials and meshes. Perturbing strain to failure yielded reasonable fracture predictions. Perturbing the yield strength caused more fragments to form, but the reason for this is not immediately clear. The number of fragments proved very sensitive to the volume scaling when perturbing the strain to failure and it should be used with caution. More work remains to determine if unbiased fragmentation simulations can be done with an Eulerian simulation in this framework.

Acknowledgements I gratefully acknowledge John Niederhaus and the rest of the ALEGRA development team (SNL) for their assistance in the use of ALEGRA in support of this work and feedback from Charles Randow (ARL). This work was supported in part by a grant of computer time from the Department of Defense High Performance Computing Modernization Program at ARL.

References

1. Mott, N.F.: Fragmentation of shell cases. In: Proceedings of the Royal Society of London. Series A, Mathematical and Physical Sciences, vol. 189, pp. 300–308 (1947)
2. Gurney, R.: The initial velocities of fragments from bombs, shell, grenades. No. BRL 405 (1943)
3. Gurney, R., Sarmousakis, J.: The mass distribution of fragments from bombs, shell, and grenades. No. BRL 448 (1944)
4. Grady, D.E.: Local inertial effects in dynamic fragmentation. J. Appl. Phys. **53**, 322–325 (1982)
5. Grady, D., Kipp, M.: Mechanisms of dynamic fragmentation: factors governing fragment size. Mech. Mater. **4**, 311–320 (1985)
6. Glenn, L.A., Chudnovsky, A.: Strain-energy effects on dynamic fragmentation. J. Appl. Phys. **59**, 1379–1380 (1986)
7. D. Grady, Fragmentation of Rings and Shells: The Legacy of N.F. Mott. Springer, Berlin (2006)
8. Niordson, F.I.: A unit for testing materials at high strain rates. Exp. Mech. **5**, 29–32 (1965)
9. Walling, H.C., Forrestal, M.J.: Elastic-plastic expansion of 6061-t6 aluminum rings. AIAA J. **11**, 1196–1197 (1973)
10. Grady, D., Benson, D.: Fragmentation of metal rings by electromagnetic loading. Exp. Mech. **23**, 393–400 (1983)

11. Gourdin, W.H., Weinland, S.L., Boling, R.M.: Development of the electromagnetically launched expanding ring as a high-strain-rate test technique. Rev. Sci. Instrum. **60**, 427–432 (1989)
12. Gourdin, W.H.: Analysis and assessment of electromagnetic ring expansion as a high–strain–rate test. J. Appl. Phys. **65**, 411–422 (1989)
13. Zhang, H., Ravi-Chandar, K.: On the dynamics of necking and fragmentation – i. Real-time and post-mortem observations in al 6061-o. Int. J. Fract. **142**(3), 183–217 (2006)
14. Zhang, H., Ravi-Chandar, K.: On the dynamics of necking and fragmentation—ii. Effect of material properties, geometrical constraints and absolute size. Int. J. Fract. **150**(1), 3–36 (2008)
15. Han, J.-B., Tvergaard, V.: Effect of inertia on the necking behaviour of ring specimens under rapid radial expansion. Eur. J. Mech. A. Solids **14**(2), 287–307 (1995)
16. Pandolfi, A., Krysl, P., Ortiz, M.: Finite element simulation of ring expansion and fragmentation: the capturing of length and time scales through cohesive models of fracture. Int. J. Fract. **95**, 279–297 (1999)
17. Becker, R.: Ring fragmentation predictions using the gurson model with material stability conditions as failure criteria. Int. J. Solids Struct. **39**, 3555–3580 (2002)
18. Moxnes, J.F., Prytz, A.K., Frøyland, Ø., Skriudalen, S., Børve, S., Ødegårdstuen, G.: Strain rate dependency and fragmentation pattern of expanding warheads. Def. Technol. **11**, 1–9 (2015)
19. Meyer, H.W., Brannon, R.M.: A model for statistical variation of fracture properties in a continuum mechanics code. Int. J. Impact Eng. **42**, 48–58 (2012)
20. Johnson, G.R., Cook, W.H.: Fracture characteristics of three metals subjected to various strains, strain rates, temperatures and pressures. Eng. Fract. Mech. **21**(1), 31–48 (1985)
21. Meulbroek, J., Ramesh, K., Swaminathan, P., Lennon, A.: CTH simulations of an expanding ring to study fragmentation. Int. J. Impact Eng. **35**(12), 1661–1665 (2008)
22. Barton, P.T.: A level-set based Eulerian method for simulating problems involving high strain-rate fracture and fragmentation. Int. J. Impact Eng. **117**, 75–84 (2018)
23. Vitali, E., Benson, D.J.: Modeling localized failure with arbitrary Lagrangian Eulerian methods. Comput. Mech. **49**, 197–212 (2012)
24. Bova, S., Hansen, G., Labreche, D.A., Love, E., Luchini, C.B., Roberts, N.V., Robinson, A.C., Sanchez, J.J., Siefert, C., Voth, T.E., Carleton, J.C., Niederhaus, J.H.J., Drake, R.R., Hensinger, D.M., Kramer, R.M.J.: ALEGRA user manual. No. SAND2018-DRAFT (2018)
25. Johnson, G.R., Holmquist, T.J.: Test data and computational strength and fracture model constants for 23 materials subjected to large strains, high strain rates, and high temperatures. No. LA-11463-MS (1988)

Chapter 24
Development of a New Testing Method to Capture Progressive Damage in Carbon Fiber Reinforced Polymers Subject to a Simulated Lightning Strike

Brandon Hearley, Kara Peters, and Mark Pankow

Abstract This paper will present a new testing method to simulate lightning strikes and capture the progressive damage that occurs in carbon fiber polymer matrix systems. The simulated lightning strike contains two major components that must occur simultaneously: a normal pressure pulse that impacts the carbon specimen, representative of the impulse shock wave associated with a lightning strike, and a rapid temperature rise, which represents the thermal shock from the lightning strike. The pressure pulse is applied using a shock tube, a device that forms a controlled shock that will impact the sample. The thermal shock is simulated with a capacitive discharging circuit, in which capacitors are charged to a maximum of 400 V and then, due to the relatively low resistance associated with carbon fiber materials, quickly discharged into the sample. The distance between the brass contacts will be varied, ultimately changing the resistance of the sample, in order to achieve the correct timescale and temperature spike. Various discharge voltages and fiber orientations relative to the direction of the current flow will be tested in order to study the effect these parameters have on the response of the sample. Through the use of Digital Image Correlation and an infrared thermal camera, independent measurements of deformation and temperature, respectively, will be found as the damage progresses, and is to be compared to a network of Fiber Bragg gratings (FBG) sensors applied to the sample. The results will help produce a better understanding of the temperature profile and localizations that occur during lightning strike events.

Keywords Carbon fiber · Lightning strike · Progressive damage · Resistive heating

Introduction

Due to the high strength-to-weight ratio that carbon fiber reinforced polymers can offer, their use in various engineering fields where minimizing weight is paramount, such as the aerospace industry, has seen widespread growth. As these materials see increased use in aerospace structures, the means in which these structures are tested and analyzed for safety becomes increasingly important. Furthermore, as aerospace structures shift from traditional engineering materials, new challenges arise that will need inexpensive and reliable testing in order to ensure safety. One such event that is more prevalent in composite structures than in metal structures are lightning strikes on aircraft wings. Unlike traditional aerospace materials, such as aluminum, carbon fiber reinforced polymers have a much lower conductivity, due to the dielectric properties of the matrix [3]. Lightning strikes can cause various forms of damage on aircraft, including resistive heating, acoustic shock, and melting or burning at lightning attachment points [1]. Simulated lightning strike experiments have been presented by previous researchers, including Feraboli and Miller [2] and Hirano et al. [1], in which both present methods to both simulate and analyze a lightning strike event. Both methods use a high voltage capacitive discharge circuit and use ultrasonic imaging and C-scans to assess damage. Feraboli et al. developed a lightning strike generator capable of discharging 44 kV through a 52 μF capacitor [1]. Hirano et al. used an impulse high-voltage generator (IVG) produced by Haefely test AG and an impulse high-current generator (ICG) produced by Nisshin Electric Co. that could produce peak currents of 10–40 kA [2]. The limitations that exist within current lightning strike are largely associated with cost and the data that is attainable. To test specimens at a high enough voltage to simulate the various forms of damage associated with a lightning strike event, the cost to run each test can be very expensive, on the order of $10,000 per test. Also, the damage analysis performed using these testing methods provide no information on the rate of energy dissipation and damage progression was obtained.

B. Hearley (✉) · K. Peters · M. Pankow
Department of Mechanical and Aerospace Engineering, College of Engineering, North Carolina State University, Raleigh, NC, USA
e-mail: blhearle@ncsu.edu

L. E. Lamberson (ed.), *Dynamic Behavior of Materials, Volume 1*, Conference Proceedings of the Society for Experimental Mechanics Series, https://doi.org/10.1007/978-3-030-30021-0_24

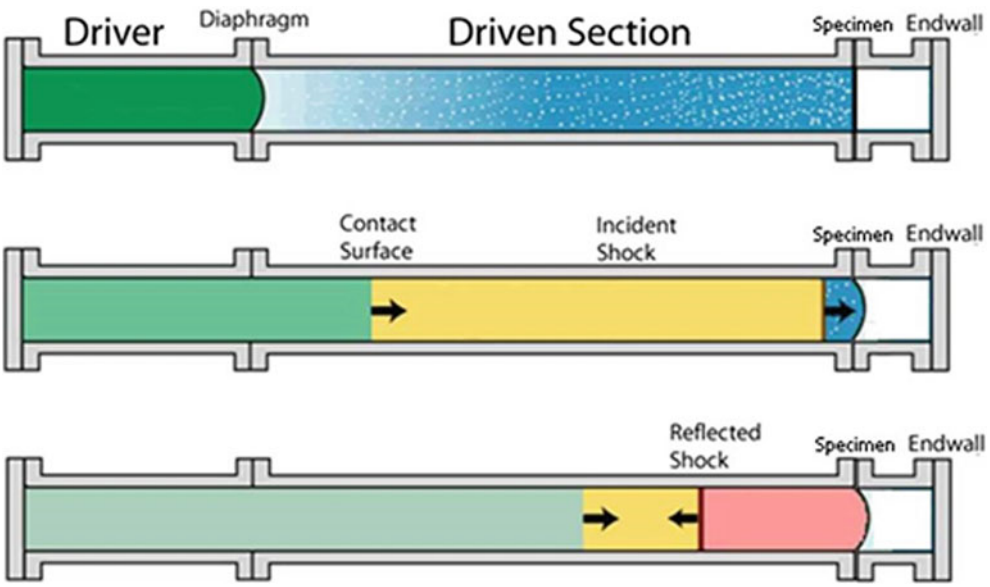

Fig. 24.1 Shock Tube Schematic

Rather, damage to the specimen is assessed after the event has taken place. There is also no recorded data presented for the temperature rise observed in the laminate [2]. The aim of this study is to develop a new testing method to simulate a lightning strike and capture progressive damage by simultaneously applying an acoustic shock and voltage to a carbon fiber specimen. Progressive damage is captured through the use of Digital Image Correlation and an infrared thermal camera, providing deformation and temperature data respectively. These independent measurements are then compared to a network of Fiber Bragg gratings (FBG) sensors.

Experimental Procedure

To simulate a lightning strike event on a carbon fiber reinforced polymer, two separate damage scenarios must occur simultaneously: a normal acoustic shock and resistive heating. Unlike the previous work in this area, the two damage types for this experimental setup are imposed by separate mechanisms. Resistive heating is still accomplished through a capacitive discharge circuit, but at much lower voltages than the work by Feraboli et al. and Hirano et al. [1, 2]. The acoustic shock is applied to the specimen using the shock tube located at North Carolina State University. A shock tube is an instrument often used to simulate bomb blasts by propagating a normal shockwave down. They are generally comprised of two sections, a driver section and a driven section, separated by a diaphragm. The driver section is filled with a high-pressure gas until the diaphragm bursts, and the incident shock wave propagates downstream to impact the sample, causing out-of-plane deformation (Fig. 24.1).

Sample Preparation

Samples prepared for the experiment are fabricated from 3 K plain woven carbon fiber and an epoxy/resin matrix system. Each sample consists of two or four plies of carbon, all aligned in the 0/90 orientation, and are constructed using a wet layup with vacuum-bagging. Once cured, both sides of the laminate need to be prepared for testing. First, on the impact-side of the sample, the leads for the application of the thermal load need to be attached. The leads are made from 15 mm x 25 mm pieces of brass shim with soldered wire connections. Brass leads were spaced at distances from 15 mm to 45 mm, denoted by the letter d in Fig. 24.2b. While carbon fibers themselves are fairly good conductors, the matrix is a dielectric [3]. Therefore, for a conductive path through the sample, the outer layer of the epoxy/resin matrix on the surface must be removed to expose the bare carbon by sanding the areas on the surface where the brass leads will be bonded. Once sanded and cleaned with acetone,

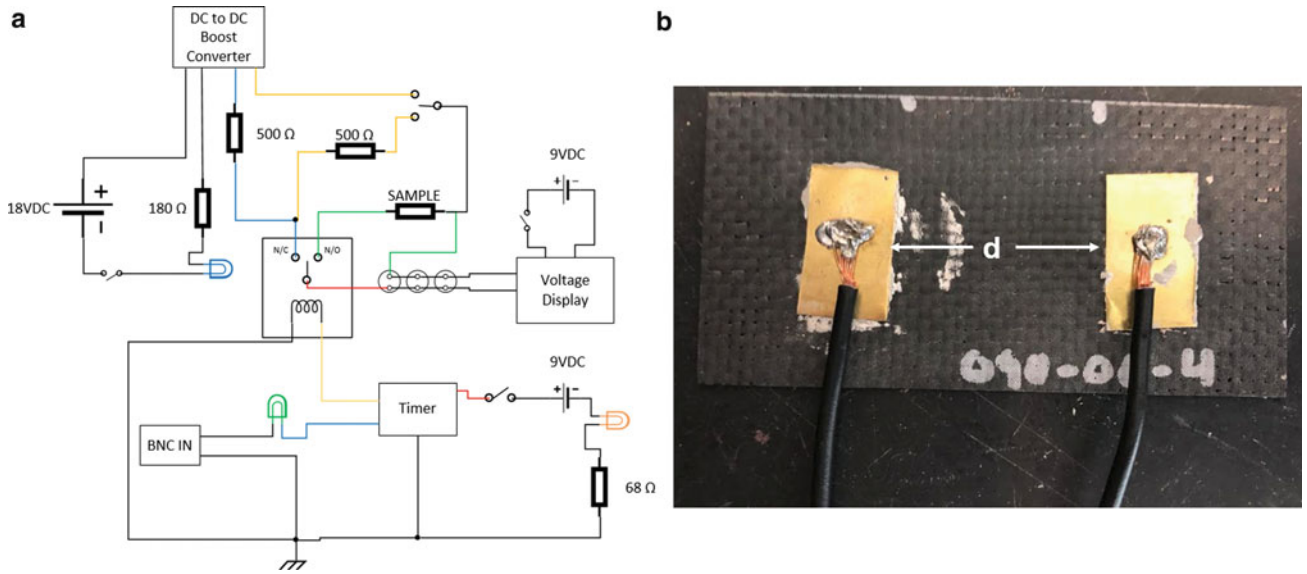

Fig. 24.2 (**a**) Lightning Strike Circuit Diagram and (**b**) Prepared Carbon Fiber Sample with bonded brass leads

the brass leads are then bonded to the prepared composite surface with a conductive silver epoxy. The FBG is placed on the center of the sample on the opposite side of the brass leads, with the fiber aligned with the global x-axis, such that the strain read from the FBG is compared with the global strain in x-direction from the DIC measurements. The FBG is then bonded to the sample using superglue. Once the FBG sensor is bonded, the sample is then speckled for DIC measurements.

Resistive Heating

The resistive heating component of the simulated lightning strike is applied to the sample through a capacitive discharging circuit. The full circuit diagram can be seen below in Fig. 24.2a. The entire circuit is powered by a single 9-volt battery, which is connected to a DC-DC Boost Converter. The boost converter amplifies the input voltage anywhere from 45 V to 392 V, adjusted by a potentiometer on the converter. When the circuit is activated, the three 1000 μF capacitors, connected in parallel, are charged to the desired voltage. When the trigger signal to discharge is received by the timer, a signal is then sent from the timer to the electromechanical solid-state relay to switch from the charging portion of the circuit to the discharging portion for the length of the discharge. Due to the high voltages and amperages associated with the application of the thermal loads, various safety features are also present in the circuit that don't affect its functionality, including safety switches, voltage displays, and light indicators.

Acoustic Shock

The impulse shock component of the simulated lightning strike is applied to the sample using the shock tube located at NC State University, seen below in Fig. 24.3. The driven section is filled with helium gas, and sheets of Mylar are used as breakable diaphragms. Samples are impacted with a burst pressure of 50–250 psi, measured by pressure transducers along the length of the tube. Due to the discharge that occurs during the impact, custom fixtures for clamping the samples were fabricated out of a glass-reinforced nylon. Not only did the newly designed fixtures allow for the wiring for the circuit and FBG sensors, but also provided an insulation to the rest of the shock tube, both for safety and to avoid the disturbance of pressure measurements.

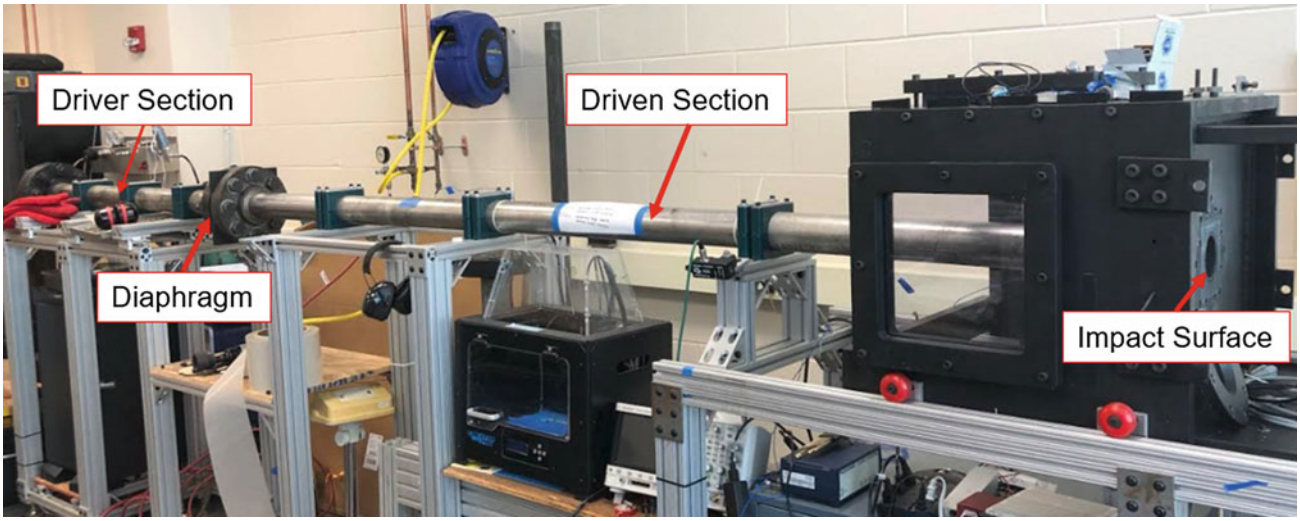

Fig. 24.3 Shock Tube located at North Carolina State University

Simulated Lightning Strike

To observe the maximum deformation in the sample from the two loading components, the impact is to occur at the time of maximum temperature rise on the impact surface of the sample. This is accomplished through the use of a programmable delay/impulse generator. Temperature measurements were found using an infrared thermal camera, capturing at 1000 frames per second, on the opposite surface from where the voltage is applied. Deformation measurements were found using high speed cameras, capturing at 100,000 frames per second, and Digital Image Correlation software VIC-3D, which are then compared to the FBG sensor that measures both.

Results

In order to understand the combined effects that occur locally during a heating and acoustic shock, and for the maximum damage from each load to occur simultaneously, both events must be well understood individually (Fig. 24.4). For the two and four layer samples, independent heating tests were conducted at various voltages to study the temperature profile as a function of time. Applied voltages ranged from 175 V to 260 V. Figure 24.5a, b show a typical temperature vs. time and the temperature profile at the maximum shown in Fig. 24.5a, respectively, on the opposite side of the sample. After the start of the discharge, which in its entirety lasts on the order of milliseconds, the temperature in the sample rises relatively quickly, reaching a maximum between 0.5 and 1.0 s. At this maximum average temperature, the temperature is highest at the attachment points, where the brass leads are bonded to the specimen, as expected.

Figure 24.6 shows the relationship between the maximum applied voltage and the maximum average temperature on the opposite side of the voltage application reached in the sample. It can be seen that increasing the voltage does lead to an increased temperature, though as the thickness of the sample increases, larger voltages have less of an effect on temperature rise.

Pure pressure tests were also conducted in order to establish a baseline for expected strain due to the acoustic shock only, as well as to compare the DIC calculated strain to the strain measured by the FBG sensor. Burst pressures for shock tube tests were between 45 psi and 130 psi. Figure 24.7a, b show the DIC measurement from a shock tube test, and the comparison of the measurement between DIC and the FBG sensor, respectively. It can be seen in Fig. 24.7b that the measurements between the two matched well.

With a benchmark for expected strain and temperature change due to the acoustic shock and resistive heating separately determined, and with the necessary data to properly synch the two events such that the acoustic shock occurs at the time of maximum temperature rise, the combined simulated lightning strike test can proceed.

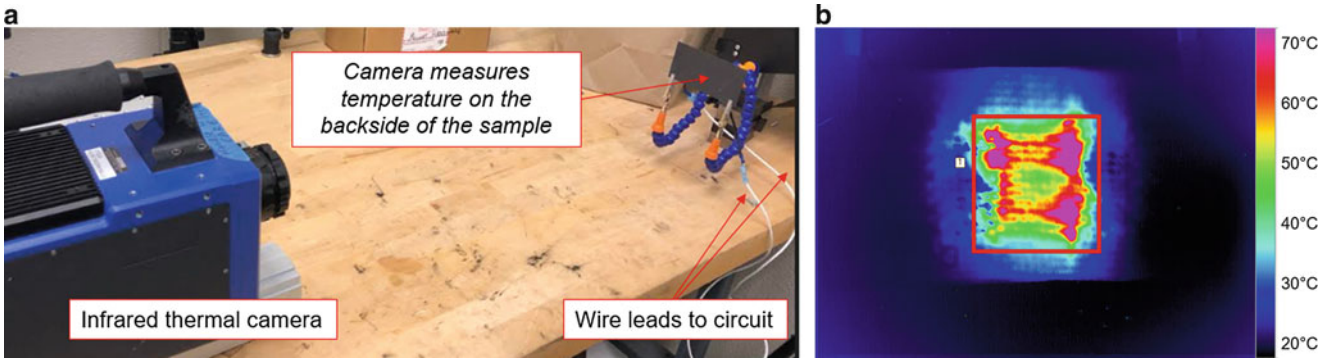

Fig. 24.4 (**a**) Resistive heating experimental setup showing the camera measures temperature on the backside of the specimen and (**b**) Infrared image of a sample at the maximum average temperature with the area defined brass leads defined

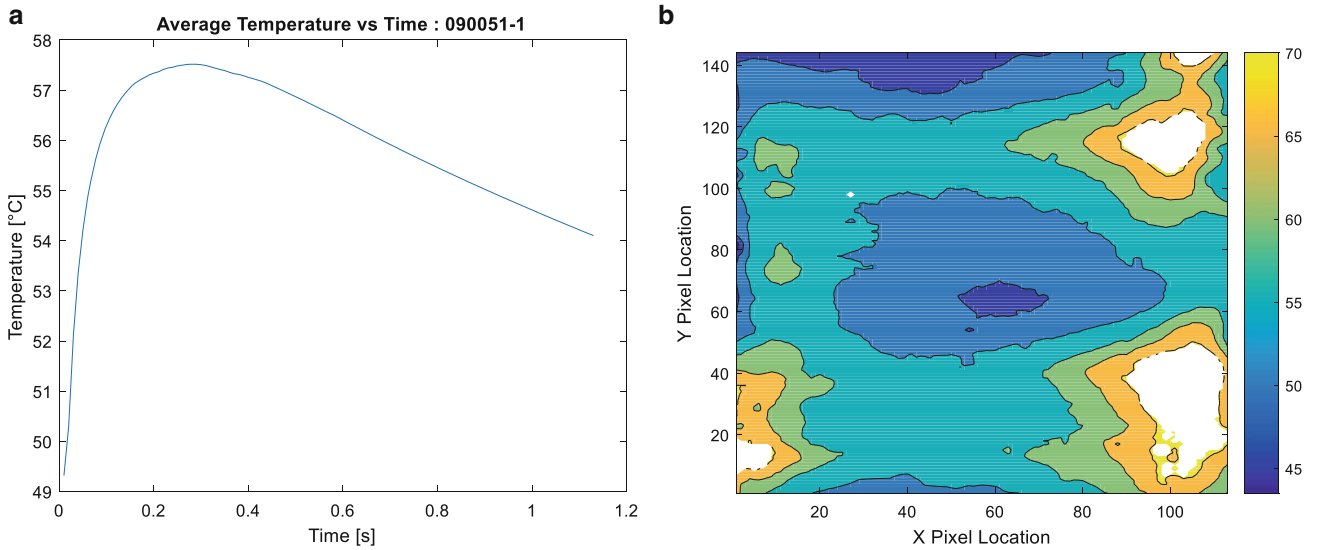

Fig. 24.5 (**a**) Average temperature between brass leads vs. time in the defined area and (**b**) Temperature profile of area between brass at maximum average temperature area

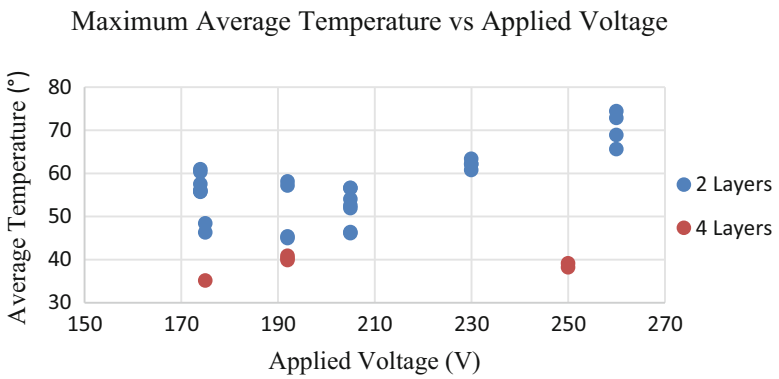

Fig. 24.6 Maximum Average Temperature vs. Applied Voltage

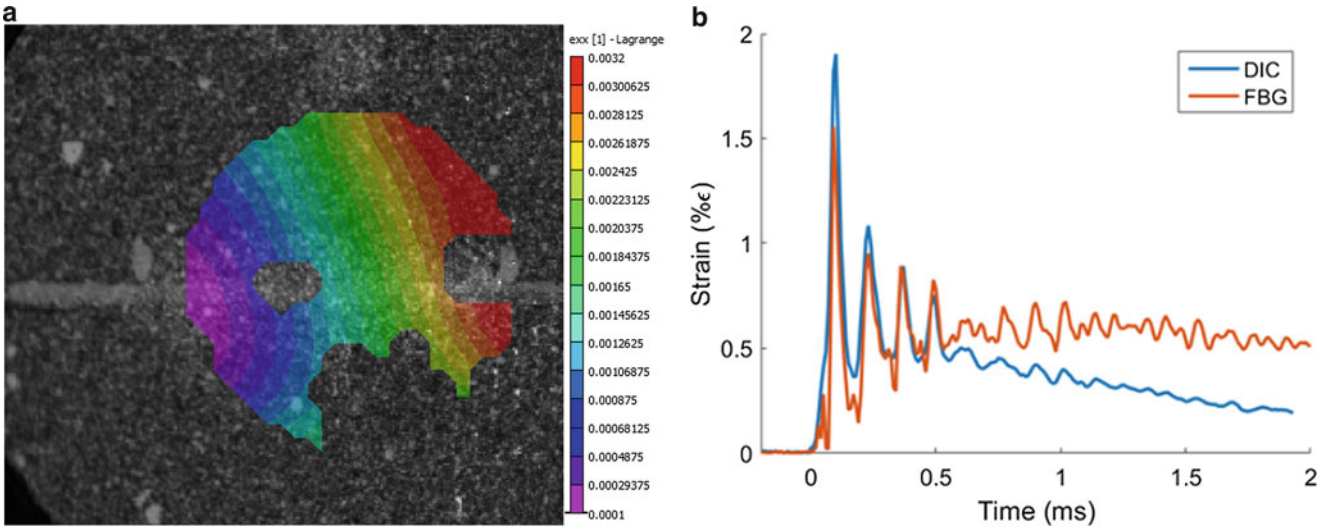

Fig. 24.7 (**a**) DIC measurement from a shock tube test and (**b**) Comparison of DIC and FBG measured strain vs. time

Conclusion

In this study, a new testing method for capturing damage in carbon fiber reinforced polymers subject to a Simulated Lightning Strike is developed. Unlike previous work, this method isolates the acoustic shock and resistive heating associated with a lightning strike on a composite wing, obtains temperature data, and looks to assess the damage and localizations progressively. Independent measurements of purely heating and purely deforming samples have provided the necessary data to combine the loads such that the acoustic shock impact occurs at the time of the maximum temperature rise in the sample, as well as a benchmark to compare to in order to understand the effect that the damages can have on one another.

References

1. Hirano, Y., Katsumata, S., Iwahori, Y., Todoroki, A.: Artificial lightning testing on graphite/epoxy composite laminate. Compos. A: Appl. Sci. Manuf. **41**(10), 1461–1470 (2010)
2. Feraboli, P., Miller, M.: Damage resistance and tolerance of carbon/epoxy composite coupons subjected to simulated lightning strike. Compos. A: Appl. Sci. Manuf. **40**, 954–967 (2009)
3. Zantout, A.E., Zhupanska, O.I.: On the electrical resistance of carbon fiber polymer matrix composites. Compos. Part A. **41**, 1719–1727 (2010)

Chapter 25
Overview of the First SHPB Experiments on Oriented Single Crystal Explosives

Christopher Meredith, Daniel Casem, Cheng Liu, Benjamin Morrow, Carl Cady, and Kyle Ramos

Abstract Under plate impact experiments (uniaxial strain) single crystal explosives exhibit elastic-plastic mechanical behavior, however at quasi-static rates (uniaxial stress) they are brittle. We have conducted Split-Hopkinson Pressure Bar (SHPB) experiments to bridge the strain rate gap between the two extremes in an effort to tease out the effects of strain rate and pressure on the plasticity, and to probe the mechanisms of failure in single crystal RDX, PETN and PBX9501. Samples were compressed in different crystallographic orientations to promote different proposed deformation and fracture mechanisms, while utilizing in-situ synchrotron X-ray diffraction, phase contrast imaging, or high speed visible light imaging. Researchers have postulated that in sub-shock impacts, the mechanisms of stress dissipation an explosive possesses are very important to "hot spot" formation—which initiates the first chemical reactions within an energetic. What is "unpredictable" or "stochastic" for an observer at the macroscale, might in fact, be deterministic when a complete understanding of the microscale physics is understood. This paper will focus on the development of the mini- and micro-Kolsky bars utilized in order to maximize the strain rate within the samples, the initial results on the mechanical behavior and fracture mechanisms of these high explosives, and the challenges we have encountered and overcome.

Keywords Single crystal explosives · Cyclotrimethylene trinitramine · Pentaerythritol tetranitrate · PBX9501 · Split-Hopkinson pressure bar

Introduction

Many accidents involving explosives begin as an unintended impulse upon a mass of an explosive formulation, either by dropping it or by an impact from an external object traveling at some velocity. The impact or impulse is usually a sub- or weak-shock that is not strong enough such that detonation immediately follows the impact. Thus, there is usually a deflagration to detonation transition or a sub-detonative explosion that risks injuring people or causing damage to property. These events are "unpredictable" because reactive models are not robust enough to predict the scenarios when simulations are run because the underlying physics is poorly understood. Thus, it is of critical importance that probing these sub-detonative regimes to gain a greater insight into the physical processes be undertaken to protect life and property.

The physics is reasonably well understood when a strong shock is input into an explosive because the shock creates enough heat such that the chemistry that leads to detonation occurs almost instantaneously. In the sub- or weak-shock regime, the impulse itself does not create enough heat to directly lead to detonation, but rather a combination of processes occur, creating a feedback loop, that can lead to detonation or an explosive event. These processes are hypothesized as pore collapse, pore jetting, explosive crystal fracture, shear localization, etc. [1–4] What all of these processes have in common, is that to fully understand which ones are dominant in a particular scenario requires Engineers/Scientists to factor in the underlying solid mechanics properties of the explosives. Typical explosives, RDX, PETN, HMX, etc., are molecular crystals with low symmetry crystal structures, orthorhombic, triclinic, etc. [5] Thus, they have highly anisotropic elastic [6] and inelastic properties [7–10]. Inelastic properties include plastic deformation mechanisms and fracture properties. Very little is understood about these properties, but they are generally brittle under low rate loading [11] and elastic-plastic under shock loading [9, 12–14].

C. Meredith (✉) · D. Casem
U.S. Army Research Lab, Aberdeen Proving Ground, Aberdeen, MD, USA
e-mail: christopher.s.meredith3.civ@mail.mil

C. Liu · B. Morrow · C. Cady · K. Ramos
Los Alamos National Lab, Los Alamos, NM, USA

L. E. Lamberson (ed.), *Dynamic Behavior of Materials, Volume 1*, Conference Proceedings of the Society for Experimental Mechanics Series, https://doi.org/10.1007/978-3-030-30021-0_25

This paper reports on the initial results obtained of the mechanical behavior of single-crystal RDX and PETN loading in different crystallographic directions at strain rates between 200 and 5000 s^{-1}. Additionally, the mechanical behavior of PBX9501 at 9000 s^{-1} is presented. The challenges we have encountered, their solutions, and the future work is detailed.

Experimental Procedures

High quality single crystals of RDX and PETN were grown at the explosive crystal lab at Los Alamos National Lab. In short, commercial RDX and PETN powders were dried, purified, and recrystallized. Then single crystals were grown by controlled evaporation in a solvent (acetone for RDX and ethyl acetate for PETN). When the correct saturation was reached, seed crystals were added to the solution and allowed to grow for a few weeks [9, 15]. X-ray diffraction was used to determine the crystallographic orientations of the grown crystals. For each explosive crystal, thin pucks of about 25 mm in diameter were cut such that the thickness direction corresponded to the desired loading direction, and both faces were polished flat and parallel. Cubic samples for the Split-Hopkinson Pressure Bar (SHPB) experiments were cut using a diamond wire saw equipped with a sample positioning stage. The stage had a micrometer for the exact positioning of multiple parallel cuts, and a rotation stage for rotating the puck 90° to make the second set of parallel cuts. During cutting, the puck was bathed in mineral oil for lubrication and to prevent any temperature rise in the puck, which are necessary to prevent the puck from fracturing. The diamond wire saw cutting process introduces very little damage or deformation into the individual samples, so no subsequent polishing of samples is required. Figure 25.1 shows the orientations loaded for the RDX and PETN single crystal samples. Some of the experiments were conducted at the Dynamic Compression Sector (DCS) at the Advanced Photon Source at Argonne National Lab and used the X-ray beam to probe the samples deforming using in-situ X-ray diffraction (XRD) or phase contrast imaging (PCI). Results from the XRD and PCI will not be presented in this paper. The plastic bonded explosive, PBX9501, consisting of 95% HMX, 2.5% Estane, and 2.5% BDNPA-F, was produced and pressed into a rectangular shape. Similarly to the single crystals, a puck of PBX9501 was cut and the diamond wire saw was used to create the PBX9501 samples.

The samples were loaded using the SHPB, where two separate sets of experiments were conducted. One set was conducted at DCS and utilized 4.76 mm (3/16″) diameter x 762 mm (30″) long incident and transmitted bars, and a 102 mm (4″) long striker. The second set were conducted at LANL and utilized 2.1 mm (0.083″) square x 203 mm (8″) long incident and transmitted bars, and a 25.4 mm (1″) long striker. The striker was 2.38 mm (3/32″) diameter which is impedance matched to the square bars. All bars from both sets of experiments were made of Al7075-T6. The sample size for the first

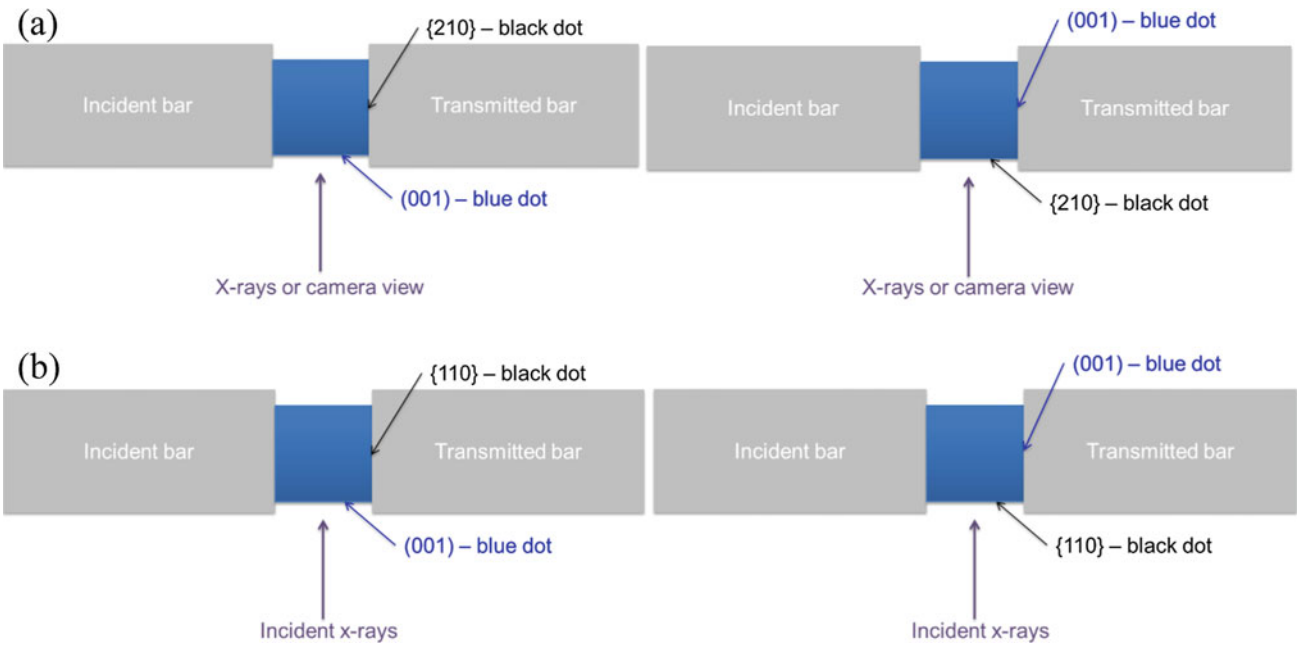

Fig. 25.1 Sample orientations that were produced and their placement in the SHPB for (**a**) RDX and (**b**) PETN single crystals

set of experiments with the 4.76 mm diameter bars was 2.7 mm cubes (nominal), and the square bars was 1.6 mm cubes (nominal). Strain gages were mounted on both sets of bars to determine the stress, strain, and strain rate in the sample using the conventional equations. Micro-Measurements EA-13-062AQ-350 gages were mounted diametrically opposite for the 4.76 mm diameter bars, and Kyowa KFG-1 N-120-C1-23 were mounted on opposite sides for the 2.1 mm square bars. For the experiments conducted a LANL, a Shimadzu HPV-X2 high speed camera recording at five million frame per second was used.

The 2.1 mm square bars were tried on purpose. The strengths of the materials tested are relatively low which results in low transmitted signals. With round bars and cubic samples, the diagonal of the cube has to be smaller than the diameter of the bar, which reduces the area ratio between the sample and bars. In order to increase the transmitted signal, square bars allow for a larger area ratio. The area ratio is 0.41 with the 4.76 mm diameter bars and 2.8 mm cubic samples, but the ratio is 0.58 between the 2.1 mm square bars and 1.6 mm cubic samples. Increasing the ratio for the PBX samples is more important because they are weaker, and have more ductility and, thus, expand more due to poisson's effect, than the single crystal explosive samples.

Results

The mechanical behavior is presented as engineering stress-strain (Figs. 25.2 and 25.3), where the given strain rates correspond to the strain rate at and just prior to failure. The drops in the curves following the peak stress indicate the samples have failed, i.e. they lose their load carrying ability.

Figure 25.2 shows the mechanical behavior for RDX in two loading directions, [210] and [001] at different dynamic strain rates. The lower strain rate experiments were performed on the 4.76 mm diameter bars, while the higher strain rates were from the 2.1 mm square bars. First, there is no clear strain rate effect for either direction, but the rates only differ by about one order of magnitude. Second, the compression strength is basically the same for both directions, within a large variation. Third, there is a small difference in the Young's Modulus, about 13 and 10 GPa for the [210] and [001], respectively. The final takeaway is there is little or no evidence for plasticity occurring. The samples fail in a brittle manner.

Figure 25.3 shows the mechanical behavior of PETN single crystals and PBX9501. The PETN was loaded with the 4.76 mm diameter bars and in two directions, the [110] and [001] (Fig. 25.3a). Even though we have only performed a few experiments, there appear to be clear differences between the loading direction and strain rate. First, the Young's Modulus and compression strength are lower for the [001] versus the [110]. The Young's Moduli are about 7 and 5 GPa for the [110] and [001], respectively. Second, there is large compression strength increase in the [110] at a strain rate of 1000 s^{-1} as compared to 300-400 s^{-1}. We have not performed any higher rate experiments in the other loading direction to determine if this increase occurs in the [001]. Finally, there is some evidence for plasticity, more so in the [001] because there could be yielding prior to the peak stress, as the slope of the curve drops. However, this is far from conclusive based on the limited number of experiments conducted, and would only represent a small amount of plasticity occurring. A few experiments

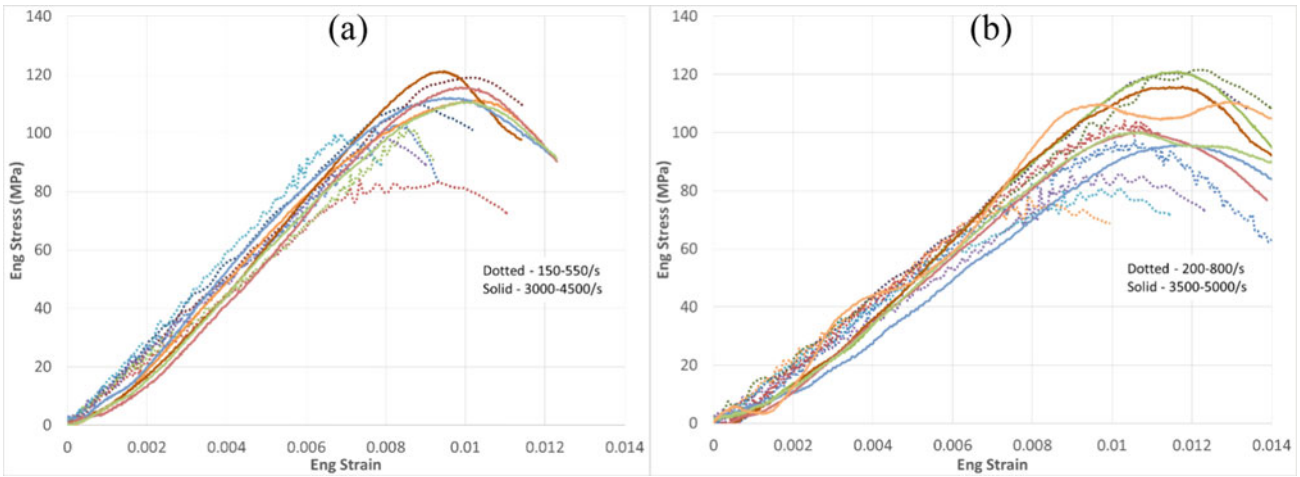

Fig. 25.2 Mechanical behavior of RDX single crystal samples loaded in the (**a**) [210] and (**b**) [001] at different strain rates

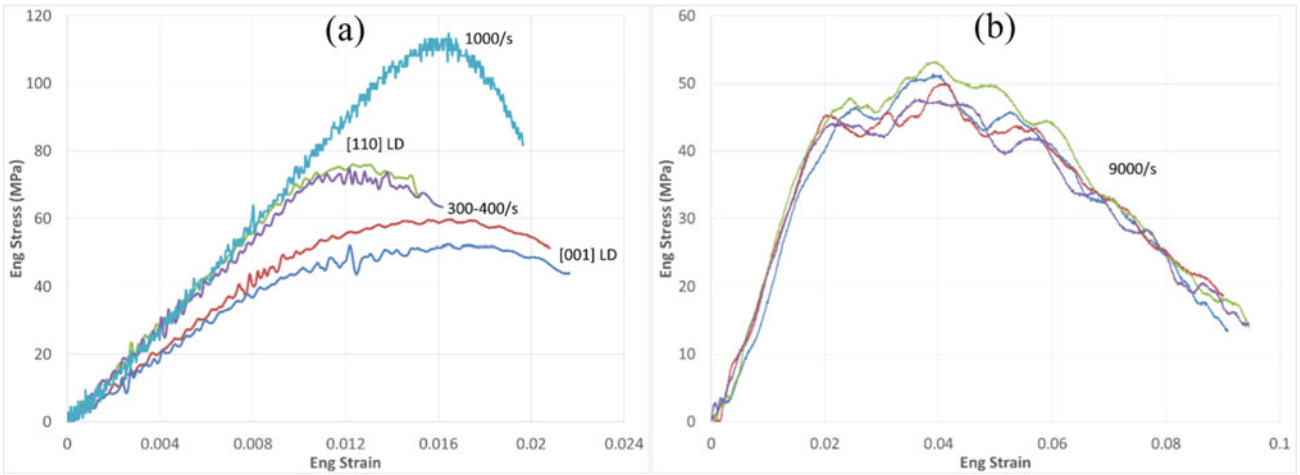

Fig. 25.3 Mechanical behavior of (**a**) PETN single crystal samples with different orientations, and (**b**) PBX9501

on PBX9501 are shown in Fig. 25.3b, where all of the samples were subjected to an average strain rate of approximately 9000 s^{-1}. The higher strain rate than the other experiments is due to the greater ductility present. The Young's Modulus is approximately 2.1 GPa, and there is "yielding" behavior, however this is different than the typical definition. Since the PBX9501 is compacted HMX crystals and binder, the "yield strength" corresponds to the point at which crystals start to fracture and move relative to each other. The elastic regime is mostly the compression of the binder. The large oscillations present following yielding is likely due to wave dispersion that's created as the wave passes through the very heterogeneous sample. As the samples continue to compress, it starts to break apart via poisson's effects because the crystals are only loosely bound together. As the sample continues to break apart, its load carrying ability decreases, but the "stickiness" of the binder keeps the sample from breaking apart completely, thus, it takes several percent engineering strain for the sample lose its load carrying ability. Note that converting to true stress-strain would likely be inappropriate because the sample is most likely not conserving volume, due to the sample breaking apart.

Overall, the RDX is stiffer, stronger, and more brittle than the PETN, however with the apparent large strain rate effect in the [110], the strength advantage mostly disappears. The PBX9501 is about half the strength of RDX and a bit lower in strength as compared to the PETN, however the strain rates are higher, and especially so versus the PETN experiments, so conclusive comparisons cannot be drawn.

Complications and Future Work

There have been a couple complications that we have overcome during these initial experiments. The most significant was cutting the single crystal explosive samples. They are very fragile (they can fracture just holding them due to thermal differences), and can easily be chipped when cutting. The small sample size only makes things more challenging, but with practice the samples are much better than they were in the beginning. Even with a "perfect" sample, the crystals themselves are never perfect. Each crystal has random defects that will increase the data scatter. The next complication was the square bars, which was a noble attempt at maximizing the transmitted signal, but there is possibly greater noise. Figure 25.4 shows the raw voltage-time data for the four strain gages for one of the RDX experiments. The strain gages are in the middle of each bar, so the reflected and transmitted waves should arrive at their respective gages at the same time (the time to travel through the sample is negligible). The vertical line is the start of the transmitted wave, however the reflected wave was rising a few microseconds before that. Additionally, the time difference between the arrival of the incident wave and the arrival of the incident (or transmitted) should be ~40 μs (5050 m/s wave speed in Al, which we measured). The timing is correct for the transmitted but not for the reflected. We have not seem this before with round bars, so it is unclear what is causing it. Both bars slid freely in the bushings, so clamped bushings cannot be the culprit. Since both strain gages do not rise together at the start of the reflected wave, there is likely a small bending component to the wave, but the timing and magnitude should not be affected as much as it is, if it was due to bending. However, in square bars certain bending modes might be more favorable because a square is not axis symmetric like a circle is, which could result in greater error relative to a round bar, but this is speculation.

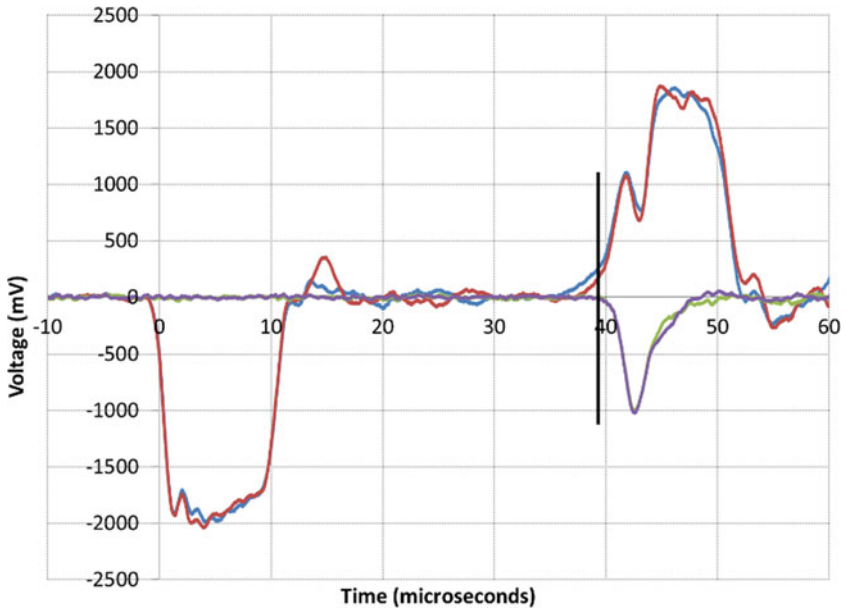

Fig. 25.4 Raw voltage-time data of an experiment on RDX using the 2.1 mm square bars

Future work will focus on miniaturizing the SHPB still further so that we can go to higher strain. One of the main goals is to maximize the achievable strain rate because this increases the likelihood that plasticity will occur. We will go down to a bar diameter of about 0.8 mm, which could increase the achievable strain rate by about an order of magnitude versus what is presented here. We have also been developing in situ measurements. Stokes/Anti-stokes Raman Thermography will be used to measure the temperature, and Impulsively Stimulated Light Scattering will measure the thermal diffusivity in situ. Additionally, Crossed Polarized Microscopy will reveal the microstructure of PBX formulations much more clearly, and the crystal orientations can be ascertained based on the light intensity differences between crystals. Further experiments will be conducted at DCS using in situ XRD and PCI. Taken together, these experiments will inform us on the active deformation and fracture mechanisms present in single crystal explosives and PBX formulations subjected to sub-shock impulsive loading. This will inform the modelers who will be able to run more accurate simulations of events which could cause an accident scenario, allowing for countermeasures to be employed before an accident occurs.

Acknowledgements Thanks to Nick Sinclair (DCS, WSU), Adam Schuman (DCS, WSU), and Nick Lorenzo (ARL) for their help with experiments at DCS. This publication is based upon work performed at the Dynamic Compression Sector, which is operated by Washington State University under the U.S. Department of Energy (DOE)/National Nuclear Security Administration award no. DE-NA0002442. This research used resources of the Advanced Photon Source, a DOE Office of Science User Facility operated for the DOE Office of Science by Argonne National Laboratory under contract no. DE-AC02-06CH11357.

References

1. Bowden, F.P., Mulcahy, M.F.R., Vines, R.G., Yoffe, A.: The Detonation of Liquid Explosives by Gentle Impact. The Effect of Minute Gas Spaces. Proc. Roy. Soc. London. Ser. A. **188**, 291 (1947)
2. Bowden, F.P., Stone, M.A., Tudor, G.K.: Hot Spots on Rubbing Surfaces and the Detonation of Explosives by Friction. Proc. Roy. Soc. London. Ser. A. **188**, 329 (1947)
3. Bowden, F.P., Gurton, O.A.: Initiation of Solid Explosives by Impact and Friction: The Influence of Grit. Proc. Roy. Soc. London. Ser. A. **198**, 337 (1949)
4. Bowden, F.P., Chaudhri, M.M.: Initiation of Explosion in AgN3 and b-PbN6 Single Crystals by a Collapsing Bubble. Nature. **220**, 690 (1968)
5. Miller, G. R., Garroway, A. N.: A Review of the Crystal Structures of Common Explosives Part I: RDX, HMX, TNT, PETN, and Tetryl. Naval Research Lab Report, NRL/MR/6120-01-8585, (2001)
6. Hooks, D.E., Ramos, K.J., Bolme, C.A., Cawkwell, M.J.: Elasticity of crystalline molecular explosives. Propellants Explos. Pyrotech. **40**, 333 (2015)
7. Dick, J.J.: Effect of crystal orientation on shock initiation sensitivity of pentaerythritol tetranitrate explosive. Appl. Phys. Lett. **44**, 859 (1984)
8. Dick, J.J., Ritchie, J.P.: Molecular mechanics modeling of shear and the crystal orientation dependence of the elastic precursor shock strength in pentaerythritol tetranitrate. J. Appl. Phys. **75**, 2728 (1994)

9. Hooks, D.E., Ramos, K.J., Martinez, A.R.: Elastic-plastic shock wave profiles in oriented single crystals of cyclotrimethylene trinitramine (RDX) at 2.25 GPa. J. Appl. Phys. **100**, 024908 (2006)
10. Ramos, K. J., Cawkwell, M. J., Bolme, C. A., Hooks, D. E.: Effects of orientation, pressure/strain rate, and microstructure on the quasi-static deformation and shock response of single crystal explosives Carney, J. R., Maienschein, J. L. (eds.) 15th International Detonation Symposium (2017) Office of Naval Research, Arlington (in press)
11. Rae, P. J., Hooks, D. E., Liu, C.: The Stress Vs. Strain Response of Single b-HMX Crystals in Quasi-Static Compression, in 13th Symposium (International) on Detonation, Norfolk, VA, USA, (2006), p. 293
12. Dick, J.J., Hooks, D.E., Menikoff, R., Martinez, A.R.: Elastic-plastic wave profiles in cyclotetramethylene tetranitramine crystals. J. Appl. Phys. **96**, 374 (2004)
13. Cawkwell, M.J., Ramos, K.J., Hooks, D.E., Sewell, T.D.: Homogeneous dislocation nucleation in cyclotrimethylene trinitramine under shock loading. J. Appl. Phys. **107**, 063512 (2010)
14. Ramos, K.J., Hooks, D.E., Sewell, T.D., Cawkwell, M.J.: Anomalous hardening under shock compression in (021)-oriented cyclotrimethylene trinitramine single crystals. J. Appl. Phys. **108**, 066105 (2010)
15. Whitley, V.H., Hooks, D.E., Ramos, K.J., Pierce, T.H., O'Hara, J.F., Azad, A.K., Taylor, A.J., Barber, J., Averitt, R.D.: Orientation dependent far-infrared terahertz absorptions in single crystal pentaerythritol tetranitrate (PETN) using terahertz time-domain spectroscopy. J. Phys. Chem. A. **115**(4), 439–442 (2011)

Chapter 26
Hydrodynamic Richtmyer-Meshkov Instability of Metallic Solids Used to Assess Material Deformation at High Strain-Rates

Joseph D. Olles, Matthew Hudspeth, Christopher F. Tilger, Christopher Garasi, Nathaniel Sanchez, and Brian Jensen

Abstract Material strength properties for metals under shock loading conditions were investigated using high-fidelity, ultra-high-speed X-ray diagnostics. High-strain rate Richtmyer-Meshkov instability (RMI) experiments were performed with an explosive powder driven gas gun at the Advanced Photon Source (APS) located at Argonne National Laboratory. Metal targets (copper and aluminum) with a prescribed sinusoidal interface, were studied using photonic Doppler velocimetry (PDV) and X-ray phase contrast imaging (PCI). The metal targets were impacted at velocities up to ~2.25 mm/μs with subsequent maximum strain rates ranging between 10^7–10^8 s^{-1}. The instability was recorded using X-ray PCI having a spatial resolution of 2–3 microns with sub-nanosecond exposures. Due to the constructive/destructive interference of X-rays and other challenges with artifacts associated with PCI, edge extraction must be robust against deviations in brightness, contrast, and noise. For the experimental images, a phase congruency feature detection algorithm outputs quantitative descriptors of edges for the metal jet size and shape. Computational hydrocode simulations were used to fit parameters for various strength models, with good agreement. The spatial and temporal resolution of our measurements allow validation and expansion of previously documented literature on these materials.

Keywords High strain-rate material strength · Shock physics · Richtmyer-Meshkov instability · X-ray phase contrast imaging

Introduction

Shock waves generated from impact systems; gas gun, powder gun, or explosive driver, are typically on the order of picoseconds to microseconds in duration, with velocities in the km s^{-1}. Traditional shock wave measurements are used to study deformations, phase transitions, equation of state, and material strength. Material strength at high strain-rates is of significant interest to the condensed matter community. Post-shock material strength is difficult to calculate due to generation of well-defined loading conditions, where the evidence of strength is overdriven in high-pressure 1-D loading cases. In order to model material deformations, analytically or through simulation, the behavior relevant physical characteristics need to be addressed.

Here oxygen-free high thermal conductivity copper (Cu) and 1100 aluminum alloy(Al) are investigated under extreme conditions in an untamped environment, metal/vacuum interface, where the Atwood number is -1. To intensify the sensitivity of the material strength property of interest in a post-shock state, a Richtmyer-Meshkov instability (RMI) experiment was utilized. From a 1-D loading of a plate impactor, this technique gives access to non-planar deformation, thereby exhibiting the presence of strength. By taking advantage of Argonne National Laboratory's Advanced Photon Source (APS), we show

J. D. Olles (✉) · M. Hudspeth · C. Garasi
Sandia National Laboratories, Albuquerque, NM, USA
e-mail: jdolles@sandia.gov

C. F. Tilger · N. Sanchez · B. Jensen
Los Alamos National Laboratory, Los Alamos, NM, USA

L. E. Lamberson (ed.), *Dynamic Behavior of Materials, Volume 1*, Conference Proceedings of the Society for Experimental Mechanics Series, https://doi.org/10.1007/978-3-030-30021-0_26

the current spatial and temporal resolution capabilities of X-ray phase contrast imaging (XPCI). This work validates and expands upon many previous works of strength at high-strain rate for metals [1, 2], where displacement of jetting material is typically the basis of the diagnostic used for material strength model creation.

Background

Traditionally, RMI experiments were performed using a two fluid system, where compressibility can be accounted for [3, 4]. More recently, the condensed matter physics community has begun to investigate the utility to infer material strength under high-strain conditions [1, 5, 6]. In this work, RMI experiments were performed using a Cu or Al target with a perturbed free surface which is impulsively accelerated from a shock wave. The shock compression in the target is generated from a powder gun driven Cu impactor at a measured velocity, u_0. All of these experiments were conducted within the Dynamic Compression Sector, Sector 35, at APS using the powder gun for the relatively quick turn-around time between shots (~1–2 h).

The perturbations in the Cu or Al target are machined using a wire electrical discharge machining (EDM). The initial machined perturbations are a well-defined sinusoid, having wavelength, λ, and amplitude, η_0. When the shock breaks out of the perturbation, at the metal/vacuum interface, the large density gradient causes instability growth of a jet (or spike) and bubble. Dependent upon the material strength, the jet displacement, η, growth rate, $\dot{\eta}$, and shape of the ejecting material is reminiscent of the traditional fluid experiments. A schematic of the shock impact, and subsequent profile, is sown in Fig. 26.1.

To measure the RMI instability, the velocity of the jet and impactor were measured using photonic Doppler velocimetry (PDV) [7, 8]. For all of the experiments, frequency-shifted PDV [9] was utilized, where two fiber lasers were set slightly off-frequency from one another with wavelengths near 1550 nm. One laser was sent to the target and the other used as a reference. A single mode collimated gradient-index (GRIN) lens probe, having approximately 0.5 mm spot size, was used to send and receive the light passing through a circulator. The return and reference light were combined to create a beat frequency in a fiber optic receiver, then digitized and recorded with an oscilloscope. The recorded beat frequency indicates the velocity of a reflective surface, here the impactor and jet.

To validate the velocity and gather the jet profile XPCI was used at Argonne's APS in the DCS [10, 11]. A four-camera system acquired eight images of successive X-ray pulses from each shot. Images were acquired during 24-bunch mode, using a first harmonic undulator with white beam tuned to ~18 keV. The beam is operated in standard mode with one 80 ps pulse (33.5 ps FWHM) every 153.4 ns, and a slow shutter (60 ms) synchronized with the impactor (projectile) launch. The camera frames consisted of 1024x1024 pixel images, and having a pixel resolution of ~2.5 μm with the optical setup used [6, 12]. The X-rays are manipulated to generate a spatially coherent beam where a propagation based, phase diffraction effect is observed on a scintillator. XPCI is a technique sensitive to refractive Features within the beam path are enhanced by contrast such as edges or voids, which are proportional to density. A schematic of the entire setup, powder gun/impactor, target, X-ray beam path, scintillator, and collecting optics can be seen in Fig. 26.2.

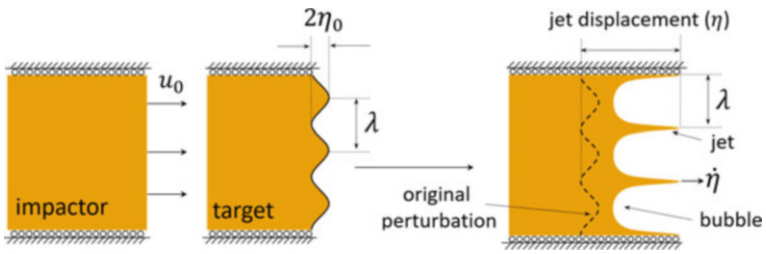

Fig. 26.1 Schematic of impactor and target with perturbations. (LEFT) impactor has a defined velocity u_0 which drives a shock into the target having a set wavelength, λ, and amplitude

Analysis

The metal perturbation (wavy) targets are critical to the output of RMI experiments and viability to accurately simulate computationally. Typical samples of machined targets are shown in Fig. 26.3.

In order to define the sinusoidal surface of the machined targets, a Dektak profilometer was utilized. Profiles of all the targets were collected and a sinusoid was fit numerically. Table 26.1 reports the deviation of the target's designed, measured,

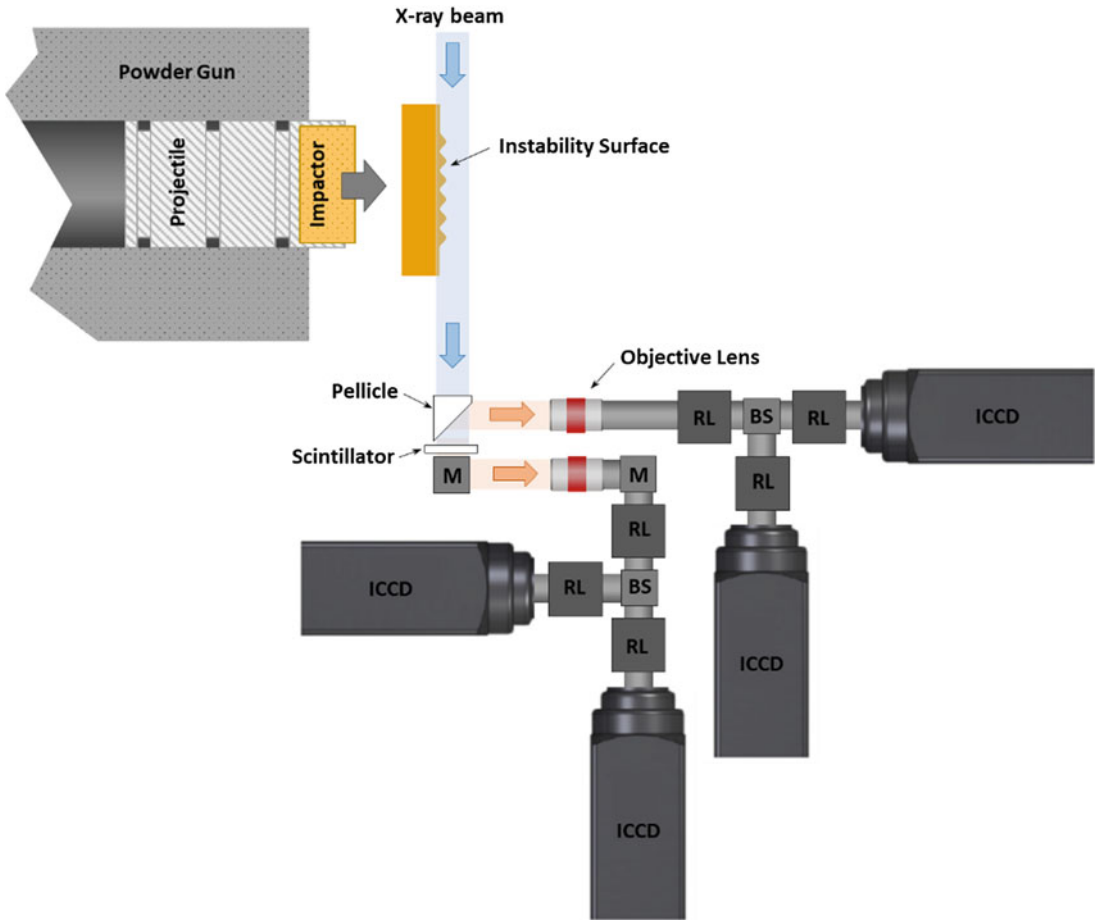

Fig. 26.2 Schematic of experimental setup used at Argonne's APS DCS for shock compression of target with perturbations. X-ray phase contrast imaging is used to capture Richtmyer-Meshkov instability. Item abbreviations are as follows: *ICCD* intensified charge-coupled device, *M* mirror, *RL* relay lens, *BS* beam splitter

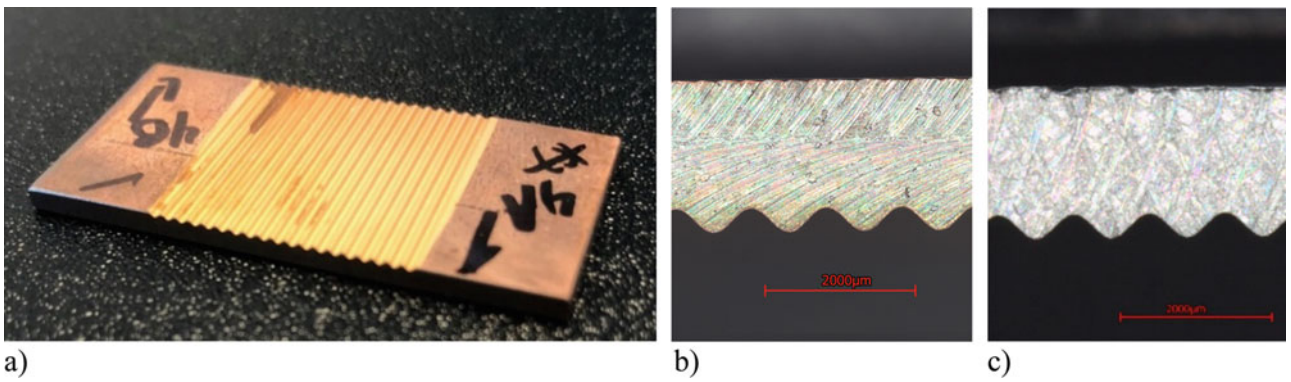

Fig. 26.3 Typical samples of machined metal targets. (**a**) Macro-image of a Cu target manufactured using wire EDM. Side profiles of targets imaged using a digitized microscope are shown with the perturbation surface enlarged of Cu (**b**) and Al (**c**)

and standard deviation of the mean wavelength, λ, mean peak-to-trough amplitude, $2\eta_0$, and the resultant wavenumber, $\eta_0 k$. The wavenumber often can give insight into the regime the RMI will undergo; from little to no jet growth at wavenumbers close to zero, to growth and arrest, and growth and breakup as the wavenumber approaches and goes beyond one [1, 2]. These targets were designed to ensure jet growth occurred and evaluate the level, if any, of jet arresting within the experimental setup.

The high-speed XPCI image sets acquired during the experiment have good contrast between the image intensity of the features, I, and the background, I_b, $(I - I_b)/I_b \approx 7$. An examination of the experimental XPCI images indicates that the interfacial features will appear as a gradient (step) in intensity. The width of this intensity step is approximately 10 pixels for static images and grows to ~15 pixels in the centerline region of the fastest jets. This static gradient is caused by the imaging system and optics, whereas the larger dynamic width is likely due to the less uniform object in the X-ray axis. A dark field, bright field, and static image is also acquired on each image channel before the dynamic experiment is performed. The set of these images, except for the dark fields, effectively show the same underlying grain pattern originating from the scintillator, camera sensor, and/or experimental geometry. Some of this noise can be addressed with a background subtraction routine. After these preprocessing steps, the dynamic images still present constructive/destructive interference of X-rays and other challenges with artifacts associated with XPCI. Edge extraction must be robust against deviations in brightness, contrast, and noise.

The robust edge extraction for the experimental images, utilized a phase congruency feature detection algorithm that outputs quantitative descriptors of edges for the metal jet size and shape [13, 14]. This edge finding implementation forms a non-biased edge estimator by comparing the local response of the experimental image to Gabor filters of various length scales and orientations. By isolating even and odd responses, an estimator for edge type (step, bright line, or dark line) is also generated.

The matrix of edge estimators is then horizontally and vertically raked to obtain a collection of points estimating a parameterized curve which maps the metal interface. A final calculation of the interface position is determined by extracting the maximum edge strength estimator location on a line segment locally normal to each of a series of equidistant points along this curve. These steps are repeated for the static and dynamic images of each experiment. The curves can be mathematically manipulated to provide crest and trough positions, jet lengths, etc. However, the unique lobes that evolve in time at tips of the jets preclude transforming the parametric form of the curve into a more convenient two-dimensional function, $y = f(x)$, illustrated clearly by a failure of the vertical/horizontal line test.

Experiments were performed at two nominal impact velocities, 1.0 and 2.2 km s^{-1}. The eight-image sequences, from the XPCI, in Figs. 26.4 and 26.5 shows the evolution of the jet growth as predicted [1]. The bubble region of the RMI however, does not reflect the traditional pure fluids description. The bubble appears to provide mass to allow jet growth but shows damage in the form of spall or shear zone. This damage is more pronounced in the higher impact velocity experiment, Fig. 26.5.

Table 26.1 Description of image

	Designed [mm]	Measured [mm]	Standard deviation [mm]
Mean λ	1	1.0098	0.027
Mean $2\eta_0$	$1/(2\pi)$	0.303	0.010
$\eta_0 k$	1	0.94	

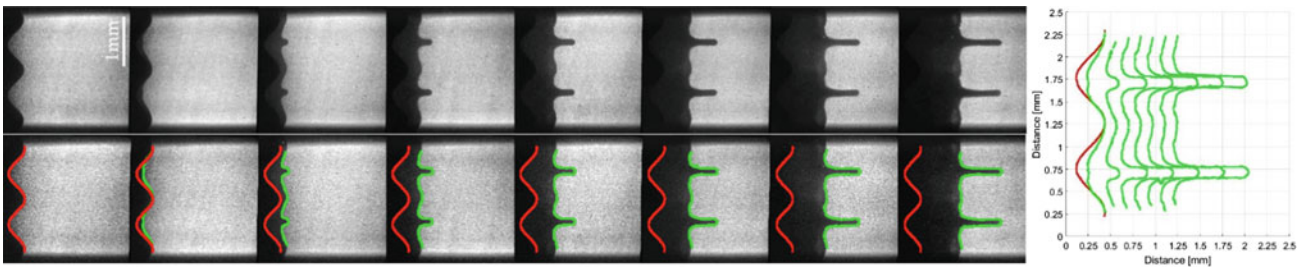

Fig. 26.4 Eight-image sequence of Cu target impacted at approximately 1.0 km s^{-1}. Top sequence, interframe time is 153.4 ns, shows processed images to reduce noise and set intensity to same range within the sequence. Bottom sequence has overlay of extracted edges, original perturbation in red, and dynamic jet profile in green. The plot to the right shows the extracted edges of each image

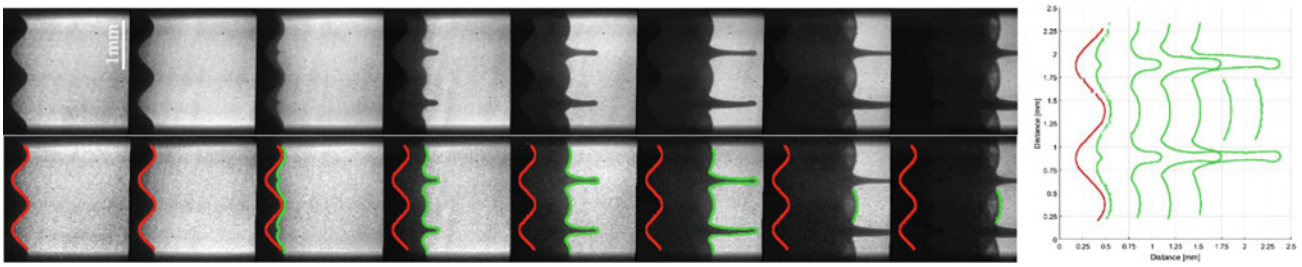

Fig. 26.5 Eight-image sequence of Cu target impacted at approximately 2.2 km s^{-1}. Top sequence, interframe time is 153.4 ns, shows processed images to reduce noise and set intensity to same range within the sequence. Bottom sequence has overlay of extracted edges, original perturbation in red, and dynamic jet profile in green. The plot to the right shows the extracted edges of each image

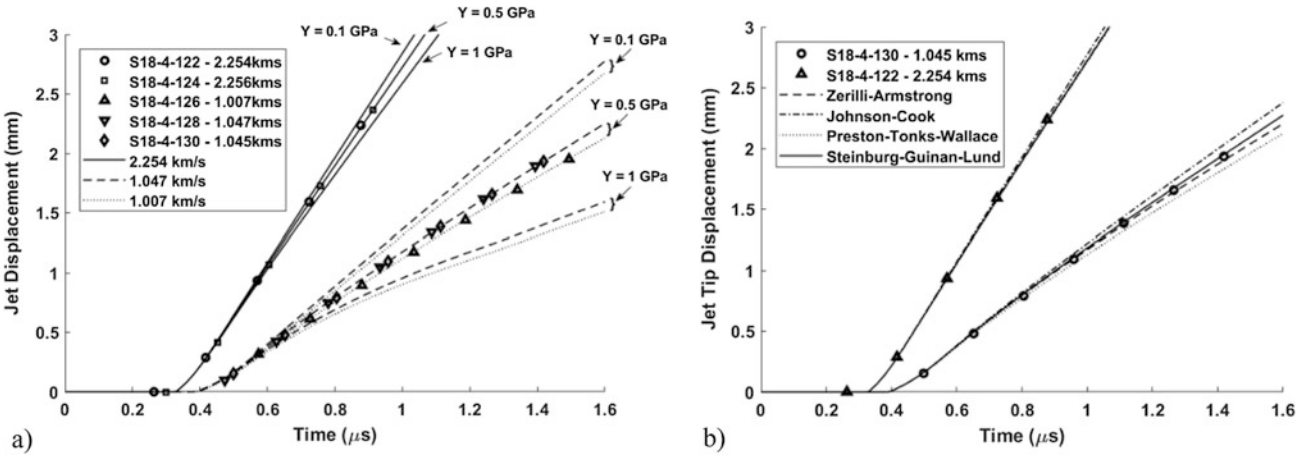

Fig. 26.6 Computationally simulated experiments using (**a**) EPP and (**b**) standard strength models in CTH. Yield strength was tuned to fit experimental jet displacement data collected

Computational simulations were performed in CTH [15] where the experimental geometry and impact conditions were prescribed. Performing a parametric sweep of the material strength, the simulations were tuned using the extracted jet displacement in time. A simple elastic-perfectly plastic (EPP) model was used, shown in Fig. 26.6a), with good agreement to the extracted jet displacement data. A yield stress, Y, of 0.5 GPa aligns well to both sets of impact velocities. The lower impact velocity does show a greater sensitivity to changes in Y. Other, more complex, material strength models were used and showed good agreement, shown in Fig. 26.6b), again the lower impact velocity case showed the greatest senility to the model used. With the more complex strength models tested, the Steinburg-Guinan-Lund and Zerilli-Armstrong appeared to match throughout the data collected.

Velocity data from the experiments was also collected, and as shown in previous works [1, 2] can be used to infer yield strength of a material either analytically or computationally. PDV data from the RMI growth has a relatively well-defined jet profile, however the bubble region almost immediately following breakout has a broad range in velocities. This is apparent due to the probe spot size and the target λ being close in size, and as seen in the bubble region of Figs. 26.4 and 26.5, spallation and shear zones cause an initially large spread in measured velocities. Still this data was utilized as verification of the image dataset, by overlaying the mean velocity (due to interframe time) from the extracted images and also correlating to the simulated traces from CTH. Figure 26.7 shows that the mean velocity from the images aligns well, the simulated trace was not shown for clarity, but matches within a 2%.

Experiments for Al were also conducted and showed similar results to the Cu shots. The i mages in Figs. 26.8 and 26.9 show jet growth, as expected, but dramatic damage in the form of spall and shear zones in the bubble region. The damage in the bubble region is even more visible with Al than the Cu case. The experimental images have been processed and edges extracted, and analysis of Al jetting can be performed similarly to copper (displacement and velocity) to tune material strength.

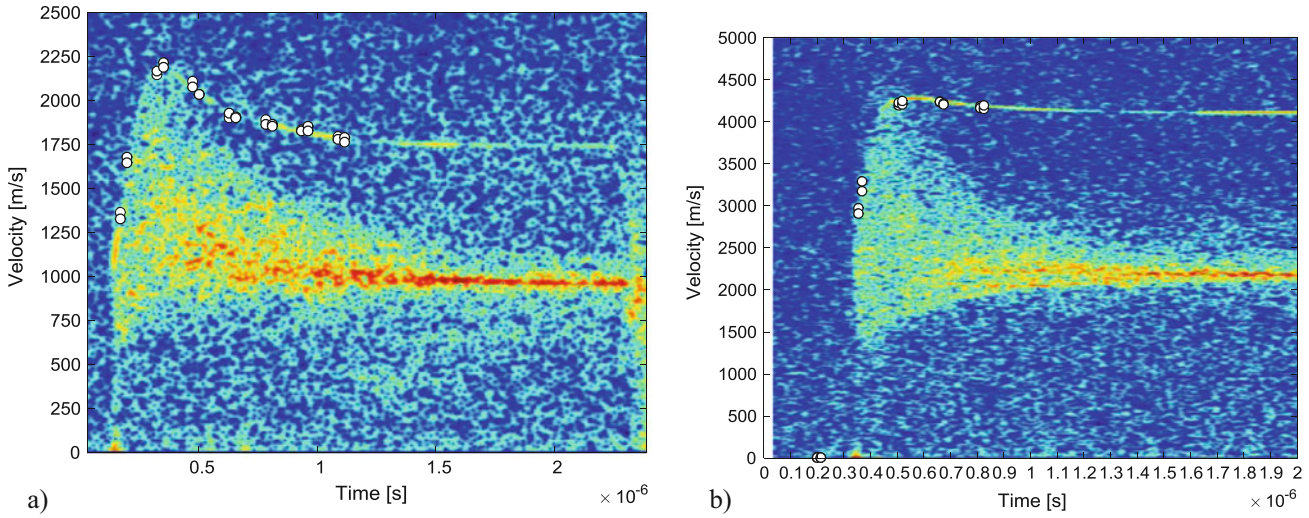

Fig. 26.7 Spectrograms of (**a**) shot 128 Cu impacted at 1047 m s^{-1} (**b**) shot 122 Cu impacted at 2254 m s^{-1}. Extracted mean velocity from the images of shot 128 and 130 shown overlayed on the spectrogram with white circles in (**a**) and images from shot 122 and 124 in (**b**). The maximum jet velocity from the PDV trace is (**a**) 2200 m s^{-1} [CTH simulation 2221 m s^{-1}] (**b**) 4285 m s^{-1} [CTH simulation 4289 m s^{-1}]

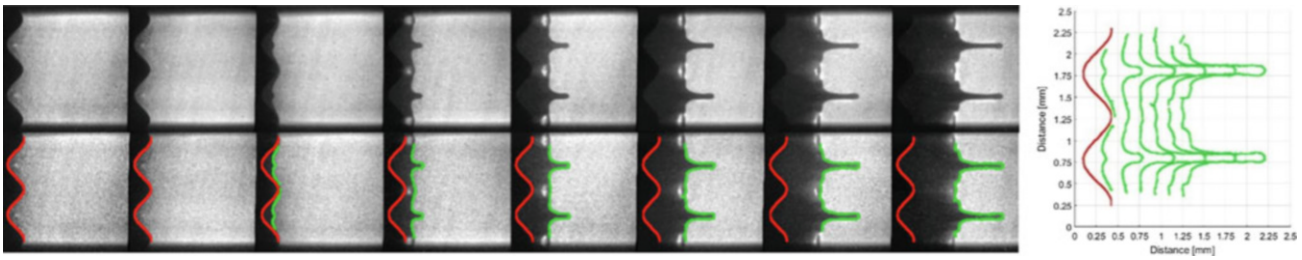

Fig. 26.8 Eight-image sequence of Al target impacted at approximately 1.0 km s^{-1}. Top sequence, interframe time is 153.4 ns, shows processed images to reduce noise and set intensity to same range within the sequence. Bottom sequence has overlay of extracted edges, original perturbation in red, and dynamic jet profile in green. The plot to the right shows the extracted edges of each image

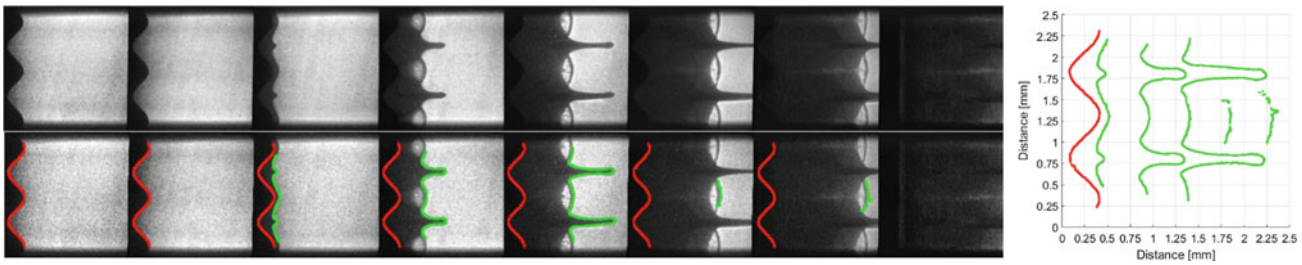

Fig. 26.9 Eight-image sequence of Cu target impacted at approximately 2.2 km s^{-1}. Top sequence, interframe time is 153.4 ns, shows processed images to reduce noise and set intensity to same range within the sequence. Bottom sequence has overlay of extracted edges, original perturbation in red, and dynamic jet profile in green. The plot to the right shows the extracted edges of each image

Conclusion

Here, RMI experiments were shown for Cu and Al to investigate material strength and the fidelity of using high resolution ultrafast XPCI from Argonne's synchrotron source. Multiple shots at the same impact velocity were performed to show repeatability. The jet displacement and velocity align well with previously published data and we showed similar yield stress from computational simulations. Various material strength models were used, and it appears a simple EPP model captures the material strength of Cu accurately for the strain rates tested.

Interesting behavior was shown to occur within the bubble region of the RMI. To the authors knowledge, this phenomenon has never been shown for these materials. This new data and use of the diagnostic allows for the study of damage such as

spall (crazing) and shear zones seen during RMI with micron resolution. Also, now microscale hydrocode simulations can be used for model validation by calibrating strength, not only based on velocity, but size/shape/and length of jet tip.

Acknowledgements The authors would like to thank J. Patrick Ball, Ben Hanks (Sandia National Laboratories), Adrian Akinci, Patrick Kennedy, and Marshall Maez (Los Alamos National Laboratory) for target preparation, and Nicholas Sinclair, Adam Schuman, and the DCS team (WSU and Argonne National Laboratory) for projectile fabrication, gun setup, and shot execution. Sandia National Laboratories is a multi-mission laboratory managed and operated by National Technology and Engineering Solutions of Sandia, a wholly owned subsidiary of Honeywell International Inc., for the U.S. Department of Energy's National Nuclear Security Administration under contract DE-NA0003525. Los Alamos National Laboratory is operated by Los Alamos National Security, LLC for the U.S. Department of Energy (DOE) under Contract No. DE-AC52-06NA25396.

References

1. Dimonte, G., et al.: Use of the Richtmyer-Meshkov instability to infer yield stress at high-energy densities. Phys. Rev. Lett. **107**(26), 264502 (2011)
2. Prime, M.B., et al.: Using growth and arrest of Richtmyer-Meshkov instabilities and Lagrangian simulations to study high-rate material strength. J. Phys. Conf. Ser. **500**, 11.. IOP Publishing (2014)
3. Richtmyer, R.D.: Taylor instability in shock acceleration of compressible fluids. Commun. Pure Appl. Math. **13**(2), 297–319 (1960)
4. Meshkov, E.E.: Instability of the interface of two gases accelerated by a shock wave. Fluid Dyn. **4**(5), 101–104 (1969)
5. Piriz, A.R., et al.: Richtmyer-Meshkov instability in elastic-plastic media. Phys. Rev. E. **78**(5), 056401 (2008)
6. Jensen, B.J., et al.: Jet formation in cerium metal to examine material strength. J. Appl. Phys. **118**(19), 195903 (2015)
7. Lowry, M., et al.: Photonic Doppler velocimetry. Tech. Rep. (Lawrence Livermore National Laboratory (LLNL), Livermore, CA (1999)
8. Jensen, B.J., et al.: Accuracy limits and window corrections for photon Doppler velocimetry. J. Appl. Phys. **101**(1), 013523 (2007)
9. Strand, O.T., et al.: Compact system for high-speed velocimetry using heterodyne techniques. Rev. Sci. Instrum. **77**(8), 083108 (2006)
10. Willey, T.M., et al.: X-ray imaging and 3D reconstruction of in-flight exploding foil initiator flyers. J. Appl. Phys. **119**(23), 235901 (2016)
11. Jensen, B.J., et al.: Dynamic experiment using impulse at the advanced photon source. J. Phys. Conf. Ser. **500**, 4.. IOP Publishing (2014)
12. Luo, S.N., et al.: Gas gun shock experiments with single-pulse x-ray phase contrast imaging and diffraction at the Advanced Photon Source. Rev. Sci. Instrum. **83**(7), 073903 (2012)
13. Kovesi, P.: Image features from phase congruency. Videre. **1**(3), 1–26 (1999)
14. Kovesi, P.D.: MATLAB and Octave Functions for Computer Vision and Image Processing. In: Peter's Functions for Computer Vision. Centre for Exploration Targeting, School of Earth and Environment, The University of Western Australia, Crawley. www.peterkovesi.com/matlabfns/
15. McGlaun, J., Thompson, S., et al.: Sandia National Laboratories report SAND89–0607 (1989)

Chapter 27
Combined Compression and Shear Impact Response of Polycrystalline Metals at Elevated Temperatures

Bryan Zuanetti, Tianxue Wang, and Vikas Prakash

Abstract In this paper, we present results from a series of elevated temperature combined pressure-and-shear plate impact (PSPI) experiments conducted on polycrystalline commercial purity aluminum (99.999%) and magnesium (99.9%) samples at temperatures ranging from 23 °C to 320 °C. These experiments are designed to study the effect of temperature on flow stress of fcc and hcp metals at ultra-high shear strain rates (greater than 10^5/s) and high shear strains (approaching 50%). In order to conduct this research, the single-stage gas-gun facility at Case Western Reserve University was modified to include a breech-end sabot heater system and a fully fiber-optics based combined NDI/TDI interferometer. The flow stress of commercial purity aluminum and magnesium, as inferred from the transverse particle velocity record measured at the free surface of a fully elastic Tungsten Carbide (WC) target plate reveal that both sample materials soften when heated to temperatures approximately 50% of their melt temperatures.

Keywords Combined compression-and-shear plate impact · High shear strain rates · Elevated temperatures · Dynamic flow stress · Pure aluminum · Pure magnesium · Viscous drag

Introduction

Plastic flow in metals is known to be accommodated primarily through the motion of a large number of crystalline defects (e.g. dislocations). At low loading rates, it's well accepted that the mobility of dislocations is controlled primarily by the stress-temperature assisted glide motion passed short-range obstacles; however, at higher strain-rates, the dominant mechanism controlling the mobility of dislocations is believed to shift from thermal activation to a viscous drag mediated regime, where temperature may play a positive role in the determination of flow stress.

The plastic response of the metals at high strain-rates and elevated temperatures has recently gained renewed interest because of observations of a considerable increase in the Hugoniot Elastic Limit (HEL) made in of several polycrystalline pure metals under normal plate impact when heated in the vicinity of their melting temperature (up to 99% of the melting temperature) [1–5]. Mechanisms other than thermal activation, such as phonon drag [6, 7] and/or Frenkel disorder [8] have been put-fourth to explain these observations. However, the current experimental data available in literature is not sufficient to inform/calibrate physics-based models to capture the response of these metals over a wide range of conditions, especially at high plastic strains. The current study is particularly motivated in providing experimental data on the plastic response of metals over relevant loading regimes, such as ultra-high strain-rates and elevated temperatures, with the intent of assisting in the development/validation of the current state-of-science constitutive models.

In the present work, elevated temperature PSPI experiments are employed in order to investigate the effect of temperature on the dynamic flow stress of fcc and hcp metals at shear-strain rates of $>10^5$/s, temperatures up to 320 °C, and shear strains approaching 40%. Recent modifications to the single-stage gas gun facility at Case Western Reserve University, including a breech-end sabot heater system and a fully fiber-optics based NDI/TDI, are employed to enable this approach. Commercial purity polycrystalline aluminum and magnesium are been chosen as the sample materials due to the availability of experimental data in other relevant loadings regimes and because of their relatively low strength/melting point, making the regimes of interest accessible at relatively low stress/temperature/strain-rate combinations. The results from this study, as indicated by the transverse particle velocity history measured at the free surface of an elastic WC target plate, reveal a progressive decrease in the flow stress of both materials with increasing test temperatures up to 50% of their melt temperatures.

B. Zuanetti · T. Wang · V. Prakash (✉)
Department of Mechanical and Aerospace Engineering, Case Western Reserve University, Cleveland, OH, USA
e-mail: vikas.prakash@case.edu

L. E. Lamberson (ed.), *Dynamic Behavior of Materials, Volume 1*, Conference Proceedings of the Society for Experimental Mechanics Series, https://doi.org/10.1007/978-3-030-30021-0_27

Experimental Procedure

Elevated temperature pressure-shear plate impact (PSPI) experiments were conducted using the heating capabilities of the recently modified single-stage gas-gun facility at CWRU [9–11]. A detailed protocol for conducting an elevated temperature plate impact experiment can be found in our previous work [12, 13]. The gun barrel has a broached keyway along its entire length making the rig well suited for conducting normal and oblique plate impact. In the current experiment, the flyer/target plates are pre-aligned to 22° angle of inclination with respect to the direction of approach so that the maximum achievable normal/deviatoric stresses during impact exceed the shear stress-bearing capacity of the sample material while keeping the target plate elastic, and also to prevent undesirable slip at the flyer/target interface. The sample and the target plates are aligned parallel to within 0.5 mrads using an optical alignment scheme [14]. The gun barrel is evacuated down to a rough vacuum (~70 mTorr) to minimize the oxidation of the samples during the heating process and to reduce the possibility of an air cushion between the sample and the target plates at the moment of impact. The samples (held at the front-end of a heat resistant sabot) are heated to the desired temperature by free radiation using an 800 W resistive coil heater at the breech-end of the gun barrel; the temperature of the sample is monitored continuously using K-type thermocouple probe attached directly on the front surface of the sample. Once the desired temperature is reached, the sabot is accelerated down the gun barrel by means of compressed nitrogen gas and is made to impact against the target plate. The inadvertent tilt between the sample and the target plate at impact is estimated by monitoring the times at which the individual voltage-biased pins are shorted to the ground. An in-house built custom fiber optics-based heterodyne combined NDI/TDI [15] is used for measuring the normal and transverse particle displacement history at the free surface of the target plate. The particle velocity versus time profile is obtained by numerical differentiation of the measured displacement with respect to time history using an in-house developed data analysis program in conjunction with the commercial package MATLAB.

The flyer and target plates were made from 99.6% purity WC (no binder) procured from Research and PVD Materials LLC. Samples are 100 μm thick foils (obtained from ESPI Metals Inc.) fabricated from 99.999% polycrystalline aluminum and 99.9% magnesium. Three equi-spaced thru-thickness bolt holes, which match the ones on the foil samples, were fabricated on the WC flyer plates (76 mm in diameter and ~5.8 mm in thickness). In order to achieve the required flatness tolerance, the WC flyer plates were first ground flat and parallel to within 12 μm, and then lapped flat on both sides to within 2–3 Newton's rings over the diameter. The foil samples were diffusion bonded to the front surface of the WC flyer plate, and subsequently lapped to the same flatness tolerance. Later the flyer/sample assembly is secured to an a 22° inclined H13 steel holder on the front-end of the sabot using ceramic screws. More detailed description of the strategical designed heat-resistant sabot can be found in our previous work [12]. The sabot configuration used in the current experiments is shown schematically in Fig. 27.1. Moreover, a schematic of the elevated temperature PSPI is shown in Fig. 27.2.

In the interpretation of the results we refer to the T-X, and S-V diagram of a typical elevated temperature PSPI experiment shown in Fig. 27.3.

PSPI experiments are performed by impacting a soft foil specimen between two hard elastic plates. The inclination of the sample/target/flyer with respect to the direction of approach imposes normal and transverse particle velocity at the impact interface resulting in normal and shear stresses, which travel through the spatial dimensions of the sample/plates as

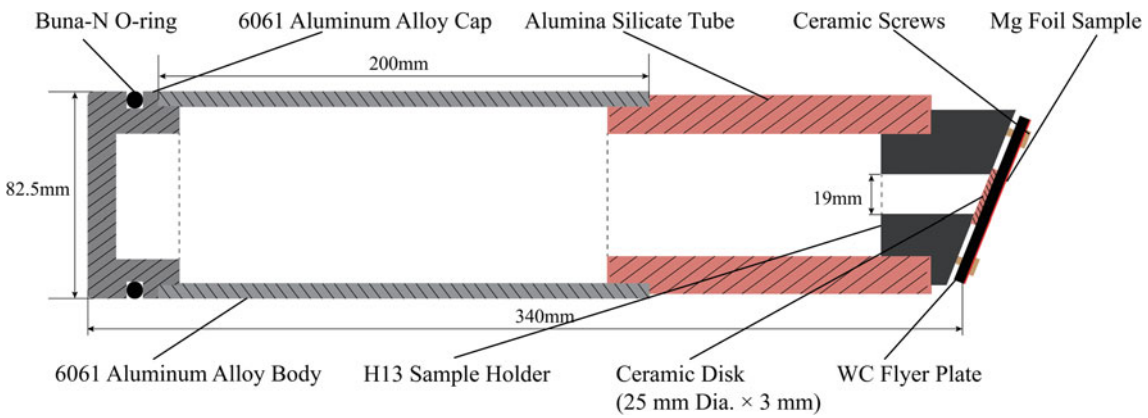

Fig. 27.1 Shows a schematic of the sabot used in current experimental configuration. The alumina silicate tube helps mitigate heat flow from the heated thin metal specimen to the sabot body, thus minimizing the risk of seizure of the sabot within the gun-barrel due to possible thermal expansion of the sabot body

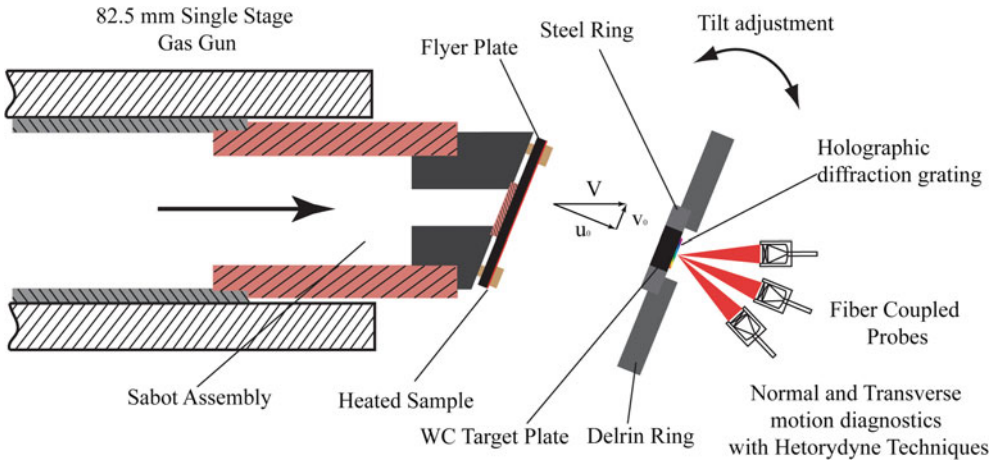

Fig. 27.2 Schematic of the high temperature pressure-shear plate impact experiment. Here a heated flyer plate is carried by a custom heat-resistant sabot and is made to impact a stationary target plate

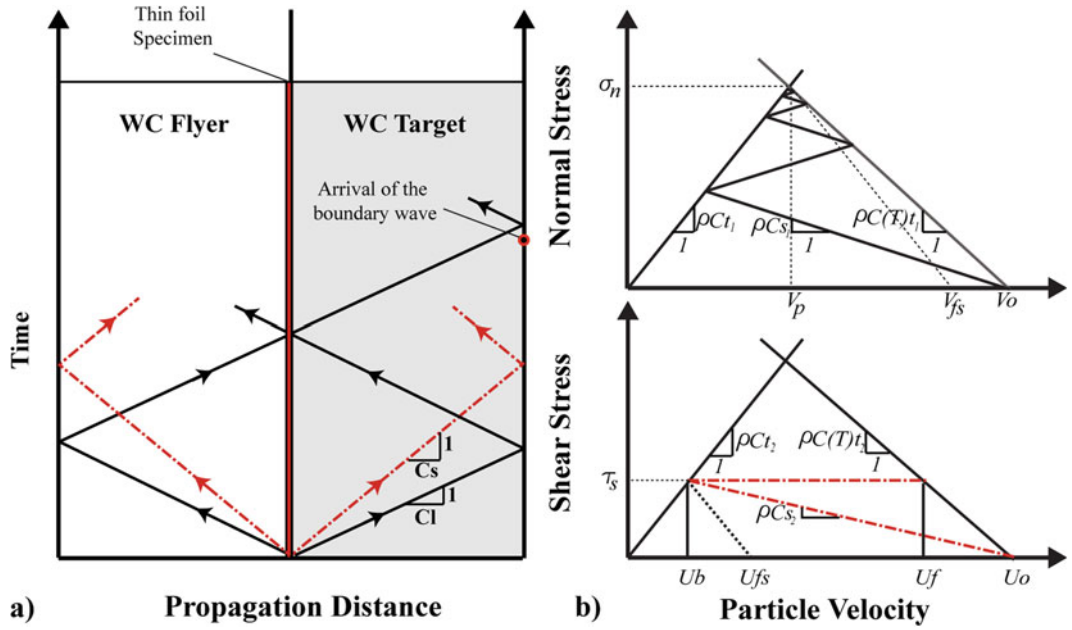

Fig. 27.3 Shown on the left is the T-X diagram for the current PSPI experiment configuration. On the top right is the generic locus of states for the normal component of stress, and bottom right shows the locus of states for the shear stress

longitudinal and transverse plane stress waves. At t = 0, the sample/flyer plate are initially unstressed and traveling at a speed, V_{P_O}, the projectile velocity, while the target plate is unstressed and at rest. Post-impact, the normal component of stress/particle velocity in the sample and plates is described by the S-V diagram on the top right; the transverse component is shown in the bottom right of Fig. 27.3. The normal stress/particle velocity in the sample quickly rings up to the impedance matched stress/particle velocity between the flyer and target plates reaching a hydrodynamic state (shown by the intersection of the two solid lines), this value of stress can be estimated from the initial projectile velocity by

$$\sigma_{nmax} = \frac{\rho C_{T_1} V_{p_o} \cos(\theta)}{1 + \frac{\rho C_{T_1}}{\rho C_{F_1}(T)}}, \tag{27.1}$$

where ρC_{T1} is the longitudinal impedance of the elastic target plate, and $\rho C_{F_1}(T)$, refers to the impedance of the heated flyer plate. Moreover, normal stress history can be estimated from the normal free surface particle velocity, V_{fs} record by

$$\sigma_n(t) = \frac{1}{2}\rho C_{T1} V_{fs}(t). \tag{27.2}$$

Once the hydrodynamic state is achieved, the inherent resistance to volume change in the sample prevents a normal particle velocity difference between the front and back surfaces of the sample bringing the longitudinal strain-rate to zero. The levels of strain caused by normal compression are very small in comparison to those caused by shear stresses. The shear transverse particle velocity in the sample initially increases, but quickly reaches the shear flow stress of the sample; moreover, the shear stress in the sample becomes nearly uniform, while the plastic behavior of the sample maintains a transverse particle velocity difference between the front and back surface of the sample. The shear stress history on the sample can be inferred from the transverse particle velocity, U_{fs} by

$$\sigma_t(t) = \frac{1}{2}\rho C_{T2} U_{fs}(t), \tag{27.3}$$

where, C_{T2} is the transverse wavespeed in the target plate. Moreover, the strain-rate on the sample is defined as

$$\dot{\gamma}_s(t) = \frac{U_f - U_b(t)}{L}. \tag{27.4}$$

In Eq. (27.4), L is the thickness of the sample. From the diagram, it can be seen that the strain-rate history can be estimate by knowing the transverse component of the projectile velocity and from the transverse free surface particle velocity history via

$$\dot{\gamma}_s(t) = \frac{1}{L}\left[V_{p_o}\sin(\theta) - \frac{1}{2}\left(1 + \frac{\rho C_{T_2}}{\rho C_{T_2}(T)}\right) U_{fs}\right], \tag{27.5}$$

where the temperature dependent transverse wave impedance is from estimated from calculated values of temperature dependent density of WC, and shear modulus. Lastly, the strain is given by the time integral of the strain-rate, as

$$\gamma(t) = \int_{\frac{L}{C_{T_2}}}^{t_f} \dot{\gamma}_s(t)dt. \tag{27.6}$$

Results and Discussion

Figures 27.4 and 27.5, show the measured normal and transverse free surface particle velocity record from PSPI experiments on aluminum and magnesium. In both series, the normal free surface particle velocity is shown to quickly reach a plateau region corresponding to a stress level of about 4.5–5 GPa, which corresponds to the impedance matched stress/particle velocity state given by Eq. (27.1). In contrast, the transverse free surface particle velocity record does not reach an impedance matched velocity, and is instead controlled by the shearing resistance of the foil samples. In both metal samples, the transverse free surface particle velocity is shown to decrease progressively with increasing initial sample temperature.

A further indication of this is revealed in Fig. 27.6, which shows the dynamic shear stress versus shear strain for pure aluminum and magnesium at select temperatures in the range of 23–320 °C, and shear strains of up to 40%, and shear strain-rates on the order of 10^5/s. In the case of pure aluminum (shown on the left), the shear stress versus shear strain is marked by two regions, a gradual non-linear hardening, followed by a perfect plastic response with a flow stress of around 0.2 GPa, starting from 10% deformation and sustaining for the duration of the experiment (about 40%). The overall shear stress versus shear strain profile remains the same for all three test temperature cases, however, the shear flow stress is observed to decrease to about 0.14 GPa at the highest test temperature of 320 °C. For the case of magnesium (shown on the right), the shear stress versus shear strain is marked by three regions: an initial non-linear hardening (up to 4% deformation), followed by a more gradual hardening behavior (between 4–26%), and finally a third abrupt hardening regime. The flow stress in magnesium

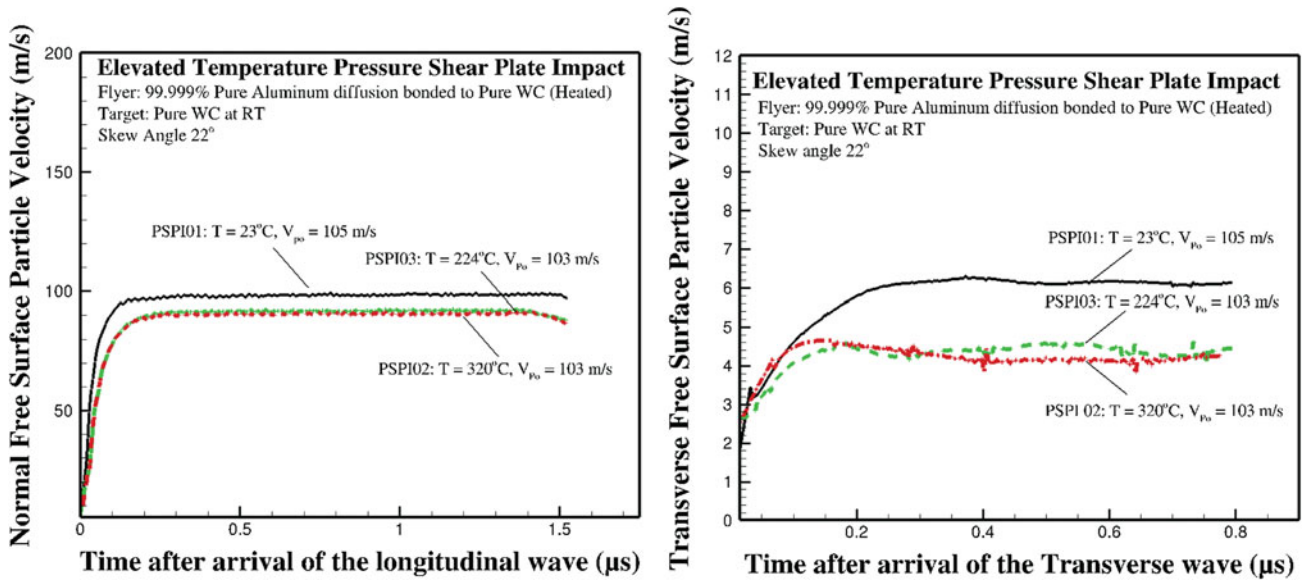

Fig. 27.4 Shows the normal and transverse free surface particle velocity record obtained from PSPI experiments on commercial purity aluminum

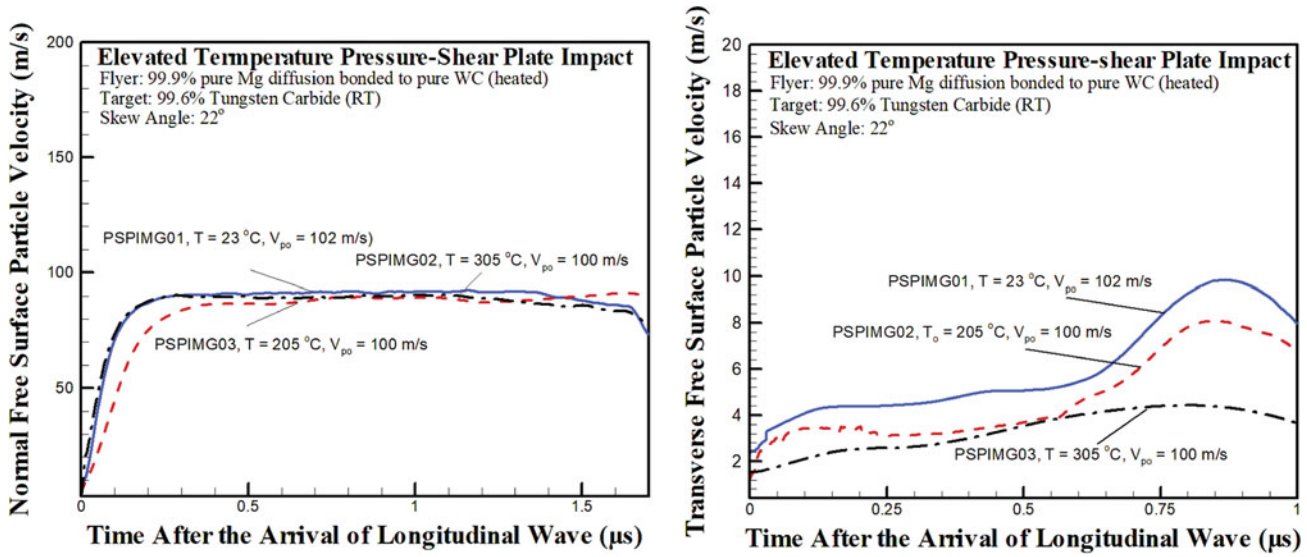

Fig. 27.5 Shows the normal and transverse free surface particle velocity record obtained from PSPI experiments on commercial purity magnesium

at similar levels of strain is observed to monotonically decrease with increasing sample temperatures. Interestingly, in the highest test temperature case of around 305 °C, the third region (abrupt hardening behavior) is not observed. This is due to the end of the window time for this experiment, which does not allow transition of inelastic deformation to the abrupt hardening regime.

Summary

In this paper, results from a series of elevated temperature pressure-shear plate impact (PSPI) experiments carried out on commercial purity polycrystalline aluminum (99.999%) and magnesium (99.9%) at temperatures ranging from 23 °C to around 320 °C were presented. These experiments were designed primarily to study the effect of temperature on the flow stress of these metals at ultra-high strain-rates (greater than 10^5/s) and very high levels of strains (approaching 50%). Recent modifications to the single-stage gas gun facility at Case Western Reserve University, including a breech-end sabot heater

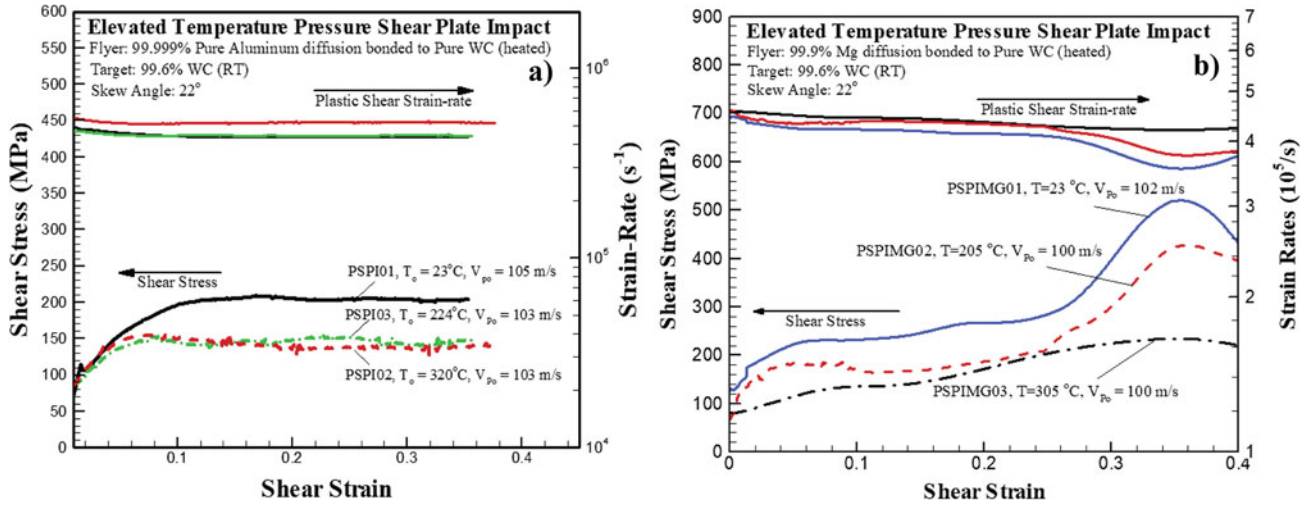

Fig. 27.6 Shows the dynamic flow stress versus strain behavior of aluminum and magnesium at select temperatures in the range of 23–320 °C, and strains of up to 40%

system and a fully fiber-optics based NDI/TDI, are employed to enable this approach. The flow stress of commercial purity aluminum and magnesium, as inferred from the transverse particle velocity record measured at the free surface of a fully elastic Tungsten Carbide (WC) target plate, showed a progressive decrease with increasing initial sample temperature. These results reveal that both sample materials soften when heated up to 50% of their melting temperatures.

Acknowledgments The authors would like to acknowledge the financial support of the U.S. Department of Energy through the Stewardship Science Academic Alliance (DE-NA0001989 and DE-NA0002919).

References

1. Frutschy, K., Clifton, R.: High-temperature pressure-shear plate impact experiments on OFHC copper. J. Mech. Phys. Solids. **46**(10), 1723–1744 (1998)
2. Grunschel, S.E., Clifton, R.J.: Dynamic plastic response of aluminum at temperatures approaching melt. Metall. Mater. Trans. A. **38**(12), 2885–2890 (2007)
3. Wang, T., Zuanetti, B., Prakash, V.: Shock Response of Commercial Purity Polycrystalline Magnesium Under Uniaxial Strain at Elevated Temperatures. J. Dyn. Behav. Mater. **3**(4), 497–509 (2017)
4. Zuanetti, B., Wang, T., Prakash, V.: Mechanical response of 99.999% purity aluminum under dynamic uniaxial strain and near melting temperatures. Int. J. Impact Eng. **113**, 180–190 (2018)
5. Zuanetti, B., et al.: Measurement of elastic precursor decay in pre-heated aluminum films under ultra-fast laser generated shocks. J. Appl. Phys. **123**(19), 195104 (2018)
6. Kumar, A., Hauser, F., Dorn, J.: Viscous drag on dislocations in aluminum at high strain rates. Acta Metall. **16**(9), 1189–1197 (1968)
7. Regazzoni, G., Kocks, U., Follansbee, P.S.: Dislocation kinetics at high strain rates. Acta Metall. **35**(12), 2865–2875 (1987)
8. Frenkel, J.: Über die Wärmebewegung in festen und flüssigen Körpern. Z. Phys. **35**(8–9), 652–669 (1926)
9. Prakash, V., Mehta, N.: Uniaxial compression and combined compression-and-shear response of amorphous polycarbonate at high loading rates. Polym. Eng. Sci. **52**(6), 1217–1231 (2012)
10. Prakash, V., Clifton, R.J.: Experimental and analytical investigation of dynamic fracture under conditions of plane strain. In: Fracture Mechanics: Twenty-Second Symposium, (1990)
11. Okada, M., et al.: Tribology of high-speed metal-on-metal sliding at near-melt and fully-melt interfacial temperatures. Wear. **249**(8), 672–686 (2001)
12. Zuanetti, B., Wang, T., Prakash, V.: A novel approach for plate impact experiments to determine the dynamic behavior of materials under extreme conditions. J. Dyn. Behav. Mater. **3**(1), 64–75 (2017)
13. Zuanetti, B., Wang, T., Prakash, V.: Conducting elevated temperature normal and combined pressure-shear plate impact experiments via a breech-end sabot heater system. JoVE. (138), e57232 (2018)
14. Kumar, P., Clifton, R.: Optical alignment of impact faces for plate impact experiments. J. Appl. Phys. **48**(3), 1366–1367 (1977)
15. Zuanetti, B., Wang, T., Prakash, V.: A compact fiber optics-based heterodyne combined normal and transverse displacement interferometer. Rev. Sci. Instrum. **88**(3), 033108 (2017)

Chapter 28
Dynamic Failure of Pure Tungsten Carbide Under Simultaneous Compression and Shear Plate Impact Loading

Bryan Zuanetti, Tianxue Wang, and Vikas Prakash

Abstract In this paper, we present the results from a series of plate impact experiments designed to study dynamic response of commercial 99.6% purity tungsten carbide (WC) under simultaneous compression-and-shear stress wave loading. The symmetric oblique plate-impact experiments are conducted using progressively increasing angles of inclination (5°, 10°, and 22°). The longitudinal and transverse components of the measured particle velocity history at the free surface of the target plate in experiments with inclination angles of up to 10° and impact velocities ~100 m/s coincide well with their corresponding elastic particle velocity predictions. However, the normal particle velocity profiles for experiments conducted at an oblique impact angle of 22° are markedly different and exhibit a sudden increase in particle velocity from their plateau levels reminiscent of failure waves observed by other investigators in soda lime glass and silicon carbide (SIC-B). The increase in normal particle velocity (recompression/re-acceleration signal) in the shocked state of the target and the relatively large undulations present in the measured transverse particle velocity profiles are indicative of heterogeneous dynamic brittle failure processes in WC under the simple-shear state of stress, and are used to provide estimates for the critical range of pure-shear (tensile) loading that can initiate catastrophic failure in pure WC.

Keywords Plate impact · High strain-rates · Normal shock compression · Simultaneous compression-and-shear impact loading · Oblique plate impact · Pure shear loading · Tungsten carbide · Brittle failure/fragmentation

Introduction

Hexagonal closely-packed (HCP) Tungsten Carbide (WC) combines the characteristics of covalent compounds (i.e. high hardness, low plasticity, and thermal stability) and metallic compounds (i.e. relatively high thermal conductivity and low electrical resistivity). WC and its alloys are ideal for armor and armor-piercing applications due to their high-density, hardness, and ability to dissipate energy [1–4]. Owing to the excellent wear resistance, they have also found wide use in tooling for metal-working, drilling and surface coatings [5–7]. Another important application for these materials has been in high-pressure mechanical characterization equipment, where they are used as platens in universal loading frames and/or as target/flyer plates [8–12] in shock wave experiments.

WC and its alloys are generally subjected to the thermo-mechanical extremes in the aforementioned applications; however, knowledge of their dynamic response, including inelasticity and failure, is still limited by the deficiency of experimental data in such extreme conditions. Information regarding the physical, chemical, and structural properties of WC can be found in several sources [6, 13–15], but only a few studies have been conducted to characterize their dynamic response, especially for pure WC (w/no-binder). Shock velocity versus particle velocity ($U_s - U_p$) data on WC with 5% cobalt is provided in the LASL Shock Hugoniot Data Handbook [16] at pressures up to 200 GPa. The shock-induced compression behavior and Hugoniot Elastic Limit (HEL) for WCs with select amounts of cobalt, tantalum, and nickel binders have been investigated at pressures up to 80 GPa [17]. Compared to WCs with a Ni and Co binder, pure WC has been found to have a higher HEL but with a lower spall strength [4]. The Ni and Co binder materials, with their much lower compressive strengths, can assist in activating ductile failure modes in WC by accommodating plastic strains [18]. In addition, the measured shock Hugonoit levels are observed to be consistently higher than the corresponding hydrodynamic pressures, suggesting that WC maintains significant shear-strength under planar shock compression at pressures up to 80GPa. The shear strength of monolithic tungsten carbide has been investigated by Millet et al. [19]. In these experiments, the lateral stress was observed to increase with time, indicating a decrease in shear strength of WC behind the shock front. Two possible mechanisms were

B. Zuanetti · T. Wang · V. Prakash (✉)
Department of Mechanical and Aerospace Engineering, Case Western Reserve University, Cleveland, OH, USA
e-mail: vikas.prakash@case.edu

L. E. Lamberson (ed.), *Dynamic Behavior of Materials, Volume 1*, Conference Proceedings of the Society for Experimental Mechanics Series, https://doi.org/10.1007/978-3-030-30021-0_28

put forward – the first was based on failure initiated in the shock front itself, and the second based on plasticity due to dislocation motion and generation [20].

The present series of experiments is motivated by the critical need for experimental data on dynamic response of pure WC, which can provide a deeper understanding of inelasticity and failure processes in WC under dynamic multi-axial loading conditions. In this regard, a series of oblique plate impact (OPI) experiments are conducted at increasing angles of inclination (5°, 10°, and 22°) with respect to the direction of travel of the sabot in the gun barrel, to obtain critical data for the onset of pure-shear failure (in tension) of WC plates under simultaneous compression-and-shear plate impact loading.

Experimental Procedures

Material Preparation

The target and flyer used in the present experiments were WC disks with diameters of 76.2 and 31.75 mm, respectively, and a thickness of 6.35 mm. These flyer and target plate dimensions are strategically chosen to allow a window-time for experimental measurements of about 2 μs. Both sides of the target and flyer disks were ground and subsequently lapped flat to within 2–3 Newton's rings across the diameter [21]. The free-surface of the target plate is polished to a mirror surface using 1 μm diamond polishing paste to enable fabrication of a diffraction grating for laser interferometry measurements [22–24]. For conducting the oblique plate impact experiments, a 500 lines/mm holographic diffraction grating is fabricated on the rear surface of target plate via photolithography using Shipley's 1805 series photoresist and a CD-26 developer.

Oblique Plate Impact Combined Compression-and-Shear Experiments

The oblique plate impact experiments are conducted using a modified 82.5 mm bore single-stage gas-gun at CWRU. The schematic of the experimental configuration is shown in Fig. 28.1a. The flyer plate is held at the front of a custom designed sabot, which is accelerated down the gun barrel by means of compressed nitrogen gas and is made to impact a stationary target plate in an impact chamber. To ensure the generation of plane-waves with a wave front sufficiently parallel to the impact face, the flyer and target plates are aligned to be parallel and inclined at a pre-set angle θ relative to the direction of approach. The gun-barrel has a broached keyway along its full length, which prevents the rotation of the sabot during travel. The misalignment angle (tilt) between the flyer and target plates at impact is estimated by recording the times at which voltage-biased pins (located on the same plane as the front surface of the target plate) are shorted to the ground [25]. Figure 28.1b shows the schematic of the oblique plate impact experimental configuration. Under the simultaneous compression-and-shear loading, both normal and transverse particle velocity motions are generated within the flyer and target plates and are monitored at the free surface of the target using an all-fiber-optics combined normal and transverse displacement interferometer [26].

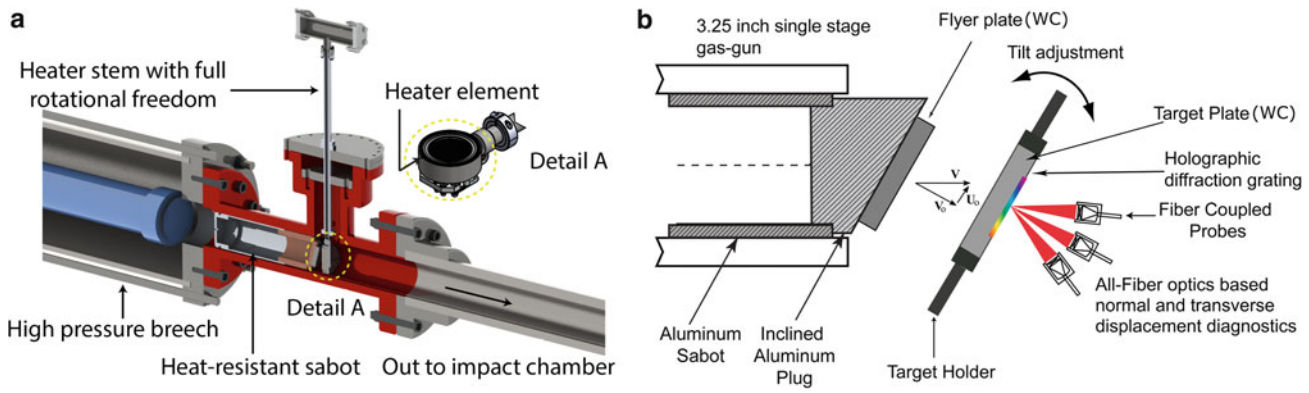

Fig. 28.1 (**a**) Schematic of the breech-end of the gas gun. (**b**). Schematic of the OPI experimental configuration

Experimental Results and Discussion

In order to investigate the critical state of stress for the initiation of dynamic failure in WC target under combined compression-and-shear loading, the oblique plate impact experiments, designated as Shots OPI04, OPI05, OPI06 and OPI07, are conducted at impact velocities in the range 84 to 101 m/s and at inclination angles of 5°, 10°, 20° and 20°, respectively. As the angle of inclination is varied from 5° to 22°, the amplitude of the pure shear stress in the WC target plate increases from 0.29 to 1.24 GPa (the corresponding tensile stress in the WC target is 0.42–1.9 GPa). From our previous work [27], the WC plates are expected to remain elastic in the aforementioned impact velocity range. However, due to the interaction of the normal compression release wave, propagating away from the free surface of the target plate, with the slower propagating shear wave traveling towards the free surface of the target plate, brittle failure of the WC target can occur under the simple-shear state of stress. The measured normal and transverse free surface particle velocity profiles for Shots OPI04 and OPI05 are shown in Fig. 28.2. Shots OPI04 and OPI05 for were conducted at skew angles of 5° and 10° with impact velocities of 84 and 92 m/s, respectively. The solid black and solid red lines correspond to the measured normal and transverse free surface particle velocity profiles for Shot OPI04, while the normal and transverse free-surface particle-velocity profiles for Shot OPI05 are described by the dash-dot black and red lines respectively. For symmetric plate impact experiments, the elastic prediction levels for transverse and normal components of the free surface particle velocity are given by $v^e_{fs} = V_o \sin\theta$ and $u^e_{fs} = V_o \cos\theta$. As shown in Fig. 28.2, the measured normal and transverse particle velocity profiles coincide well with their corresponding elastic prediction levels (shown by the dashed lines), indicating that the WC target plate remains essentially elastic under the simultaneous compression-and-shear loading corresponding to maximum longitudinal and shear stresses of 4.5 GPa and 0.5 GPa, respectively.

The measured normal and transverse free surface particle velocity profiles for Shots OPI06 and OPI07 are shown in Fig. 28.3**.** In these two experiments, the skew angle of impact is increased (from 5° and 10°) to 22°, while the impact velocities are kept nearly the same at 101 and 92 m/s, respectively. The solid black and red lines correspond to the normal and transverse free surface particle velocity profiles for Shot OPI06, while the dash-dot black and red lines correspond to the normal and transverse free surface particle velocity profiles for Shot OPI07. Compared to Shots OPI04 and OPI05, the free surface particle velocity profiles for the Shots OPI06 and OPI07 reveal a more complicated wave structure. For Shots OPI06 and OPI07, the measured particle velocity levels in the plateau region initially coincide well with the elastic predictions; however, at about 1.55 μs after impact, an anomalous increase in normal particle velocity is observed to occur within the "window-time" of both experiments. These features in the normal velocity profiles are reminiscent of free surface velocity profiles observed by Kanel et al. [28] in K8 glass, Dandekar and Beaulieu [29] in soda-lime glass, and Dandekar [30] in SiC-B,

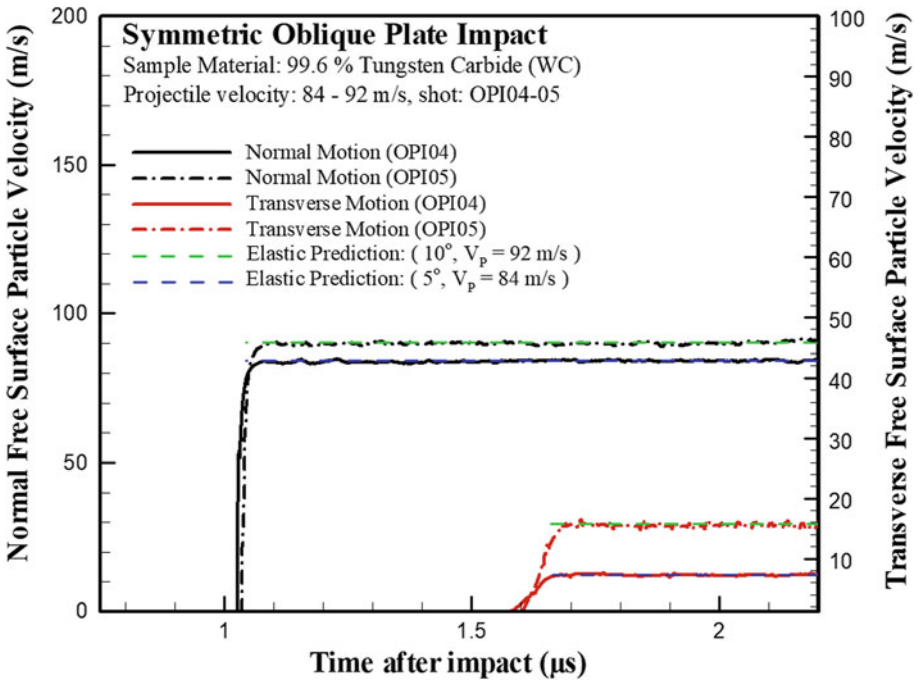

Fig. 28.2 Shows the measured normal and transverse particle velocity traces for OPI04 (Shown as solid black and red curves) and 05 (dash-dot)

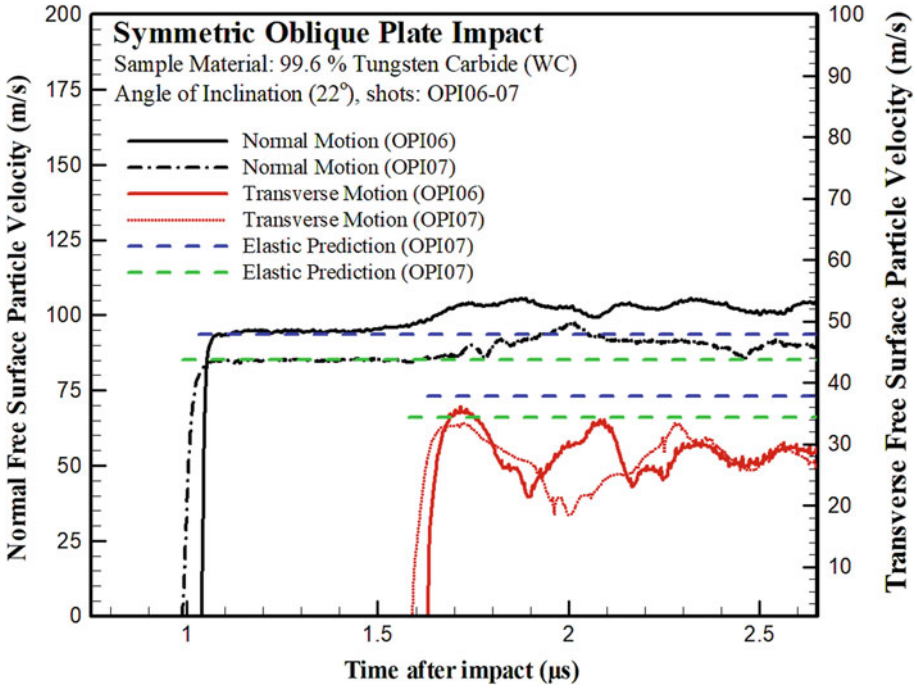

Fig. 28.3 Shows the measured normal and transverse particle velocity traces for OPI06 (shown as solid black and red curves) and 07 (dash-dot)

which they attributed to the development of failure waves under the shock-induced normal compression in brittle materials. The authors believe that the origin of the recompression/re-acceleration observed in the normal particle velocity profiles is due to dynamic failure of WC occurring under the oblique plate impact loading.

Simultaneous compression-and-shear loading waves are generated in the flyer and target plates at impact in the oblique plate impact experiments conducted in the present study. Prior to the arrival of the lateral release waves, owing to the higher propagation speed of the longitudinal wave in comparison with that of the transverse wave, a point in the interior of the WC target plate first experiences a state of normal shock compression, followed by combined compression-and-shear loading at the arrival of the shear wave, and then a state of simple-shear at the arrival of the longitudinal release wave reflected from the target plate free surface. The brittle failure of WC is understood to occur in a direction perpendicular to the principal tensile loading, which is attributed to the development of the state of pure shear in the WC target. The recompression observed in the normal particle velocity profile(s) as well as the oscillations in the transverse particle velocity are understood to be a result of a complex interaction of failure waves with the incident and release waves in the WC target. These features are not observed in any of the NPI experiments [27], or oblique plate impact experiments with skew angles of 5° and 10° (OPI03 and OPI04), indicating that the development of brittle failure in the WC target is activated by the simple-shear state of stress with an amplitude (related to the impact velocity and skew angle) above a critical level.

Analysis of the Equivalent Stress State in the Target Plate During the Oblique Plate Impact Experiment

To estimate the onset of inelasticity and this critical stress level which causes the dynamic failure in the pure WC samples, the von Mises yield criterion (also known as the maximum distortion energy criterion) is used. The criterion suggests that yielding of a material occurs when the second deviatoric stress invariant J_2 reaches a critical value k^2, where $k = \sigma_y/\sqrt{3}$ is the yield stress of the material in pure shear and σ_y is the tensile yield strength of the material. Accordingly, we estimate J_2 at a material point in the target plate corresponding to the two different states of stress achieved in the current oblique plate impact experiments: (1) combined compression-and-shear (C + S), and (2) pure-shear loading (PS).

During the duration of the experiment, a state of plane strain prevails in the region of the sample behind the transverse wave (and interior of the release wave in the target plate), i.e. only $\varepsilon_{xx} \neq 0$, $\varepsilon_{xy} \neq 0$, $\varepsilon_{yy} = \varepsilon_{zz} = \varepsilon_{yz} = \varepsilon_{zx} = 0$). From isotropic Hooke's law, the corresponding stresses are given by

$$\begin{aligned} \sigma_{xx} &= (\lambda + 2\mu)\,\varepsilon_{xx}, \\ \sigma_{yy} &= \sigma_{zz} = \sigma = \lambda\varepsilon_{xx}, \\ \tau_{xy} &= 2\mu\varepsilon_{xy}, \qquad \tau_{yz} = \tau_{zx} = 0, \end{aligned} \tag{28.1}$$

where λ and μ are the Lame parameters. Hence, the J_2 deviatoric stress invariant is given by

$$J_2 = \frac{1}{3}(\sigma_{xx} - \sigma)^2 + \tau_{xy}^2 \tag{28.2}$$

Since, $C_{LT}^2 = (\lambda + 2\mu)/\rho$, and $C_s^2 = \mu/\rho$, Eq. (28.2) can be re-written in terms of σ_{xx} as

$$J_2 = \frac{4}{3}\left(\frac{C_s}{C_{LT}}\right)^4 \sigma_{xx}^2 + \tau_{xx}^2. \tag{28.3}$$

The corresponding von Mises stress (also referred to as equivalent stress) for the C + S state of stress can be estimated using $\sigma_e = \sqrt{3J_2}$ as

$$\sigma_e = \sqrt{4\left(\frac{C_s}{C_{LT}}\right)^4 \sigma_{xx}^2 + 3\tau_{xx}^2}, \tag{28.4}$$

where $\sigma_{xx} = \frac{1}{2}\rho C_{LT} V_o \cos\theta$ and $\tau_{xx} = \frac{1}{2}\rho C_s V_o \sin\theta$.

Subsequent to the arrival of the release wave, a state of pure shear prevails in the target; the corresponding equivalent stress can be expressed as

$$\sigma_e = \sqrt{3}\tau_{xx}. \tag{28.5}$$

Table 28.1 provides a summary of the stress states in WC for Shots OPI04 to OPI07. Subsequent to the arrival of the release wave, dynamic failure of pure WC occurs when the maximum principal stress under simple-shear are between 0.53GPa and 1.19GPa. These results are particularly important in the use of pure WC plates while designing high strain-rate oblique plate impact experiments for investigation of dynamic response of materials. Also, for the range of impact velocities and skew angles used in the present study, the equivalent stress levels at any point within the shocked WC target (column 4) during the OPI experiments lie consistently below the equivalent yield strength of WC obtained from the normal plate impact experiments (i.e. 4.7–4.9 GPa) [31].

Table 28.1 Summary of the Stress States attained at an interior point of the WC Target for the OPI Experiments Conducted in the Present Investigation

Expt No.	Longitudinal stress at impact (GPa)	Shear stress at impact (GPa)	Total equivalent stress under C + S (GPa)	Maximum principal stress under PS (GPa)
OPI04	4.47	0.24	3.54	0.24
OPI05	4.79	0.53	3.87	0.53
OPI06	5.01	1.19	4.45	1.19
OPI07	4.50	1.1	4.02	1.1

Shear Stress versus Shear Strain Profiles Estimated from the Free Surface Transverse Particle Velocity Profiles Obtained from the Oblique Plate Impact Experiments

Next, a simple wave strain-rate independent longitudinal wave analysis, similar to the one used in [27] for analyzing the normal particle velocity profiles, is used in the interpretation of the transverse particle velocity profiles. A shear stress state τ_T^n, in a region interior of the free surface of the target plate (and prior to the development of the state of pure-shear loading at any point in the target plate), in terms of the measured transverse particle velocity at the free surface of the target plate u_{fs}^n, after the arrival of a transverse wave propagating at an average speed of C_2^n. The shear stress, τ_T^n, and shear strain, γ^n, can be expressed as

$$\tau_T^n = \tau_T^{n-1} + \frac{\rho C_2^e}{1 + \frac{C_2^e}{2}\left[\frac{1}{C_2^n} + \frac{1}{C_2^{n-1}}\right]}\left[u_{fs}^n - u_{fs}^{n-1}\right], \tag{28.6}$$

and

$$\gamma^n = \gamma^{n-1} + \frac{u_{fs}^n - u_{fs}^{n-1}}{C_2^n + C_2^{n-1}}, \tag{28.7}$$

where c_2^e corresponds to the elastic transverse wave-speed in WC. The estimated shear stress versus shear strain is shown in Fig. 28.4.

As shown in Fig. 28.4, up to a shear stress of 0.53 GPa, (the estimated transition from the steep-to-gradual rise in the particle velocity), which corresponds to a shear strain of about 0.18%, pure WC remains linear elastic. The stress-strain curve deviates slightly the the elastic prediction line when the shear stress level exceeds 0.53 GPa. This deviation from the elastic prediction is understood to be as a result of dispersion of the transverse shear waves by microstructural heterogeneities present in pure WC and not plastic deformation.

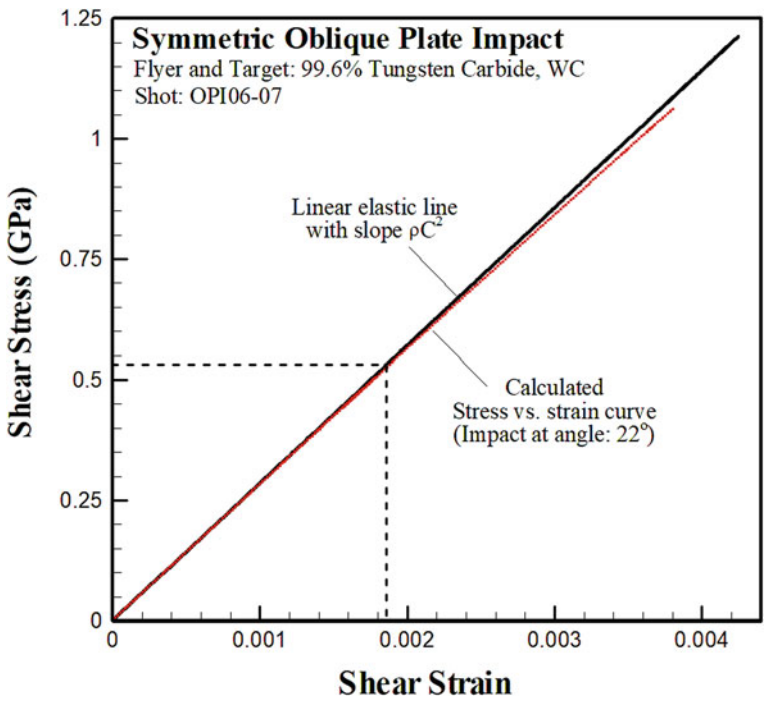

Fig. 28.4 Shows the shear stress versus shear strain estimated from the transverse free surface particle velocity traces for OPI 06–07. The plot reveals a linear elastic behavior up to around 0.5 GPa, followed by a slight deviation from the linear elastic line

Conclusion

The dynamic response of pure tungsten carbide was evaluated using oblique plate impact experiments. The simultaneous compression-and-shear loading experiments are conducted using a symmetric oblique plate impact experimental configuration with progressively increasing angles of inclination (5°, 10°, and 22°), resulting in increasing shear to longitudinal stress ratios upon impact in the WC flyer and target plates. The measured longitudinal and transverse components of the free surface particle velocity in experiments with inclination angles of up to 10° and impact velocities ~100 m/s (corresponding to shear and longitudinal stress levels of 0.5 GPa and 4.5 GPa, respectively), coincide well with their corresponding elastic particle velocity predictions. However, the free-surface normal particle velocity profiles for experiments conducted at an oblique impact angle of 22° (corresponding to shear stresses ~1.3GPa and longitudinal stress of ~4.9GPa) are remarkably different and exhibit a sudden increase in particle velocity from their plateau levels reminiscent of failure waves observed by other investigators in soda lime glass and silicon carbide (SIC-B). This increase in normal particle velocity (recompression/re-acceleration signal) exceeds the value of impact velocity, suggesting failure of the WC target during the stress wave loading process. This anomalous increase in the particle velocity in the shock plateau region is understood to occur due to the development dynamic failure of WC target plate under a pure-shear state of stress immediately following the interaction of the release wave propagating away from the free surface of the WC target plate towards the impact surface, with the slower-moving transverse wave-front in the target propagating away from the impact surface. The relatively large undulations present in the measured free-surface transverse particle velocity profiles provide further evidence for the heterogeneous brittle failure processes in WC under the simple-shear state of stress, and are used to provide estimates for the critical range of simple-shear tensile loading that can initiate catastrophic failure in pure WC.

Acknowledgements The authors would like to acknowledge the financial support of the U.S. Department of Energy through the Stewardship Science Academic Alliance (DE-NA0001989 and DE-NA0002919) in conducting the present research.

References

1. Appleby-Thomas, G., et al.: Shock propagation in a cemented tungsten carbide. J. Appl. Phys. **105**(6), 064916 (2009)
2. Zhu, D., Kriven, W.M.: Advances in Ceramic Armor: A Collection of Papers Presented at the 29th International Conference on Advanced Ceramics and Composites, Jan 23–28, 2005, Cocoa Beach, FL, vol. 296. John Wiley & Sons, Hoboken (2009)
3. Yadav, S., Ramesh, K.: The mechanical properties of tungsten-based composites at very high strain rates. Mater. Sci. Eng. A. **203**(1–2), 140–153 (1995)
4. Grady, D.: Impact failure and fragmentation properties of tungsten carbide. Int. J. Impact Eng. **23**(1), 307–317 (1999)
5. Kurlov, A.S., Gusev, A.I.: Tungsten carbides. Springer Series Materials Science. **184**, 34–36 (2013)
6. Kosolapova, T.Y.: Carbides: properties, production, and applications. Springer Science & Business Media, Berlin (2012)
7. Prakash, V.: Time-resolved friction with applications to high speed machining: experimental observations. Tribol. Trans. **41**(2), 189–198 (1998)
8. Frutschy, K., Clifton, R.: High-temperature pressure-shear plate impact experiments using pure tungsten carbide impactors. Exp. Mech. **38**(2), 116–125 (1998)
9. Yuan, F., Prakash, V., Lewandowski, J.J.: Shear yield and flow behavior of a zirconium-based bulk metallic glass. Mech. Mater. **42**(3), 248–255 (2010)
10. Grunschel, S., Clifton, R.J., Jiao, T.: Shearing resistance of aluminum at high strain rates and at temperatures approaching melt. in AIP Conference Proceedings. AIP, College Park (2012)
11. Yuan, F.P., Prakash, V., Lewandowski, J.J.: Spall strength of a zirconium-based bulk metallic glass under shock-induced compress ion-and-shear loading. Mech. Mater. **41**(7), 886–897 (2009)
12. Prakash, V., Yuan, F.: Results of a pilot study to investigate the feasibility of using new experimental techniques to measure sliding resistance at seismic slip rates. EOS Trans. AGU Fall Meeting Suppl. **85**(47), 435 (2004)
13. Exner, H.: Physical and chemical nature of cemented carbides. Int. Met. Rev. **24**(1), 149–173 (1979)
14. Samsonov, G.V.: Refractory carbides. Consultants Bureau, New York (1974)
15. Storms, E.K.: The refractory carbides. Academic, New York (1967)
16. Marsh, S.P.: LASL Shock Hugoniot data, vol. 5. Univ of California Press, Berkeley (1980)
17. Grady, D.E., Moody, R.L.: Shock compression profiles in ceramics. Sandia National Labs, Albuquerque, NM (1996)
18. Lee, H.-C., Gurland, J.: Hardness and deformation of cemented tungsten carbide. Mater. Sci. Eng. **33**(1), 125–133 (1978)
19. Millett, J., Bourne, N., Dandekar, D.: Lateral stress measurements and shear strength in shock loaded tungsten carbide. J. Appl. Phys. **96**(7), 3727–3732 (2004)
20. Bolton, J., Redington, M.: Plastic deformation mechanisms in tungsten carbide. J. Mater. Sci. **15**(12), 3150–3156 (1980)
21. Prakash, V., Clifton, R.J.: *Experimental and analytical investigation of dynamic fracture under conditions of plane strain*. in *Fracture Mechanics: Twenty-Second Symposium,* (1990)

22. Liou, N.-S., Okada, M., Prakash, V.: Formation of molten metal films during metal-on-metal slip under extreme interfacial conditions. J. Mech. Phys. Solids. **52**(9), 2025–2056 (2004)
23. Yuan, F., Liou, N.-S., Prakash, V.: High-speed frictional slip at metal-on-metal interfaces. Int. J. Plast. **25**(4), 612–634 (2009)
24. Tsai, L., Prakash, V.: Structure of weak shock waves in 2-D layered material systems. Int. J. Solids Struct. **42**(2), 727–750 (2005)
25. Prakash, V., Clifton, R.J.: Experimental and Analytical Investigations of Dynamic Fracture under Conditions of Plane-Strain. In: Ernst, H.A., Saxena, A., McDowell, D.A. (eds.) Fracture Mechanics: Twenty Second Symposium (vol. 1) ASTM STP 1131, pp. 412–444. American Society of Testing Materials, Philadelphia, PA (1992)
26. Zuanetti, B., Wang, T., Prakash, V.: A compact fiber optics-based heterodyne combined normal and transverse displacement interferometer. Rev. Sci. Instrum. **88**(3), 033108 (2017)
27. Zuanetti, B., Wang, T., Prakash, V.: A Novel Approach for Plate Impact Experiments to Obtain Properties of Materials Under Extreme Conditions. In: Dynamic Behavior of Materials, vol. 1, pp. 19–26. Springer, Berlin (2019)
28. Bless, S.J., et al.: Failure waves in glass. J. Am. Ceram. Soc. **75**(4), 1002–1004 (1992)
29. Dandekar, D.P., Beaulieu, D.: Failure wave under shock wave compression in soda-lime glass. In: Murr, L.E., Staudhammer, K.P., Meyers, M.A. (eds.) Mettalurgical and Materials Applications of Shock wave and High Strain Rate Phenomena, pp. 211–218. Elsevier, New York (1995)
30. Dandekar, D.P.: Spall strength of silicon carbide under normal and simultaneous compression-shear shock wave loading. Int. J. Appl. Ceram. Technol. **1**(3), 261–268 (2004)
31. Zuanetti, B., Wang, T., Prakash, V.: Plate impact investigation of the dynamic response of commercial tungsten carbide under shock-induced compression and combined compression-and-shear loading. Int. J. Imp. Eng. Manuscript sumbitted for publication, (2019)

Chapter 29
A Kolsky Bar with a 50 ns Rise-Time: Application to Rates Beyond 1 M/s

Daniel T. Casem

Abstract Miniature Kolsky bars, or Split Hopkinson Pressure Bars, are used to increase the strain-rate range accessible by the technique. A number of authors have developed miniature versions in both Kolsky bar and direct impact configurations (Jia and Ramesh, Exp. Mech. 44:445–454, 2004; Casem, A Small Diameter Kolsky bar for High-rate Compression, 2009; Ames, Shock compression of condenser matter, 2005; Casem et al., Exp. Mech. 52:173–184, 2012; Lea and Jardine, Int. J. Plas. 102:41–52; Casem et al., Mims High-rate Mechanical Response of Aluminum Using Miniature Kolsky Bar Techniques, 2018), and rates as high as 1 M/s have been obtained with bars as small as 127 μm diameter (Casem et al., Mims High-rate Mechanical Response of Aluminum Using Miniature Kolsky Bar Techniques, 2018). Even higher rates are possible, provided challenges related to manufacture, alignment, and instrumentation can be overcome.

Keywords Kolsky bar · Split Hopkinson pressure bar · Dispersion · Interferometry · High strain-rate

One reason miniaturization allows higher strain-rate testing is that the reduction in bar diameter decreases the bar's rise-time. This permits higher frequency signals to propagate in the bars, which is necessary for short duration, high strain-rate experiments. A fundamental assumption in the analysis of the test assumes the bar wave theory applies, and this assumption breaks down when wavelengths approach the bar diameter. This leads to well-known dispersion effects and although corrections have been developed [7–9], they cannot make the one-dimensional theory apply to what are essentially three-dimensional waves. Thus there is a limiting frequency, or rise-time, that can propagate in any given bar. This frequency is not precisely defined, but it is directly related to the bar diameter, and is one of the limiting factors that dictate the maximum strain-rate achievable with that bar.

This issue is particularly important for miniature bars. While there are many reasons why the behavior of a bar in an actual experimental set-up might deviate from the ideal uniaxial theory, they are exacerbated at small scales. These include (1) poor alignment and/or clearance through the supporting bushings, (2) deviations in the bar straightness, shape and/or diameter, (3) the microstructure of the bar, and (4) friction along the bushings. In the prior work mentioned above [6], it is clear that the full potential of these bars has not been realized, i.e., they do not have measurable rise-times that approach that expected by the linear elastic theory. This has prohibited the application of the technique at higher strain-rates.

The present work attempts to address this. There is a well-established theory regarding the variation of phase speed with frequency for longitudinal waves in cylindrical elastic bars, and so comparison of experimentally measured relationships to the theoretical is an ideal way to identify the cut-off frequency with minimal subjectivity. To do so, steel bars with diameters as small as 100 μm are loaded by single pulses using simple projectile impacts and measured at multiple points along the path of propagation. By using the method of Bacon [10], phase speed as a function of frequency is determined, and compared to that predicted by the elastic theory [7]. The point at which the experimentally measured curve begins to deviate from the theory is taken as the maximum frequency, and is used to determine a rise-time. We also compare this rise-time with that measured from a numerical simulation of the experiment, again determined using the method of [10] but using numerical data.

Figure 29.1 shows an example of one such experiment. A 7.1 mm long, 101 um diameter steel pressure bar is impacted in such a way as to create a single pulse at the impact end. The free-end is instrumented with a normal displacement interferometer, which measures the initial pulse and two of the subsequent reflections, shown in Fig. 29.2. Figure 29.3 shows FFT magnitudes of the first two pulses, and Fig. 29.4 shows the calculated phase speed, along with the theoretical data. We note the pulse does not deviate appreciably from the theory until 20 MHz, indicating that frequencies up to this

D. T. Casem (✉)
US Army Research Laboratory, CCRL-WMP-C, APG, Adelphi, MD, USA
e-mail: daniel.t.casem.civ@mail.mil

L. E. Lamberson (ed.), *Dynamic Behavior of Materials, Volume 1*, Conference Proceedings of the Society for Experimental Mechanics Series, https://doi.org/10.1007/978-3-030-30021-0_29

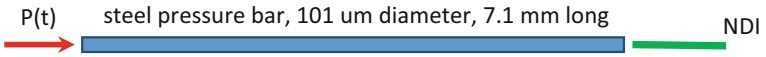

Fig. 29.1 An impulsive load is applied to a pressure bar. The initial pulse and two of the subsequent reflections are measured with an NDI applied to the free-end

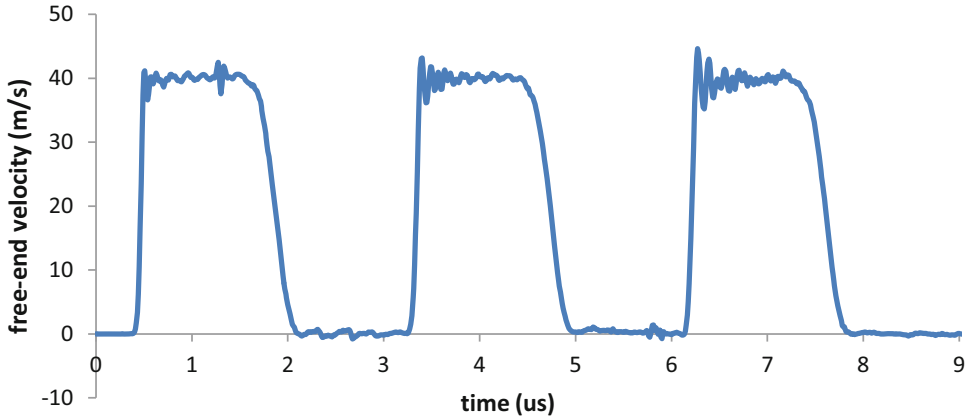

Fig. 29.2 Measurements of the initial pulse and two reflections

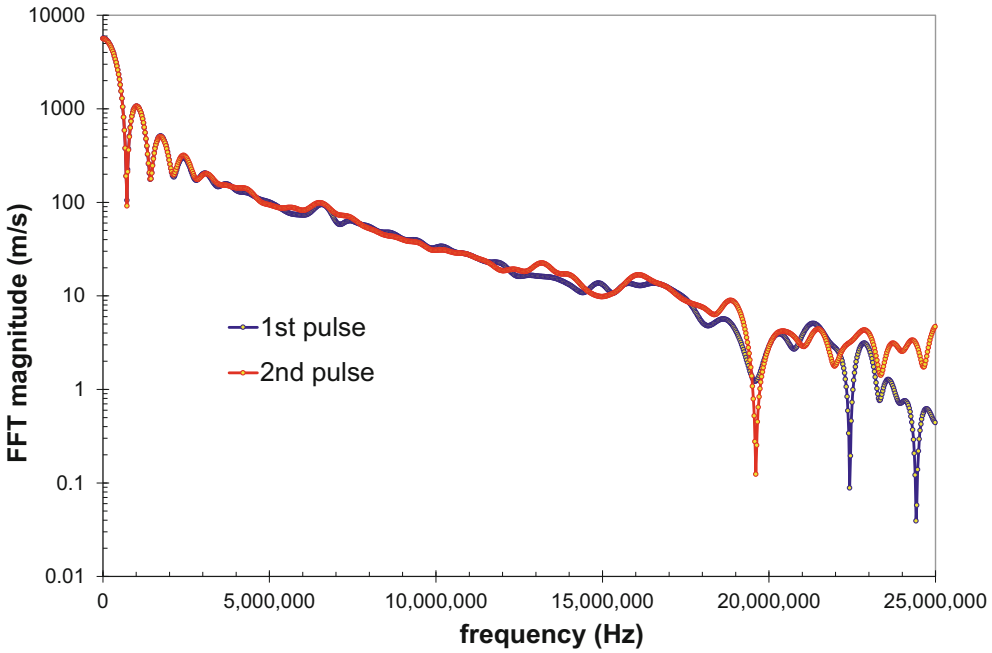

Fig. 29.3 FFT magnitudes of the first two pulses

propagate as one-dimensional waves, i.e., the one-dimensional theory applies. This corresponds to a wavelength of about 2.5 bar diameters, and a period of 50 ns, which compares well to the experimentally measured rise-time of the first pulse, shown with a shorter time scale in Fig. 29.5. We are currently experimenting with alternate methods of bar alignment to improve this.

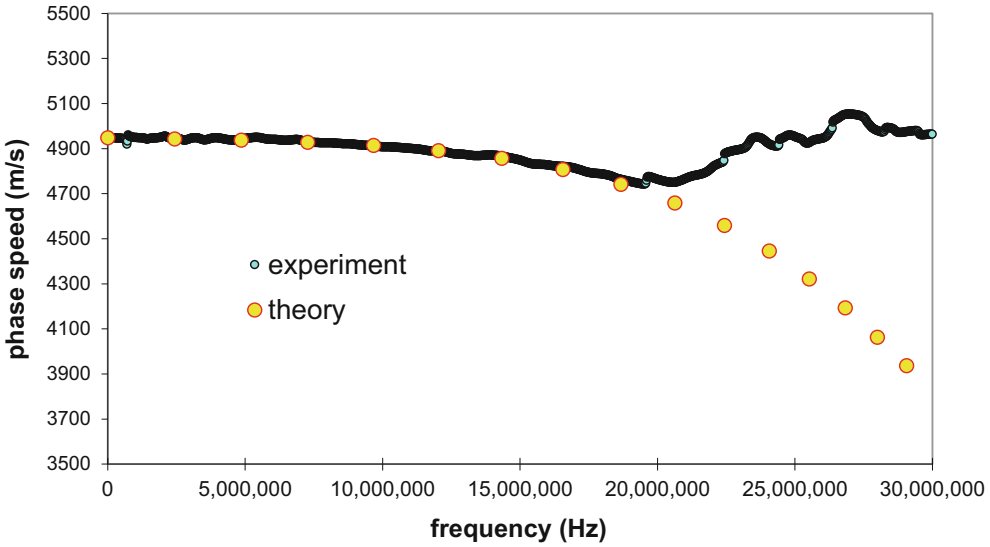

Fig. 29.4 Phase speed vs. magnitude for the first two pulses compared to theory. Note good agreement until almost 20 MHz

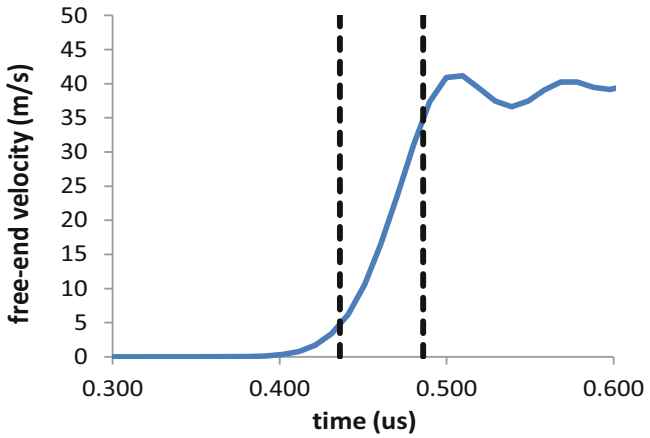

Fig. 29.5 The rising edge of the first pulse shown in Fig. 29.2. The dashed lines show a rise-time of 50 ns

References

1. Jia, D., Ramesh, K.T.: A rigorous assessment of the benefits of miniaturization in the Kolsky Bar system. Exp. Mech. **44**, 445–454 (2004)
2. Casem, D.T.: A Small Diameter Kolsky bar for High-rate Compression. Proc. of the 2009 SEM Annual Conference and Exposition on Experimental and Applied Mechanics, Albuquerque, NM, June 1–4, (2009)
3. Ames, R.G.: Limitations of the Hopkinson Pressure Bar for High-Frequency Measurements. In: Furnish, M.D., Elert, M., Russell, T.P., White, C.T. (eds.) Shock compression of condenser matter, pp. 1233–1237 (2005)
4. Casem, D.T., Grunschel, S.E., Schuster, B.: Normal and transverse displacement interferometers applied to small diameter Kolsky bars. Exp. Mech. **52**, 173–184 (2012)
5. Lea, L.J., Jardine, A.P.: Characterisation of high rate plasticity in the uniaxial deformation of high purity copper at elevated temperatures. Int. J. Plast. **102**, 41–52 (2018)
6. Casem, D.T., Ligda, J.P., Schuster, B.E., Mims, S.: High-rate mechanical response of aluminum using miniature Kolsky bar techniques, pp. 147–153. Springer International Publishing, Cham (2018)
7. Follansbee, P.S., Franz, C.: Wave propagation in the split- Hopkinson pressure bar. J. Eng. Mat. Tech. **105**, 61 (1983)
8. Gong, J.C., Malvern, L.E., Jenkins, D.A.: Dispersion investigation in the split-Hopkinson pressure bar. J. Eng. Mat. Tech. **112**, 309 (1990)
9. Gorham, D.A., Wu, X.J.: An empirical method for correcting dispersion in pressure bar measurements of impact stress. Meas. Sci, Tech. **7**, 1227 (1996)
10. Bacon, C.: An experimental method for considering dispersion and attenuation in a viscoelastic Hopkinson bar. Exp. Mech. **38**, 242 (1998)

Chapter 30
Strain Stiffening Effects of Soft Viscoelastic Materials in Inertial Microcavitation

Jin Yang and Christian Franck

Abstract Mechanical characterization of soft materials, e.g. hydrogels, tissues, and various polymeric specimens, at high strain-rates (10^3 s^{-1}–10^6 s^{-1}) is challenging due to their compliance, slow wave speeds, and non-linear viscoelasticity. However, knowledge of their material is important in many biological and engineering applications from minimizing tissue damage in ultrasound and laser surgeries to diagnosing and mitigating impact injuries. Recently, a minimally invasive, local 3D micro-rheology technique based on inertial microcavitation rheometry (IMR) has been developed to determine the general viscoelastic material properties of soft matter as compliant as a few kilopascals. For example, material behavior of polyacrylamide undergoing large, finite deformations ($|E_{rr}| > 0.05$) at strain-rates of up to 10^6 s^{-1} has been measured and fitted using nonlinear Kelvin-Voigt model, which extends the traditional quasi-static neo-Hookean description of polyacrylamide to include a dynamic material viscosity in the order of 10^{-1} Pa·s.

In the classical case study of polyacrylamide, the nonlinear neo-Hookean Kelvin-Voigt model fitting results shows that the shear moduli obtained during cavitation are stiffer than their quasi-static counterparts. This strain stiffening effects needs additional consideration and treatment. Here we address the issue of strain stiffening by replacing the traditional neo-Hookean spring in the nonlinear Kelvin-Voigt model with a higher order constitutive relation inspired by the Fung model.

Keywords Inertial microcavation rheometry (IMR) · Viscoelastic · High strain rates · Strain-stiffening · Fung model

Introduction

Cavitation is a common phenomenon in hydrodynamics and biology [1–6]. Recently, it was recognized that inertial microcavitation rheometry (IMR) can be used to characterize the mechanical behavior of viscoelastic materials since the cavitation bubble collapse is very sensitive to the constitutive equations of the surrounding medium [7–8]. By analyzing the bubble dynamics, the viscoelastic properties of soft materials can be characterized where the strain rates can reach O (10^3) s^{-1} ~ O (10^6) s^{-1} [10]. Recently, Estrada et al. [7] demonstrated experiments to probe viscoelastic mechanical properties of soft materials using IMR, where time-resolved data for the temporal evolution of bubble radii is fitted to the prediction of the governing equations of bubble dynamics, combined with a neo-Hookean Kelvin-Voigt constitutive model for surrounding soft medium. In the case of polyacrylamide hydrogels, the neo-Hookean Kelvin-Voigt model fitting results show that the shear moduli obtained during cavitation are stiffer than their quasi-static counterparts. This strain stiffening effect, which is a very common feature of soft materials because of structural transitions such as ordering, crystallization, or shear banding under large strain, needs additional consideration and treatment in IMR.

In this paper, we first review the physical model of IMR in Section "Physical model". We address the issue of strain stiffening by replacing the traditional neo-Hookean spring in the nonlinear Kelvin-Voigt model with a higher order material constitutive relation inspired by the Fung model [9] in Section "Strain Stiffening Effects". Our experimental setup is introduced in Section "Experimental Setup". We demonstrate our Fung Kelvin-Voigt model in Section "Results and Discussion". Finally, we present some conclusions in Section "Conclusions".

J. Yang (✉) · C. Franck
Department of Mechanical Engineering, University of Wisconsin, Madison, WI, USA
e-mail: jyang526@wisc.edu

L. E. Lamberson (ed.), *Dynamic Behavior of Materials, Volume 1*, Conference Proceedings of the Society for Experimental Mechanics Series, https://doi.org/10.1007/978-3-030-30021-0_30

Physıcal Model

Bubble Dynamics with Viscoelastic Surroundings

We consider the spherical dynamics of a bubble in an infinite viscoelastic medium, where the surrounding medium is assumed to be incompressible in the near field, and compressible in the far field. The bubble dynamics are represented by the Keller-Miksis equation [11]:

$$\left(1-\frac{\dot{R}}{c}\right)R\ddot{R}+\frac{3}{2}\left(1-\frac{\dot{R}}{3c}\right)\dot{R}^2=\left(1+\frac{\dot{R}}{c}+\frac{R}{c}\frac{d}{dt}\right)\frac{p-p_\infty(t)-\Theta_{ve}-\frac{2\gamma}{R}}{\rho}, \tag{30.1}$$

where $R(t)$ is the bubble radius, and the overdots denote derivatives with respect to time t; ρ and c are the density and sound speed of the surrounding soft materials; γ is the surface tension between bubble inside gas and surroundings; p is the internal bubble pressure given by the sum of the partial pressures of non-condensible gas (p_g) and vapor (p_v); $p_\infty(t)$ is the far-field driving pressure; Θ_{ve} is the viscoelastic stress integral defined as

$$\Theta_{ve}=\int_R^\infty \frac{2}{r}\left(\tau_{rr}-\tau_{\theta\theta}\right)dr. \tag{30.2}$$

The specifics of the stress integral depend on the constitutive properties of the material at hand. For example, assuming the surrounding material obeys neo-Hookean Kelvin-Voigt formulation, the stress tensor can be expressed as

$$\tau_{rr}=\frac{2}{3}G\left[\left(\frac{r_0}{r}\right)^4-\left(\frac{r}{r_0}\right)^2\right],\quad \tau_{\theta\theta}=-\frac{1}{2}\tau_{rr}, \tag{30.3}$$

where $r_0(r,t)=\left(r^3-R^3+R_\infty^3\right)^{1/3}$is the radial location in the original configuration. The viscoelastic stress integral Θ_{ve} can be further integrated analytically:

$$\Theta_{ve}=\frac{4\mu\dot{R}}{R}+\frac{G}{2}\left[5-4\frac{R_\infty}{R}-\left(\frac{R_\infty}{R}\right)^4\right], \tag{30.4}$$

where μ is the viscosity of the surrounding soft material, G is the shear modulus, and R_∞ is the bubble radius corresponding to the final equilibrium state.

Strain Stiffening Effects

In addition to a neo-Hookean material model, we also explored strain-stiffening effects and apply a higher order material model inspired by Fung model [9] whose strain energy density is

$$\Psi_{\text{Fung}}(\mathbf{F})=\frac{G_\infty}{2\alpha}\exp\left(\alpha\left(I_1-3\right)\right)=\frac{G_\infty}{2\alpha}\left[\alpha\left(I_1-3\right)+\frac{\alpha^2}{2}(I_1-3)^2\right]+\text{h.o.t}, \tag{30.5}$$

and its stress integral is

$$\Theta_{ve,\text{Fung}}=2G_\infty\int_{R(t)}^\infty\left[\left(\frac{r_0}{r}\right)^4-\left(\frac{r}{r_0}\right)^2\right]\exp\left[\alpha\left(I_1-3\right)\right]\frac{dr}{r}. \tag{30.6}$$

Heat and Mass Transfer at the Bubble Wall

The pressure inside the bubble is assumed to be homobaric. The inclusion of heat and mass transfer [12] modify bubble pressure evolution:

$$\dot{p} = \frac{3}{R}\left[-\kappa p\dot{R} + (\kappa - 1)\, K_w \left.\frac{\partial T}{\partial r}\right|_w + \kappa \mathcal{R}_v T_w \dot{m}_v''\right], \tag{30.7}$$

where $T(r,t)$ is the instantaneous, spatially varying temperature, K is the mixture thermal conductivity inside the bubble ($K = AT + B$), $\mathcal{R}_v$ is the gas constant of vapor, specific heats ratio κ of vapor is assumed equal to that of air, and $\dot{m}_v''$ the vapor mass flux across the interface. The subscript w denotes variables evaluated at the bubble wall. The vapor mass flux is related with mass transfer at the bubble wall:

$$\dot{m}_v'' = D\frac{\rho_{m,w}}{1 - C_w}\left.\frac{\partial C}{\partial r}\right|_w, \tag{30.8}$$

where C is the mass fraction of vapor gas; D is the diffusion coefficient between water vapor and air; ρ_m is the mass density of the mixed vapor that satisfies $p = \mathcal{R}\rho_m T$, where $\mathcal{R} = C\mathcal{R}_v + (1 - C)\,\mathcal{R}_g$ is the mixture gas constant, $\mathcal{R}_g$ is the gas constant of non-condensible gas, and $\mathcal{R}_v$ if the gas constant of vapor.

Mass diffusion is assumed to follow Fick's law such that the mass balance equation for vapor reads

$$\frac{\partial C}{\partial t} + \left(\dot{R} + \frac{\mathcal{R}_v - \mathcal{R}_g}{\mathcal{R}}\frac{\partial C}{\partial r}\right)\frac{\partial C}{\partial r} = \frac{[\nabla\cdot(D\rho_m\nabla C)]_r}{\rho_m}. \tag{30.9}$$

To account for heat transfer and energy balance, we apply Fourier's law both inside and outside the bubble:

$$\frac{\kappa}{\kappa - 1}\frac{p}{T}\left(\frac{\partial T}{\partial t} + \dot{R}\frac{\partial T}{\partial r}\right) - \dot{p} = [\nabla\cdot(K\nabla T)]_r, \quad \frac{\partial T_s}{\partial t} + \frac{R^2\dot{R}}{r^2}\frac{\partial T_s}{\partial r} = D_s\left[\nabla^2 T_s\right]_r + \frac{12\mu}{\rho C_p}\left(\frac{R^2\dot{R}}{r^3}\right)^2, \tag{30.10}$$

where T is the temperature inside bubble and T_s is the temperature in the outside surroundings; $C_p = CC_{p,\,v} + (1 - C)C_{p,\,g}$ is the heat capacity at constant pressure where $C_{p,\,v}$ and $C_{p,\,g}$ are the constant specific heats at constant pressure for the vapor and non-condensible gas, respectively; $D_s = K_s/(\rho C_p)$ is the thermal diffusivity, and K_s is the constant thermal conductivity of the soft surrounding medium.

Boundary Conditions

Regarding boundary conditions for the vapor mass fraction and the temperature, at the origin, we have

$$\left.\frac{\partial C}{\partial r}\right|_{r=0} = \left.\frac{\partial T}{\partial r}\right|_{r=0} = 0 \tag{30.11}$$

due to spherical symmetry. At the bubble wall, we assume that the vapor is in equilibrium with the condensed layer and the vapor partial pressure is equal to its saturation pressure. We also assume that the surrounding material remains isothermal with constant temperature T_∞ everywhere. All the boundary conditions near the wall are summarized as follows:

$$T_s|_w = T|_w = T_\infty, \quad \left.\frac{\partial T_s}{\partial r}\right|_w = \left.\frac{\partial C}{\partial r}\right|_w = 0, \quad p_{v,\mathrm{sat}}\,(T_w) = p_{\mathrm{ref}}\exp\left(-\frac{T_{\mathrm{ref}}}{T_w}\right). \tag{30.12}$$

where $p_{v,\,sat}(T)$ is the temperature-dependent saturation pressure of the vapor with empirical constants p_{ref} and T_{ref}.

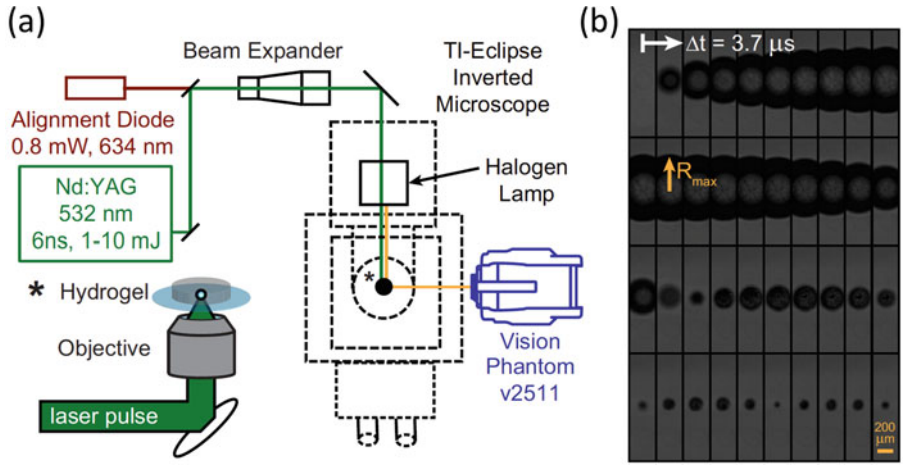

Fig. 30.1 Experimental setup and schematic of inertial microcavitation rheometry. (**a**) A single 6 ns, Q-switched 532 nm Nd:YAG laser pulse of 1–10 mJ passes through a beam expander to fill the back aperture of an objective mounted into an inverted TI-Eclipse microscope, and (inset, star) converges into a cylindrical hydrogel sample. Bright-field illumination is supplied by a condensed halogen lamp. (**b**) Bubble growth, collapse, and subsequent oscillation are imaged using a Phantom v2511 high speed camera (Vision Research, Wayne, NJ). Image size 512×128 pixels, filmed at 270,000 fps. Scale bar, 200 $\boldsymbol{\mu m}$ (Image courtesy of Estrada [7])

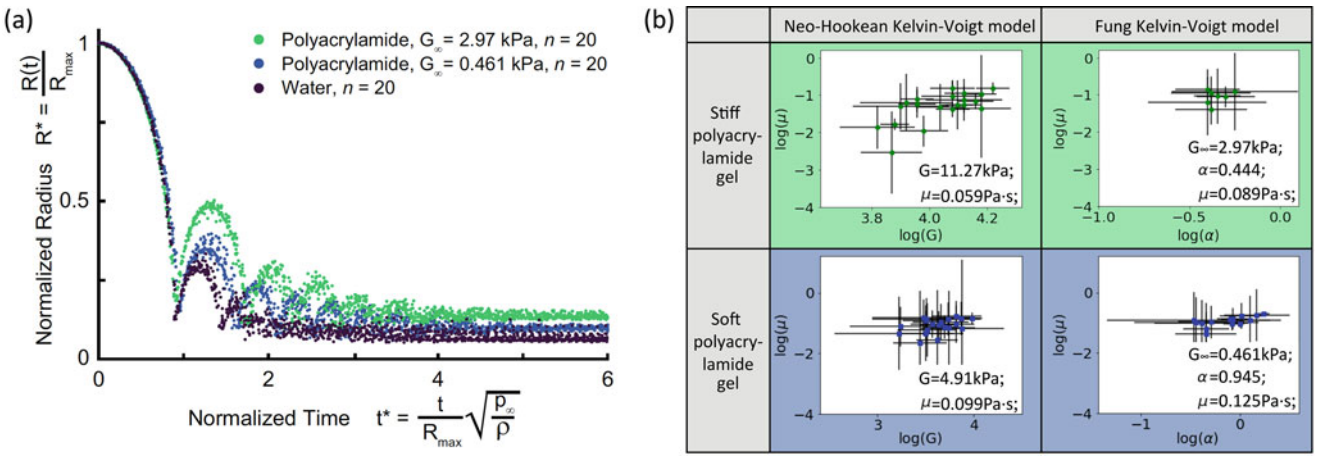

Fig. 30.2 IMR characterizes stiff & soft polyacrylamide hydrogels viscoelastic properties using neo-Hookean Kelvin-Voigt model and Fung Kelvin-Voigt model. (**a**) Bubble radius *R-t* curve of IMR cavitation experiments inside stiff & soft polyacrylamide hydrogels and water (reference). (**b**) Characterized viscoelastic properties of the tested stiff & soft polyacrylamide hydrogels using two types of nonlinear material models (neo-Hookean Kelvin-Voigt & Fung Kelvin-Voigt)

Experimental Setup

In this study, the experimental setup is the same as in Estrada *et al* [7] where single bubble inertial cavitation is generated via single pulses of a frequency-doubled Q-switched Nd:YAG 532 nm laser as shown in Fig. 30.1a. We use a Phantom v2511 CCD high speed camera (Vision Research, Wayne, NJ) to take a sequence of images (exposure time of single frame is set to be 2 μs) of bubble growth, collapse and subsequent oscillations as shown in Fig. 30.1b. Bubble images were then fit for their centroid and radius $R(t)$ using a circle fit algorithm (see Figs. 30.1b and 30.2a). Here we tested cavitation experiments using two types (stiff & soft) of polyacrylamide hydrogels, whose quasi-static shear moduli have also been characterized using quasi-static compression indentations [7].

Table 30.1 Material properties used in the present study

Symbol	Value	Symbol	Value	Symbol	Value	Symbol	Value
ρ	1060 kg/m^3	γ	5.6×10^{-2} N/m	D	24.2×10^{-6} m^2/s	A	5.3×10^{-5} W/mK^2
c	1430 m/s	κ	1.4	K_s	0.55 W/m	B	1.17×10^{-2} W/mK
p_∞	101.3 kPa	$C_{p,v}$	1.62 kJ/kg · K	p_{ref}	1.17×10^8 kPa		
T_∞	298.15 K	$C_{p,g}$	1.00 kJ/kg · K	T_{ref}	5200 K		

Results and Discussion

Following Barajas *et al* [8], a fifth-order explicit Dormand-Prince Runge-Kutta method with adaptive step-size control is used to evolve the governing equations forward in time. Quantitative values of material parameters for the surrounding medium and the bubble contents used in this study are summarized in Table 30.1. Least squares error (LSE) is defined by minimizing the perpendicular offset between experimental data points and the numerical simulations. Minimizing the discrete LSE in the *R-t* curves gives the best estimate of the viscoelastic properties for each polyacrylamide gel. Figure 30.2b shows the characterized viscoelastic properties of the tested stiff & soft polyacrylamide hydrogels using neo-Hookean Kelvin-Voigt and Fung Kelvin-Voigt models.

We find that for both stiff & soft polyacrylamide hydrogels, the nonlinear neo-Hookean Kelvin-Voigt model fitting results show that the shear moduli obtained during cavitation are stiffer than their quasi-static counterparts (see Fig. 30.2b). On the other hand, when we account for strain stiffening by replacing the traditional neo-Hookean spring in the nonlinear Kelvin-Voigt model with a constitutive relation inspired by the Fung model [9], we recover the quasi-static shear modulus at long time scale. We also find that by applying the Fung Kelvin-Voigt model, the accuracy of the measured dynamic material viscosity is also improved compared to the neo-Hookean Kelvin-Voigt formulation.

Conclusions

In this paper, we use inertial microcavitation rheometry (IMR) experiments to characterize viscoelastic properties of stiff & soft polyacrylamide hydrogels undergoing large, finite deformations ($|E_{rr}| > 0.05$) at strain-rates of up to 10^6 s^{-1}. We explore the strain stiffening effects of these two types of hydrogels by implementing Fung Kelvin-Voigt model. Compared with our previous neo-Hookean Kelvin-Voigt model, we find the accuracy of the measured dynamic material viscosity (in the order of 10^{-1} Pa·s) is also improved.

Acknowledgement We gratefully acknowledge the funding support from the Office of Naval Research (Dr. Timothy Bentley) under grants N000141612872 and N000141712058. JY acknowledges discussions and help from Prof. David L Henann and Dr. Jonathan B Estrada.

References

1. Maxwell, A., et al.: Noninvasive thrombolysis using pulsed ultrasound cavitation therapy – histotripsy. Ultrasound Med. Biol. **35**(12), 1982–1994 (2009)
2. Venugopalan, V., et al.: Role of laser-induced plasma formation in pulsed cellular microsurgery and micromanipulation. Phys. Rev. Lett. **88**(7), 078103 (2002)
3. Xu, Z., et al.: High speed imaging of bubble clouds generated in pulsed ultrasound cavitational therapy – histotripsy. IEEE Trans Ultrason. Ferroelect. Freq. Control. **54**(10), 2091–2101 (2007)
4. Meaney, D., Smith, D.: Biomechanics of concussion. Clin. Sports Med. **30**, 19–31 (2011)
5. Nyein, M., et al.: In silico investigation of intracranial blast mitigation with relevance to military traumatic brain injury. Proc. Natl. Acad. Sci. U. S. A. **107**(48), 20703–20708 (2011)
6. Ramasamy, A., et al.: Blast-related fracture patterns: a forensic biomechanical approach. J. R. Soc. Interface. **8**(58), 689–698 (2010)
7. Estrada, J.B., Barajas, C., Henann, D.L., Johnsen, E., Franck, C.: High strain-rate soft material characterization via inertial cavitation. J. Mech. Phys. Solids. **112**, 291–317 (2018)
8. Barajas, C., Johnsen, E.: The effects of heat and mass diffusion on freely oscillating bubbles in a viscoelastic, tissue-like medium. J. Acoust. Soc. Am. **141**(2), 908–918 (2017)
9. Fung, Y.C.: Biomechanics: mechanical properties of living tissues. Springer Science & Business Media, Berlin (2013)
10. Chen, D.T.N., Wen, Q., Janmey, P.A., et al.: Rheology of soft materials. Annu. Rev. Condens. Matter. Phys. **1**(1), 301–322 (2010)
11. Keller, J.B., Miksis, M.: Bubble oscillations of large amplitude. J. Acoust. Soc. Am. **68**, 628–633 (1980)
12. Prosperetti, A.: The thermal behavior of oscillating gas bubbles. J. Fluid Mech. **222**, 587–616 (1991)

Chapter 31
Assessment of Dynamic Fracture in Ultra-High Performance Concrete Using Synchrotron X-ray Source

Nesredin Kedir, Shane Paulson, Cody Kirk, Tao Sun, Kamel Fezzaa, and Wayne Chen

Abstract Ultra-high-performance concretes (UHPCs) retain higher ultimate (compressive) strengths and greater durability relative to traditional concrete materials. As a result, they are enabling construction materials for blast resistant structures, where a higher capacity for energy absorption is required. In past investigations, the strength of UHPCs was shown to retain a dependency on strain rate. Still, the failure mechanisms which govern this rate dependency have yet to be completely elucidated. In the current study, the dynamic fracture behavior of Cor-tuf UHPC was assessed, *in-situ,* using a Synchrotron X-ray source in phase contrast imaging (PCI) mode. Prior to testing, the material's morphology was characterized using X-ray computed tomography (CT) and scanning electron microscopy (SEM). A polychromatic pulsed X-ray source, high-speed camera and Kolsky bar apparatus were used in tandem, to observe the transient failure modes. A pin was placed at the end of the incident bar to control the location of damage initiation, and tests were performed at a constant velocity of ~6 m/s. These test conditions were observed to yield cracks with median and/or cone like geometries. Despite the variation in the crack paths, a significant difference in peak load was not observed. The failure mode was also observed to depend on the microstructure of the concrete samples.

Keywords UHPCs · Synchrotron source · Phase contrast imaging · X-ray computed tomography (CT) · Kolsky bar

Introduction

The performance of concrete is traditionally associated with load bearing capacity (or compressive strength). Traditional concrete has a compressive strengths <65 MPa [1]. The latter is primarily composed from a mixture of water, coarse aggregate, sand and cement. The high-side of compressive strength is attained by reducing the water to cement (W/C) ratio. However, a lower W/C ratio diminishes the workability and formability of the concrete mixture. In more modern concrete, higher strengths are attained by use of plasticizers and pozzolan admixtures. The resulting high-strength concrete (HSC) retains a compressive strength in the range of 50–130 MPa [1]. Even higher strengths (>150 MPa) are attained in ultra-high-performance concrete (UHPC) by reducing the aggregate size.

One key advantage of UHPC is the potential for enhanced energy absorption. This property is crucial for sustainment of structural integrity under dynamic loading conditions including earthquakes and explosions. Past studies evaluating the dynamic response of concrete have shown a dependency of mechanical properties on loading rate. This is readily noted in the work by Bischoff et al. where an increase in apparent compressive strength was observed to result from increase strain up to 10^2 s^{-1} [2]. Similar behaviors have also been reported at even higher strain rates including blast loadings [3]. Various aspects of the microstructure are deemed responsible for the observed behavior including a weak interfacial transition zone (ITZ) in traditional concrete and crack bifurcations (multitrack formation) in HSC/UHPC. However, there still lacks a comprehensive understanding of the mechanisms operating during dynamic loading.

N. Kedir (✉)
School of Materials Engineering, Purdue University, West Lafayette, IN, USA
e-mail: nkedir@purdue.edu

S. Paulson · C. Kirk
School of Aeronautics and Astronautics Engineering, Purdue University, West Lafayette, IN, USA

T. Sun · K. Fezzaa
Advanced Photon Source (Sector 32), Argonne National Laboratory, Lemont, IL, USA

W. Chen
School of Aeronautics and Astronautics Engineering & School of Materials Engineering, Purdue University, West Lafayette, IN, USA

L. E. Lamberson (ed.), *Dynamic Behavior of Materials, Volume 1*, Conference Proceedings of the Society for Experimental Mechanics Series, https://doi.org/10.1007/978-3-030-30021-0_31

The current work utilizes a unique *in-situ* dynamic loading technique to determine the propagation of failure modes during dynamic loading of Cor-tuf UHPC. Thin rectangular specimens are impacted by the horizontal segment of a hardened steel pin. The use of a pin enables control over the location of damage initiation and tracking of subsequent events. A modified Kolsky compression bar is used to impact the sample. A pulsed synchrotron X-ray source simultaneously produces visual representations of the transient event with the aid of an X-ray luminescing optic setup and high-speed camera.

Background

The Cor-tuf UHPC samples were produced by the U.S. Army Engineering Research and Development Center (ERD) and machined into cylindrical pucks at the U.S. Air Force Research Laboratory in Eglin Air Force Base. The samples were sectioned, first using a surface grinder and then a slow-speed diamond saw, to produce cuboid specimens (6.71 ± 0.58 mm x 4.75 ± 0.12 mm x 1.02 ± 0.05 mm). Prior to impact testing, a few samples were characterized using X-ray computed tomography (CT) at beamline 2BM of the advanced photon source (APS), in Argonne National Laboratory. A detailed account of the tomography procedure is found elsewhere [4]. In these experiments, a monochromatic beam with 25 keV energy and 5× magnification were used. A scanning electron microscope (SEM) was also used to image a polished surface of the concrete.

Schematics of the modified Kolsky compression bar setup and Synchrotron X-ray source for real-time phase contrast imaging (PCI) are provided in Fig. 31.1. The experimental method and loading configuration have been described in detail previously [4]. A hardened steel pin (60 HRC) with a diameter of 1.59 mm was used to dynamically load the short transverse face of the concrete sample at a constant bar-end velocity of 6 m/s. The support fixture for the concrete was threaded into a load cell to measure the applied force. Corresponding X-ray PCI images were captured at a frame rate of 5 MHz using a U-18 undulator.

An X-ray CT reconstruction slice and SEM micrograph for the Cor-tuf concrete are shown above in Fig. 31.2. Note that in the CT slice, four phases of the concrete are clearly discerned by their disparate intensities. Based on previous work by Parab et al. the brightest (highly absorptive) phase corresponds to silica fume, the large darkgrey agglomerates corresponds to the aggregate, and the lightgrey phases of smaller size decorating the aggregate represent silica flower embedded in cement [4]. Additionally, the dark phases with well-defined edges highlight the pores. The SEM micrograph obtained using backscatter mode (Fig. 31.2a) shows a nearly identical color scheme with improved contrast between the aggregate and silica flower phases.

A total of ten samples were used for experiments with seven samples yielding complete capture of the impact event. The primary modes of fracture consisted of median, angle and combined median/angle cracks. The occurrence of these cracks was found to be independent of the maximum/peak load which ranged between 150 and 315 N. This behavior is attributed to the variation in the microstructure of the concrete, especially in the distribution of the pores [4].

Figure 31.3, shows a sequence of images and associated force-displacement curve for one of the samples (Tuf #6). Note that in the initial stages, the concrete is deformed at the contact interface. This is accommodated by microfracture of the aggregate and collapsing of nearby pores. Further displacement of the pin results in extension of the primary median and/or angled cracks (highlighted by arrows) from the initial deformation zone. Final failure results by extension of microcracks and opening of the primary crack interfaces. The cracks tend to traverse around the silica fume particles and divert along the network of porosities.

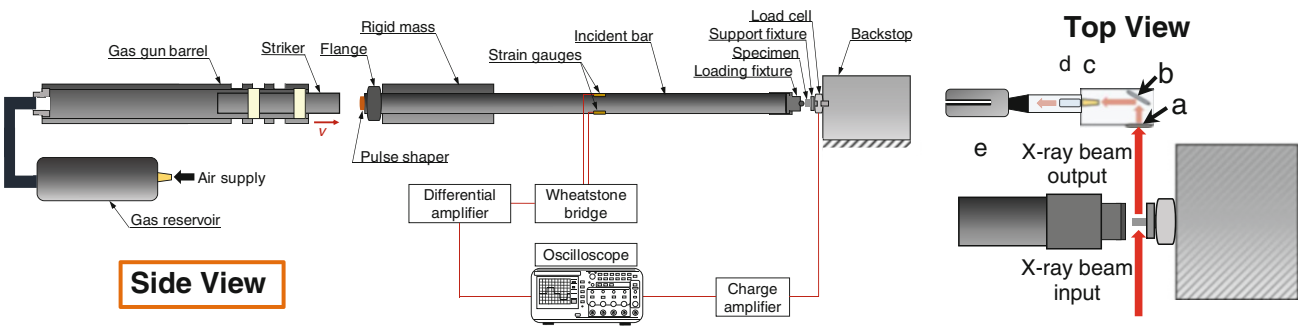

Fig. 31.1 Schematic of the modified Kolsky compression bar system as viewed from the side (left). A close up top-view of the pin loading—X-ray setup (right): (**a**) Scintillator, (**b**) 45° mirror, (**c**) 5× objective lens, (**d**) Tube lens, and (**e**) high-speed camera

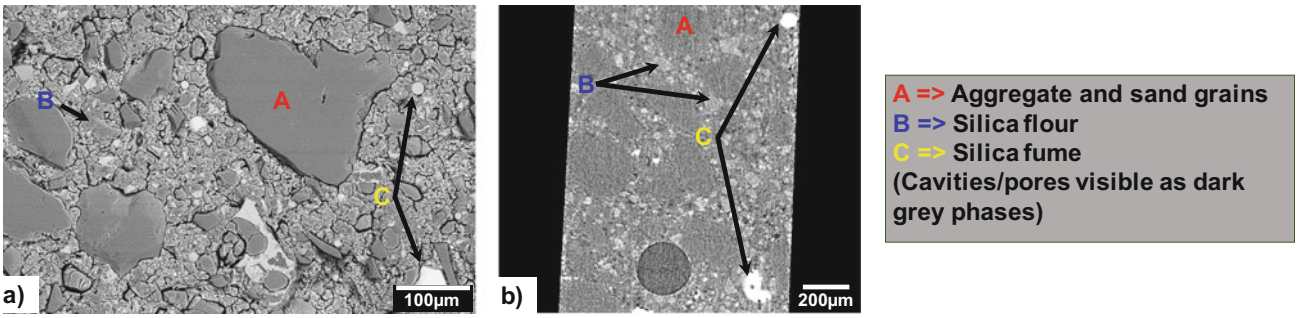

Fig. 31.2 Computed tomography (CT) slice (**a**) and scanning electron micrograph (**b**) of the Cor-tuf concrete material

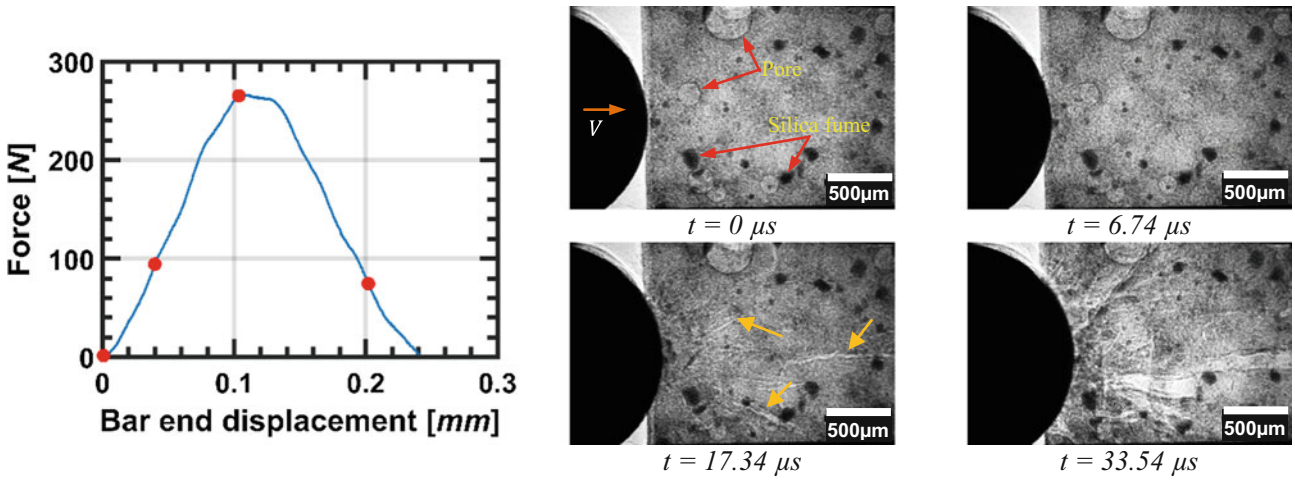

Fig. 31.3 Force—displacement plot and condensed sequence of high-speed X-ray phase contrast images showing the fracture in Cor-tuf concrete (Tuf#6) during impact by a hardened steel pin

Conclusion

Cor-tuf concrete specimens were impacted by a pin using a compression Kolsky bar apparatus and the transient failure was visualized in real-time using synchrotron X-ray source. The resulting image sequences and load histories showed microstructural inhomogeneity to be a governing factor for the variation in failure modes. A preferred crack path through pore networks was confirmed. This method clearly enables understanding of the failure in concrete for dynamic loading conditions.

Acknowledgements The authors extend their gratitude to ERDC and U.S. AFRL for providing materials for experiments. We would also like to thank the staff and scientists at APS 32-IDB for guidance and assistance during the experiments.

References

1. Hammer, T.A.: Ultra High Performance Fiber Reinforced Concrete – State of the art. COIN. (2012)
2. Bischoff, P.H.: Compressive behavior of concrete at high strain rates. Mater. Struct. (1991)
3. Grote, D. L.: Dynamic behavior of concrete at high strain rates and pressures: I. Experimental Characterization. Int. J. Impact Eng., (2001)
4. Parab, N. D.: *In situ* Observation of fracture process in high-strength concretes and limestone using high-speed X-ray phase contrast imaging" Phil. Trans. A, (2016)

Chapter 32
High Rate Mechanical Characterization of Sensitized 5083-H131 Aluminum Alloy

Timothy Walter, Heather Murdoch, Paul Moy, Denise Yin, and Julia Cline

Abstract For many years 5000 series aluminum alloys have played an important role in weight reduction of air, land and sea vehicles. However, sensitization of these alloys has been a major concern regarding the performance of aging vehicles. As the aluminum ages, magnesium, supersaturated in the matrix, segregates out to grain and precipitate boundaries as Al_3Mg_2 (β phase). The β phase is more electrochemically active than the solid solution, leading to increased sensitivity to corrosion including stress corrosion cracking and costly repairs or replacement (Lim et al., Corrosion 72:198–220, 2015). Studies have mostly focused on the effectiveness of various methods (grain boundary engineering, stabilization, coatings) in reducing corrosion but very little work has been performed on the high rate mechanical response of sensitized aluminum. This study will try to elucidate the effect of sensitization on the mechanical response of AA5083-H131. Specimens will be conditioned up to 28 days at 100 °C. Tension and compression tests will be performed at various loading rates to examine strength and elongation to failure. Results from this study will correlate mechanical response to corrosion criteria while aiding in the development of new alloys resistant to the effects of sensitization.

Keywords High rate · Sensitization · Failure · 5083 aluminum · Digital image correlation

Preliminary Testing

A 1″ thick plate of AA5083-H131 was provided by Constellium. This plate was from new production and serves as the "as received" unsensitized baseline for comparison. Sensitized samples were conditioned at 100 °C for 28 days, a treatment chosen to exhibit severe sensitization [1–3]. Specimens were machined in the rolling direction including 12.7 mm diameter compression cylinders and 7.62 mm diameter tension specimens. In addition to ASTM standard tension specimens [4, 5], short specimens were machined for the purpose of high rate testing using the split Hopkinson pressure bar (SHPB). Initial tests focused on tensile behavior since both strength and strain to failure may be affected by sensitization. Tests were performed using a 1323 Instron servo hydraulic load frame. Stereoscopic digital image correlation (DIC) was used for strain measurements [6]. Quasi-static tests used 2.1MP Point Grey cameras and VicSnap (Correlated Solutions) for accusation. For intermediate rate tests (1.0/s) a pair of IDT Os5 cameras operating at 5000 fps were used. Motion Pro (IDT) was used to capture images while load and displacement were acquired using an HBM GEN7t high speed data acquisition system synchronized with the cameras. In both cases, Vic3D (Correlated Solutions) was used to correlate the images to produce full field strain measurements. As received and sensitized specimens both were tested using these methods and the true-stress true-strain results are shown in Fig. 32.1.

Results

From the preliminary tests, data was analyzed to determine the effect of 28 day sensitization and its resulting microstructural evolution on the deformation and failure of the aluminum. Yield stress, ultimate strength and failure strain were determined. It is clear that the yield behavior of the material is greatly affected by sensitization. The loss in yield strength at both quasi-static and intermediate rates is approximately 24–26%. Despite the loss in yield, the hardening response of the sensitized aluminum was increased resulting in a minimal loss of ultimate strength. It was also noted that the strain to failure increased

T. Walter (✉) · H. Murdoch · P. Moy · D. Yin · J. Cline
U.S. Army Combat Capabilities Development Command Army Research Laboratory, Aberdeen Proving Ground, Aberdeen, MD, USA
e-mail: timothy.r.walter3.civ@mail.mil

L. E. Lamberson (ed.), *Dynamic Behavior of Materials, Volume 1*, Conference Proceedings of the Society for Experimental Mechanics Series, https://doi.org/10.1007/978-3-030-30021-0_32

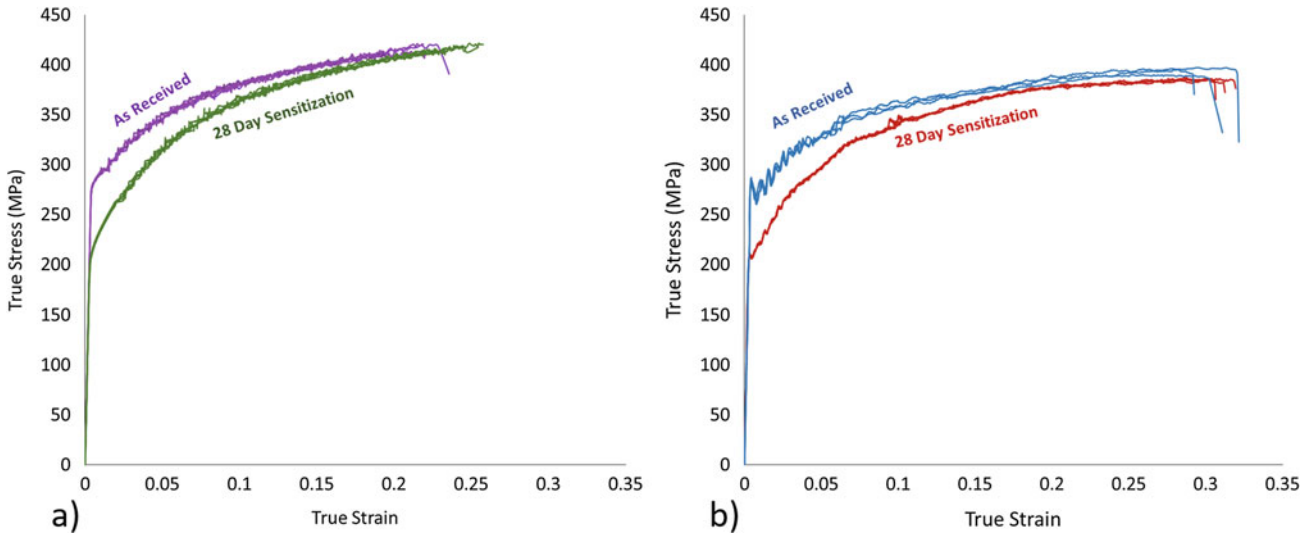

Fig. 32.1 Stress-Strain plots of representative tension tests at (**a**) 0.001/s and (**b**) 1.0/s

Table 32.1 Average results from tensile tests at quasi-static and intermediate rates

	ε rate (/s)	σ_y (MPa)	σ_{ult} (MPa)	ε fail
As received	0.001	283.54	416.00	0.2195
Sensitized 28 days	0.001	214.78	404.7	0.2523
As received	1.0	286.11	394.11	0.3133
Sensitized 28 days	1.0	210.18	386.16	0.3296

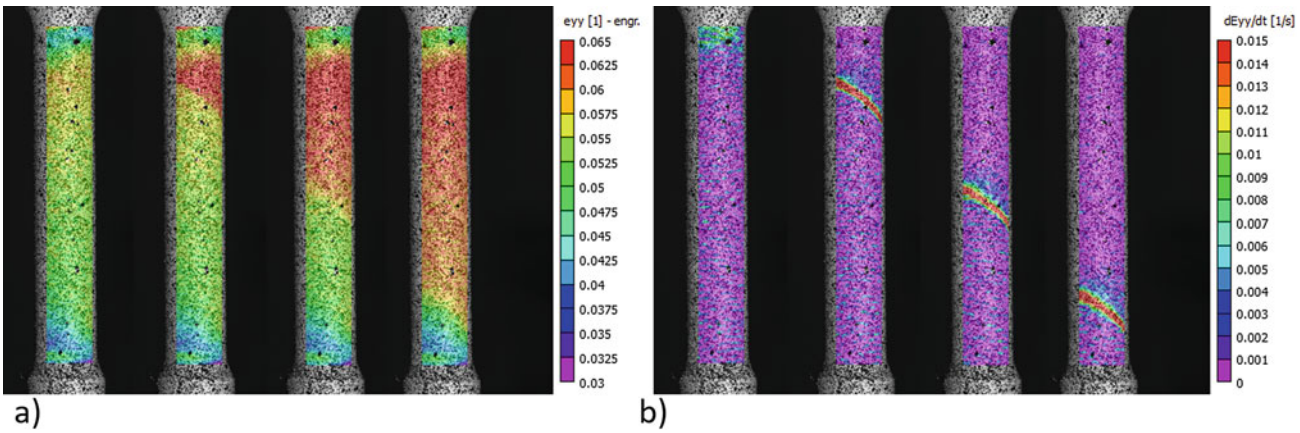

Fig. 32.2 Tensile deformation behavior observed using Digital Image Correlation (**a**) engineering strain (**b**) strain rate

with sensitization. Results from intermediate rate tests show little change in the yield stress and a small decrease in the ultimate stress relative to the quasi-static loading rate. This result is consistent with previously published results, showing little to no strain rate sensitivity [7]. However strain to failure appears to increase with loading rate. Table 32.1 summarizes the results from these tests.

Al-Mg alloys are known to show serrated flow during plastic deformation. This behavior is known as the Portevin–Le Chatelier effect and is associated with dynamic strain aging [8]. The serrated flow can be seen in the stress strain curves in Fig. 32.1a. By using DIC, full field strain measurements allow localized strains to be observed. Figure 32.2a shows a deformation band propagating down the specimen during tensile loading. Calculating the strain rate from DIC allows the deformation band to be clearly visualized in Fig. 32.2b. It should be noted that although the average strain rate is 0.001/s, the strain rate within the band is at least an order of magnitude higher. The serrated flow behavior was not observed during intermediate rate (1.0/s) tests.

Conclusion

From preliminary testing it is clear that sensitization of 5000 series aluminum alloys can have a large effect on the mechanical response. A significant decrease in yield stress was observed in AA5083-H131 after 28 days of conditioning at 100 °C. The use of digital image correlation allows the visualization of deformation band formation and propagation during plastic flow. This data may be useful in understanding the change in performance of sensitized aluminum. Additional tests will be performed at higher loading rate using a split Hopkinson pressure bar. Compression tests will also be performed at quasi-static and dynamic rates of loading. Additional specimens will be sensitized for 7 days at 100 °C and tested to further determine the effect of sensitization on the evolution of mechanical behavior. Characterization tools such as SEM and TEM will be used to help determine the microstructural changes during sensitization and deformation while high speed-high resolution digital image correlation may provide more detail into the strain evolution during deformation.

Acknowledgement Jack Franklin from Constellium for providing the aluminum plate.

References

1. Lim, M.L.C., Kelly, R.G., Scully, J.R.: Overview of intergranular corrosion mechanisms, phenomenological observations, and modeling of AA5083. Corrosion. **72**(2), 198–220 (2015)
2. Zhang, R., et al.: Experiment-based modelling of grain boundary β-phase (Mg 2 Al 3) evolution during sensitisation of aluminium alloy AA5083. Sci. Rep. **7**(1), 2961 (2017)
3. Steiner, M., Agnew, S.: Predictive sensitization modeling for AA5XXX aluminum alloys including non-isothermal cases. Corrosion. **72**(2), 169–176 (2015)
4. ASTM B557-15: Standard Test Methods for Tension Testing Wrought and Cast Aluminum- and Magnesium-Alloy Products. ASTM International, West Conshohocken, PA (2015)
5. ASTM E8-16a: Standard Test Methods for Tension Testing of Metallic Materials. ASTM International, West Conshohocken, PA (2016)
6. Sutton, M.A., Orteu, J.J., Schreier, H.: Image correlation for shape, motion and deformation measurements: basic concepts, theory and applications. Springer, New York (2009)
7. Huskins, E.L., Cao, B., Ramesh, K.T.: Strengthening mechanisms in an Al-Mg alloy. Mater. Sci. Eng. A. **527**, 1292–1298 (2010)
8. Benallal, A., et al.: An experimental and numerical investigation of the behaviour of AA5083 aluminium alloy in presence of the Portevin–Le Chatelier effect. Int. J. Plast. **24**(10), 1916–1945 (2008)

Chapter 33
Application of High-Speed Digital Image Correlation to Taylor Impact Testing

Phillip Jannotti, Nicholas Lorenzo, and Chris Meredith

Abstract Taylor impact studies were conducted using high-speed 3D digital image correlation (DIC). Taylor impact experiments are a well-established means of assessing material behavior at high strains and strain rates. Classically, the dynamic strength was determined from the final deformed shape of the sample. However, digital image correlation has been identified as a promising technique to provide time-resolved, full-field characterization of the dynamic failure behavior. This enables a better understanding of the deformation history and can provide a more robust validation of computational models, especially for complex, anisotropic problems. DIC involves applying a speckle pattern to the sample surface and tracking the deformation using two synchronized cameras. This allows for the determination of displacement, velocity, and strain field histories. In instances where the deformation is multiaxial, especially for non-planar samples, stereo DIC provides one of the only practical means of collecting full-field 3D data.

Keywords Taylor impact · DIC · Digital image correlation · High-speed

Introduction

Taylor impact testing was developed in the 1930s by G.I Taylor et al. (although not published until the 1940s) to evaluate dynamic strength of ductile materials [1, 2]. It became an attractive test because it was simple and inexpensive. Classically, the methodology entailed firing a rod into a rigid anvil at normal obliquity and relating the deformed shape to the dynamic yield strength. Taylor tests gained additional attention because they subjected a single sample to a wide spatial range of strains and strain rates—shock loading and large strains near the impact face and quasi-static loading with limited deformation towards the rear of the sample—making them particularly well-suited for exercising constitutive models. Later modifications to the classical test include symmetrical impact, where instead of an anvil the target rod is impacted by another rod of identical material and geometry [3, 4]. This eliminates boundary condition uncertainties from friction conditions at the rod/anvil interface and deformation of anvil adjacent to the interface, but requires very precise rod alignment.

More recently, *in situ* diagnostics have been coupled with Taylor testing like high-speed cameras, velocimetry, and digital image correlation (DIC) to collect time-resolved data [5–9]. However, high-speed imaging and velocimetry offer limited ability to quantify and characterize the complex multi-axial failure behavior due innate difficulties in simplifying the analysis to suit the measurement tools. On the other hand, DIC offers the ability to make full-field measurements of high-rate deformation including displacement, velocity, strain, and strain rate [10]. The basic concept of stereo (3D) DIC is to apply a random speckle pattern to a test sample and precisely track pattern deformation with multiple cameras in order to reconstruct the full-field deformation history. Digital image correlation has been around for decades, tracing its origins back to the 1980s, and has seen widespread usage in a variety of quasi-static and dynamic studies. Although its use in dynamic applications has been more limited, 3D DIC has been applied to Koskly bar testing [11, 12], terminal ballistics [13–15], blast [16, 17], and even Taylor impact testing studies [9]. The only drawback of applying high-speed stereo DIC to high-rate phenomena (e.g., Taylor test) is the limited temporal and spatial resolution. A recent study by Bigger et al. [9] demonstrated the possibility of using high-speed cameras (less than 1 MHz frame rate, e.g., Phantom v711); however, the spatial resolution and sampling rate were not sufficient to provide high-fidelity data. Therefore, it was of interest to examine the feasibility of using ultra-high-speed cameras (greater than 1 MHz frame rate). Currently, the most popular options for ultra-high-speed cameras include the Shimadzu HPV-X2 (5 Mfps, 128 frames, 400 × 250 pixel resolution) and Specialized Imaging Kirana (5 Mfps, 180 frames, 924 × 768 pixel resolution).

P. Jannotti (✉) · N. Lorenzo · C. Meredith
U.S. Army Research Laboratory, Aberdeen Proving Ground, Aberdeen, MD, USA
e-mail: phillip.a.jannotti.civ@mail.mil

L. E. Lamberson (ed.), *Dynamic Behavior of Materials, Volume 1*, Conference Proceedings of the Society for Experimental Mechanics Series, https://doi.org/10.1007/978-3-030-30021-0_33

A methodology is presented for applying ultra-high-speed 3D DIC to symmetrical Taylor impacting testing. Considerations and practical limitations of the technique are discussed to provide insight into the utility of instrumented Taylor testing. This technique can improve the understanding of the dynamic behavior of materials at a wide-range of strains and strain rates, with added potential of aiding model development and validation as well as relating a deformation history to post-mortem microscopy and microstructural features.

Experimental

Symmetrical Taylor impact experiments were conducted using a light gas gun with a 6.35 mm diameter (D) and 244 cm long (L) smoothbore barrel, as seen in Fig. 33.1. The test specimens were 6.35 (D) × 32 mm (L) copper (Cu) rods in the fully annealed condition. Each test involved firing a projectile rod into a stationary target rod. The target rod was held in a modelling foam bushing near the exit of the barrel, approximately one rod length away. Because the sample of interest was stationary, complications associated with launching a patterned target down a barrel were eliminated. The foam bushing was backed by clay (ROMA Plastilina) with the intent of recovering the impactor and target rods. Projectile velocity was determined by using a 4.5 mW laser (Thorlabs CPS635, 635 nm) and Si avalanche photodetector (Thorlabs APD410A) connected to a high-speed digital oscilloscope (Tektronix DPO7000 series, 2 GHz). As the projectile passes by it blocks the laser and thereby provides a start-stop position in the signal collected with oscilloscope. Target deformation was characterized using stereo (3D) DIC. The camera system consisted of two ultra-high-speed cameras (Shimadzu HPV-X2) recording at 2 Mhz with 200 ns exposure. Illumination was provided by two light strobes (Photogenic PL2500DRC, 1000 W/s) coupled to liquid light guides through a custom-made adapter (Hadland Imaging). A common trigger pulse was provided to the cameras and light strobes by the oscilloscope when the laser beam was crossed by the projectile.

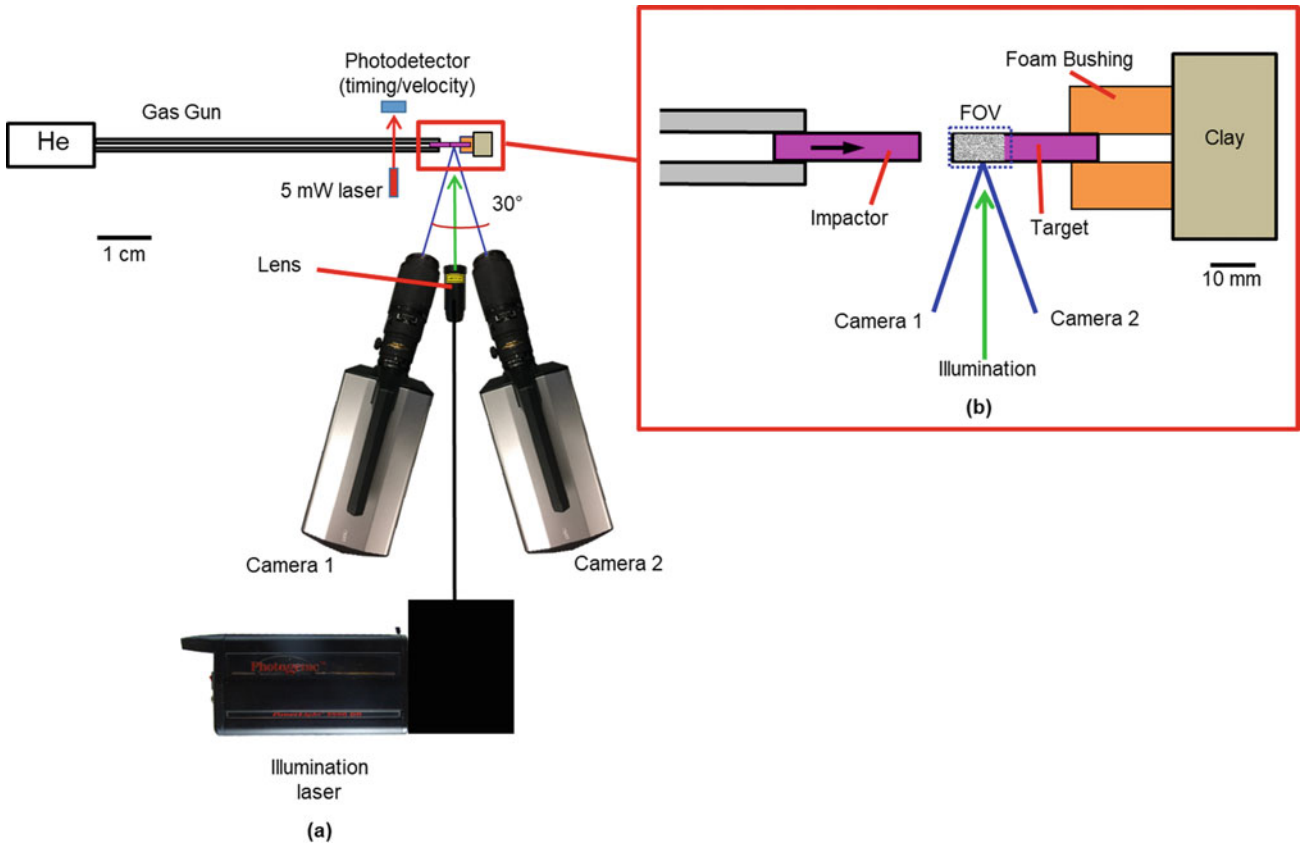

Fig. 33.1 (**a**) Schematic of the symmetrical Taylor impact test and (**b**) magnified view of the setup

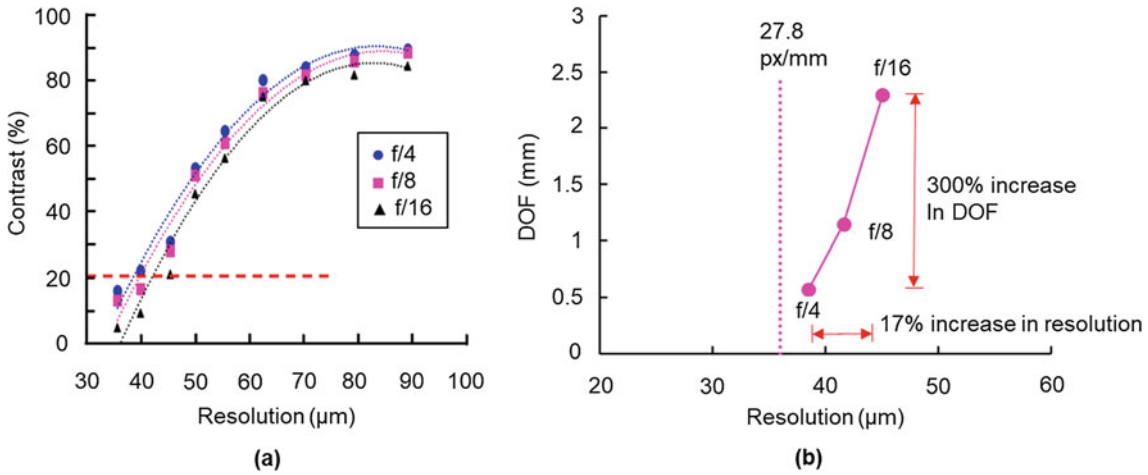

Fig. 33.2 (**a**) MTF curves for various lens aperture settings: f/4, f/8, and f/16. (**b**) DOF as a function of spatial resolution demonstrating the effect of different size apertures

Prior to patterning the target, the resolution of the camera system (camera + lens) was examined. The sensor resolution (pixel size in object space) was found to be 36 μm (28 pixels/mm) for a field-of-view (FOV) of 14.4 × 9 mm. This represented nearly 1:1 magnification (32 μm pixel, 12.8 × 8 mm sensor). The lens resolution was found using a standard resolution test chart (1951 USAF) to examine the effect of lens distortion and aperture selection. The resolution chart was made up of multiple groups of lines of different widths and frequency (line pair per mm or lp/mm), each associated with a spatial resolution (μm). A modulus transfer function (MTF) curve, which relates contrast to spatial resolution, was generated for 3 aperture settings (f/4, f/8, and f/16) on a 200 mm macro lens (Nikon #1989), as shown in Fig. 33.2a. This was accomplished by measuring a line intensity profile across each line group on the resolution chart and computing the % contrast:

$$\%\, Contrast = (Imax - Imin) / (Imax + Imin) \times 100$$

The lens resolution at a given aperture size was defined by a limiting contrast level of 20%. The lens resolution at each aperture setting was compared with the camera sensor resolution (see Fig. 33.2b). The vertical dotted line represented the sensor resolution (36 μm, based on pixel/mm) and the data points represented lens-based resolution as a function of aperture (39–46 μm). Even at the largest aperture setting, the lens resolution is greater. Thus, the camera system is lens-limited for all apertures. Given the small depth-of-field (DOF) at high magnification, an aperture setting of f/16 was chosen over f/4 (largest aperture setting) to keep the sample in focus and ensure proper calibration (especially when rotating/moving the calibration grid out-of-plane). Compared to a maximum achievable resolution of 39 μm (0.5 mm DOF), this translated to minimal (less than 20%) difference in resolution (46 μm) compared a large (greater than 300%) gain in DOF (nearly 2.5 mm).

The target rod was patterned by first applying a thin base coat of matte white rubberized spray paint (Rust-oleum #318347) followed by a light dusting of flat black spray paint (Rust-oleum #7776830). Given the resolution of the camera system, the ideal speckle size was ~135–225 μm (3–5 pixels [18]). Given the small size scale of the experiments, multiple methods were attempted to obtain the best possible speckle pattern. Alternative methods of patterning attempted included using a permanent marker, temporary tattoos (using inkjet printer, dye-based pigment), and hydroprinting (printable PVA hydrographic film). However, permanent markers could not achieve small enough features, were time consuming, and not repeatable to use. Temporary tattoos did not permit the requisite deformation before peeling off or tearing and were difficult to apply. Hydroprinting caused too much pattern distortion during application and was not repeatable. Thus, spray painting was most effective (Fig. 33.3).

An example image of the calibration grid and a summary of the imaging system is given in Fig. 33.4, including the setup and post-processing parameters (as recommended [18]). The calibration grid was a 9 × 9 backlit glass grid with 0.4 mm dots and 0.9 mm spacing. At least 50 images were taken to calibrate the stereo system and compute intrinsic/extrinsic parameters needed for 3D reconstruction and triangulation. This includes sufficient out-of-plane translation and rotation to get a proper

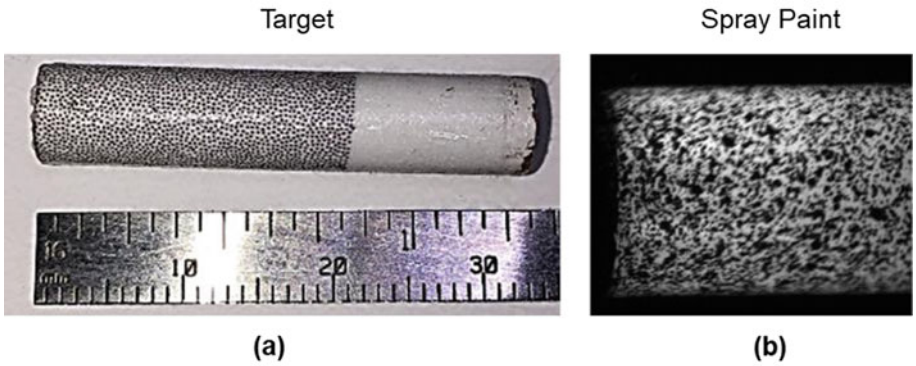

Fig. 33.3 (**a**) Target rod with speckle pattern and (**b**) representative FOV for the imaging setup

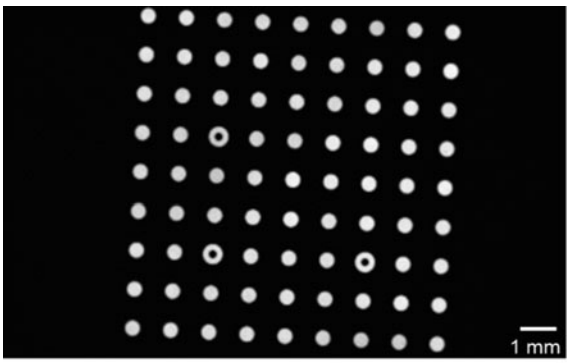

Parameter	Setting
Camera/Sensor/Digitization	Shimadzu HPV-X2 / 400 x 250 px / 10-bit
Lens/Imaging Distance	200mm macro, f/16 / 320 mm
Sampling Rate / Exposure	1 Mfps / 200 ns
Imaging Resolution / ROI	45 µm / 14.4 x 9 mm
Subset Size / Step Size	21 pixels / 7 pixels
Interpolation / Correlation	Optimized 8-tap / NSSD
Strain Filter	11
Calibration Panel	9 x 9 dots (0.89 mm spacing) – backlit glass
Noise (U / dU/dT / e / de/dt)	0.3 nm, 0.15 m/s, 0.07%, 0.25/s

(b)

Fig. 33.4 (**a**) Representative calibration image and (**b**) summary report of parameters of the physical system and data analysis process

calibration. The stereo angle was ~25 degrees based on physical limitations of the experimental setup (i.e., proximity of cameras and lenses relative to imaging distance). The validity of the camera calibration was verified by translating a flat, rigid sample in the FOV and evaluating the measurement error, projection error, and noise floor.

Results

Figure 33.5 shows symmetrical Taylor test at an impact velocity (V) of 92 m/s. Note that because of the symmetrical configuration this becomes equivalent to classical impact (rod into anvil) at a velocity, $V/2$, of 46 m/s. The displacement and strain reached only 0.3 mm and 9% after 20 µs, respectively. The velocity and strain rate experienced a maximum of ~20 m/s and 800/s within the first 5 µs. This data is useful for model validation or to correlate with post-mortem microscopy to the deformation history. Note that the rigid body motion has been removed from the analysis. For comparison, the data from the current study was compared to a recent study examining aluminum-alloys with the classical Taylor impact configuration [7]. Despite the low-resolution used in that study of 128 × 80 pixels and lower sampling rate of 320 kHz, you can see similar deformation features. However, it is necessary to sample at sub-microsecond intervals to properly characterize these dynamic events without adding errors associated with temporal interpolation schemes. Therefore, the need for ultra-high-speed cameras (greater than 1 MHz frame rate) was further emphasized.

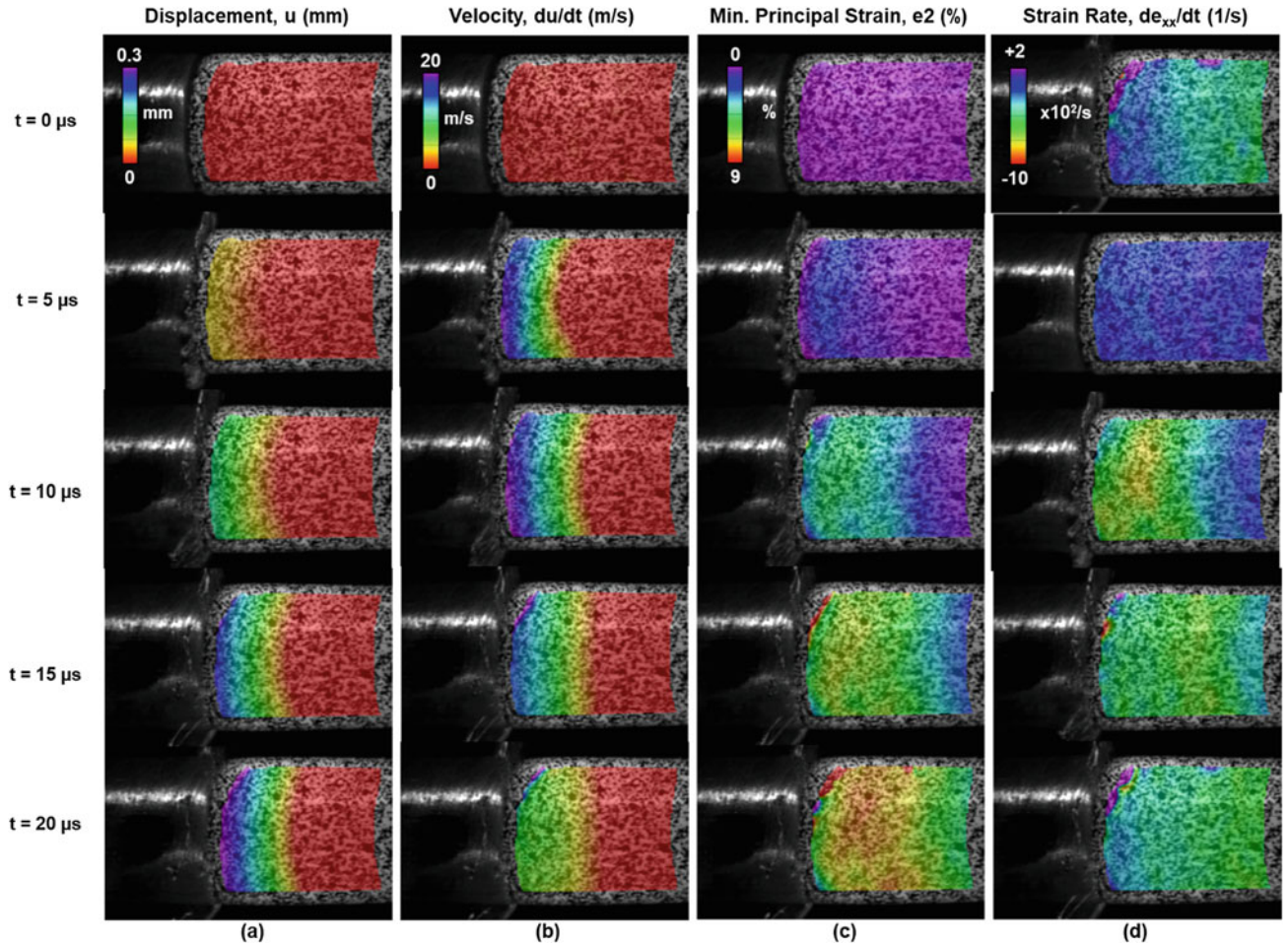

Fig. 33.5 Selected data from symmetrical Taylor impact at V/2 = 46 m/s: (**a**) displacement, (**b**) velocity, (**c**) minimum principal strain, and (**d**) axial strain rate

For reference, the relative FOV of the DIC study is shown in Fig. 33.6a. The DIC analysis is focused on the region near impact face where the deformation is greatest. Figures 33.6b, c show the maximum compressive strain and peak strain rate observed, respectively. Line plots were extracted from the field data demonstrating the time evolution of strain and strain rate at several points along the length of the rod, as seen in Fig. 33.6d, e. Note that strain and strain rate evolution are maximum just below the impact face. The strain peaks at 9% at approximately 22 µs before the rods move as a rigid body. The strain rate peaks at 800/s within 5 us before falling to 0 by around 20 us after impact.

Note that the FOV examined in this study represents the greatest feasible spatial resolution that could be achieved with this ultra-high-speed stereo camera system and standard camera optics (exempting microscope objectives). The primary limiting factor was the DOF, as greater magnification tends to reduce the DOF making stereo calibration untenable and keeping the whole (round) sample in focus impossible.

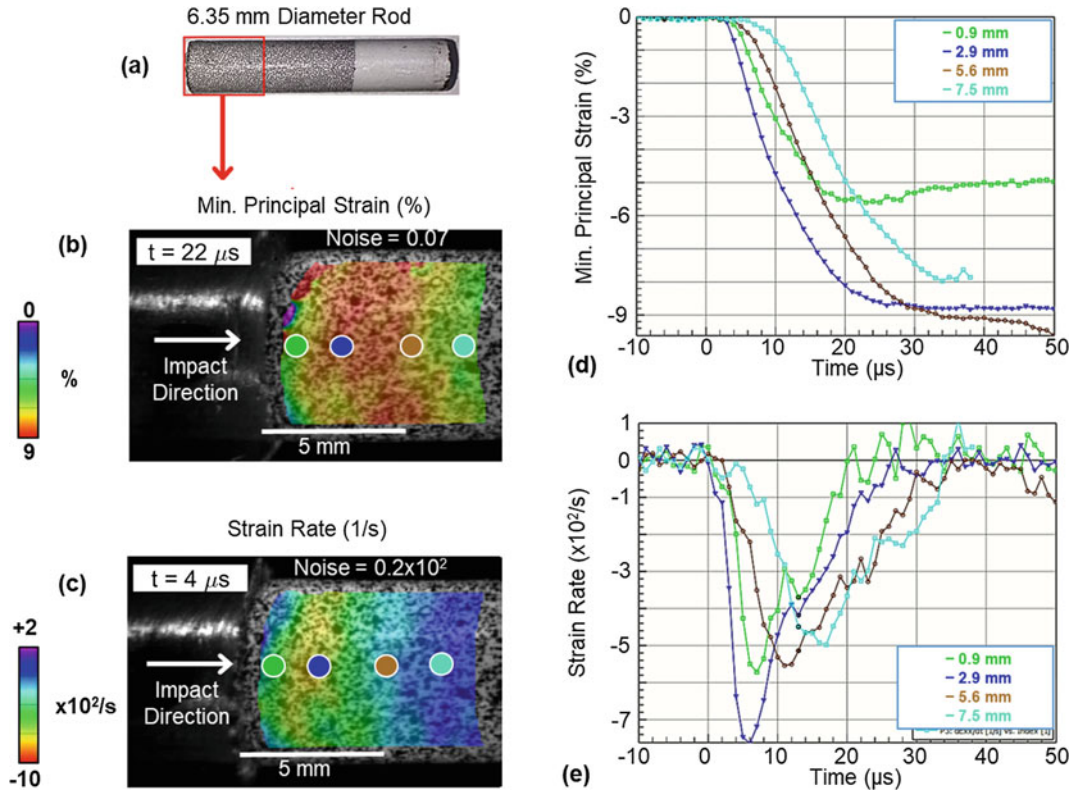

Fig. 33.6 (**a**) Relative FOV for 3D DIC, DIC field data showing (**b**) maximum compressive strain and (**c**) peak axial strain rate, and extracted time-resolved (**d**) strain and (**e**) strain rate data from selected points along the rod length

Conclusion

A methodology was presented for applying ultra-high-speed DIC to symmetrical Taylor impact. It was demonstrated that despite the impact velocity being on the order of 10s–100s of m/s, ultra-high-speed imaging (greater than 1 Mhz) was required to properly sample the high-rate deformation history occurring over several to 10s of microseconds. For these types of small-scale experiments requiring high-magnification, the narrow DOF (1–2 mm) provided a practical limit on the ability to properly calibrate the stereo DIC system. Additionally, is was found that this type of instrumented high-rate testing provides promise for characterizing a wide range of engineering material (low- to high-strength) as long as you have a means of launching the rods at sufficient velocity.

References

1. Taylor, G.I.: The testing of materials at high rates of loading. J. Inst. Civil Eng. **26**(8), 487–501 (1946)
2. Taylor, G.I.: The use of flat-ended projectiles for determining dynamic yield stress I. Theoretical considerations. Proc. Royal Soc. Lond. **194**(1038), 289–299 (1948)
3. Erlich, D.C., Shockey, D.A., Seaman, L.: Symmetric rod impact technique for dynamic yield determination. In: Shock waves in condensed matter, pp. 402–406. American Institute of Physics, New York, NY (1982)
4. Erlich, D.C.: Rod impact (Taylor) test. In: Metals Handbook, vol. 8, 9th edn, pp. 203–207. American Society of Metals, Metals Park, OH (1985)
5. Forde, L.C., Proud, W.G., Walley, S.M.: Symmetrical Taylor impact studies of copper. Proc. Royal Soc. A. **46**, 769–790 (2008)
6. Liu, J., Huang, F., Xu, K., Liu, L., Zuo, T., Pi, A.: Influence of mass ratio on forward and reverse ballistic impact equivalence: experiments, simulations, and mechanism analysis. Exp. Mech. **57**(3), 387–404 (2017)
7. Liu, J., Pi, A., Wu, H., Huang, F.: Dynamic response of reverse Taylor impact based on DIC technology. EPJ Web of Conf. **94**, 01074 (2015)
8. Ferranti Jr., L., Gagliardi, F.J., Cunningham, B.J., Vandersall, K.S.: Dynamic Characterization of Mock Explosive Material Using Reverse Taylor Impact Experiments. In: Proceedings of the 2010 Annual Conference on Experimental and Applied Mechanic, vol. 6, pp. 337–346. Springer Science & Business Media, New York, NY (2011)

9. Bigger, R.P., Carpenter, A., Scott, N., Dannemann, K., Chocron, S., Williams, C.: Dynamic response of aluminum 5083 during Taylor impact using digital image correlation. Exp. Mech. **58**(6), 951–961 (2018)
10. Sutton, M.A., Orteu, J.J., Schreier, H.: Image correlation for shape, motion and deformation measurements: Basic concepts, theory and applications. Springer Science, New York, NY (2009)
11. Foster, M., Love, B., Kaste, R., Moy, P.: The rate dependent tensile response of polycarbonate and poly-methylmethacrylate. J. Dyn.Behav. Mater. **1**(2), 162–175 (2015)
12. Moy, P., Walter, T.: Ultra-High Speed Imaging for DIC Measurements in Kolsky Bar Experiments. In: Lamberti, L., Lin, M.-T., Furlong, C., Sciammarella, C., Reu, P.L., Sutton, M.A. (eds.) Advancement of Optical Methods & Digital Image Correlation in Experimental Mechanics 3*:* Conference Proceedings of the Society for Experimental Mechanics, pp. 127–128. Springer, Cham (2019)
13. Jannotti, P., Schuster, B.E., Doney, R., Walter, T., Andrews, D.: Instrumented penetration of metal alloys during high-velocity impacts. In: Dynamic Behavior of Materials 1: Conference Proceedings of the Society for Experimental Mechanics, pp. 139–145. Springer, New York (2017)
14. Jannotti, P., Schuster, B.E.: Application of 3D digital image correlation in ballistic testing. In: Dynamic Behavior of Materials 1: Conference Proceedings of the Society for Experimental Mechanics, pp. 155–161. Springer, New York (2018)
15. Jannotti, P.: The Utility of 3D Digital Image Correlation for Characterizing High-Rate Deformation. In: Dynamic Behavior of Materials 1: Conference Proceedings of the Society for Experimental Mechanics, pp. 345–350. Springer, New York (2019)
16. Reu, P.L., Miller, T.J.: The application of high-speed digital image correlation. J Strain Anal. Eng. Design. **43**(8), 673–688 (2008)
17. Cooper, M.A., Reu, P.L., Miller, T.J.: Observations in Explosive Systems with High-Speed Digital Image Correlation. SAND2010-1099C, Sandia National Laboratories, Albuquerque, NM (2010)
18. International Digital Image Correlation Society, Jones, E.M., Iadicola, M.A.: A Good Practices Guide for Digital Image Correlation (2018)

Chapter 34
Observation of Dynamic Adhesive Behavior Using High-Speed Phase Contrast Imaging

Shane Paulson, Nesredin Kedir, Tao Sun, Kamel Fezzaa, and Wayne Chen

Abstract Composite sandwich panels provide an increase in buckling resistance to thin composite plates and shells, leading to widespread use in a variety of applications such as boat hulls, rotor blades, and rocket casings. Past research has shown that delamination between the face sheets and core of composite sandwich panels occurs under a variety of both dynamic and quasi-static load conditions. While this failure mechanism has been identified and observed, existing research has not fully investigated the mechanisms behind this adhesive failure. In this study, a carbon fiber bar was adhered using JB Weld epoxy to a variety of substrates. Bulk polymer substrates included polycarbonate, ultra-high molecular weight polyethylene, and Delrin®, while two PMI foam substrates were used: Rohacell® WF200 and Rohacell® HERO200-HT. Experiment samples were impacted using a Kolsky bar apparatus to impart simple shear on the adhesive joint. The adhesive joint was observed *in-situ* using a synchrotron X-ray source in phase contrast imaging mode. The X-ray source was used in tandem with the Kolsky bar and high-speed camera. In order to introduce simple shear in the adhesive joint, the Kolsky bar was used to impact the carbon fiber bar with an impact velocity of ~7 m/s. Adhesive failure was observed in each of the bulk polymer samples, but no failure was seen in the PMI foam samples.

Keywords Composite Sandwich · Adhesive · Dynamic behavior · Phase contrast imaging

Introduction

Fiber-reinforced composite materials have been seeing increased use over the past several years in a wide variety of applications including boat hulls, rotor blades, rocket casings, and aircraft wings. Due to the high strength-to-weight ratio of composite materials, these parts are often crafted as thin plates and shells. In order to increase the buckling resistance of these thin structures, composite sandwich materials were introduced to provide increased rigidity. The core material of these composite sandwich materials was initially composed of a honeycomb structure, often made of aluminum. Previous research has led to the use of polymer foams as a replacement for honeycomb cores as a cheaper and more effective core material.

All sandwich panels are composed of polymeric constituents, which can include the adhesive layer, the composite matrix and fibers, and the core layer of a panel. Due to the viscoelastic nature of polymeric materials, it follows that sandwich panels will display some inherent rate effects in their mechanical behavior. As a result, several studies have been done to examine the effects of impact and blast loads on composite sandwich panels. Experiments conducted by Rolfe et al. [1] and Dear et al. [2] showed that when subjected to blast loads, sandwich panels suffer failure both by core crushing and layer delamination. Another study examined the behavior of sandwich beams and panels under impact loading and found that delamination occurred between panel layers. These panels and beams were also tested after impact and showed reduced strength when

S. Paulson (✉)
School of Aeronautics and Astronautics Engineering, Purdue University, West Lafayette, IN, USA
e-mail: paulsons@purdue.edu

N. Kedir
School of Materials Engineering, Purdue University, West Lafayette, IN, USA

T. Sun · K. Fezzaa
Advanced Photon Source (Sector 32), Argonne National Laboratory, Lemont, IL, USA

W. Chen
School of Aeronautics and Astronautics Engineering & School of Materials Engineering, Purdue University, West Lafayette, IN, USA

L. E. Lamberson (ed.), *Dynamic Behavior of Materials, Volume 1*, Conference Proceedings of the Society for Experimental Mechanics Series, https://doi.org/10.1007/978-3-030-30021-0_34

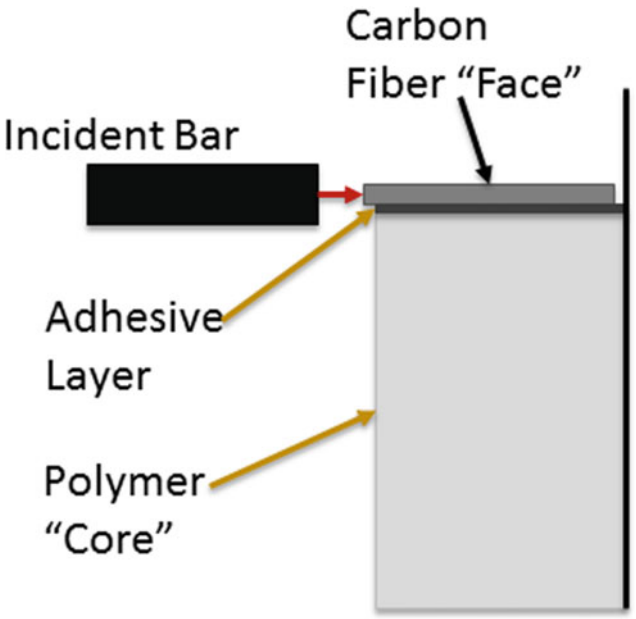

Fig. 34.1 Sample and loading configuration

compared to un-damage samples [3]. Other authors have expanded on this research and have stated that the adhesive layer between the face sheet and core layers is critical to the behavior of sandwich panels under dynamic load conditions [4].

Experiments

In order to examine the behavior of an adhesive joint between a composite layer and core layer, samples were subjected to simple shear by a modified Kolsky bar. Five different core materials were selected; monolithic Delrin®, monolithic polycarbonate, monolithic ultra-high molecular weight polyethylene, Rohacell® 200WF, and Rohacell® 200HERO-HT. In order to reduce the number of varied parameters, the face-sheet layer and adhesive remained constant. Samples were constructed using 0.25″ thick sections of core material with a 0.19″ thick layer of carbon fiber adhered with JB Weld steel-reinforced epoxy. The layer of carbon fiber was shifted slightly to overhang from the core layer. This geometry was chosen in order to isolate the impact load to the face sheet layer. Each sample was loaded by the incident bar at approximately 7 m/s and restrained with a rigid backstop. A schematic of the sample and its load configuration is show in in Fig. 34.1.

In order to visualize the behavior of the adhesive layer, the experiments were conducted at beam line 32-ID at the Advanced Photon Source, Argonne National Laboratory. Using a remote control and triggering system, X-rays were transmitted through the sample at an energy of 25.0 keV during the event. After passing through the sample, the X-rays were transmitted through a single crystal $Lu_3Al_5O_{12}$:Ce scintillator, which converted the X-rays into visible light. Images were then recorded at a frame rate of 2,000,000 frames/second using a Shimadzu Hyper Vision HPV-X2 high-speed camera.

Results

The use of high-speed phase contrast imaging allowed for good observation of an adhesive joint between two dissimilar substrates. Of the configurations examined, apparent failure of adhesion was observed in each of the samples constructed with a monolithic polymer core material. In contrast, the samples composed of rigid foam cores showed no apparent failure. The damage seen in a Delrin® core sample is shown in Fig. 34.2. While the polymer of the two foam core materials is different from those in the monolithic cores, the results suggest a relation between surface porosity of the core material and adhesive strength of the adhesive layer in a sandwich panel.

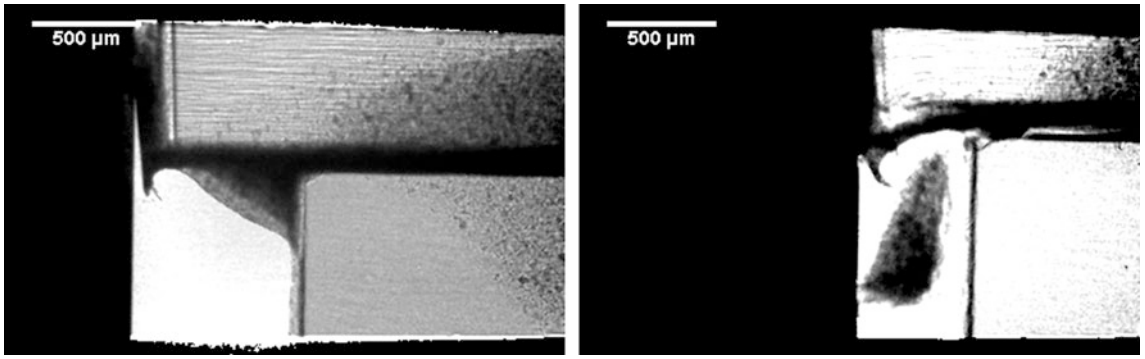

Fig. 34.2 Delrin® core sample prior to loading (left) and 110 µs into the load event (right). Apparent failure of adhesion can be seen in the image on the right at the core-side of the adhesive layer

References

1. Rolfe, E., Kelly, M., Arora, H., Hooper, P.A., Dear, J.P.: Procedia Eng. **167**, 176–181 (2016)
2. Dear, J.P., Rolfe, E., Kelly, M., Arora, H., Hooper, P.A.: Procedia Eng. **173**, 471–478 (2017)
3. Daniel, I.M., Abot, J.L., Schubel, P.M., Luo, J.J.: Exp. Mech. **52**, 37–47 (2012)
4. Mostafa, A., Shankar, K., Morozov, E.V.: Mater. Des. **50**, 92–101 (2013)

Chapter 35
Strain-Rate Effect on the Deformation Mechanisms of Agglomerated Cork

Louise Le Barbenchon, Jean-Benoît Kopp, Jérémie Girardot, and Philippe Viot

Abstract Cork is a multi-phased biosourced polymeric material. In this case study, it was agglomerated with a thermosetting resin by an uni-axial compression process. Agglomerated cork is nowadays considered for shock absorption applications. Therefore its behavior at high strain rates is of interest. The influence of the mean strain rate on the mechanical behavior of agglomerated cork and the associated strain mechanisms is studied here. Compression tests were performed in quasi-static (~4.2×10^{-3} s^{-1}) and dynamic (~70 s^{-1}) regimes. A specific assembly, the fly wheel, made it possible to obtain an almost constant loading rate during the test under dynamic conditions. As expected for a polymeric material, the Young's modulus of the material and the energy absorbed at densification (elastic and dissipated) during compression strongly depend on the average deformation rate. Using the correlation of digital images (DIC), the deformation mechanisms involved during the different stress regimes could be observed. Deformations which are highly heterogeneous take the form of localization bands. In quasi-static conditions, these localization bands are observed near interfaces between grains. At a dynamic regime, however, deformations seem more diffuse.

Keywords Dynamic loadings · Compression · Cellular materials · Cork agglomerates · DIC

Introduction

Cork is a bio-sourced material coming from the bark of the oak tree Quercus Suberus L. Most of it comes from Portugal [1]. Cork is a cellular material, meaning it is formed by a three-dimensional network called cell walls (Fig. 35.1). Suberin, a polymeric substance, is the major component of cork cell wall. The others are lignin, cellulose and hemi-celluloses [2]. Because of its cellular structure, foams like cork have unusual mechanical properties: they can be stiff, yet light, and they are capable of absorbing large deflections and thus large amounts of energy [3]. Because of it, cork by-products like agglomerated cork are now being considered for impact-absorbing applications. Ranging from the container for the transport of sensible pieces to sports items and including lightweight aeronautic components, a wide range of applications is foreseen [1]. Previous works studied the fundamental aspects of the static and dynamic mechanical behavior of agglomerated cork under simple loadings [4]. For example, the strain-rate dependency of cork products was highlighted with dynamic loadings in compression [5]. Yet strain mechanisms in compression are still unclear for this multi-scales cellular material [6, 7].

Background

Material

To obtain agglomerated cork, small beads (Ø = 0.5/1 mm) were mixed together with a bio-sourced thermoset resin reinforced with rigid short fibres (Ø = 7 ± 2 μm and l = 300 μm). It was then uniaxially compressed into a 1000 × 500 × 50 mm^3 block at a 0.42 density. Resin crossing was finally made in an autoclave at 130 °C during 12 hours. The resulting material can then be considered at several scales as shown in Fig. 35.2. This compression causes geometric and mechanical anisotropy at the grain scale [7]. Figure 35.3 shows the two induced directions. Directions in the plane (Oxy) will be called in-plane

L. Le Barbenchon (✉) · J.-B. Kopp · J. Girardot · P. Viot
Arts et Métiers ParisTech, CNRS, I2M Bordeaux, Esplanade des Arts et Métiers, Talence Cedex, France
e-mail: louise.le_barbenchon@ensam.eu

L. E. Lamberson (ed.), *Dynamic Behavior of Materials, Volume 1*, Conference Proceedings of the Society for Experimental Mechanics Series, https://doi.org/10.1007/978-3-030-30021-0_35

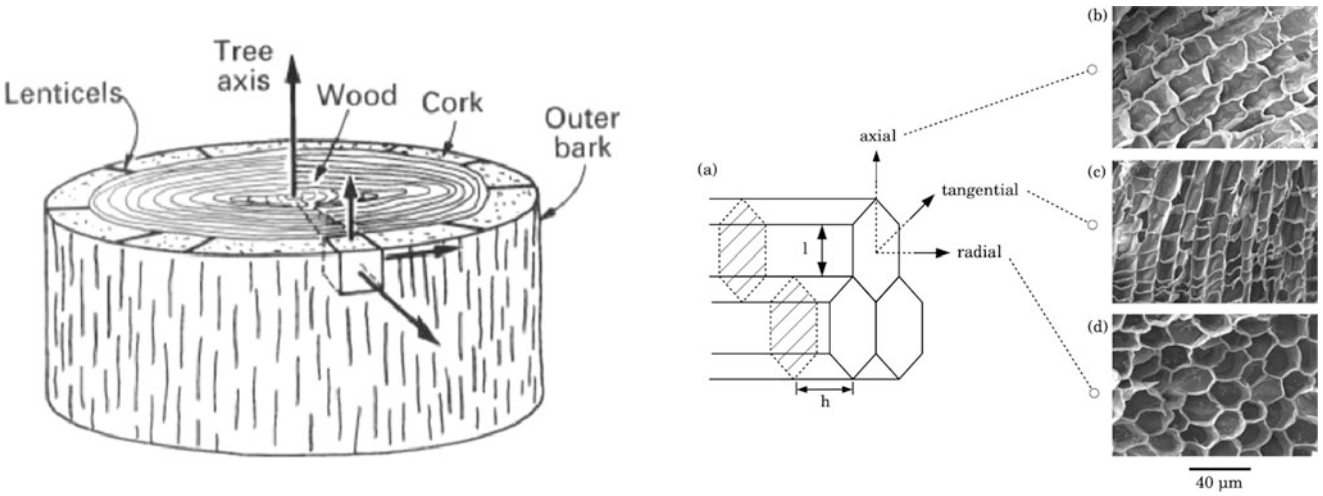

Fig. 35.1 Structure of cork in the bark of a oak tree

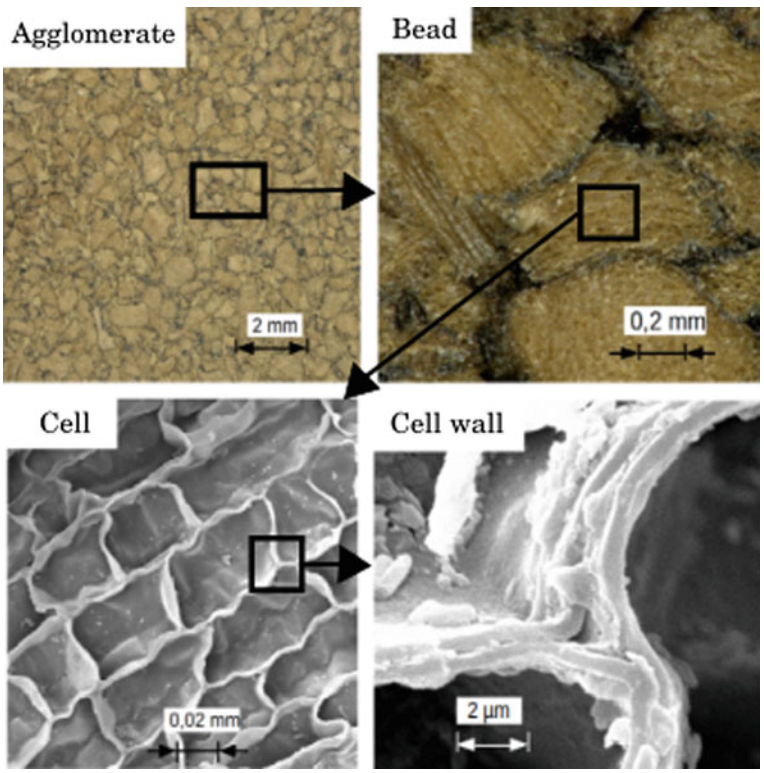

Fig. 35.2 Different observation scales for cork agglomerates. An optical microscope was used for particle and grain scale observations. A scanning electron microscope (SEM) was used for cell-scale observations

directions and the direction (Oz) will be called off-plane direction. This article focuses on the mechanical behavior in the out-of-plane direction.

Microstructure Characterization

In order to know the organization of the grains on the surface, the specimens were observed using a microscope optics before mechanical characterization. A Keyence microscope was used. The surface was observed and the picture resolution

was around 9000x9000 pixels. The microstructure of the specimens was also observed with the EVO scanning electron microscope (SEM) Zeiss after compression. The specimens were cut with new razor blades to minimize the damage done to the cells during cutting [3]. Gold was then sputtered at the samples surface to allow their observation.

Compressive Loadings at Several Strain-Rate Regimes

The specimens, previously observed under the optical microscope, were then compressed. The behavior for compression in the out-of-plane direction is presented here. In quasi-static mode, this compression was performed at 4.2×10^{-3} s^{-1} using a Zwick Roell 250kN compression machine. The tests were tracked with a Canon EOS 50D camera at a frequency of 1 Hz. The definition of the pictures was 3168x4752 pixels. Local correlation of the images was then operated in order to study the strain mechanisms.

In order to achieve the dynamic compression speed (around 70 s^{-1}), an original set-up was used. The fly wheel, visible in Fig. 35.4, consists in a steel wheel with a large moment of inertia (77 kg m^{-2}). This ensures that during loading, the strain rate is almost constant. However, the speed of unloading is not controlled. The force/displacement signals during the unloading

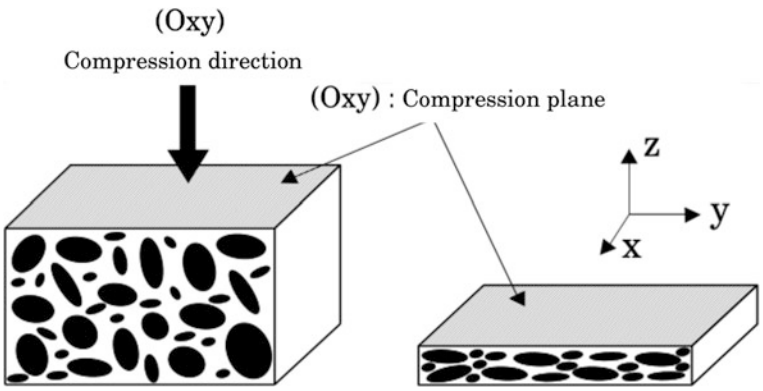

Fig. 35.3 Scheme of the fabrication process done by uniaxial compression

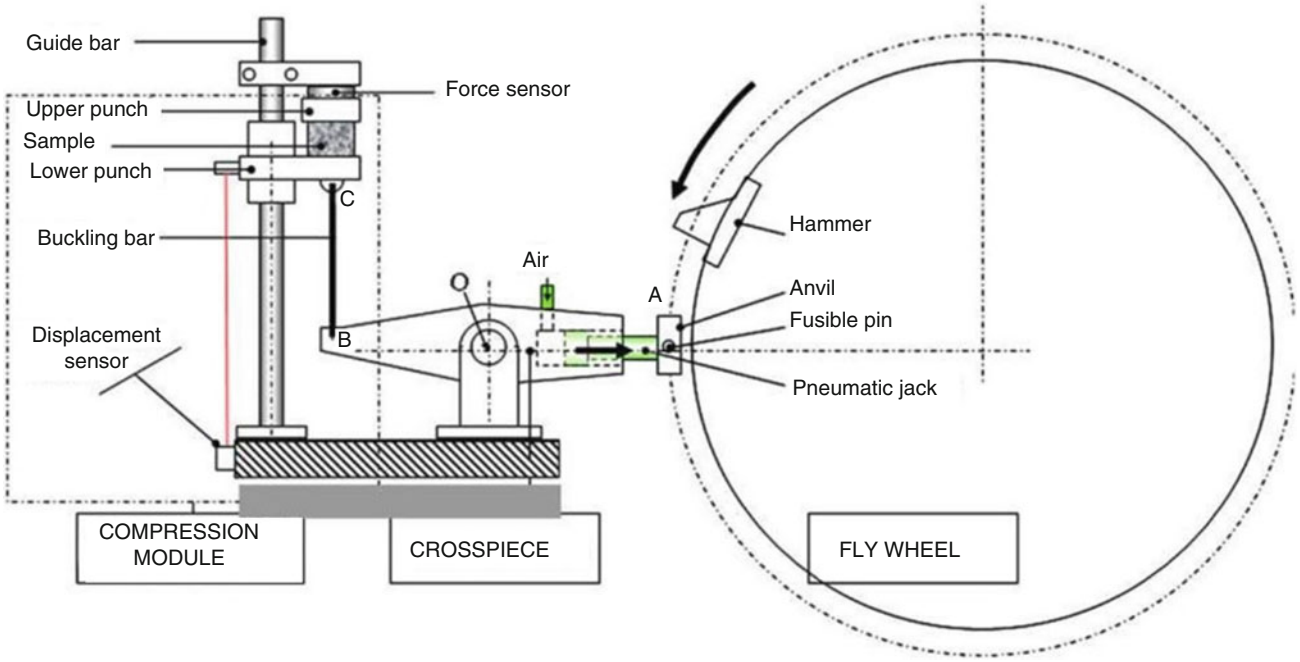

Fig. 35.4 Fly-wheel: a set-up for compressive dynamic loading at constant strain-rates

will therefore not be studied. The tests were filmed using a fast Photron SA5 camera at a frequency of 12.5 kHz. The image resolution was 640x848 pixels. For both types of tests, the stress calculation is facilitated by the Poisson coefficient close to 0 for agglomerated cork. So we have $\sigma = F/S_0$, the nominal stress and $\varepsilon = \ln(1-L/L_0)$, the nominal deformation.

Analysis

Mechanical Behavior

The compression tests provided the stress / nominal strain curves. Figure 35.5a shows that agglomerated cork behaves like a foam in compression [3]. We can therefore distinguish three main stages during deformation. First, the specimen deforms in a linear manner, which mainly corresponds to the bending of the walls. Then stress increases slowly for a wide range of deformation. This area is called the plateau. It corresponds to the progressive buckling of the cells. Finally, when all the cells have collapsed, the behavior of the material approaches that of a dense material. The stress therefore increases much more significantly. For compressions in quasi-static mode, the discharge was also recorded. There is a significant hysteresis. Immediately after the test, the deformation of the specimens was 0.20 ± 0.03 on average. Long after the test, this residual deformation was close to 0.05. The deformation mechanisms likely the buckling of the cell walls therefore seem to be mainly elastic, even at high deformation rates.

From these curves, the Young's modulus (slope of the linear part, for low deformations) as well as the energy absorbed before the densification stage (dissipated and elastic) could be determined. For low speeds, the Young's modulus in Fig. 35.5b seems to increase slightly, linearly as a function of the decimal logarithm of the solicitation speed. However, for the dynamic solicitation speed, a high increase in this module is noted. On the contrary, the absorbed energy in Fig. 35.5c seems to increase linearly according to $\log(d\varepsilon/dt)$.

The correlation of digital images shows results for the two solicitation regimes that appear similar at the agglomerate scale (Fig. 35.6). For small deformations, the deformation field seems almost homogeneous. When the plateau is reached, heterogeneities in deformations begin to appear. They then develop in the form of localization strips, perpendicular to the compression direction of the test. Some discrepancies can however be noticed. For the same mean strain, localization bands seem more intense in the dynamic regime. In order to better study it, one need to look closer, at the bead scale.

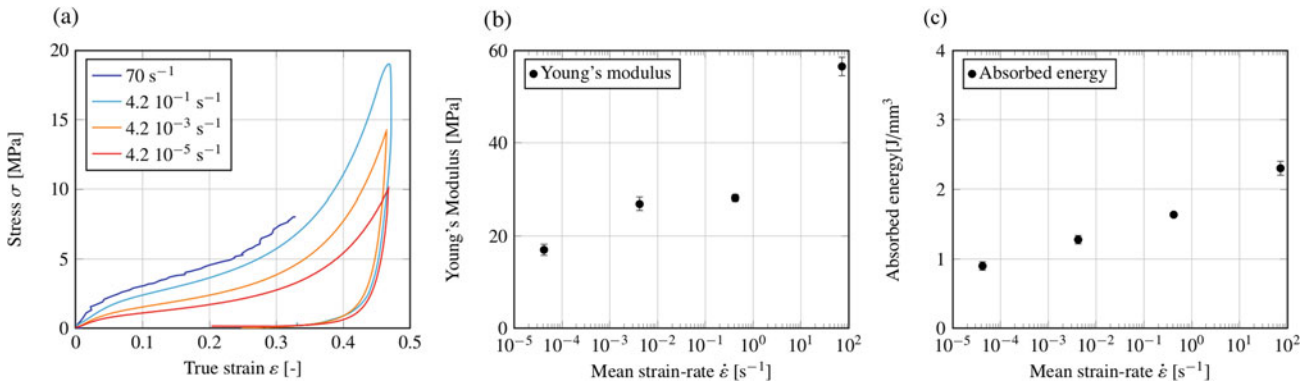

Fig. 35.5 Experimental results of the compression tests in the out-of-plane direction at several mean strain-rates. (**a**) Strain/stress experimental curves at several mean strain-rates; (**b**) Young's modulus (log scale ($\dot{\varepsilon}$)); (**c**) absorbed energy at densification (log scale ($\dot{\varepsilon}$))

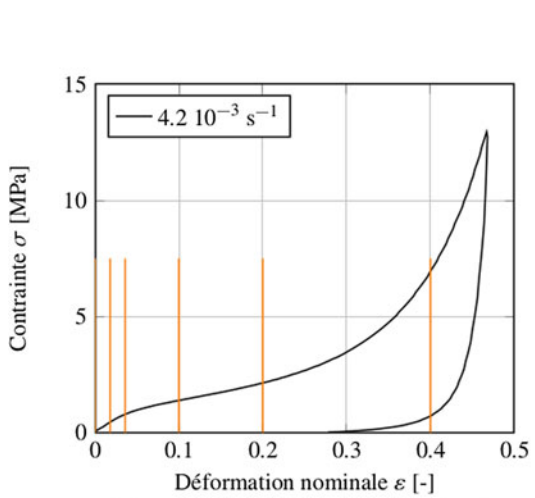

(a) Stress/strain curve at 4.2 10^{-3} s^{-1}.

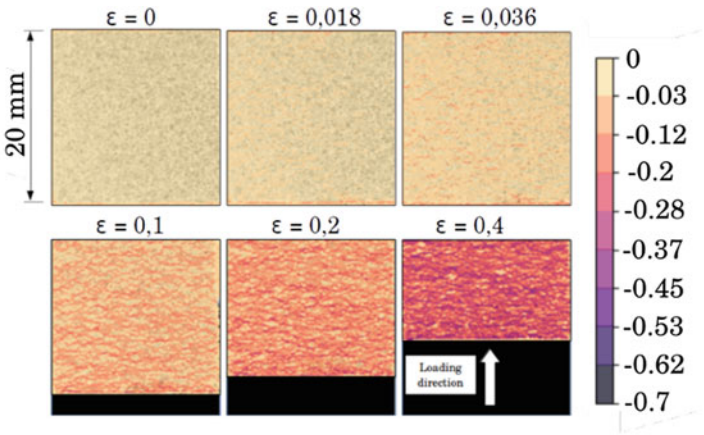

(b) Strain YY evolution in quasi-static regime

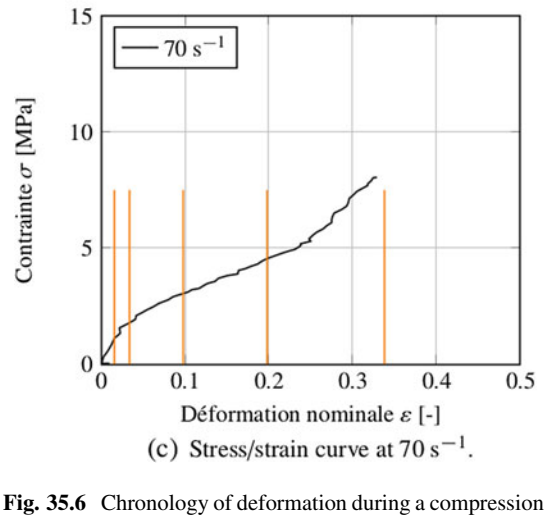

(c) Stress/strain curve at 70 s^{-1}.

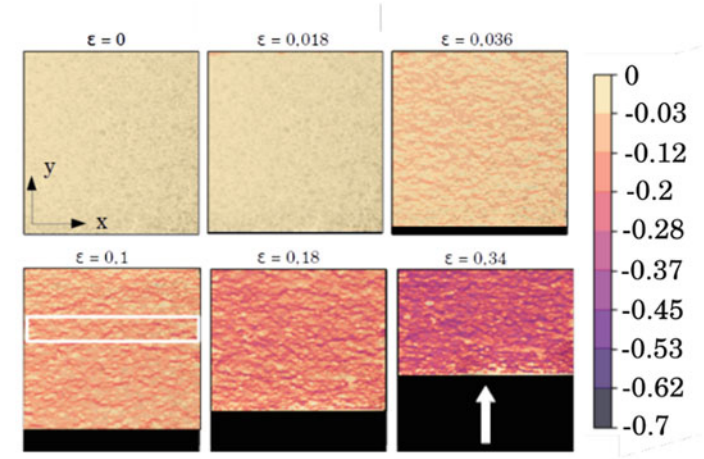

(d) Strain YY evolution in quasi-static regime. Localisation bands highlighted by the white rectangle.

Fig. 35.6 Chronology of deformation during a compression test at the two different stress regimes and the corresponding experimental stress/strain curves

Microstructure Influence

The superposition of the deformation maps and interfaces for quasi-static loadings is illustrated in Fig. 35.7. A significant localization of deformations near the interfaces can be observed. Thus, during a compression test, the localization of strains seems to begin with the stochastic buckling of cells present near the beads interfaces. This has been noticed on observations made at the SEM as shown in Fig. 35.8. This deformation then propagates to neighboring cells also close to the interfaces. Finally, according to several criteria of shape or multi-scale structure [8], this deformation propagates to neighboring beads (in the compression plane), thus taking the form of localization bands. These bands then grow on the entire sample. For dynamic loadings, the strain appeared more homogeneous inside one bead. The result is though very dependent on the picture resolution.

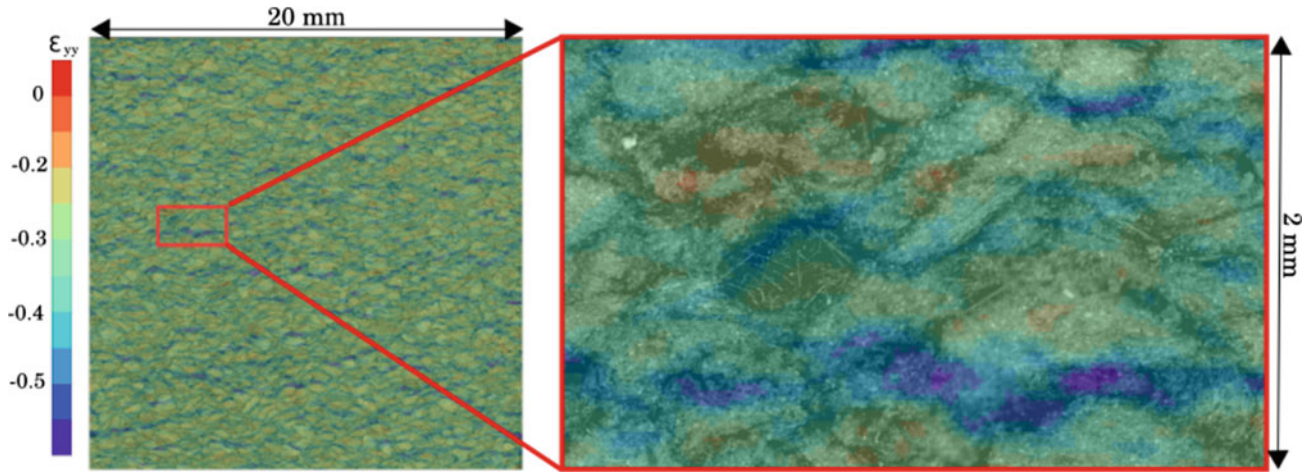

Fig. 35.7 Superposition of the YY strain map obtained by DIC and the surface taken under an optical microscope

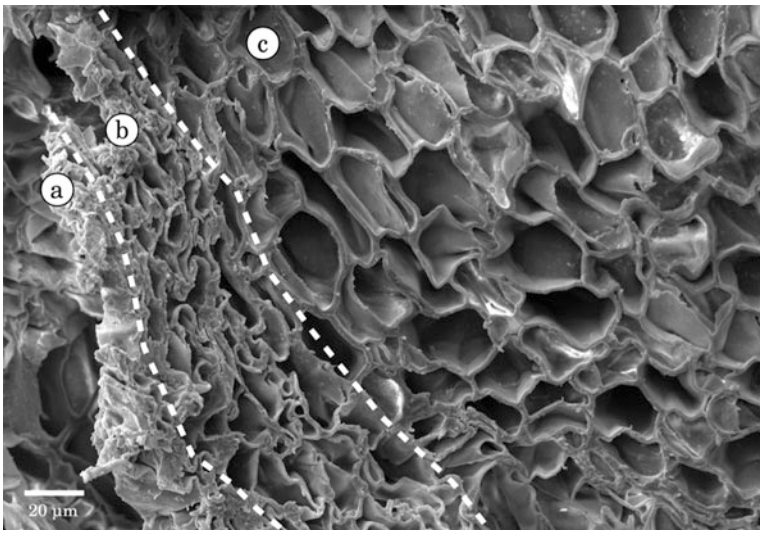

Fig. 35.8 State of the cells at the interface between beads. Photo taken at the SEM. (**a**) Interface. (**b**) Collapsed cells at the interface. (**c**) Interior of the bead

Conclusion

The effect of strain-rate on the behavior and deformation mechanisms of agglomerated cork has been studied here. Intragranular observations were therefore necessary. The deformations were studied on the surface of the specimens by DIC. The specimens were compressed either in quasi-static mode (at several speeds) or in dynamic mode using the original inertial wheel assembly (around 70 s^{-1}) allowing a quasi-constant loading speed during loading. The stress/strain curves show a dependence on the strain-rate of the material. Young's modulus increases slightly with it in quasi-static mode. It then increases more abruptly under a dynamic strain-rate. The absorbed energy seems to increase linearly over the entire range of strain-rates of this study. The strain fields obtained by DIC are very heterogeneous from the plateau phase. These heterogeneities take the form of location bands perpendicular to the direction of solicitation. In quasi-static mode, these deformations are located near the interface between two grains. Thus the deformation of the cork grains is initiated on the cells at the interface and then propagates into the neighboring cells. In dynamic these localization bands seem more intense but the strain appears more homogeneous inside one bead.

Acknowledgement This work was performed in the frame-work of the LIAMA project (supported by Lieges HPK, Safran PowerUnit and Région Nouvelle Aquitaine).

References

1. Gil, L.: Materials. **8**, 625 (2015)
2. Silva, S.P., Sabino, M.A., Fernandes, E.M., Correlo, V.M., Boesel, L.F., Reis, R.L.: Int. Mater. Rev. **50**, 345 (2005)
3. Gibson, L.J., Ashby, M.F.: Cellular Solids: Structure and Properties, Cambridge Edn. Cambridge University Press, Oxford (1997)
4. Jardin, R., Fernandes, F., Pereira, A., Alves de Sousa, R.: Static and dynamic mechanical response of different cork agglomerates. Mater. Des. **68**, 121–126 (2015)
5. Sanchez-Saez, S., García-Castillo, S.K., Barbero, E., Cirne, J.: Dynamic crushing behaviour of agglomerated cork. Mater. Des. (1980–2015). **65**, 743–748 (2015)
6. Sasso, M., Mancini, E., Chiappini, G., Sarasini, F., Tirillò, J.: Application of DIC to static and dynamic testing of agglomerated cork material. Exp. Mech. **58**(7), 1017–1033 (2018)
7. Le Barbenchon, L., Kopp, J.B., Girardot, J., Viot, P.: Multi-scale foam: 3D structure/compressive behaviour relationship of agglomerated cork. Materialia. **5**, 100219 (2019)
8. Viot, P., Beani, F.: Polypropylene foam behavior under compressive loading at high strain rate. In: E. Sciences (ed.) Dymat, pp. 543–549, Porto (2003)

Chapter 36
Dynamic Mechanical Behavior of Reinforced Cork Agglomerate

Louise Le Barbenchon, Jean-Benoît Kopp, Jérémie Girardot, and Philippe Viot

Abstract Agglomerated cork is today mainly used for its thermal insulation and acoustic properties. As cork is a cellular material, its absorbing properties at a dynamic regime are being considered for impact-absorbing applications as core material in sandwich structures. Therefore an optimization of this material would allow to strengthen its present applications and open new ones. Ranging from the container for the transport of sensible pieces to sports items and including lightweight aeronautic components, a wide range of applications is foreseen. Cork agglomerates with and without reinforcements at a quasi similar density were studied to compare their mechanical performances. This paper investigates the effect of these foreign reinforcements on the properties of agglomerated cork under a dynamic loading. The material behavior has been determined as a function of two parameters, charge presence and strain rate. The microstructure was first observed through optical and scanning electronic microscopy, spotting charges between each cork bead. The characterization of cork at different strain rates was then carried out. Agglomerated cork was tested on two specific machines. An electromechanical testing machine has been used to apply an uni-axial compression for quasi- static strain rates. These results were completed by those obtained with a specific set- up for the high strain rates assays allowing almost constant loading speed. Results depending on the presence of charges at different strain rate regimes were obtained. Elastic modulus were compared afterward. Young's modulus increased between 22 and 36% for reinforced samples depending on the strain rate.

Keywords Dynamic mechanical behavior · Cellular material · Cork agglomerates · Compressive loading · Reinforcements

Introduction

Cellular materials can be found in a large range of application domains: transport, health, energy, sport. Their main characteristics are a low density, damping properties, thermal insulation and a capability to dissipate energy during an impact loading [1]. The last one is especially interesting considering passive safety applications. Depending on the stress level required, it is possible to tailor it [2]. However it is today mainly done by changing the density of the cellular material [3]. As potential lightweight materials, it is yet important to minimize the weight while enhancing the mechanical strength for specific applications. The introduction of reinforcements is one of the most commonly used methods to improve the mechanical properties in usual composite materials. Reinforcing cellular materials with short fibers has been done on syntactic foams [4]. Another option is to add fibers while expensing the foam. However the constitutive material of the foam and the fibers are not always compatible. Thus a surface treatment seems unavoidable. Furthermore, it is hard to control how fibers will arrange themselves in the material. To overcome this problem, multi-scale foams are investigated here. It consists in agglomerated beads composed of microscopic closed cells [5]. Before agglomeration, short fibers are added to the preparation but do not damage the cellular structure. This study focuses on the influence of these short fibers on the microstructure and the mechanical behavior of a multi-scale cellular material. Quasi-static and dynamic compressive loadings were applied. The material considered here is agglomerated cork beads.

L. Le Barbenchon (✉) · J.-B. Kopp · J. Girardot · P. Viot
Arts et Métiers ParisTech, CNRS, I2M Bordeaux, Esplanade des Arts et Métiers, Talence Cedex, France
e-mail: louise.le_barbenchon@ensam.eu

L. E. Lamberson (ed.), *Dynamic Behavior of Materials, Volume 1*, Conference Proceedings of the Society for Experimental Mechanics Series, https://doi.org/10.1007/978-3-030-30021-0_36

Background

Cork is a natural polymeric cellular material which displays a closed-cell structure [6]. It is formed by small anisotropic prismatic cells disposed in successive layers exhibiting a relatively homogeneous honeycomb structure. Two materials were studied: one without and one with short fibers (Young's modulus E = 230 Gpa). This last material will be called a composite foam. To obtain agglomerated cork, small beads of cork (diameter ø = 0.5/1 mm) are mixed together with a thermoset resin (density $\rho_{resin} = 1128.5$ kg m^{-3}). For the composite material, short fibers were added at this step. It is then uni-axially compressed into a 1000 × 500 × 150 mm^3 block at a 0.42 relative density. A multi-scale cellular material is thus obtained. Figure 36.1 shows the three scales. First there is the structure scale, then the bead scale with millimetric lengths and finally each bead is made of a cellular material. Therefore by looking closer (with a scanning electronic microscope (SEM)) at the beads, cells can be spotted. This cells scale is at the micrometric scale. Each bead is characterized by a specific cellular orientation [7].

An electromechanical traction/compression machine (Zwick Roell 250 from Allround-Line) with a load cell capacity of 250 kN is used. The loading speed is set at 5 mm min^{-1} corresponding to an average strain rate of 4.2 × 10^{-3} s^{-1}.

In order to reach the dynamic compression loading (around 70 s^{-1}), an original assembly was used (Fig. 36.2). The fly wheel consists in a steel wheel with a high moment of inertia (77 kg m^{-2}). This ensures that the loading speed is considered as quasi-constant during loading. However, the speed of unloading is not controlled. Force/displacement signals during discharge were therefore not studied.

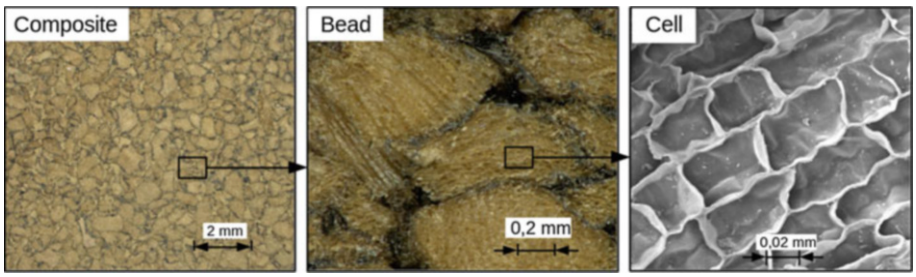

Fig. 36.1 Agglomerated cork: a multi-scale cellular material

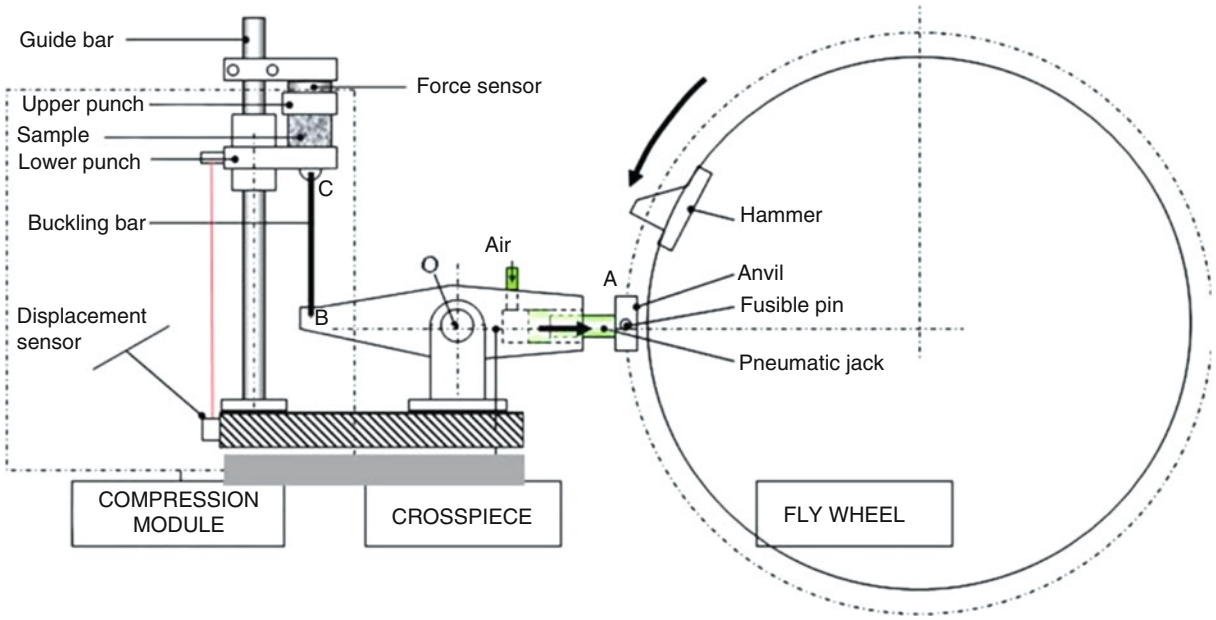

Fig. 36.2 Fly wheel set-up scheme

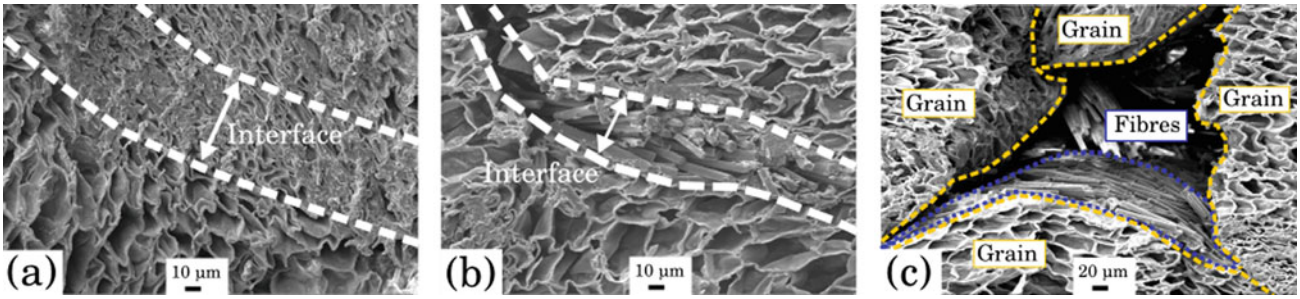

Fig. 36.3 Interfaces between cork beads depending on the fiber presence

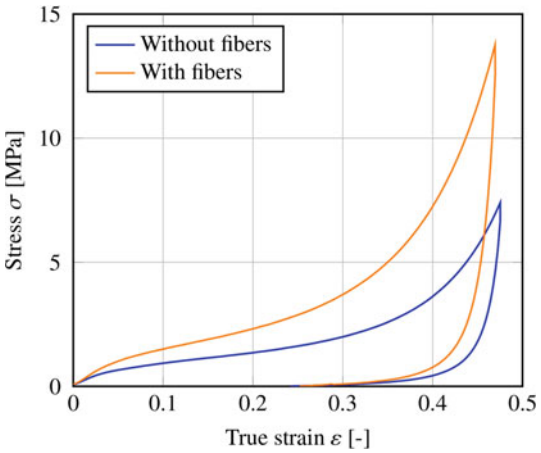

Fig. 36.4 Experimental stress/strain curve of agglomerated cork and reinforced cork composite compressed at a mean strain-rate of 4.2×10^{-3} s^{-1}

Analysis

Interfaces between the foam beads are first observed with a SEM. Figure 36.3a shows that for the agglomerated foam, interfaces are very thin. They are revealed by collapsed cells and resin. Furthermore the anisotropic nature of cork cells [6] can also help to distinguish one bead from another. On the other hand, interfaces in the composite material are thicker (around 20 µm). It seems that short fibers are well dispersed and are present between each bead. A closer look at fibers (Fig. 36.3c) shows that short fibers seem to lay mostly tangentially to the foam beads.

Cellular materials are partly used for their energy absorption properties. The compressive behavior of the two material has then been studied for quasi-static and dynamic loadings. Figure 36.4 displays the stress/strain curves of each material tested in both direction for a mean strain-rate of 4.2×10^{-3} s^{-1}. For both material, a typical foam-like behavior is noticed. For small strains, a linear behavior. It slope is characterized by the Young's modulus E. After that, stress increases slowly until large strains. This stage is called the plateau stage and is characterized by a plateau stress σ_p (where the stage starts) and a tangent modulus E_p. Finally stress rises sharply and it is called the densification. The densification strain ε_d can be calculated to delimit it. Absorbed energy E_d was then calculated until densification.

Strain-Rate Effect on the Compressive Behavior

Young's modulus increases with the mean strain-rate for both materials (Fig. 36.5). Hence both cork agglomerates demonstrate a time-dependency at static and dynamic loadings. The viscoelastic behavior of cork had already be noticed [8]. Cork is made of several polymeric components as suberin, lignin, hemi-cellulose and cellulose and the composite contains also a polymeric resin. They demonstrate themselves viscoelastic behavior [9] though time dependency was not always detected in a given speed regime.

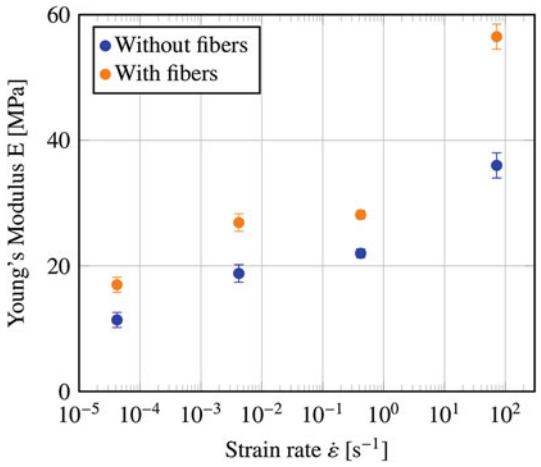

Fig. 36.5 Young's modulus of cork agglomerates and reinforced composite material at several average strain-rates

An increase in the strain-rate dependency is also noticed for both cellular materials. Several effects can drive the strength upward like this [3]. First the time dependency of the constitutive materials can change depending on whether the material is in the glassy state or the rubbery state. Another cause to this enhancement is the gas trapped in the closed cells. It was indeed shown that depending on the loading regime, different mechanisms concerning gas evacuation were activated [10]. Finally "micro-inertia" or dynamic buckling which is the inertia associated with rotation and lateral motion of cell walls when they buckle can also be cited.

Reinforcement Effect on the Compressive Behavior

The composite material is stiffer than the usual cork agglomerate at each tested strain-rate (Fig. 36.4). Young's modulus is between 22 and 36% greater. As SEM pictures show it, short fibers are placed between each cork beads. As the material is stiffer, it seems that these fibers allow to sustain higher stress by reinforcing interfaces between beads. A higher Young's modulus associated with a foam-like behavior implies that the composite foam will absorbed more energy during an impact than the cork agglomerate, but at a cost of a higher plateau stress.

Conclusion

In this article, reinforcement of cellular material by short fibers was studied. The composite material consisted in beads of cellular material mixed together with a resin and short fibers then uni-axially compressed together before polymerization in a oven. By adding fibers to the mix of beads and resin, it seems that fibers are mostly placed tangentially to the bead. Therefore after the compression process, they are most of the time at each interface. The compressive behavior of the composite foam was compared to a normal cork agglomerate on a wide range of strain rates: from quasi-static to dynamic compressive loadings. The composite foam keeps a mechanical behavior similar to a classical cellular material. Both materials were found to have a compressive behavior that depends on the strain-rate. An enhancement of this effect was noticed for dynamic loadings and associated to several causes (gas trapped, material dependence, ...). The initial rigidity described by the Young's modulus is increased between 22 and 36% for the composite foam in comparison to usual agglomerated cork. This change in rigidity is likely caused by the short fibers. Being placed between each bead, they form a stiffer network with the resin. The composite material will then absorbed more energy during a compressive loading. To conclude, short fibers appear as suitable reinforcements for multi-scale cellular materials.

Acknowledgement This work was performed in the frame-work of the LIAMA project (supported by Safran PowerUnit, Lieges HPK and Région Nouvelle Aquitaine).

References

1. Mills, N.J., Fitzgerald, C., Gilchrist, A., Verdejo, R.: Compos. Sci. Technol. **63**, 2389 (2003)
2. Maheo, L., Viot, P.: Int J Imp Eng. **53**, 84 (2013)
3. Gibson, L.J., Ashby, M.F.: Cellular Solids: Structure and Properties, Cambridge edn. Cambridge University Press, Oxford (1997)
4. Barkoula, N.M., Alcock, B., Cabrera, N.O., Peijs, T.: Polym. Polym. Compos. **16**(101), 1206.4529 (2008)
5. Viot, P., Bernard, D.: Computational Methods and Experiments in Materials Characterisation IIII, 197 (2007)
6. Gibson, L.J., Easterling, K.E., Ashby, M.F.: Proc. Royal Soc A. **377**, 99 (1981)
7. Le Barbenchon, L., Kopp, J.B., Girardot, J., Viot, P.: Multi-scale foam: 3D structure/compressive behaviour relationship of agglomerated cork. Materialia. **5**, 100219 (2019)
8. Le Barbenchon, L., Girardot, J., Kopp, J.B., Viot, P.: Strain rate effect on the compressive behaviour of reinforced cork agglomerates. EPJ Web of Conferences. (2018)
9. Silva, S.P., Sabino, M.A., Fernandes, E.M., Correlo, V.M., Boesel, L.F., Reis, R.L.: Int. Mater. Rev. **50**, 345 (2005)
10. Bouix, R., Viot, P., Lataillade, J.L.: Polypropylene foam behaviour under dynamic loadings: Strain rate, density and microstructure effects. Int J Imp Eng. **36**(2), 329–342 (2009)

Chapter 37
Use of Edge-on Impact Tests with Synchrotron-Based MHz Radioscopy to Investigate the Multiple Fragmentation Process in SiC Ceramics

Pascal Forquin, Bratislav Lukic, Yannick Duplan, Dominique Saletti, Daniel Eakins, and Alexander Rack

Abstract Ceramic materials are widely used all around the world in protective solutions as front plate of bilayered configurations, a metallic or composite material being used as backing to absorb the kinetic energy of fragments. However, during the impact, an intense fragmentation process composed of numerous oriented cracks develops in the ceramic plate due to high-loading rates tensile stresses. The edge-on impact (EOI) configurations constitute one of the best testing techniques to analysis the dynamic fragmentation process in brittle materials. A metallic cylindrical projectile hits the edge of a prismatic target of thickness smaller than the projectile diameter with an impact velocity ranging from 100 to 300 m/s. The damage process is usually observed on the lateral surface with a digital ultra-high speed camera ("open configuration"). However, the fragmentation cannot be observed in the bulk of the target except if a post-mortem analysis is conducted ("sarcophagus configuration"). In the present work, in addition to this classical testing methods, EOI experiments have been conducted in the European Synchrotron Radiation Facility (beamline ID19) with X-ray radioscopy technique using the 16-bunch operation mode. Targets, $60 \times 30 \times 6$ mm^3, made of silicon carbide were placed in an intense X-ray beam (mean photon energy about 30 keV) providing an observation field of 12.8 mm in width and 8 mm in height, and impacted with projectile velocities ranging from 150 to 200 m/s. A Shimadzu HPV-X2 camera lens-coupled to a fast scintillator (LYSO:Ce) was used to visualize the fragmentation process through the thickness with an interframe time set to 1065 ns. The fragmentation pattern was compared to data obtained in classical "open configuration" with surface visualization and to post-mortem analysis obtained in "sarcophagus configuration".

Keywords Edge-on impact · Ceramic · Dynamic fragmentation · High-speed imaging · Synchrotron radioscopy

Introduction

For more than two decades, silicon carbide ceramics have been used as front plate of bilayered configurations for personal body armors or in protective solutions of military vehicles [1, 2]. Their high hardness and compressive strength allow breaking and defeating the hard core of AP (Armor-Piercing) projectiles of small and medium calibers. However, in the wake of the compression wave, an intense fragmentation develops in the ceramic tile due to high-strain-rates tensile loading. The edge-on impact experimental method constitutes one of the most efficient testing techniques to investigate the fragmentation process at strain-rates ranging from a few thousand of s^{-1} to ten thousands of s^{-1}. A metallic cylindrical projectile hits the edge of a rectangular tile whose thickness is smaller than the projectile diameter. The compressive strength of ceramics being about 10–20 times higher than their tensile strength a large range of impact velocity can be considered to generate a tensile damage without inducing any compressive damage near the impact point. In addition, contrary to a real "normal impact" configuration for which the degradation is "hidden" in the bulk of the material the tensile damage can be observed by using ultra-high speed imaging operating at recording frequencies about 1 Mfps (million frames per second). This testing method was recently used to investigate the fragmentation process in ceramics under impact loading [3] in an "open configuration"

P. Forquin (✉) · B. Lukic · Y. Duplan · D. Saletti
Laboratory 3SR, Univ. Grenoble Alpes, CNRS, Grenoble INP, Grenoble, France
e-mail: pascal.forquin@3sr-grenoble.fr

D. Eakins
Department of Engineering Sciences, University of Oxford, Oxford, UK

A. Rack
ESRF – The European Synchrotron, Grenoble, France

L. E. Lamberson (ed.), *Dynamic Behavior of Materials, Volume 1*, Conference Proceedings of the Society for Experimental Mechanics Series, https://doi.org/10.1007/978-3-030-30021-0_37

and in a "sarcophagus configuration". In the open configuration, the ceramic tile is free with no casing. In the sarcophagus configuration the ceramic tile is placed in a casing to keep most of the fragments in place. However, small paper wedges were placed in-between the ceramic tile and the aluminum casing to ensure an impedance discontinuity. Finally, the same amount of cracks is expected for both (open and sarcophagus) configurations. The fracturing post-mortem pattern was investigated through X-ray microtomography analysis with specifically designed image analysis tools to detect fractures and fragments by [4]. The distribution of fragment sizes of two SiC ceramics was compared to sieving curves. The fragmentation properties of four SiC ceramic grades with different microstructures subjected to edge-on impact tests and normal impacts tests were compared in [5]. However, these approaches allows only for an analysis on the surface (EOI in open configuration) or after the experiment (EOI and normal impact in sarcophagus configuration).

In the present work, in addition to these classical testing methods, an EOI experiment was conducted in the European Synchrotron Radiation Facility (ESRF). The fragmentation process was visualized through the thickness of the ceramic tile by placing the target, inside an intense synchrotron radiation X-ray beam and by using an indirect X-ray image detector combined with an ultra-high speed camera (Shimadzu HPV-X2). This configuration allows visualizing the fragmentation through the target.

Silicon Carbide Tested in the Present Work

The tested silicon carbide is a porous ceramic characterized by a heterogeneous porosity across the tile thickness. Indeed, the kinetic of slurry water absorption into the two porous mold surfaces leads to the formation of a highly porous zone in the mid-thickness area of the body, called parting line. As noted on the Fig. 37.1 this flaw remains in the final product and the microstructure is made of two areas: the parting line, a 1 mm-thick area (1) presenting a high amount of porosity with pores larger than 50 μm and, on both sides of this parting line, a second area (2) containing pores with a ten times smaller size (Fig. 37.1).

Edge-on Impact Experiments

EOI experiments have been conducted at the European Synchrotron Radiation Facility (ESRF) using ultra-high speed X-ray phase-contrast imaging. The ceramic tile 60 × 30 × 6 mm^3 is illuminated by means of X-ray beam (beam energy about 30 keV) offering a large field of view (12.8 mm in width and 8 mm in height). The impact velocity was set to 94 m/s. A digital ultra-high speed camera (Shimadzu HPV-X2) lens-coupled to a fast scintillator (LYSO:Ce, Hilger Crystals, UK) was used to visualize the fragmentation process through the thickness with an interframe time set to 1065 ns. The sensor has

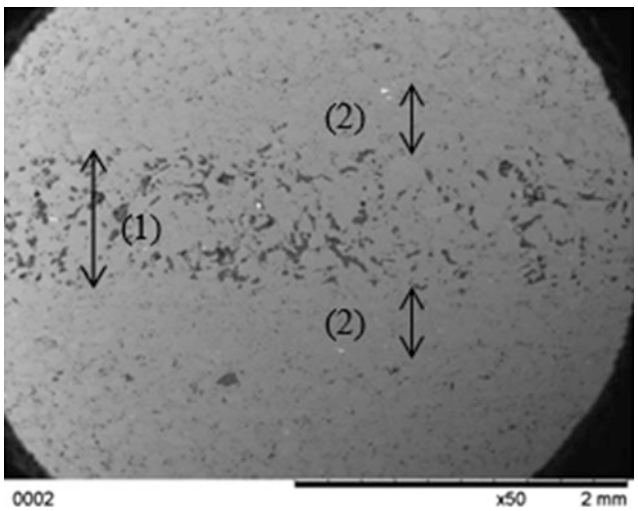

Fig. 37.1 SEM picture of a silicon carbide-binder ceramic phase composite sample cross-section

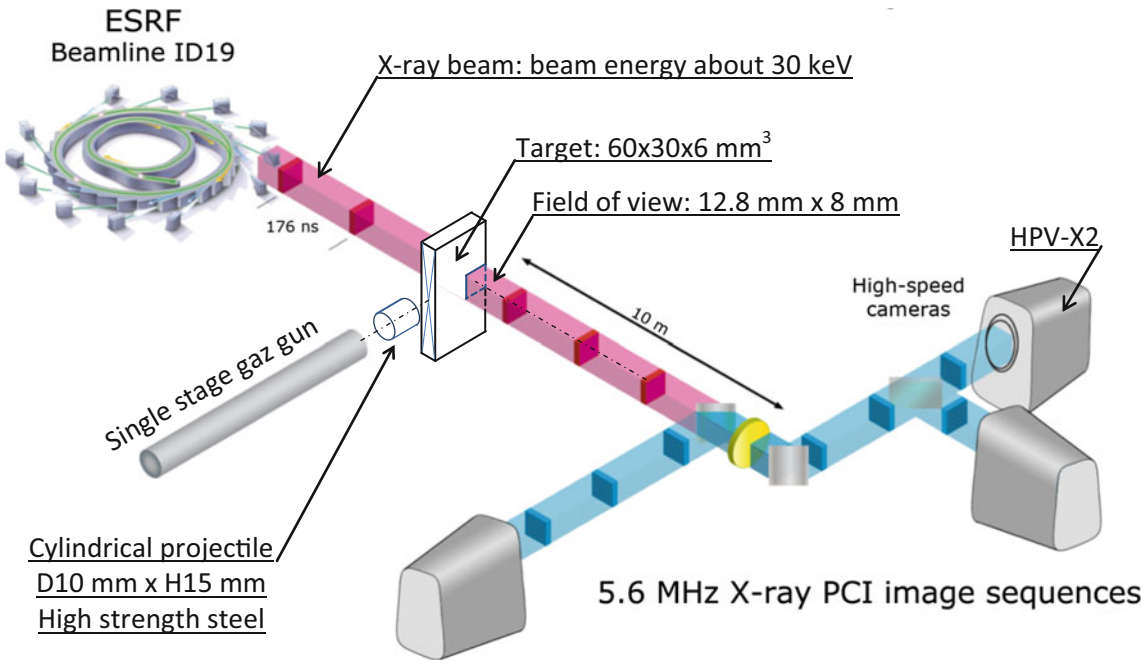

Fig. 37.2 Edge-On Impact test with synchrotron-based MHz radioscopy

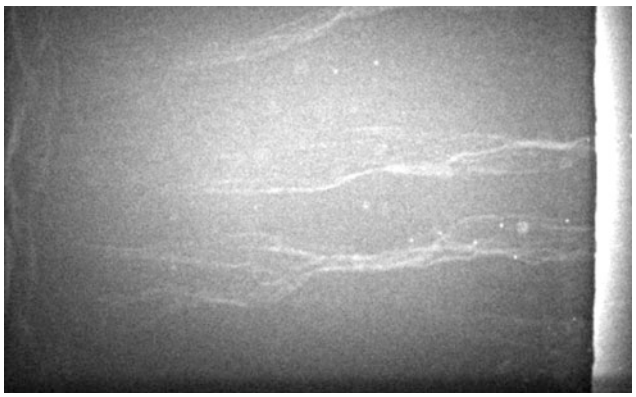

Fig. 37.3 Picture of an EOI test performed with X-ray synchrotron radiation at t ≈ 8 μs after impact (impact speed: 94 m/s). The field of view is 12.8 mm in width and 8 mm in height

400 × 256 (400 × 250 effective) pixels providing a high spatial sampling with respect to the size of the field of view (32 μm pixel pitch). The observation window is located near the rear edge as illustrated in the Fig. 37.2.

The experiments are conducted using the 16-bunch operation mode having two bunch pulses integrated over one captured frame. A picture of ultra-high speed camera is shown in the Fig. 37.3 at approximately 8 μs after impact. Several cracks seem to initiate on the rear edge propagate horizontally (i.e. perpendicularly to the rear free edge). In addition a "spall crack" initiates and propagates along the vertical direction (i.e. parallel to the rear free edge).

Conclusion

Edge-on impact experiments have been conducted at the European Synchrotron Radiation Facility (ESRF) using ultra-high speed X-ray phase-contrast imaging. The fragmentation is visualized through the target by means of a digital ultra-high speed camera lens-coupled to a fast scintillator. A comparison with classical observations made in "open configuration" and in "sarcophagus configuration" constitutes an important prospect of this experimental work.

Acknowledgements This work has been performed in the framework of the Brittle's CODEX chair supported by the UGA (Univ. Grenoble Alpes) Foundation and sponsored by the Saint-Gobain and Lafarge-Holcim companies. These sponsors are gratefully acknowledged by the authors. The authors are thankful to Saint-Gobain for providing the tested ceramic samples. The authors would like to address a sincere thank you to the team at Beamline ID19, and to the students and post-docs at the University of Oxford for their assistance with the experiments in ESRF. The authors are grateful to ESRF for supporting this research.

References

1. den Reijer, P.C.: Impact on Ceramic Faced Armour. PhD Thesis, Technical University of Delft (1991)
2. Forquin, P., Tran, L., Louvigné, P.-F., Rota, L., Hild, F.: Effect of aluminum reinforcement on the dynamic fragmentation of SiC ceramics. Int. J. Impact Eng. **28**, 1061–1076 (2003)
3. Zinszner, J.L., Forquin, P., Rossiquet, G.: Experimental and numerical analysis of the dynamic fragmentation in a SiC ceramic under impact. Int. J. Impact Eng. **76**, 9–19 (2015)
4. Forquin, P., Ando, E.: Application of micro-tomography and image analysis to the quantification of fragmentation in ceramics after impact loading. Phil. Trans. R. Soc. A. 20160166 (2017). https://doi.org/10.1098/rsta.2016.0166
5. Forquin, P., Zinszner, J.-L., Rossiquet, G., Erzar, B.: Microstructure influence on the fragmentation properties of dense silicon carbides under impact. Mech. Mater. **123**, 59–76 (2018)

Chapter 38
Low Temperature Seawater Effects on the Mechanical, Fracture, and Dynamic Behavior of E-Glass and Carbon Fiber Laminates

James LeBlanc, Paul Cavallaro, Jahn Torres, Eric Warner, Andrew Hulton, Ryan Saenger, and David Ponte

Abstract The mechanical behavior of E-Glass/Epoxy and Carbon Fiber/Epoxy laminates when exposed to low temperature and prolonged submergence operating environments has been investigated through a detailed experimental study. The temperature range which was studied consisted of room temperature (20 °C) to −2 °C, the lowest temperature expected in a submerged ocean environment. Mechanical characterization of each material has been conducted through tensile, compression and short beam shear testing. Additionally, the influence of temperature on the Mode I fracture performance of these laminates was evaluated through Double Cantilever Beam (DCB) tests. Furthermore, a Dynamic Mechanical Analyzer (DMA) was employed to evaluate the structural behavior of these laminates under a range of frequency loading and temperatures. A transition between a matrix-dominated to laminate-dominated responses as functions of strain rate were identified. The current study has resulted in the mechanical characterization of E-Glass/Epoxy and Carbon Fiber/Epoxy laminates as a function of temperature ranging from room temperature to low temperature sea water conditions. The experimental results show a dependence on the static, fracture, and dynamic properties of these laminates.

Keywords Composite materials · Low temperatures · Mechanical characterization · Water ingression · Dynamic mechanical analysis

Introduction

A key advantage to the use of fibrous composites in structural design is the ability to customize material performance to prescribed design requirements and operating environments. Fiber-reinforced polymer (FRP) composites provide many readily recognized performance benefits; lightweight, high strength- and stiffness-to-weight ratios, corrosion resistance, net shape manufacturing, and more. Proper selections of the fabric architectures, fiber and matrix materials, ply stacking arrangements, etc. can yield significant mechanical performance advantages over traditional structural materials. However, selections are often based upon experiments and analyses performed without consideration of extreme operating temperatures and water ingress. Many polymers exhibit increased stiffness and decreased toughness with colder temperatures. Additionally, polymers show strength changes caused by swelling as a result of moisture absorption. Therefore, the potential for unanticipated failure mechanisms to occur with environmentally-dependent material properties is problematic for polymer composites at extreme temperatures. Material considerations in the design of composite structures subject to cold operating environments with water absorption are necessary and require an in-depth understanding of the relationships between laminate stress distributions, ply interface mechanics, hygrothermal behaviors, damage mechanisms, and fracture mechanics.

Studies of temperature effects on FRP composites have been limited. Thermal contraction causes matrix shrinkage and forms residual inter-laminar shear stresses. These stresses degrade the inter-laminar shear strength, fatigue life, and laminate stiffness. Microcracks can lead to increased permeability, creating paths for hygrothermal effects such as moisture and fluid absorption and swelling at cold temperatures. Swelling is a major source of environmentally-induced stress when laminates are subjected to freeze-thaw cycling in the presence of water. The generation of microcracks can lead to coalescence which can cause larger meso-scale and macro-scale cracks leading to reductions in fracture toughness and damage tolerance. Thermal cycling after water ingression of composite materials presents a risk of premature failure that can lead to fracture. Water diffusing through the polymer matrix will accumulate at the interfaces of the fillers and matrix or within the matrix itself depending on the water-polymer mixing thermodynamics. Under thermal cycling around the freezing temperature, water will freeze/expand into a solid producing local inhomogeneity stress fields (Fig. 38.1) which will evolve into crack

J. LeBlanc (✉) · P. Cavallaro · J. Torres · E. Warner · A. Hulton · R. Saenger · D. Ponte
Naval Undersea Warfare Center (Division Newport), Newport, RI, USA
e-mail: James.M.LeBlanc@Navy.Mil

L. E. Lamberson (ed.), *Dynamic Behavior of Materials, Volume 1*, Conference Proceedings of the Society for Experimental Mechanics Series, https://doi.org/10.1007/978-3-030-30021-0_38

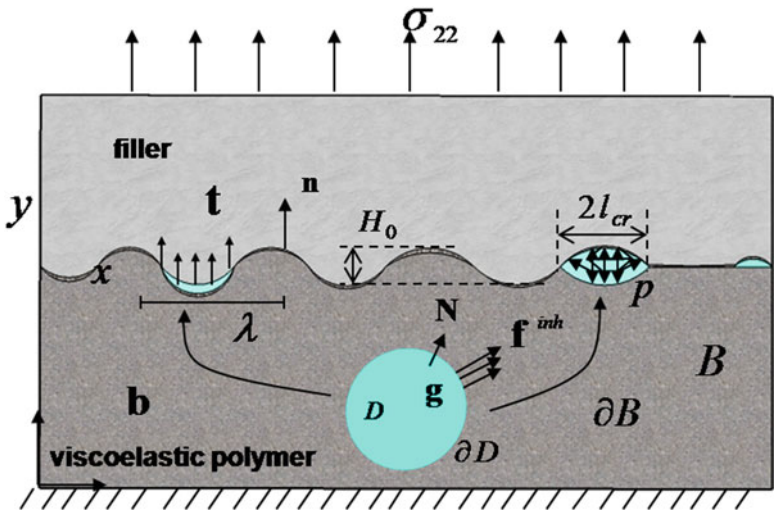

Fig. 38.1 Diagram of interface between viscoelastic polymer matrix and filler material

initiation defects that upon further application of stresses through quasi-static loading and/or impact can produce failure under design thresholds, thereby reducing the reliability of the composite structures. As the freeze-thaw cycling history increases these effects will be dominated by the pressure (p) loading within these defects, which will assist in the traction (t) opening of defects as seen in Fig. 38.1.

Materials

The materials studied in the current investigation consisted of Carbon/Epoxy and E-Glass/Epoxy laminates. The Carbon and E-Glass fabrics were "plain weave" styles in which the yarns were woven in a one-over/one-under pattern, resulting in balanced yarn counts along the warp and weft directions. The E-Glass fabric had an areal weight density of 5.61 oz./yd^2 with equal yarn counts of 18 in both the warp and weft directions. The Carbon fabric had an areal weight density of 5.88 oz./yd^2 with equal yarn counts 12.5 in both the warp and weft directions.

Results

A detailed experimental and analytical investigation of the effects of low temperature on the mechanical, water ingression/diffusion, and acoustic properties of E-Glass/Epoxy and Carbon/Epoxy laminates was conducted. The investigation was primarily aimed at establishing a foundational understanding of the temperature effects on composite laminates at temperatures of interest to the undersea marine community. Historically, mechanical properties at operating temperatures in the range of ~15 °C–20 °C have been evaluated, with minimal data pertaining to the temperatures associated with arctic seawater in the ~2 °C–4 °C regime. The Carbon/Epoxy and E-Glass/Epoxy laminates are of interest to the marine industry in support of current and future applications of composites. The key findings of the study were as follows:

Under tensile loading the E-Glass/Epoxy laminates exhibited minimal dependence on decreasing temperature in terms of elastic modulus and tensile strength. There was a measurable dependence on decreasing temperature for the Carbon/Epoxy laminates; both stiffening and strengthening were observed over the temperature range from 20 °C to −2 °C. Compressive loading of the E-Glass/Epoxy laminates resulted in differing trends in stiffness and strength with decreasing temperature; as the temperature decreased, the laminates became softer but stronger. The Carbon/Epoxy laminates exhibited decreasing stiffness with decreasing temperature. The short beam shear tests revealed a 20% increase in short beam shear strength over the temperature range from 20 °C to −2 °C for both the E-Glass/Epoxy and Carbon/Epoxy laminates. Finally, both the E-Glass/Epoxy and Carbon/Epoxy laminates, exhibited a direct dependence of G_{IC} on temperature with trends showing decreases in G_{IC} with corresponding decreases in temperature. When considering the water ingression properties of these laminates, the Carbon/Epoxy laminates exhibited water ingression that did not surpass 1.5% total mass change from water

at any temperature whereas the E-Glass/Epoxy laminates exhibited a mass change up to nearly 3% at full saturation. Finally, the DMA testing revealed that the linear viscoelastic behavior at small strains exhibited a matrix-dominated behavior with a composite-dominated behavior at higher strain rates emerging for the Carbon/Epoxy laminates at a lower strain level than for the E-Glass/Epoxy laminates.

Acknowledgement The authors gratefully acknowledge the funding support provided by NUWC Division, Newport's Chief Technology Office Strategic Investment Office (00X).

Chapter 39
Using the SURF Model to Simulate Fragment Impact on Energetic Materials

Xia Ma and Brad Clements

Abstract The Scaled Uniform Reactive Front (SURF) model developed by Menikoff and Shaw (Comb. Theory Model., 2012) is a High Explosive (HE) reactive burn model. It has been shown to accurately model plate impact shock experiments while requiring only a minimal number of calibration parameters. We have implemented SURF into the Eulerian code Pagosa. SURF has been shown to suitably model high-speed impact and accurately capture the entire Shock-to-Detonation Transition (SDT) process. SURF is also able to model short shocks and dead zones, critical for finite sized impactors such those used in fragment impact investigations. Many burn models cannot do this. The success of SURF is derived from it being based on the physics of hotspots, triggered by the leading shock, and thus can naturally account for properties like shock desensitization. SURF needs to be calibrated for each explosive modeled and for that we use plate impact experiments. For the three explosives considered in this work, PBX 9501, PBX 9502 and Composition B, we use the data of Gustavsen and Dattelbaum (Embedded electromagnetic gauge measurements and modeling of shock initiation in the TATB based explosives PBX 9502 and LX-17. LA-UR-01-3339). After discussing the model, its calibration, we apply SURF to model fragment impact experiments where the effects of release waves originating from finite sized impactors is critical. For example, we use SURF to investigate fragment impact on PBX9502, diagnosed using high speed photography, to support our numerical study of the effect of lateral and back surface release wave on the detonation process. SURF is also applied to successfully model ball impact on the explosive PBX 9501. These successes support the notion that SURF is a reliable tool for modeling impacted explosives.

Keywords Energetic material · Material response · Detonation · Shock physics · Modeling

Introduction

We need reliable simulation tools to model high-speed fragment impact of explosives. This is complicated by the fact that in any real fragment impact application two- and three-dimensional effects are always present. While important, these complications are sometimes ignored. The explosive response of an HE to a high-speed shock impact is generally considered to be a consequence of the presence of hot-spots. These are locally heated regions of the material that have temperatures that greatly exceed bulk shock heating temperatures. Over the years, many hot-spot mechanisms have been proposed [1–3], the most common one considered is heat generated by collapsing voids.

All HEs are known to contain a distribution of voids. These are the "weak points" of any solid explosive. When a strong shock sweeps over the explosive, the voids collapse, dissipating shock energy, converting it to heat to produce localized regions of high temperatures. Expounding slightly, the energy extracted from the shock in the collapsing void will cause steep pressure gradients that can drive some of the material to high speed jet-like a shapes that impinge on the walls of the collapsing voids, producing high temperatures. This *hot spot* temperature can exceed the endothermic activation energy threshold and thus initiate the HE. Once initiated, a detonation can potentially follow. Even though these hot spots tend to be micron-sized, they can sustain a burn that propagates in the HE. On the other hand, they can also quench. A determining factor whether they enhance each other or not is the density distribution of hot spots. As mentioned above, SURF [4] uses hot-spots mechanism that are triggered by the lead shock. This distinguishes from burn model based on the local pressure alone.

X. Ma (✉)
Los Alamos National Laboratory, Mail Stop B216, Los Alamos, NM, USA
e-mail: xia@lanl.gov

B. Clements
Los Alamos National Laboratory, Mail Stop P918, Los Alamos, NM, USA

L. E. Lamberson (ed.), *Dynamic Behavior of Materials, Volume 1*, Conference Proceedings of the Society for Experimental Mechanics Series, https://doi.org/10.1007/978-3-030-30021-0_39

HE is often enclosed by metal container, like a shell, characterized with a higher speed of sound than the HE. Often then, in any real impact application there exists intricate reflective weak shocks (and also rarefaction waves) originating at surface boundaries. If the lead shock striking an HE is too weak to ignite it on first pass, then SURF conjectures that any subsequent shock cannot ignite the explosive, with the view that the first passage of the shock closed existing voids. That is, the hot-spot void collapse mechanism is no longer viable. This is called shock desensitization. Since SURF use number density of active growing hot spots, called burn centers, and these depend only on strength of the lead shock strength, it naturally accounts for shock desensitization. Shock desensitization can result in the phenomena known as dead zones. A dead zone is a desensitized region of HE of finite extent that remains unburned even though much of other portions of the explosive may have undergone a complete detonation. Burn models based on local pressure, as opposed to the shock pressure, have difficulty in capturing dead zones. We will illustrate numerically simulated dead zones in the forthcoming sections. SURF can also capture short shocks, where rarefactions (releases waves from the back surface of flyer plates, for example) greatly reduce the amount of time for the build-up-to-detonation to occur. These are both critical features for fragment impact simulations. We will also give an example to show that SURF captures the details of the build up to detonation, not just the pop plot. In fragment impact, we need to be able to account for dead zones, and explosive build up in the presence of release waves originating at the boundaries (conditions off the pop plot). These are two- and three-dimensional effects that we mentioned at the beginning of this introduction. We will use the explosive PBX 9502 for our numerical study of the two-and three-dimensional effects on SURF. For that case there is an additional parameter call n In the SURF literature. We show that n controls the strength of release wave effects for SURF, thus reflecting the two- and three-dimensional behavior of dead zones. Finally, we show full three-dimensional simulations of the explosive Composition B.

Governing Equations

The Eulerian code Pagosa that we used solves the continuity equation:

$$\frac{D\rho}{dt} = -\rho \nabla \cdot \boldsymbol{u}, \tag{39.1}$$

where $\frac{D}{dt}$ is material derivative defined as

$$\frac{D}{dt} = \frac{\partial}{\partial t} + U\frac{\partial}{\partial x} + V\frac{\partial}{\partial y} + W\frac{\partial}{\partial z}, \tag{39.2}$$

and (U,V,W) are three component of velocity vector $\boldsymbol{u}$, and the momentum equation

$$\rho \frac{D\boldsymbol{u}}{dt} = \boldsymbol{F} - \nabla P + \nabla \cdot \boldsymbol{S}, \tag{39.3}$$

where $\boldsymbol{S}$ is the symmetric deviatoric stress tensor by subtracting the isotropic pressure P from the total stress tensor and

$$\nabla \cdot \boldsymbol{S} = \left[\left(\frac{\partial}{\partial x}, \frac{\partial}{\partial y}, \frac{\partial}{\partial z} \right) \cdot \begin{pmatrix} S_{xx} & S_{xy} & S_{xz} \\ S_{yx} & S_{yy} & S_{yz} \\ S_{zx} & S_{zy} & S_{zz} \end{pmatrix} \right]^{\boldsymbol{T}}. \tag{39.4}$$

Pagoa invokes the volume of fluid (VOF) equation for multi-material is

$$\frac{\partial f_m}{\partial t} + \boldsymbol{u} \cdot \nabla f_m = 0, \tag{39.5}$$

where f_m is occupancy function of a certain material m (or fluid) and is defined as

$$f_m(x, y, z, t) \equiv \begin{cases} 1 & if\ point\ (x, y, z)\ has\ m\ \ material\ at\ time\ t \\ 0 & otherwise \end{cases} \tag{39.6}$$

Equations (39.1) to (39.6) are closed by an equation of state (EOS) and stress strain relations of different model options. We used Mie-Gruneisen EOS for solid HE phase with the linear Us-Up relation given by

$$U_s = c_0 + sU_p, \tag{39.7}$$

where U_s is the shock wave speed, U_p is the particle speed behind the shock, c_0 is the sound speed of the material, and s is the slope of this linear Us-Up relation. We used Jones-Wilkins-Lee (JWL) EOS for the HE products (gas phrase)

$$P_m = A\left(1 - \frac{\omega}{R_1 V}\right)e^{-R_1 V} + B\left(1 - \frac{\omega}{R_2 V}\right)e^{-R_2 V} + \omega\rho\left(E_m + E_0\right), \tag{39.8}$$

where A, B, R_1, R_2, ω are coefficients calibrated with the experimental data. V is dimensionless volume defined as $V = \rho_0/\rho$. For mixed cells, pressure and temperature equilibrium is imposed, that is, they are equal between different phases.

SURF uses the crossing of the Hugoniot function h with value zero:

$$h = e - e_0 - 0.5\left(P + P_0\right)\left(V_0 - V\right), \tag{39.9}$$

to detect the lead shock, and thus determine P_s. Here e is specific energy, $V = 1/\rho$ is the specific volume here, and P the pressure. The subscript zero denotes initial values. The burn rate in SURF, $\dot{\lambda}$, is calculated from

$$\dot{\lambda} = 1 - e^{-s^2};\ \frac{ds}{dt} = f\left(P_s\right), \tag{39.10}$$

$$\lambda = \mathrm{g}\left(\mathrm{s}\right) = 1 - \mathrm{e}^{-s^2};\ \frac{\mathrm{ds}}{\mathrm{dt}} = \mathrm{f}\left(\mathrm{P_s}\right)$$

where s is the ratio of the burn radius divided by the separation between hotspots, P_s is leading shock pressure, and f has a relatively complicated expression, but it most important dependence is given by an exponential function of the lead shock pressure:

$$f \sim e^{(A+B\cdot P_s)}, \tag{39.11}$$

where A and B are the two parameters to be calibrated for each HE. To account for the release wave effects mentioned earlier, the burn rate $\dot{\lambda}$ is modified as

$$\dot{\lambda}_{with\ release} = \dot{\lambda}\cdot\left(\mathrm{MIN}\left(\frac{P}{P_s}, 1\right)\right)^n. \tag{39.12}$$

Thus, a single additional material parameter n is included to account for release wave effects.

That the lead shock P_s naturally accounts for the shock desensitization is illustrated pictorially as in Fig. 39.1, which shows two scenarios. The vertical lines representing shock wave traveling from left to right that will sweep across the HE containing voids. The first case has two shocks, with a weak lead shock (the shorter line) followed by a second strong shock.

Fig. 39.1 Illustration of shock desensitization due to the hot-spot mechanism. Left sketch (first case in the text) has a weak leading shock followed by a strong shock, which has the same strength as the single leading shock of the right sketch (second case mentioned in the text). The vertical line stand for shocks travelling through the HE from left to right. The shorter vertical line represents the weak shock

In the second case there is no weak lead shock, but only a single shock with the same strength as the strong shock in case 1. Intuition would say that the first case would certainly result in a detonation if the second case did, since more input shock energy is applied to the explosive. However, due to the hot-spot shock desensitization mechanism, explained earlier, the lead weak shock can close voids without igniting it. It is for this reason that Eq. (39.11) only has the lead shock P_s.

Calibration of Surf and Simulations

We calibrate SURF with 1-D plate impact experiments of Gustavsen and Dattelbaum [5] as shown in Fig. 39.2. The flyer impactor is thrown at different speeds into the PBX target. Embedded gauges are used to measure the arrival of the shock waves at different depths in the target. The middle figure shows an idealized build up to detonation process. Each curve corresponds to a different gauge. The run distance in the target to the build-up of a full propagating detonation is reflected in the Pop Plot (third figure on the right). The higher the flyer's speed (thus the higher initial shock stress), the shorter the run distance.

There are two ways to calibrate SURF: one is to use the full gauge profiles (Fig. 39.2, middle) and the other one is to calibrate it with only the information contained in the experimental Pop Plot (Fig. 39.2, right). Since there are only two free parameters (A and B in Eq. (39.11)) to be calibrated, we only need two experimental cases to determine the parameters A and B. We can then test our calibration by using any remaining experiments (typically a few dozen experiments). If A and B can be universally applied to the rest of the experiments, we gain confidence in SURF and our calibration. In practice, we usually adjust A and B to *best fit* most of the data (excluding outliers). Fig. 39.3 shows typical agreement between simulation and experiments data, with the third figure being a short shock (1.6 mm flyer) comparison, which also agrees reasonably well.

Simulations tend to have a higher peak velocity than the experiment. This is due to insufficient resolution in the experiment to fully resolve the so-called von Neumann spike. While not shown, many other cases have similar agreement. Consequently, SURF fits SDT experiments well with a single set of material parameters, A and B, of Eq. (39.11). Fitting the velocity profile data requires much more effort than fitting with the Pop plot, but the effort is worthwhile.

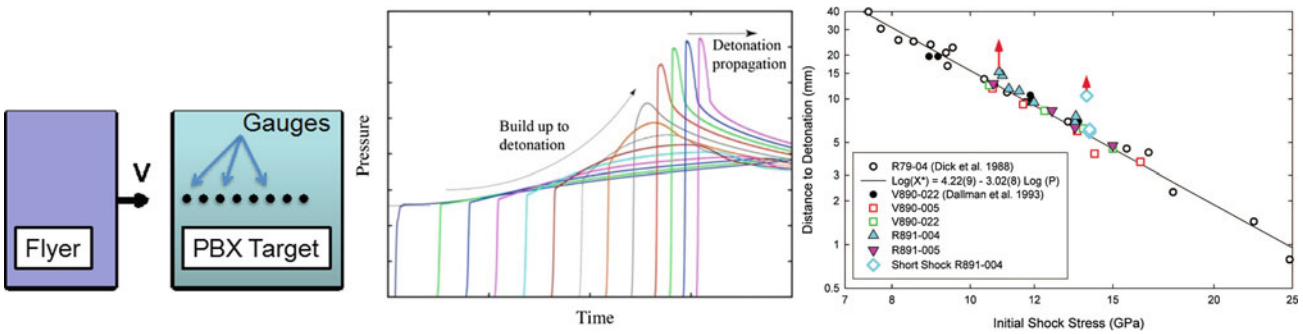

Fig. 39.2 (Left) Schematic of the experiment plate impact set-up used to calibrate SURF. (Middle) shock build-up-to-detonation pressure profiles for a series of gauges, (Right) Experimental Pop Plot for PBX 9502 [5]

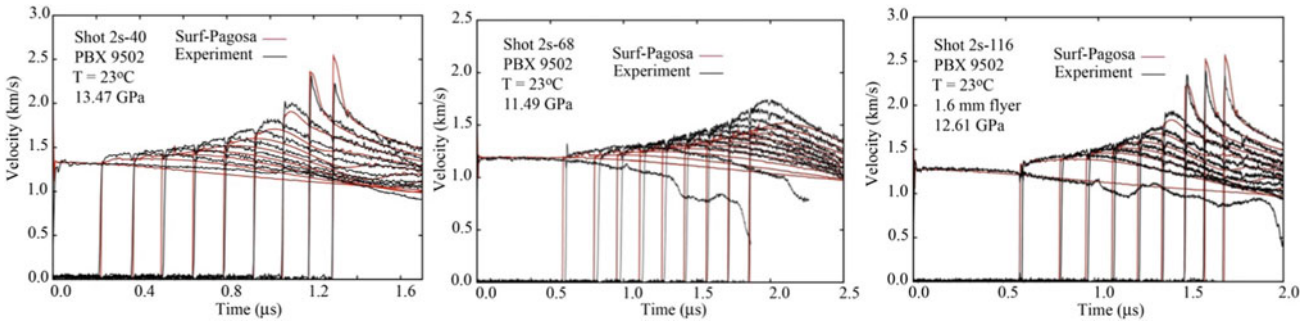

Fig. 39.3 Comparison between calibrated SURF simulations and experimental data. The smooth lines are from simulation, the slightly more noisey lines are from experiment measurements. The third plot is for short shock with 1.6 mm thin flyer (non-supportive shock wave)

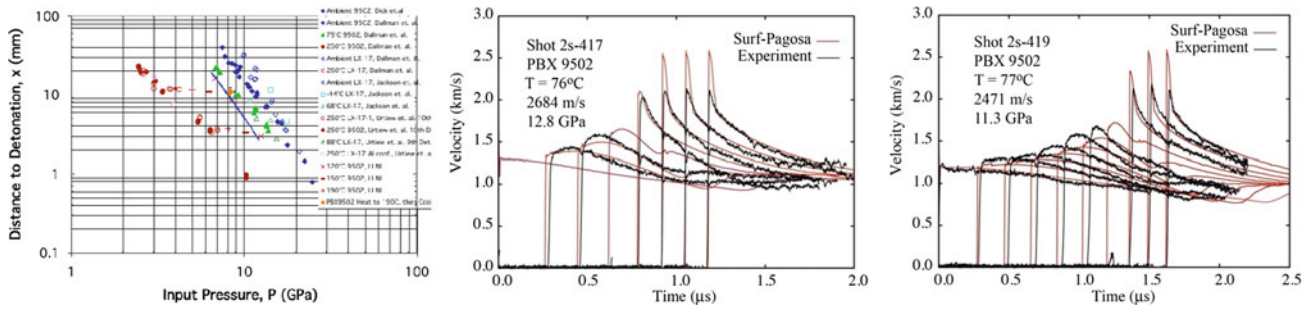

Fig. 39.4 Left: Pop Plot from LLNL report [6] showing the increased sensitivity of HE at elevated temperature. Middle and Right: Comparing simulations with experimental data at elevated temperature [5] for two cases after recalibration of the parameters

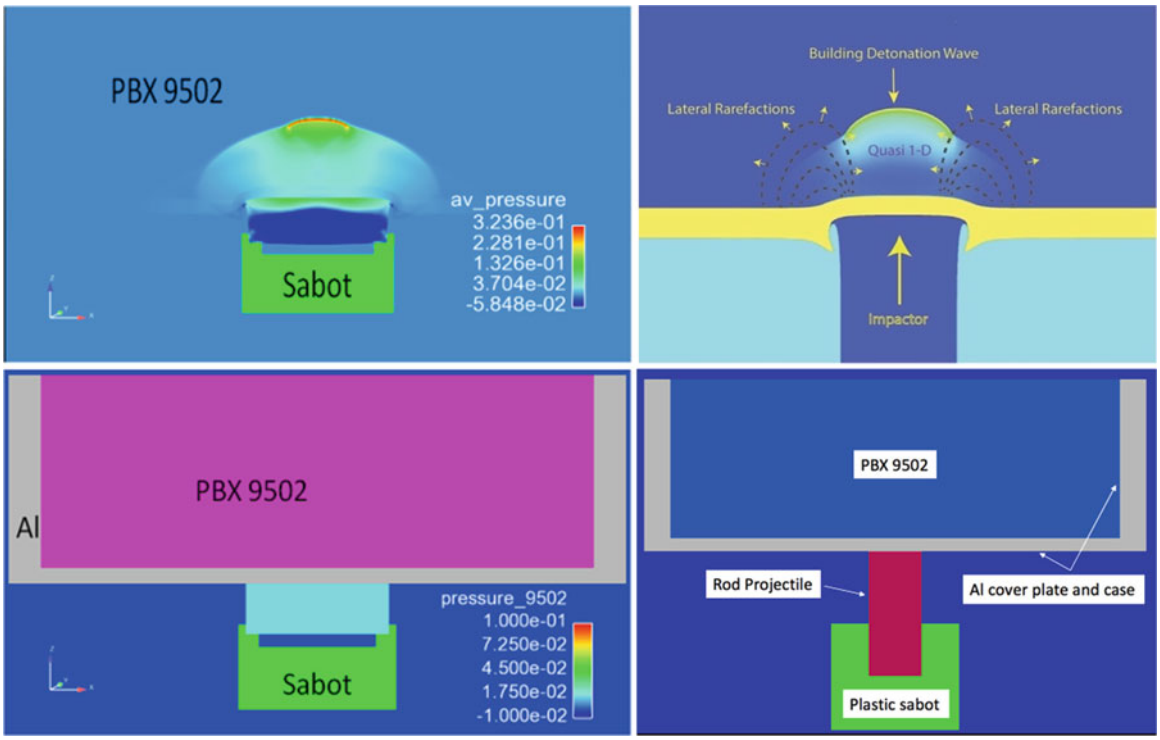

Fig. 39.5 Experimental design to study two-dimensional release wave effects from back (bottom left) and from sides (bottom right). The exact set-up is used for both experiment and simulations, even including details of the sabot containing the flyer. (top left) Simulated pressure field resulting in a weak detonation shock (red arch about 0.3Mbar), that eventually extinguishes from the influence of release waves. For the case shown, the flyer velocity is at the threshold of "go" / "no-go" condition. (Top right) figure depicting release waves for the thin rod case

It has long been known that elevated initial temperature can increase the sensitivity of HEs [6] as shown in Fig. 39.4. The increased sensitivity of HE at elevated temperatures can be modeled by recalibration of the material parameters (A and B in Eq. (39.11)). This would be important for fragments striking an explosive in the environment of a fire. For PBX 9502 we show wave profiles up to 77 °C (Fig. 39.4, Middle and Right). Note that the Pop Plot has been extended to 250 °C for PBX 9502. Surf can handle the temperature dependence up to 77 °C with a simple linear temperature scaling of one of its material parameters, as seen in Fig. 39.4 (Middle and Right) where the simulation and experiment agree well. Similar calibrations have been done for other explosives, including PBX 9501 and Composition B used in the forthcoming discussions.

We now apply the one-dimension-calibrated SURF model to investigate fragment and ball impact. As stated previously, the n parameter in SURF in Eq. (39.12) accounts for the two- and three-dimensional release wave effects. Experiments using a thin disk (Fig. 39.5, bottom left) are used to study release waves from the back surface (similar to short shocks) while a long thin rod are used to study the release wave effects originating from the lateral sides as shown in the bottom right figure.

The top right figure in Fig. 39.5 explains the situation. Near the center of the impact, a cylindrical quasi 1-D shock region exixts. This is basically the 1-D compression regime used in our previous calibrations. Laterial release waves reduce the

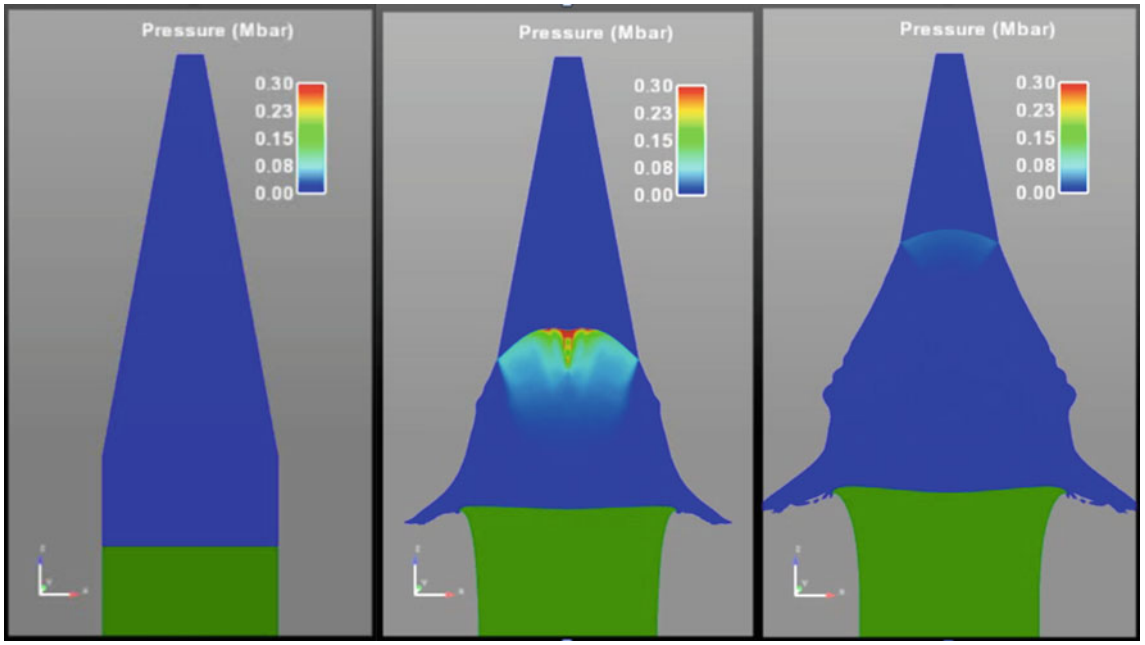

Fig. 39.6 Detonation failure diameter test. The green rod is the impact striker and the blue represents the HE. The evolving pressure field is shown

pressure required to achieve a detonation. By altering the parameter n in Eq. (39.12) we can adjust the strength of the release waves to make SURF predictions agree with the corresponding experiment. The set-up of both experiment and simulation are made as close as possible. In Fig. 39.5 (top left) we show the pressure field for one particular case. This is a critical condition close to the threshold of 'go' / 'no-go', which tends to be sensitive to the geometry and fragment projectile. The experiment corresponded to a no-go. We adjusted the strength of n to make SURF agree with the experiment (a value of $n = 5$). We then found that the same single value of n would gave agreement with a wide range of fragment-type experiments. Our conclusion supported the notion that the simple modification of SURF as expressed in Eq. (39.12) was sufficient. This gave us a comprehensive grasp of the parameter n in SURF and its ability to account for two- and three-dimensional effects for real applications.

As an aside, a release wave can extinguish a detonation if the rod diameter in a fragment impact is too small. The same is true if the HE diameters is too small and the explosive is laterally unconfined. This is the essence of the failure diameter of an explosive. Figure 39.6 shows a tapered HE in a high-speed impact simulation. The impact is such that initially there is a strong detonation. As the detonation propagates down the length of the tapered cylinder, the detonation weakens and at some point dies. This is measure of the failure diameter of the explosive. It also provides a challenging test for a HE burn model. It reflects the competition between the release wave from the side and pressure build-up at the detonation center. Figure 39.6 shows the Pagosa simulation with SURF. The left frame is the initial state. The impact striker (lower green) moving upwards strikes the HE (blue). The middle frame shows that, after a run to detonation distance is reached, the HE is fully detonated. However when the detonation wave travels upward a further, release waves quench the detonation as shown on the right frame.

We also studied 1/2 inch and 5/8 inch diameter ball impacts and compared with associated experiments [7] performed earlier. This was done for the explosive PBX 9501. A SURF simulation with impact velocity 1882 m/s is shown in Fig. 39.7, showing the details of the impact event. Note the presence of the dead zone predicted by SURF.

Simulations matched all the experimental shots [7] predicting either a "go" or "no-go" result for both ball diameters. In several cases, SURF simulations matched even the details of the pin data as show in Fig. 39.8. In the experiment, pins are used to record the arrival time of the detonation. Three sets of pin rails (each pin rail has seven pins) are placed down the length of the cylinder. The three pin rails are displaced by an angle of 120° between them. A ball striking exactly at the center line of the cylindrical system would have all three pin rails recording identical arrival times. On the other hand, the three sets of pin rails giving slightly different arrival times implies that the ball missed the centerline. In our simulation we measured the shock arrival at identical positions to the seven pins, labelled 1 to 7, according to the experiment. Figure 39.8 shows our pin location, a 3-D SURF simulation (centerline impact) and the experimental pin record for all three pin sets. Note, most of our simulations assumed axial symmetry. It is clear from Fig. 39.8 that the experimental records of the pin

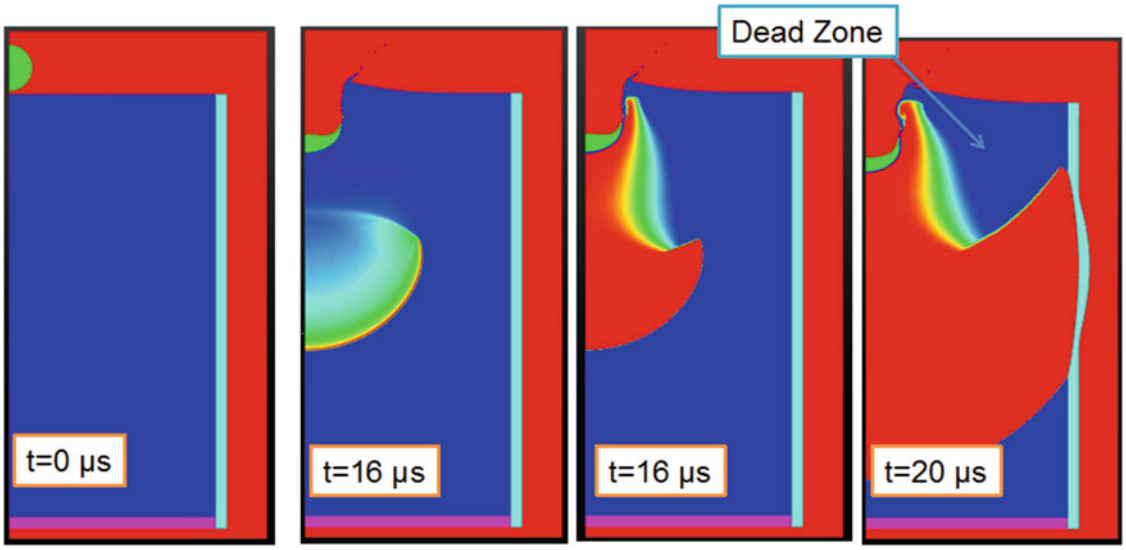

Fig. 39.7 Ball impact simulation, showing half of an axial symmetric simulation. From left to right: 1) t = 0 μs set-up; 2) pressure field at t = 16 μs showing the propagating detonation wave; 3) the corresponding burn fraction burn fraction at t = 16 μs (red indicates that the explosive is totally burned, while blue is unburned explosive); 4) burn fraction field at t = 20 μs. The dead zone is clear as labeled

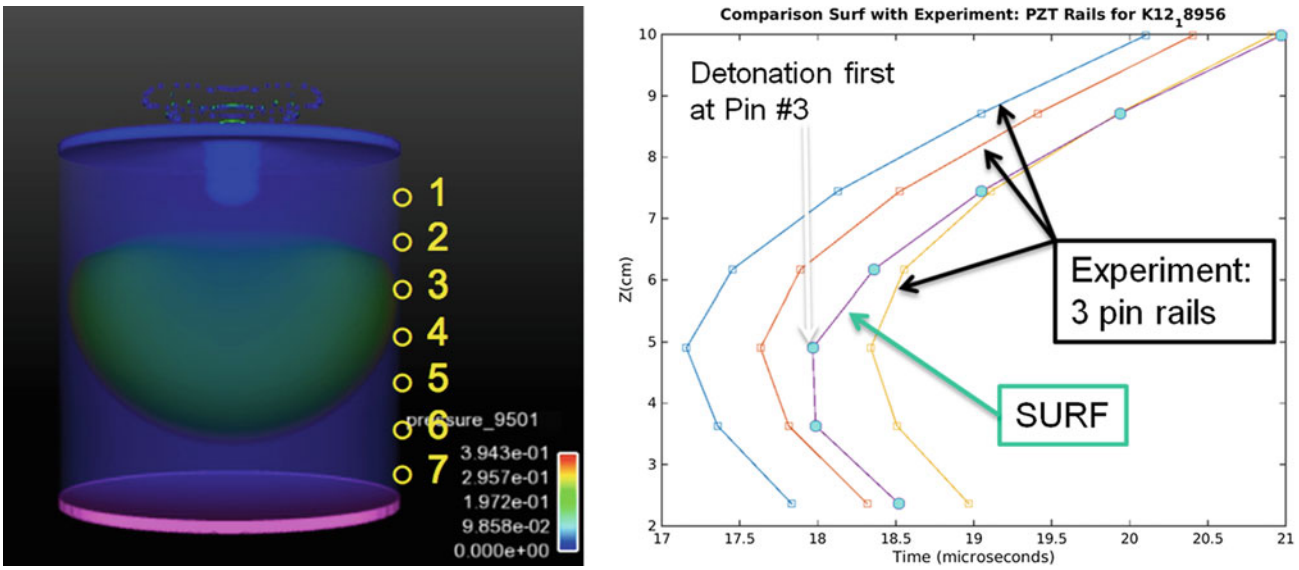

Fig. 39.8 A spherical ball projectile penetrates the cover plate of encased PBX 9501. The left figure is a Pagosa SURF 3-D simulation with pins used to detect detonation shock arrival times as labeled from 1 to 7. In the right figure, pin data (shock arrival time vs. pin position Z) are compared to the experiment [7]

rails do not overlap by a shift of about a microsecond. This uniform shift is easily accounted for by the ball slightly missing the centerline in the experiment. Another point worth mentioning is that the lines formed by the pin loci are curved back in both the experiment and the simulation. The 3-D simulation shown in Fig. 39.8 easily explains this. Because the build-up-to detonation process requires a run distance into the HE, the fully-formed detonation actually reaches the pin located at position 3 before it reaches pins at location 1 and 2.

We conclude this section with a comment regarding real fragment impact applications. After careful and extensive study of SURF as it is implemented in Pagosa on simple geometry, we can now compute more complicated problems. Fig. 39.9 shows an example of an oblique impact of covered Composition B explosive with a steel flyer. In this simulation the pressure shows that the impact results in a full detonation.

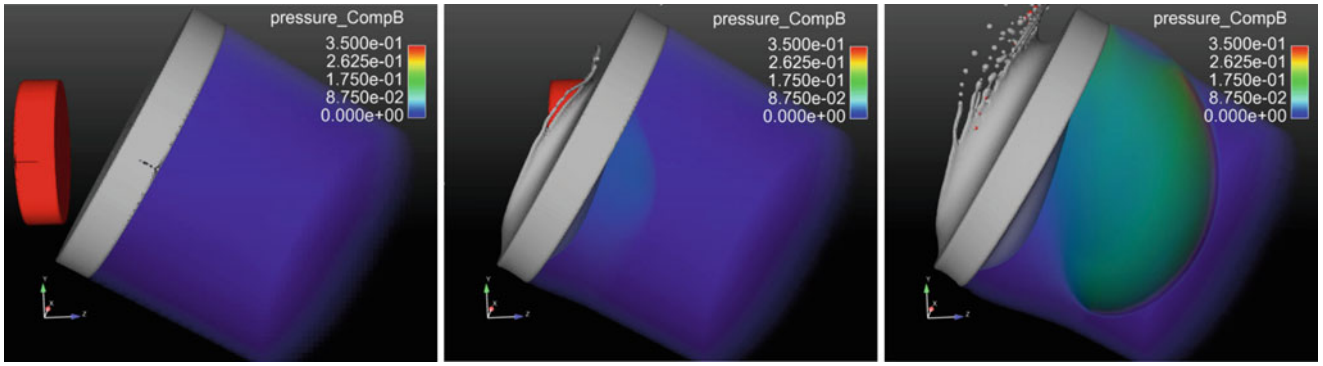

Fig. 39.9 Pagosa SURF simulation of three-dimensional oblique fragment impact. (left) set-up of the simulation; (middle) the fragment penetrates the cover plate and begins to build to a detonation; (right) a propagating detonation shock

Conclusion

SURF has been shown to accurately model plate impact experiments (used for calibration) with a minimal number of parameters. It captures the entire SDT process, including that observed with short shocks. We implemented SURF into the Eulerian code Pagosa and studied two- and three-dimensional release wave effects based on Eq. (39.12). This research was supported by an experimental team and portions were previously published [8, 9]. SURF has then been shown to successfully model ball and fragment impact on PBX 9501 and PBX 9502, as well as other explosives.

Acknowledgements This work was funded by ASC-PEM-HE and ASC Safety Program. We gratefully thank Tariq Aslam, Mike Burkett, and Brandon Smith for their support of the project. We also thank the experimental fragment impact team of Lee Perry and plate impact team of Rick Gustavsen and Dana Dattelbaum. Finally, we thank Ralph Menikoff and Sam Shaw for discussions on the SURF model.

References

1. Fields, J.E., Bourne, N.K., Palmer, S.J.P., Walley, S.M., Smallwood, J.M., Gray, P.: Hot-spot ignition mechanisms for explosives and propellants. Philosophical Transactions of the Royal Society A, Mathematical, Physical and Engineering Sciences. 15 May 1992. https://doi.org/10.1098/rsta.1992.0034
2. Tarver, C.M., Chidester, S.K., Nichols III, A.L.: Critical conditions for impact- and shock-induced hot spots in solid explosives. J. Phys. Chem. **100**, 5794–5799 (1996)
3. Handley, C.A., Lambourn, B.D., Whitworth, N.J., James, H.R., Belfield, W.J.: Understanding the shock and detonationresponse of high explosives at the continuum and meso scales. Appl. Phys. Rev. **5**, 011303 (2018). https://doi.org/10.1063/1.5005997
4. Menikoff, R., Shaw, M.S.: The SURF model and the curvature effect for PBX 9502. Comb. Theory Model. (2012). https://doi.org/10.1080/13647830.2012.713994
5. Gustavsen, R.L. et al.: Embedded electromagnetic gauge measurements and modeling of shock initiation in the TATB based explosives PBX 9502 and LX-17. LA-UR-01-3339
6. Chidester, S.K., et al.: Shock Initiation of Damaged Explosives, (2009). LLNL report LLNL-CONF-418560 https://e-reports-ext.llnl.gov/pdf/380356.pdf
7. Pemberton, S.J. et al.: PBX-9501 SMIS shots with 1/2 inch and 5/8 inch round ball ammunition. LANL report: LA-UR-11-06457
8. Lee Perry, W., Clements, B., Ma, X., Mang, J.T.: Relating microstructure, temperature, and chemistry to explosive ignition and shock sensitivity. Combust. Flame. **190**, 171–176 (2018)
9. Clements, B., Ma, X., Perry, L., Rae, P., Armstrong, C., Haroz, E., Dickson, P.: Shock Initiation Response of PBX 9502 Considering Rarefaction Wave Effects, Proceedings of the 16th Internation Detonation Symposium (in press)